

Mathematical modelling of information processing in the olfactory bulb

Andrew P. Davison
King's College

A dissertation submitted to the University of Cambridge
for the degree of Doctor of Philosophy

December 2000

Declaration

This dissertation is not substantially the same as any I have submitted for a degree, or diploma, or any other qualification at any other university. No part of my dissertation has already been or is being concurrently submitted for any such degree, diploma or other qualification. It is the result of my own work, and includes nothing which is the outcome of work done in collaboration.

Andrew Davison

December 2000

*To my wife Melanie,
who has supported me throughout
with encouragement, tolerance,
understanding and love.*

Contents

Declaration	ii
Contents	v
List of Figures	viii
List of Tables	x
Abstract	xi
Acknowledgments	xii
Abbreviations	xiii
1 Introduction	1
1.1 Olfactory anatomy and physiology	2
1.1.1 Anatomy of mammalian olfactory systems	2
1.1.1.1 Olfactory epithelium	2
1.1.1.2 Bulb size and lamination	2
1.1.1.3 Glomeruli	2
1.1.1.4 Periglomerular cells	2
1.1.1.5 Mitral and tufted cells	4
1.1.1.6 Granule cells	4
1.1.1.7 Short-axon cells	4
1.1.1.8 Projections to cortex and axon collaterals	4
1.1.1.9 Centrifugal inputs	5
1.1.1.10 Accessory olfactory bulb	5
1.1.2 Non-mammalian olfactory systems	5
1.1.3 Responses of the olfactory bulb to electrical and odour stimulation	5
1.1.3.1 Electrical stimulation	5
1.1.3.2 Odour stimulation	6
1.1.3.3 Spatial distribution of activity	6
1.1.3.4 Oscillations and synchronization	6
1.1.4 The olfactory code	7
1.2 Review of olfactory bulb modelling	9
1.2.1 Network modelling	9
1.2.2 Modelling of individual components	11
1.3 A strategy for modelling the olfactory bulb	12
1.4 Thesis outline	13

2 Reduction of compartmental models	15
2.1 Introduction	15
2.2 Method	16
2.2.1 Mitral cell models	16
2.2.1.1 Modification of the Bhalla-Bower model	16
2.2.1.2 Description of reduced models	16
2.2.1.3 Fitting the models	20
2.2.2 Granule cell models	22
2.2.2.1 Description of reduced models	22
2.2.2.2 Fitting the models	22
2.2.3 Numerical methods	24
2.3 Results	24
2.3.1 Mitral cell model	24
2.3.1.1 Fitting to the spike shape	24
2.3.1.2 Fitting to spike times	24
2.3.1.3 Simulation time	30
2.3.2 Granule cell model	30
2.3.2.1 Fitting to spike times	30
2.3.2.2 Simulation time	30
2.4 Discussion	33
3 Mitral cell interactions	35
3.1 Introduction	35
3.2 Direct mitral-mitral inhibition	37
3.2.1 The integrate-and-fire model	37
3.2.2 Existence of phase-locked solutions	37
3.2.2.1 Derivation of return map	38
3.2.2.2 Equilibrium time lags	40
3.2.2.3 Stability of phase-locked solutions	40
3.2.2.4 Threshold of 1:1 firing	41
3.2.3 Harmonic (mode) locking	42
3.2.4 Suppression	44
3.2.5 Alternative synaptic models	44
3.2.6 Conductance-based synapses	47
3.2.7 Reduced biophysical mitral model	51
3.3 Inhibition via an interneurone	53
3.3.1 The model	53
3.3.2 Perfect integrator	53
3.3.3 Leaky integrator	57
3.3.4 Biophysical interneurone model	58
3.4 Discussion	64
4 An olfactory bulb network model	67
4.1 Introduction	67
4.2 Description of the model	67
4.2.1 Cells	67
4.2.2 Synapses	68
4.2.2.1 Which synapses to include	68
4.2.2.2 Synaptic models	69
4.2.2.3 Synaptic parameters	70
4.2.3 Connections	71
4.2.3.1 Connection statistics	71
4.2.3.2 The scaling problem	73

4.2.4	Input	73
4.2.4.1	Sensory input	73
4.2.4.2	Centrifugal connections	74
4.3	Numerical methods	74
4.4	Response to olfactory nerve shock	76
4.4.1	Introduction and Methods	76
4.4.2	Results	76
4.4.2.1	Contributions of AMPA and NMDA receptors	76
4.4.2.2	Effect of $[Mg^{2+}]$	79
4.4.2.3	Extended stimulus	79
4.4.2.4	Influence of network connectivity	79
4.4.3	Discussion	81
4.5	Response to odour stimulation	86
4.5.1	Introduction and Methods	86
4.5.2	Results	87
4.5.2.1	Effect of odour intensity	87
4.5.2.2	Effect of varying the ratio of granule:mitral cells	89
4.5.2.3	Responses to similar odorants	89
4.5.3	Discussion	96
5	Discussion and Conclusions	101
5.1	Comparison of the model with the real bulb	101
5.2	Validity of the model	102
5.2.1	Validity of detailed single-cell models	102
5.2.1.1	Morphology	102
5.2.1.2	Active channel properties	102
5.2.2	Validity of simplified models	105
5.2.3	Validity of the network model	105
5.3	Conclusions	105
5.4	Further work	106
A	Mathematical appendix	109
A.1	Calculation of inter-spike-interval envelope for harmonic locking	109
A.2	Periods and time lags for alternative synaptic models	111
B	Program listings	115
B.1	Mitral cell model	115
B.2	Granule cell model	116
B.3	Olfactory bulb network model	116
References		121

List of Figures

1.1	The principal neurones of the olfactory epithelium and olfactory bulb, their connections and their locations	3
1.2	A schematic representation of the results of Yokoi <i>et al</i>	8
1.3	A representation of the hypothesized mapping of ‘physical/chemical’ odour space onto a ‘behaviourally-important’ odour space	9
2.1	Response of full mitral cell model to current input, with varying potassium conductance	17
2.2	Comparison of regions in the full and reduced mitral models	18
2.3	Schematic of four-compartment mitral cell model	19
2.4	Comparison of synaptic input with constant current approximation	21
2.5	Schematic of the three compartment granule cell model	23
2.6	Somatic membrane potential trace for full and reduced models with $I_{\text{full}} = 0.4 \mu\text{A cm}^{-2}$ after fitting to spike shape	25
2.7	Somatic membrane potential trace for full and reduced models with $I_{\text{full}} = 0.8 \mu\text{A cm}^{-2}$ after fitting to spike shape	26
2.8	Comparing fit-to-shape to fit-to-time for the four-compartment model	27
2.9	Somatic membrane potential trace for full and four-compartment models after fitting to spike timing	28
2.10	Comparing reduced models with two, three and four compartments, with fit-to-time parameters	29
2.11	Comparing reduced and full granule cell models: firing frequency as a function of injected current	30
2.12	Comparing reduced granule cell models with two and three compartments	31
2.13	Somatic membrane potential trace for full and three-compartment granule cell models . .	32
3.1	Two mitral cell system with direct and indirect inhibition	36
3.2	Possible firing patterns of two neurons with inhibitory connections	38
3.3	The return map for 1:1 firing	39
3.4	Time lags and firing periods for A and B types of 1:1 firing as functions of α	41
3.5	Transitions from Type A to Type B firing and from Type B firing to harmonic locking .	42
3.6	Thresholds of A- and B-type firing in terms of α , as functions of δ	43
3.7	Return map for 8:7 firing	43
3.8	Bifurcation diagram for equilibrium inter-spike intervals as a function of α	45
3.9	Bifurcation diagrams of T_1 and T_2 for various parameter values.	46
3.10	Bifurcation diagram of time lag t_L^n as a function of α	47
3.11	The number of spikes in Cell 2 in one repeat period as a function of α	48
3.12	Maximum/minimum inter-spike interval envelope	49
3.13	Equilibrium phase lags for A- and B-type 1:1 firing, as functions of α , for various forms of synaptic interaction	49
3.14	α -thresholds for A- and B-type 1:1 firing, as functions of δ , for various forms of synaptic interaction	50
3.15	Thresholds for suppression in δ -space, as functions of α	50

3.16 Effect of varying synaptic decay time τ_s on firing patterns	51
3.17 Comparison of voltage-step and conductance-change synapses	52
3.18 Bifurcation diagrams of ISI and time lag vs. α for the two-cell model with reduced mitral cells, weak coupling	54
3.19 Bifurcation diagram of time lag vs. α for the two-cell model with reduced mitral cells, strong coupling	55
3.20 Bifurcation diagram of time lag vs. \bar{g}_s for the two-cell model with reduced mitral cells . .	56
3.21 Bifurcation diagram of inter-spike interval vs. alpha for a high level of input to Cell 2 . .	56
3.22 Bifurcation diagram for T_1 and T_2 as functions of α for the three-cell system with non-leaky interneurone	58
3.23 Bifurcation diagram and firing rates as functions of α for the three-cell leaky integrator model	59
3.24 Bifurcation diagrams of ISI and time lag vs. α for the three-cell, biophysical model with large \bar{g}_E	60
3.25 Bifurcation diagram of time lag vs. \bar{g}_I for the three-cell, biophysical model, large \bar{g}_E	61
3.26 Bifurcation diagrams of ISI vs α for the three-cell, biophysical model with large \bar{g}_E and large \bar{g}_I	62
3.27 Bifurcation diagrams of ISI and time lag vs. α for the three-cell, biophysical model with small \bar{g}_E	63
4.1 The mitral and granule cell arrays	71
4.2 The effect of integration parameters on accuracy	75
4.3 Response of the network to glomerular stimulation	77
4.4 The contribution of AMPA and NMDA receptors to the network response	78
4.5 The effect of magnesium on the mitral cell IPSC	80
4.6 Response of the network to an extended stimulus	81
4.7 Effect on response to glomerular stimulation of changing the number of synapses	82
4.8 Effect on response to glomerular stimulation of changing the number of granule cells while keeping the number of synapses per mitral cell constant	83
4.9 Effect on response to glomerular stimulation of changing the number of granule cells and the number of synapses per mitral cell to keep the average number of synapses per granule cell constant	84
4.10 Determination of time lags	86
4.11 Response of the mitral-granule network to a simulated odour stimulus	88
4.12 The effect of input intensity on mitral cell response: Mitral cell raster plots	90
4.13 The effect of input intensity on mitral cell response: Spike-time histograms	91
4.14 Effect of input intensity on synchronization indices	92
4.15 Effect on synchronization of changing the ratio of granule:mitral cells	93
4.16 Comparison of inputs and outputs for two similar odours, with a dense odour mapping . .	94
4.17 Comparison of inputs and outputs for two similar odours, with a sparse odour mapping .	95
4.18 Granule cell raster plots with different odour→input mappings and different connection ranges	97
4.19 Granule cell raster plots for stimulation with two similar odours	98
5.1 Activation and steady-state inactivation curves for the granule cell KA channel	104
A.1 The minimum firing period for Cell 2, for a given α	110
A.2 Illustration of T_2^{\min} when n_1/n_2 is just less than 2.00	112

List of Tables

2.1	Channel distribution for the reduced mitral cell models	20
2.2	Channel distribution for the reduced granule cell models	23
2.3	Best fit parameter values for reduced mitral cell models	25
2.4	Best fit parameter values for reduced granule cell models	30
4.1	Summary of network model parameters	70
4.2	Summary of the effects of changing network parameters on the model response to a glomerular shock stimulus	79
4.3	Parameters used to assess effect of number of granule cells on network synchronization	89
5.1	Comparison of mitral cell channel parameters from Bhalla and Bower (1993) and Wang <i>et al</i> (1996)	103
5.2	Comparison of granule cell channel parameters from Bhalla and Bower (1993) and Schoppa and Westbrook (1999)	104

Abstract

The aim of this dissertation is to investigate the processing of sensory signals in the mammalian olfactory bulb, using analysis and computer simulation of mathematical models. A biologically-detailed mathematical model provides a framework which integrates the results of experiments at different levels of enquiry, and enables study of problems which cannot easily be addressed using only the methods of experimental neuroscience.

Specific biological and computational problems which are addressed include: the existence, origin and role of oscillations/synchronization; how the properties of individual cells/synapses influence the network behaviour; the role of lateral inhibition; how the connectivity between cells influences network behaviour.

The dissertation has four main parts: (i) a review of the anatomy and physiology of vertebrate olfactory systems, and of previous modelling studies of the olfactory bulb; (ii) development of biophysical models of the principal neurone types of the olfactory bulb, based closely on experimental data, but simple enough to allow simulation of large networks; (iii) an examination of the fundamental interaction in the bulb – that between two mitral cells – using simulation of the biophysical cell models and analysis of the simpler integrate-and-fire neurone model; (iv) development of network models of the olfactory bulb incorporating the biophysical neurone models. These are tested using experimental data from the literature, and then the properties of the network are studied, leading to predictions which could be tested experimentally.

Acknowledgments

I have been extremely fortunate in having had twice the normal complement of guidance through my PhD studies. Jianfeng Feng, my supervisor, and David Brown, my mentor, have brought different perspectives and skills which together have greatly enriched my understanding of what it is we're trying to do by modelling biological systems, and of how best to do it. A great many thanks to you both.

Thanks also to the people with whom I've shared a Lab and afternoon coffee for the past three years: to Stuart Feerick and Guibin Li for making the computer systems so easy to use; to Stuart also for his wonderfully cynical wit and for introducing me to Perl; to Peter Roper for many conversations about mathematics, neuroscience, trans-Atlantic relocation and life in general. And thank you all guys, for the many coffees you bought me when I'd forgotten my GiroVend card!

I'd like to thanks the organisers of the Crete Course in Computational Neuroscience, for enabling me to attend a course which had a profound influence on the direction of my research, and which introduced me to many kindred spirits (Marshall, Jonathan, Volker...) and to a beautiful island. Very importantly, I'd like to thank Michael Hines, author of NEURON, for an intuitive and powerful tool without which this thesis would have been very different.

Last but by no means least are my family and friends. Ben and Emma, Chris and Laura, thank you for your friendship and hospitality, which have made our life 'down South' so much more enjoyable. Mam and Dad, thank you for the support and encouragement you've given me during this period, especially the last few months. To Melanie, my wife, I owe the deepest debt of gratitude, not least for helping me keep a sense of perspective about the whole thing. This dissertation is for you.

Abbreviations

ACh	acetylcholine	ISI	inter-spike interval
AL	antennal lobe	LIF	leaky integrate-and-fire
AMPA	α -amino-3-hydroxy-5-methyl- -4-isoxazolepropionic acid	LFP	local field potential
AOB	accessory olfactory bulb	LVTS	local variable time step
CF	connection fraction	MCF	mutual connection fraction
CNQX	6-cyano-7-nitroquinoxaline-2,3-dione	MCL	mitral cell layer
EEG	electroencephalogram	MRI	magnetic resonance imaging
EPL	external plexiform layer	mRNA	messenger ribonucleic acid
EPSC	excitatory post-synaptic current	MRR	molecular receptive range
EPSP	excitatory post-synaptic potential	NMDA	N-methyl-D-aspartate
FIBE	fully implicit backward Euler	OB	olfactory bulb
GABA	γ -aminobutyric acid	OE	olfactory epithelium
GCL	granule cell layer	ON	olfactory nerve
GL	glomerular layer	ONL	olfactory nerve layer
GVTS	global variable time step	OR	olfactory receptor
IPL	internal plexiform layer	ORN	olfactory receptor neurone
IPSC	inhibitory post-synaptic current	PG	periglomerular
IPSP	inhibitory post-synaptic potential	TTX	tetrodotoxin

Chapter 1

Introduction

How does the brain interpret the outside world? More specifically, what signals does the world induce in sensory cells and how are these signals processed by the deeper layers of the brain? The mechanisms by which light, sound, pressure, force and environmental chemicals are transduced into electrical signals in the retina, cochlea, skin, tongue and nasal epithelium are now fairly well understood. What happens to these signals next, and to the information which they carry, is much less well understood, despite continuing and accelerating progress.

The root problem is the vast complexity of the central nervous system. Each of the billions of cells receives many hundreds of inputs and has many hundreds of output connections. Progress depends on identifying modules, sub-regions of the brain, within which the pattern of connections is more or less stereotyped. The main olfactory bulb (OB) is one such module, with many advantages as a system for studying neural information processing. The advantages are:

- The bulb receives direct sensory input – the olfactory receptor neurones synapse directly with neurones in the bulb. This means that the input to the bulb can be well characterised and is in contrast to other much-studied areas such as the hippocampus and visual cortex.
- The bulb has a very well defined laminar structure, is divided into functionally and anatomically distinct modules (the glomeruli and associated cells) and is mainly a feed-forward network with lateral interactions but few recurrent connections. There are only four principal neurone types. In summary, the bulb has a simple and well-defined structure.
- The olfactory stimulus is simpler than visual or auditory stimuli. Firstly, the dynamics of odour signals are generally slower. Secondly, a natural olfactory ‘scene’ contains usually only one or two ‘objects’, with two main properties–identity and intensity. A natural visual scene, by contrast, will usually contain several objects, each with several properties: size, shape, brightness, colour, texture, velocity and position in space. This suggests that the information carried by the olfactory signal is less.
- the bulb exhibits phenomena – field potential oscillations [1], spike synchronization [67], synaptic plasticity related to behavioural changes [17, 69] – which are of considerable interest in understanding neural coding in many brain regions.

An understanding of information processing in the olfactory bulb will require integration of data from numerous levels (sub-cellular, single neurone, local circuit, system) and modalities (molecular biology, neurophysiology, imaging, psychology) of investigation. Mathematical/computational modelling is a powerful and necessary tool for integration of these disparate strands of data. According to Bower (quoted in [115]), ‘*models based on the real anatomy and physiology of the nervous system ... constitute ... a compact and self-correcting database of neurobiological facts and functional relationships*’.

In this chapter I first summarize the anatomy and neurochemistry of olfactory systems, concentrating on mammalian systems. I then discuss the ‘olfactory code’ and highlight current unsolved problems in

our understanding of this. A review of computational modelling studies in the olfactory bulb leads to a proposal for a strategy for modelling the olfactory bulb which can shed light on some of the current problems, act as a framework for the integration of experimental findings and make experimentally-testable predictions. Finally, I list the specific aims of the research presented in this dissertation.

1.1 Olfactory anatomy and physiology

1.1.1 Anatomy of mammalian olfactory systems

The principal neurone types of the olfactory epithelium and olfactory bulb, and their connections, are shown in Figure 1.1.

1.1.1.1 Olfactory epithelium

The olfactory receptor neurones (ORNs) lie in a single-cell-thickness layer – the olfactory epithelium – in the inner, upper regions of the nasal passages. There are about 10^7 ORNs in the olfactory epithelium of rats [91]. The epithelium is covered by a mucus layer through which air-borne molecules diffuse until they reach the ORN cell membrane. ORNs are small bipolar neurones, with a single dendrite extending to the epithelium surface, from which several cilia project into the mucus layer. Odorant molecules bind to G-protein coupled receptors on the cilia surfaces. This leads to depolarisation of the neurone and action potential generation via a complex series of transduction events (see [18] for a detailed review). The temporal structure of the ORN response can be complex [39], but in general the frequency of action potential firing is an increasing function of odour concentration.

1.1.1.2 Bulb size and lamination

The axons of ORNs bunch to form the olfactory nerve (ON), which passes through a thin part of the skull – the cribriform plate – then innervates the main olfactory bulb. The olfactory bulb is shaped as its name suggests, and has a volume of about 9 mm^3 in mouse [111, 121], $20\text{-}30\text{ mm}^3$ in rat [57, 121] and 90 mm^3 in rabbit [121] (all figures are for adult animals). In common with most cortical regions it has a laminar structure. From outside in, the layers are the glomerular layer, the external plexiform layer (EPL), the mitral cell layer, the internal plexiform layer and the granule cell layer. The innermost part of the bulb, the olfactory tract, consists of mitral and tufted cell axons projecting to other olfactory areas.

1.1.1.3 Glomeruli

The ORN axons form synapses in the outermost layer of the bulb, the glomerular layer. This consists of several thousand well-defined neuropil (approximately 1800, 4200 and 6300 in mouse, rat and rabbit respectively [121]), called glomeruli, each comprising the axon terminals of ORNs, and the dendrites of mitral, tufted and periglomerular (PG) cells. Each ORN axon branches within a single glomerulus, with on average 27 terminals [71]. ORNs make excitatory, glutamatergic synapses onto PG, mitral and tufted cells. Mitral/tufted cells have both NMDA- and non-NMDA glutamate receptors. PG cell dendrites receive glutamatergic synapses from and make GABAergic synapses onto mitral/tufted cell dendrites within the glomeruli. The presence of GABA suggests that the action of PG cells on mitral/tufted cells is inhibitory, although there is some evidence that it is excitatory [89]. The PG cell population is functionally [117] and chemically [9, 50, 72] heterogeneous. Olfactory nerve axon terminals contain GABA_B receptors [16] which inhibit transmission from the ON to mitral cells [102], although ON axons do not receive chemical synapses [135].

1.1.1.4 Periglomerular cells

The periglomerular cells are small neurones (soma diameter 8–9 μm in hamster [86]) whose somata surround the glomeruli. They send dendrites into one or more nearby glomeruli, and axons to more

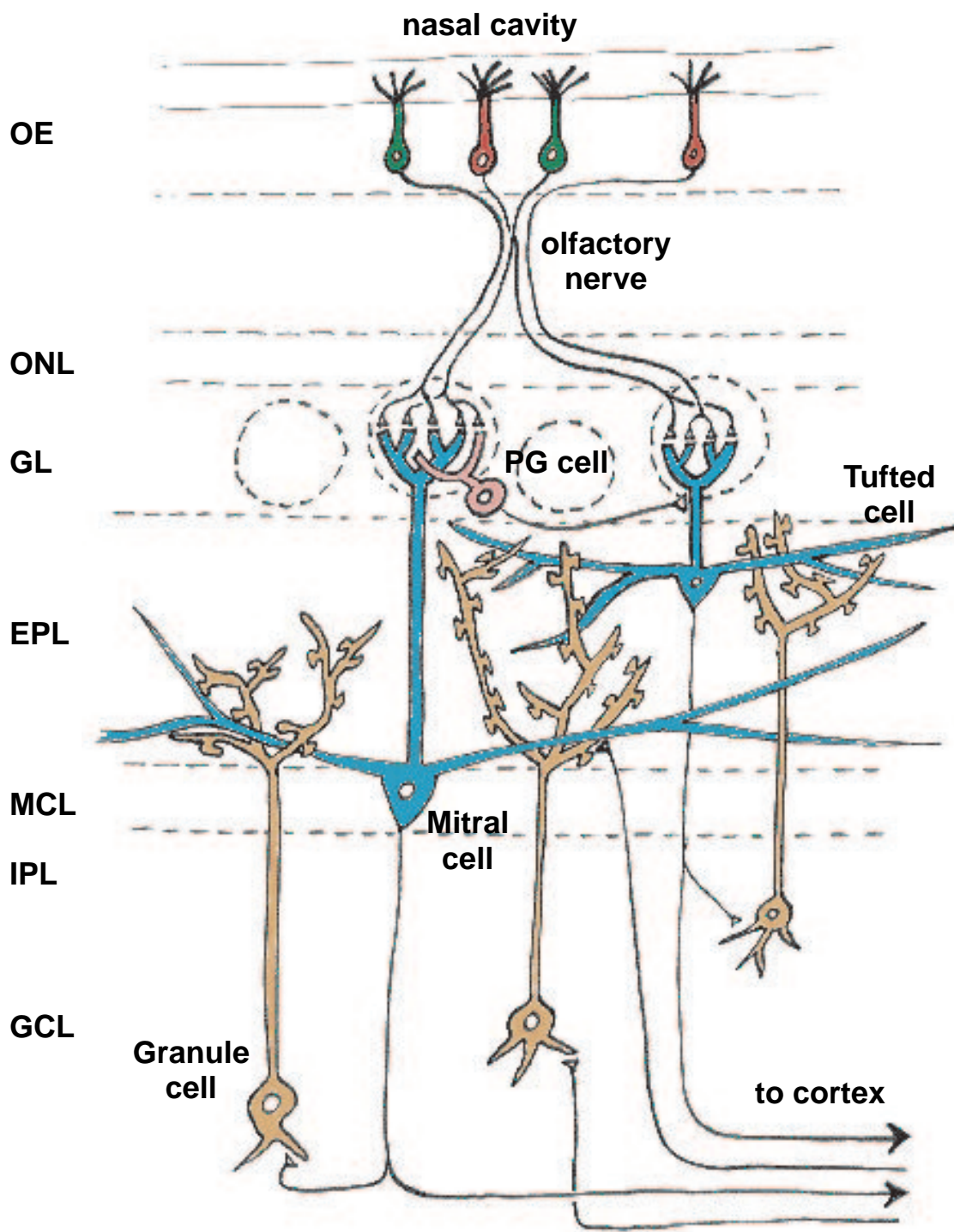


Figure 1.1: The principal neurones of the olfactory epithelium and olfactory bulb, their connections and their locations. Abbreviations: OE, olfactory epithelium; ONL, olfactory nerve layer; GL, glomerular layer; EPL, external plexiform layer; MCL, mitral cell layer; IPL, internal plexiform layer; GCL, granule cell layer.

distant glomeruli. There are about 10^6 PG cells in the rodent olfactory bulb [135], or about 500 per glomerulus.

1.1.1.5 Mitral and tufted cells

Mitral and tufted cells are the output neurones of the olfactory bulb – they are the only ones to send axons outside the bulb, to the cortex. Mitral and tufted cells both have a single primary dendrite which branches copiously within a single glomerulus, and several long (average length 1.2 mm in rabbits [94]), secondary (basal) dendrites which project radially from the soma, approximately parallel to the bulb laminae. Mitral and tufted cells are distinguished by their size, location and projection patterns. Mitral cells are larger and have their somata within a narrow band only a few cells wide – the mitral cell layer. Tufted cells are smaller (the total length of the secondary dendrites is 4000-5000 μm for middle tufted cells in rat and rabbit, compared to 15000-17000 μm for mitral cells [94, 106]) and have cell bodies distributed throughout the external plexiform layer. The differences in axonal projections and collaterals are discussed below. Both mitral and tufted cells have been divided into sub-classes, based on size, on the position of the soma and on the distribution of dendrites [86, 94, 106]. The number of mitral cells is in the region 40–60,000 in rodents [57, 107, 121] and in humans [13]. Tufted cells are 2–3 times as numerous [133].

1.1.1.6 Granule cells

The most numerous cell type in the olfactory bulb is the granule cell (around 5×10^6 per bulb [135]). These are small-bodied cells (soma diameter 6-8 μm [135]) with somata in the broad granule cell layer and dendrites extending outwards into the EPL, where they form reciprocal, dendrodendritic synapses with the secondary/basal dendrites of mitral and tufted cells. At these synapses mitral/tufted cells release glutamate and granule cells release GABA; granule cells have both NMDA and non-NMDA glutamate receptors; mitral/tufted cells have GABA_A receptors. Mitral/tufted cells also possess autoreceptors, although these may be extra-synaptic: NMDA [109], AMPA [108] and the mGluR1 metabotropic glutamate receptor [145]. It has been demonstrated that granule cells receive GABAergic synaptic input [152]. However, the identity of the presynaptic cells is not known. There is morphological evidence for gap junctions between granule cells in clusters [120]. The granule cell response to synaptic excitation is somewhat unusual, in that activation of the fast, AMPA receptors only is insufficient to produce action potentials in the neurone [63, 125], due to the presence of an A-type potassium current in the granule cell [126]; co-activation of both NMDA and AMPA receptors is required.

1.1.1.7 Short-axon cells

Short-axon neurones form a very small population, scattered in the granule cell layer. Little is known about their function (see reference [133]).

1.1.1.8 Projections to cortex and axon collaterals

Mitral and tufted cell axons group to form the lateral and medial olfactory tracts. These project to a number of cortical regions: the anterior olfactory nucleus, the olfactory tubercle, the piriform cortex, the cortical nucleus of the amygdala and the entorhinal area [36]. Tufted cell projections are more limited in extent, innervating only the anterior portion of the piriform cortex with no connections to the entorhinal cortex. The anatomy and function of the olfactory cortex are outside the scope of this dissertation, but two points are worth noting: firstly, the synapses onto the pyramidal neurones of piriform cortex (often regarded as the main olfactory cortical region [155]) are excitatory; secondly, extracellular recordings in piriform cortex show prominent 30-100 Hz oscillations. These are relevant in considering how the olfactory epithelium and bulb encode olfactory information, since it is the piriform cortex which first makes use of the signal from the bulb. Both mitral and tufted cell axons give off collaterals. The collaterals of tufted cells are distributed in the internal plexiform layer and superficially in the granule cell layer; those of mitral cells are distributed throughout the granule cell layer [70].

1.1.1.9 Centrifugal inputs

Central or centrifugal inputs come from several brain regions. Cholinergic fibres originating in the basal forebrain have a number of targets in the OB. These axons form synapses with periglomerular and granule cells. Acetylcholine (ACh) increases the firing of periglomerular and of mitral cells through nicotinic receptor activation. Through muscarinic receptors, ACh inhibits granule cell firing when acting on the granule cell soma, and increases GABA release when acting on granule cell peripheral dendrites [23]. Noradrenergic inputs originating in the locus coeruleus terminate mainly in the internal plexiform and granule cell layers [28]. Reports of the effects of noradrenergic activation are somewhat contradictory: reported effects include a depression-potentiation sequence in dendrodendritic inhibition, mediated by β -adrenergic receptors [105], and an increase in sensitivity of mitral cells to weak ON input mediated by α -1-adrenergic receptors [28]. There are also axon collaterals from olfactory cortex pyramidal neurones which terminate mainly in the granule cell layer, and inputs from the anterior olfactory nucleus [135].

1.1.1.10 Accessory olfactory bulb

Embedded in the side of the main olfactory bulb is the accessory olfactory bulb (AOB). This is a structure with cell types and organisation very similar to those of the main bulb, but which is much smaller in size, receives input from the vomeronasal organ rather than the olfactory epithelium, and is concerned with pheromones, rather than with general odours. Because of this it probably has much more finely tuned receptors than the main olfactory system, and it is interesting that the AOB has nevertheless such a similar structure to the main OB. Any model of the main bulb is likely to have some relevance also to understanding of the AOB.

1.1.2 Non-mammalian olfactory systems

There is a very considerable degree of similarity in olfactory systems across vertebrates [40]. All classes of vertebrates possess mitral, tufted and granule cells in their olfactory bulbs. However, the mitral cells of most non-mammals do not have basal dendrites and they may have multiple primary dendrites [38]. Fish do not have periglomerular cells [38]. It is possible that periglomerular cells and basal dendrites were present in early vertebrate ancestors and have been lost in certain branches of vertebrate evolution. However, the most likely explanation is that these structures are later refinements. This suggests that the fundamental tasks of vertebrate olfaction do not require either intra/inter-glomerular inhibition or long-range lateral inhibition and that these features improve upon the basic apparatus.

The organisations of insect and vertebrate olfactory systems are similar [140]. Olfactory receptor neurones on insect antennae project to the antennal lobe (AL), which is an analogue of the vertebrate OB. In the AL the ORN axons and the dendrites of the projection neurones form glomeruli as in the OB. One type of local interneurones, comparable to PG cells, receives input from ORNs and sends output to projection neurones. Another, anaxonal, local interneurone type is comparable to the granule cell in its connections. Despite this remarkable similarity, it is probable that vertebrate and insect olfactory systems have arisen independently [140]. For example, the recently discovered olfactory receptor family in the fruitfly *Drosophila Melanogaster* shows no significant homology to the olfactory receptors of vertebrates [29, 148]. This suggests that the similarity in organisation may have arisen through convergent evolution, with independent evolutionary sequences converging on the same, or similar, algorithms.

In general, this similarity between the olfactory systems of very different organisms suggests that experimental results from non-mammalian species may, with caution, be used to guide investigation and modelling of the mammalian olfactory bulb.

1.1.3 Responses of the olfactory bulb to electrical and odour stimulation

1.1.3.1 Electrical stimulation

In intact olfactory bulb preparations, sub-threshold electrical stimulation of the olfactory nerve produces a small, brief depolarisation of the mitral/tufted cell membrane followed by an extended hyperpolarisation. Supra-threshold stimulation produces a single action potential followed by an extended hyperpolarisation.

This is seen in isolated turtle OB [97], in salamander OB *in vivo* [51] and in rat OB *in vivo* [42]. Sometimes there is a short inhibitory-excitatory sequence between the initial excitation and the extended inhibition [42, 97].

In non-intact preparations, such as the hemisected turtle OB or rat OB slice, in which fewer of the secondary dendrites are preserved intact, a prolonged excitation with a number of action potentials is seen [10, 103]. This is also seen in the intact turtle bulb in the presence of the GABA_A antagonist bicuculline [104].

Output cell responsiveness to ON stimulation decreases with depth in the bulb (type I mitral cells are least responsive; superficial tufted cells most responsive). This is most likely due to connectivity (deeper layers have longer dendrites and so receive more inhibitory synapses) rather than to intrinsic differences in cell properties [42].

Current-source-density analysis in rat OB slices indicates that ON activation produces prolonged activation in the primary dendrites of mitral/tufted cells and relatively brief excitation in the granule cell peripheral dendrites [5].

1.1.3.2 Odour stimulation

On a coarse time scale, the response of mitral/tufted cells to odour stimulation is an increase, a decrease, or no change in firing rate. ‘Rebound’ increases in firing rate when the stimulus is removed are also sometimes seen [99]. Nearby cells are more likely to have similar firing patterns than are widely separated cells [12, 20].

On a finer time scale, firing rates can vary within the period of odour stimulation. Response patterns change considerably with stimulus concentration, but in a graded manner (given the responses to three consecutive odour concentrations, the response to the intermediate concentration is intermediate between the other two responses) [53]. Near-threshold concentrations induce simple phasic increases or decreases in firing rate. At higher concentrations the temporal patterns of the responses become more complex, comprising alternating periods of increased and decreased firing rates [52, 53]. The same patterns of excitation and suppression are seen in membrane depolarisation and hyperpolarisation in intracellular recordings [52].

Responses of individual neurones are variable over time (on the scale of hours and days), although the variability of a single neuron over time is less than the variability between different neurones. These changes are not odour-specific, but seem to be determined by central control [12].

1.1.3.3 Spatial distribution of activity

The degree of activation by odour stimuli of glomeruli, and the distribution of activated glomeruli, have been studied by *c-fos* mRNA expression [48], by functional MRI [157] and by optical imaging of calcium-sensitive dyes [44], voltage-sensitive dyes [45], and intrinsic signals [122]. All these studies reveal that most odorants activate multiple glomeruli, and that the patterns of activated glomeruli are distinct but overlapping for different odorants, i.e. an individual glomerulus may be activated by many odorants, but the pattern across the bulb is specific to a single odorant. Studies using stimulation with a series of homologous aldehydes and with amino acids have revealed that glomeruli are tuned to detect molecular features and that the response patterns to similar molecules are correlated [44, 122].

1.1.3.4 Oscillations and synchronization

Odorant-induced oscillations in local field-potential (LFP) recordings in the olfactory bulb were first reported in hedgehog by Adrian [1], and have since been reported in the OBs of many vertebrate species, in the antennal lobes of insects and in the olfactory processing areas of other invertebrates.

These oscillations are thought to reflect rhythmical, synchronous firing of populations of neurones [37]. Indeed, it has been shown in locusts [77, 151] and in rabbits [67] that the spiking of individual neurones is phase-locked to the LFP, and that spiking in simultaneously recorded pairs of neurones is closely synchronized. Different sub-populations of neurones may be synchronized with the global oscillation at different periods during the response [77, 151], and oscillations with different (although sometimes

harmonically-related) frequencies may be elicited in different regions of the bulb [74]. In honeybees, oscillatory synchronization has been shown to have functional relevance: chemically-induced desynchronization impairs the ability to discriminate between similar odorants but has no effect on discrimination of dissimilar odorants [138].

It is generally thought that the oscillations are purely a network phenomenon, generated by alternate excitation and inhibition at the dendrodendritic mitral–granule cell synapse [135], but the finding of intrinsic sub-threshold oscillations in the membrane potential of rat mitral cells, with a frequency range similar to that of the LFP oscillations, suggests a role for intrinsic cell properties in the generation of synchrony [33].

1.1.4 The olfactory code

The basis of the olfactory code is the family of 7-transmembrane-domain G-protein-coupled proteins which are the olfactory receptors (ORs) [18, 19]. Information about the intensity and identity of an odour stimulus is encoded in the pattern of activation of OR types. At the simplest level this means which receptor types are activated and how much, but it is possible that temporal factors, due to the different rates and durations of binding of different molecules, may form part of the encoding. The degree of receptor activation is transduced into action potential firing. It is probable that the average rate of firing carries most of the information, since the firing rates of ORNs are much faster than the rate of any modulation of the stimulus.

Any given ORN expresses only a single receptor type [88], and all ORNs expressing the same receptor project to only one or two defined glomeruli [93, 149]. It is hypothesized that any given glomerulus receives inputs from only one ORN type (the *one glomerulus–one receptor* hypothesis [95]) and it has been demonstrated for particular glomeruli that all axons innervating those glomeruli are from a single ORN type [8]; however, a study in transgenic mice has found glomeruli that are innervated by two ORN types [144]. Each mitral or tufted cell has a single primary dendrite which forms synapses in a single glomerulus (note this is not true in amphibians, which tend to have two primary dendrites). Therefore, assuming the *one glomerulus–one receptor* hypothesis is approximately correct, the pattern of activation of ORs is represented directly by the pattern of input to mitral/tufted cells at the glomeruli.¹ So it seems that all the brain would need to do to determine which odour is present is to determine how much input each glomerulus is receiving. In that case, why have an olfactory bulb? Why don't ORN axons go directly to the cortex?

An olfactory system must enable an animal to perform several tasks: detection and identification of odours, segmentation of a mixture of odours, discrimination between similar odours, association of previously encountered odours with other sensory memories, tracking of space- and time-varying odour plumes. The relative importance of these tasks depends on the animal's needs. All olfactory systems have a hierarchical structure, and each task is split into sub-tasks, each of which is assigned to a different level of the hierarchy: for example, olfactory receptor cells transduce the chemical signal into an electrical one, this signal is passed to the olfactory bulb or antennal lobe, where it is processed in a number of ways to facilitate the tasks of the subsequent cortical stages, recognition, association, multi-modality integration, etc. The task of the olfactory receptors is conceptually simple, even if less than well understood in many details. The tasks of the cortex are also readily understood as concepts, although the mechanisms by which they are accomplished remain almost opaque. In contrast, the very tasks which the olfactory bulb/antennal lobe must perform are not understood, let alone the mechanisms involved.

Various hypotheses have been advanced for the function of the olfactory bulb/antennal lobe. One is that it narrows the ‘molecular receptive range’ – i.e. a mitral cell responds to a narrower range of odorants than does the receptor cell population that projects to it – thus reducing the overlap between the representations of similar odorants [81, 95, 96]. The mechanism for this narrowing is the lateral inhibition between mitral cells, mediated via granule and PG cells. There is experimental support for this hypothesis: Yokoi *et al* [158] measured the firing rate response of mitral cells to a series of straight-

¹a caveat – there is some evidence for interactions within the epithelium or olfactory nerve, supported by, for example, gaseous messengers or ephaptic interactions [37]. This would tend to produce interference between the signals from different receptor types.

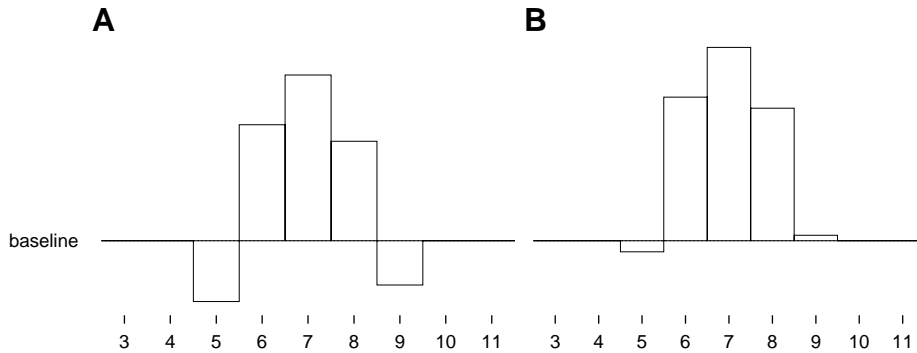


Figure 1.2: A schematic representation of the results of Yokoi *et al* [158]. Each bar graph shows the change in firing rate relative to baseline for a single cell in response to stimulation with a straight-chain aldehyde with between 3 and 11 carbon atoms in the chain. (A) Normal response showing inhibitory responses to certain aldehydes, leading to narrowing of the molecular receptive range (MRR). (B) Response with glutamate or GABA_A antagonists showing abolition of inhibition and broadening of the MRR.

chain aliphatic aldehydes, differing only in the number of carbon atoms in the chain. They found that a given mitral cell is maximally excited by one aldehyde, and is also excited by the aldehydes with one more and one fewer carbon atom. Aldehydes with two more or two fewer carbon atoms often produce inhibition, while all other members of the series produce no response. When lateral inhibition was abolished or reduced by application of the glutamate-receptor antagonist 6-cyano-7-nitroquinoxaline-2,3-dione (CNQX) or the GABA_A receptor antagonist bicuculline, those aldehydes which had produced inhibition now produced excitation or no response (see Figure 1.2 for a summary of these results). In modelling studies, Linster and colleagues also found that lateral inhibition reduces overlap in the representation of different odours [81, 82] (these studies are discussed in more detail in §1.2).

A second hypothesis for the role of the bulb, which is consistent with the one discussed above, is that the bulb circuitry introduces temporal correlations, such as spike synchronization, between the signals from different receptors responding to the same odour, thereby ‘binding’ those components of the signal together, representing a single object to the cortex [75]. The cortex could recognize such an object using neurones that function as coincidence detectors, for example. This hypothesis is based on the theoretical presumption that some sort of binding mechanism is necessary (see [136] for a review of binding in the visual system), and on the experimental evidence for spike synchronization in mammalian olfactory bulb and insect antennal lobe discussed in §1.1.3 above. Further support comes from the finding that desynchronization of signals in the locust antennal lobe degrades the specificity of odour responses in neurones which receive the signals from the antennal lobe [85].

A third possibility is that the bulb separates out information about the intensity of an odour stimulus from information about its identity. Psychophysically, a known odour is recognized over a very wide range of stimulus concentration, but the pattern of activation of glomeruli [122] and the temporal firing rate response of mitral/tufted cells [53] both change greatly. Modelling studies have suggested that odour intensity could be encoded by the number of mitral/tufted cells firing [3].

Other modelling studies have suggested that the bulb functions as an associative memory [55, 56, 60], such that an input causes the bulb activity to converge to one of a number of previously stored patterns or ‘memories’. These models are evaluated in §1.2.1.

Finally, the bulb may produce a mapping between a physical/chemical odour space and a ‘behaviorally-important’ odour space. In other words, two odours which are chemically very different may have exactly the same behavioural significance to an animal, whereas it may be very important for an animal to discriminate between two extremely similar odours, such as the odour of a ewe’s own lamb from that of another lamb [68, 69]. It is likely that evolution, in assembling the repertoire of olfactory receptor molecules, has allowed for this necessity by producing many receptor types to cover an ‘interesting’ region of odour space while having few receptors to cover an ‘uninteresting’ region. However, the bulb may take this further (Figure 1.3). Where it is important for an animal to discriminate between two

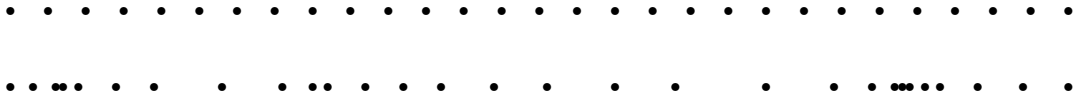


Figure 1.3: A representation of the hypothesized mapping of ‘physical/chemical’ odour space (top) onto a ‘behaviourally-important’ odour space (bottom). Where it is important for an animal to discriminate between two very similar odours, the differences between the spatio-temporal patterns of receptor activation may be amplified by the bulb. The differences between the representations of odours which have little or no behavioural significance would be correspondingly reduced.

very similar odours, the differences between the spatio-temporal patterns of receptor activation may be amplified by the bulb. The differences between the representations of odours which have little or no behavioural significance would be correspondingly reduced. This hypothesis was inspired by consideration of the heterogeneity of bulb circuitry, and by experimental findings on olfactory learning. The bulb is not homogeneous in its connectivity or synaptic weights, and the heterogeneity is unlikely to be entirely random. Therefore, some inputs will have a larger influence on bulb output than others. Recordings of mitral cell activity in the olfactory bulb of sheep before and after giving birth showed that before, the majority of cells responded preferentially to food odours, and after, the majority responded preferentially to lamb odours, with about one third of these responding differently to own-lamb than to other-lamb odours [69]. Accompanying this were increases in neurotransmitter release in the bulb. The odorants and the receptors are the same before and after, so it is apparent that synaptic changes in the bulb have increased the representation of lamb odours in output space, possibly at the expense of the extent of output space representing food odours. This hypothesis is consistent with the first three discussed above (narrowing receptive range, binding, intensity compensation).

1.2 Review of olfactory bulb modelling

1.2.1 Network modelling

Since the pioneering work of Rall and Shepherd [119] there have been many attempts to advance our knowledge of olfactory bulb function using computational modelling. I use two classifications to structure the analysis of the published studies: ‘top-down’ *vs* ‘bottom-up’ and rate-coding *vs* time-coding.

A top-down model is designed, constrained to a greater or lesser degree by known bulbar anatomy, to achieve certain high level tasks of the olfactory system, which are hypothesized to be carried out in the bulb. These models tend to be ‘minimal’, in that the model is made as simple as possible within the constraints.

A bottom-up model is designed to closely mimic known anatomy and physiology, using experimental recordings to constrain unknown parameters where possible. In general, little *a priori* prejudice regarding the function of the network is used in constructing the model. Such models are limited by the amount of experimental knowledge and sometimes by computational constraints.

The value of top-down models is that they show what bulb-like systems may be doing, and so may be a useful source of hypotheses for experimental testing. The problem is that while they may be useful for opening up avenues of investigation, they are not biologically detailed enough to narrow possibilities down. They can suggest what the bulb may be doing but have (almost) nothing to say about what it *is* doing.

Bottom-up models are in a sense more objective, in that the network behaviour arises naturally out of the experimental data on the components and is not imposed upon the model. Such models can test whether existing knowledge is sufficient to explain experimental observations and can produce new ideas about the bulb’s functions. The main weakness of such an approach is the necessity for simplification and approximation, due to lack of experimental data and/or computational limitations.

The division of modelling studies into these two classes is not rigid, and many studies combine elements of both approaches. This classification is similar to Bower *et al*'s concept of 'realistic' (bottom-up) *vs* 'demonstration' (top-down) models [115].

The rate-coding hypothesis is that all information in the output signal of a neurone is carried in the mean firing rate. The time-coding hypothesis is that information is also, or instead, carried in the time of occurrence of individual spikes (usually the time relative to some other signal). The extent to which these two hypotheses are true is widely discussed (see [131] and [137] for two contrasting views on the subject). The main reason for using this distinction as a classification is the evidence that the temporal structure of the olfactory response is important in olfactory processing (§1.1.3.4).

One possible 'top-down' function of the olfactory bulb is to act as an associative memory, i.e. given a distorted input the network converges to a stored pattern. Hendin, Horn and Tsodyks [56] have synthesized their previous work on this topic [54, 55] with the model of Hopfield [58]. Their model '*... is schematic, trying to capture general principles of information processing rather than present a realistic description of all details.*' Hopfield's model [58] is identified with the glomeruli, and performs blind separation of independent sources based on temporal fluctuations, i.e. during each sniff cycle, one odour is dominant. The external plexiform layer (EPL) acts as an associative memory, as in [55], but is now oscillatory, so that the stored pattern is not a fixed point attractor but a limit cycle. The oscillation is imposed locally, and is not a product of network interactions. Learning in the EPL uses generalised Hebbian learning rules during training periods. The model of the inputs is consistent with experimental knowledge. The EPL has all-to-all connectivity. The memory capacity grows as a function of the ratio of granule:mitral cells.

Another scheme for the OB as an associative memory is put forward by Hoshino, Kashimori and Kambara [60]. It is again an oscillatory system, with a particular odour producing a particular learnt limit cycle attractor state. The identity of each constituent molecule is encoded into a single spatial pattern, and the mixing ratios of component molecules are encoded into the temporal sequence using the intensity-to-time delay coding scheme proposed by Hopfield [59]. A weakness of this model is that an important component is the direct interconnection of mitral cells with excitatory synapses. The authors suggest that these connections may be made by axon collaterals, but anatomical studies have shown that mitral/tufted cell axon collaterals terminate only in the granule cell layer (see §1.1.1). Another weakness is that a given odorant molecule is assumed to activate only a single receptor type, in contrast to the distributed representation seen experimentally (§1.1.3).

Neither of the associative-memory models use the timing of spikes for computation; both use mean firing rate. However, the temporal sequence of changes in firing rate is important, particularly in [60].

The model of Li and Hopfield [80] is highly simplified, but realistic in that specification of connections and cell behaviour is based on experimental data. The model uses a continuous input-output function rather than discrete spikes; however, the authors report similar behavior from simulations in which single 'continuous' cells are replaced by groups of spiking cells. The model reproduces physiological electroencephalogram (EEG) data. The authors suggest that their model encodes the non-oscillatory input into oscillatory output, and that downstream components of the olfactory system can extract odour information from the amplitudes and phases of the oscillations in mitral cell activities. This model uses 'rate-coding', in that no information is carried by precise spike timing. However, the temporal variation of the rate on a short time scale – the oscillatory response – is important.

The previous model is extended [78] by adding feedback from higher centres to produce the psycho-physical phenomena of adaptation and sensitivity enhancement. The original model is essentially 'bottom-up', since it is based on experimental data and aims to reproduce physiological observations rather than to implement some computational algorithm. The extension is top-down since the feedback was designed to give previously specified high-level behaviour. This work is extended further in [79]: a model of olfactory cortex is added as an associative memory. The bulb encodes the odour inputs as oscillating patterns which resonate with stored patterns in the cortex. Feedback from the cortex to bulb allows segmentation of odour mixtures.

Antón, Lynch and Granger [3] use a hybrid top-down and bottom-up approach. The model, of a single glomerulus, is biologically detailed, with spiking neurones based on experimental results, with

conductance-based synapses and realistic synaptic decay times. However, the most important feature of the model is designed to produce a particular encoding scheme for receptor inputs, which is decided upon *a priori*. This encoding scheme is suggested by certain experimental findings, but the imposition of this scheme on the model represents a top-down approach. The main idea is that the decrease in excitability of projection neurones with increasing depth [42, 124] could result in an encoding of odour intensity (i.e. frequency of receptor firing) by a spatial element – how many projection neurones are firing. An argument against this hypothesis is the observation that mitral and tufted cells have different projection patterns [70](see §1.1.1) and so are not a single population for the purpose of transmitting information to cortex.

The intention of White *et al* [153] was ‘*to investigate whether available data are sufficient for formulating a simulated bulb circuit that can generate realistic mitral cell output.*’ ‘Realistic’ is judged here by qualitative comparison of model and experimental voltage traces. The model is very successful in this respect, but it would be more useful if it went further, e.g. the authors assert that (i) ‘*the model’s output can now be the basis for analysing how ensemble events might arise from interactions among these many individual cellular elements*’ and (ii) ‘*the various aspects of bulbar behaviour described by these other models may also potentially be investigated with our model*’, but do not go on investigate either avenue.

Linster and collaborators have produced a series of models of both mammalian olfactory bulb [81, 82] and insect antennal lobe [83, 84, 90]. The models are based on known anatomy, with unknown parameters (such as synaptic weights and transmission delays) tuned by comparing model output to experimental physiological data – individual neurone activities and population activities (field potentials and EEG). Having constructed the models, they are then used to address questions about the role of different parts of the system, e.g. the distinction between the role of granule and periglomerular interneurones. The main conclusion of [81] and [82] is that the bulb acts to make the odour representation more sparse: periglomerular cell activity affects the number of active mitral/tufted neurones, while granule cell activity determines the response intensity of active mitral cells. Both granule and PG cell activities may be controlled by centrifugal inputs.

The model of Meredith [92] is a simplified model which attempts nevertheless to represent faithfully the essential elements of the olfactory bulb. Mitral and PG cells are represented explicitly. Granule cells are not represented explicitly, but only as mediating recurrent/lateral inhibition: the connection strength between two mitral cells is proportional to the overlap of their dendritic fields. This is a ‘steady-state’ model, with no consideration of the time course of activity, in which the steady-state output of the system under a given input is found by an iterative method. The most important assumptions, given Meredith’s conclusions, are of (i) local connectivity, with connection strengths falling off with distance, and (ii) localized inputs, i.e. activation of glomeruli falls off radially with distance from a maximal centre. The model has some interesting properties, for example, that a given cell might be both excited and inhibited by the same odour, depending on intensity. A corollary is that during an odour pulse (intensity rises then falls), a given cell may fire or be silent at different phases of the pulse, and that different cells will fire at different points in time. This is seen in experimental recordings [52, 53]. This property is a consequence of the locality of the input and of the connections.

1.2.2 Modelling of individual components

In contrast to the large number of network modelling studies of the OB, only a few studies of information processing in the individual cells of the bulb have been published.

Bhalla and Bower [11] developed extremely detailed, multi-compartmental models of mitral and granule cells. The morphology of the cells is based on, and cell membrane properties are inferred from, published data. The only experimentally unknown parameters in their models are the channel densities in the different regions of their models. These parameters were found by a comprehensive search through parameter space, based on fitting the model output to experimental current-clamp recordings. Two weaknesses of the models are that, (i) the anatomical data is from mammalian species while the electrophysiological data used to fit the parameters is from turtle (however, the authors claim, mammalian and turtle recordings are qualitatively similar) and, (ii) the physiological data are from single-point recordings in the soma, so very distal segments of the neurones (e.g. the mitral cell primary dendrite tuft) are much

less well constrained than the soma and proximal sections. The validity of this model in light of more recent experimental findings is discussed in §5.2.1.

Aradi and Érdi [4] investigated the behaviour of mitral and granule cell models with the same ion channels as the Bhalla and Bower models but with simpler morphology. Their findings do not add significantly to the results of Bhalla and Bower.

A more recent model of olfactory bulb mitral cells was published by Shen *et al* [132]. This is a less general model than that of Bhalla and Bower, in that it was created to model a specific phenomenon – back-propagation and initiation of action potentials in the mitral cell primary dendrite. The model was fitted closely to current-clamp recordings from two points in the cell – the soma and the distal part of the primary dendrite, and the primary dendrite of the model is very well constrained. However, the parts of the cell distal to the recording sites – most importantly the olfactory tuft and the secondary dendrites – are modelled with little detail, since they have little influence on action potentials in the primary dendrite shaft, and are not well constrained by the experimental recordings. For this reason this model is not well suited to be a component of a network model.

Antón, Granger and Lynch [2] developed a compartmental model of a granule cell dendrite with spines, intended to determine the effect of spines on lateral and recurrent inhibition. The model assumes fairly fast, graded synapses, and the main result is that high resistance spines and low activity favour reciprocal over lateral inhibition, and vice versa.

Woolf, Shepherd and Greer [156] present morphologically-detailed, compartmental models of mouse granule cells, based on camera lucida reconstructions. With entirely passive membrane throughout the cell, they show that ‘*the degree of spread of synaptic potentials can define functionally related subsets of spines within the dendritic tree . . . that can mediate discrete localized inhibition onto subsets of mitral or tufted cell secondary dendrites*’.

1.3 A strategy for modelling the olfactory bulb

There is no shortage of top-down, abstract models of olfactory bulb function. Such models can be useful in stimulating and structuring ideas, and in suggesting hypotheses. However, such models are so abstract that it is very difficult to relate them to experimental data. Even for those models which do not contain entirely unphysiological connections as crucial elements (such as direct, excitatory, mitral–mitral synaptic connections), it is hard to conceive of experiments which could be used to choose between competing explanations.

Bottom-up models are more closely inspired by experimental data, and their predictions are potentially easier to test. Even here, though, in the published literature, the models for the individual cells of the network are very simple, either integrate-and-fire or rate models, with at most three compartments per cell. Many nerve cells do not behave only, or at all, as integrating elements, and it has been shown in other neural systems that the details of information processing in different cell types can have a large influence on network behaviour (e.g. [115]).

Detailed models of single cells or components of single cells are the most closely based on experimental data, and are useful for elucidating principles of information processing by single cells, but it is a truism that complex behaviours may arise from interacting networks of elements which cannot be predicted from the behaviour of individual elements.

Given the above considerations, great benefits could be obtained from developing a system of models to unify the various levels of model-based enquiry into olfactory bulb function. Such a system needs at least three levels: detailed models of single cells and synapses; networks using simplified versions of the detailed models; abstract, high-level models based upon the intermediate network models, which can make predictions at the algorithmic level. Each level must constrain and be constrained by the ‘neighbouring’ levels. Such an approach has been used to good effect in the cerebellum (starting with detailed single cell models [127, 128, 129] and developing network models based on these [87]), the olfactory cortex (starting with a network-level simulation [154] which motivated more detailed single cell models. This process is reviewed in reference [115]) and the hippocampus (from single cell [142, 143] to network [141] models).

It is a primary aim of this dissertation to develop such a system, using where possible existing work. Top-down models seem adequately represented in the literature, therefore I do not attempt to produce

another, rather to use my framework to test existing models, where possible. Detailed single-cell models already exist, notably those of Bhalla and Bower, and though they will need updating as new experimental data become available, they are good enough for current purposes. The greatest void is in the middle, and that is where I have concentrated my research effort. An intermediate-level model should have the following properties:

- i. explanatory value – the model aids understanding, giving insight into how the olfactory system functions and why it is built as it is.
- ii. an integrative function - the model provides a framework which integrates the results of different experiments at different levels of enquiry, to evaluate their consistency with each other and reconcile conflicting results.
- iii. predictive value – the model suggests novel experiments and correctly predicts the results.

Specific biological and computational problems I wish to address are:

- i. the existence, origin and role of oscillations/synchronisation;
- ii. how the properties of individual cells/synapses influence the network behaviour;
- iii. the role of lateral inhibition in the olfactory bulb;
- iv. the problem of scaling: how can a model with ten thousand cells approximate a bulb with more than two million cells? In different terms, how does connectivity influence network behaviour?

1.4 Thesis outline

The structure of this dissertation is as follows:

Chapter 1 Review of the anatomy and physiology of olfactory systems, preparatory to a discussion of current theories about information processing in the early stages of the olfactory system – ‘the olfactory code’ – and a review of existing OB models.

Chapter 2 Development of reduced models of the principal cell types of the olfactory bulb, based closely on experimental data, but simple enough to allow simulation of large networks.

Chapter 3 An examination of the fundamental interaction in the bulb – that between two mitral cells – using both the cell models developed in the previous chapter and the integrate-and-fire neurone model.

Chapter 4 Development of network models of the OB. These are calibrated using experimental data from the literature, and then the properties of the network are investigated, allowing us to make a number of predictions.

Chapter 5 In the final chapter the findings are summarized and suggestions made for future work.

Chapter 2

Reduction of compartmental models

2.1 Introduction

Morphologically- and physiologically-detailed, multi-compartmental models have been developed for a number of neurone types [11, 128, 142]. The compartmental approach to neuronal modelling is based on the representation of neurone axons and dendrites as electrical cables [118]. A compartmental model is a spatial discretisation of the cable model, approximating the spatially continuous neuronal structure by chains of discrete, isopotential compartments. This makes the model equations amenable to numerical solution by computer. For a more detailed introduction to compartmental modelling, see reference [130]. Highly detailed compartmental models have the advantage that the morphology can be accurately measured and so can provide a strong constraint on the model's behaviour. However, because of the high level of detail, simulation of such models is very computationally intensive and the large number of parameters can make it difficult to interpret or generalise the results.

In order to simulate large networks of these neurones it is necessary to reduce the size and complexity of the models. A number of strategies have been used to construct such reduced single-cell models. All take as their starting point a detailed compartmental neurone model and attempt to simplify it while retaining the electrotonic properties and/or input-output behaviour of the detailed model. One strategy is to concentrate on the electrotonic properties and reduce the number of compartments in the cell while conserving the membrane time constants and the cell input resistance [22, 139]. A more drastic strategy is to attempt to abstract the key features of the cell into as few compartments and channel types as possible, and constrain the simplified model to have the same input-output properties as the detailed model, in terms of firing rate response to synaptic or electrical stimulation [110]. Both strategies give both shorter simulation times and potentially greater understanding than the fully-detailed models.

In this chapter I have used the second strategy mentioned above to construct simplified models of olfactory bulb mitral and granule cells. The models are based on the detailed, 286-compartment mitral cell and 944-compartment type I granule cell models published by Bhalla and Bower [11], which were themselves based on intra-cellular recordings and detailed morphological measurements. I have found that at least three compartments are necessary for an adequate model of an olfactory mitral cell, with at least one compartment for each of the soma, secondary (basal) dendrites and glomerular tuft. Four compartments gives a substantial improvement on three, with little increase in processing time. For the granule cell, a model with three compartments, representing the deep dendrites, soma and peripheral dendrite, is optimal. The reduced models give a good fit to the full models over a wide range of firing rates. The reduced models have the potential to be a useful tool in realistic network modelling of the olfactory bulb.

2.2 Method

Bhalla and Bower's mitral and granule cell models were re-implemented in the neural simulator NEURON and tested against their original GENESIS implementation. The two implementations gave qualitatively the same results but had small quantitative differences (of a few percent in firing rates) which were pinpointed as being due to alternative numerical strategies, mainly the use of symmetric compartments by NEURON and asymmetric compartments by GENESIS.¹

2.2.1 Mitral cell models

2.2.1.1 Modification of the Bhalla-Bower model

The results presented by Bhalla and Bower are for stimulating electrodes in the soma. This provides a fairly weak constraint on the models – as Bhalla and Bower noted, some parameters can be varied by an order of magnitude with minimal effect on the output.

Since all or almost all of the excitatory input received by mitral cells is to the glomerular dendritic tuft, I first briefly examined the response of their model to glomerular input. When depolarising current is injected into the soma of Bhalla and Bower's mitral cell model, the cell responds with regular firing. With current injected into the glomerular compartments the model produces a double spike at the soma then settles down to regular firing (Figure 2.1A). This double spike is produced by a large, extended calcium spike in the glomerulus (Figure 2.1B). Is such behaviour observed experimentally?

In about half of recorded rat mitral cells, Chen and Shepherd [25] observed fast pre-potentials in response to olfactory nerve stimulation, indicative of dendritic excitability, but these are small amplitude events, not full action potentials. Chen, Midtgård and Shepherd [24] recorded from the primary dendrite just proximal to the glomerular tuft as well as from the soma, and on some occasions observed an action potential in the dendrite preceding that in the soma. These were of similar width to the somatic action potentials, not the extended depolarisation seen in the Bhalla-Bower model. Apparent double spikes have been observed when the cell is already depolarised (see Figure 6A of [103]), but these appear to be rare occurrences. Therefore, I conclude that the glomerular tuft in Bhalla and Bower's model, as it stands, is over-excitable. A simple parameter change was found to eliminate the double spiking – increasing the density of slow potassium delayed rectifier (K) channels in the glomerular compartments by a factor of five produces only a short calcium spike which gives rise to a single spike at the soma (Figure 2.1). Increasing the K channel density by a further factor of five eliminates the glomerular/dendritic calcium spike and increases the latency of the somatic spike. These changes in K channel density have no visible effect on the model response to somatic current injection (data not shown). For fitting of the reduced models I used a K channel density in the glomerular compartment of $\bar{g}_K = 0.02 \text{ S cm}^{-2}$, about seven times larger than that used by Bhalla and Bower. All other parameter values were as published by them.

2.2.1.2 Description of reduced models

To simplify the models I used the same strategy as Pinsky and Rinzel [110] in their simplification of Traub's hippocampal pyramidal neurone model [142, 143] – namely to retain the same active currents and gating kinetics, with the same channel densities/maximum conductances, but to reduce drastically the number of compartments.

The full Bhalla and Bower mitral cell model has 286 compartments; I investigated simplifications with two, three or four compartments. The two-compartment model has one compartment for the soma and one for the primary dendrite tuft in the glomerulus. The three-compartment model adds a compartment for the secondary dendrites. The four-compartment model (Figures 2.2 and 2.3 show schematic representations) adds a compartment for the primary dendrite shaft between the soma and glomerular tuft. It should be made clear that the relationship between the reduced models is one of adding or removing entire compartments. It is not the case that compartment number is reduced by merging compartments and averaging their properties, although that would also be a valid approach.

¹With symmetric compartments, the axial resistance between child and parent compartments is the average of the resistances of the two compartments. With asymmetric compartments, the axial resistance is that of the child compartment.

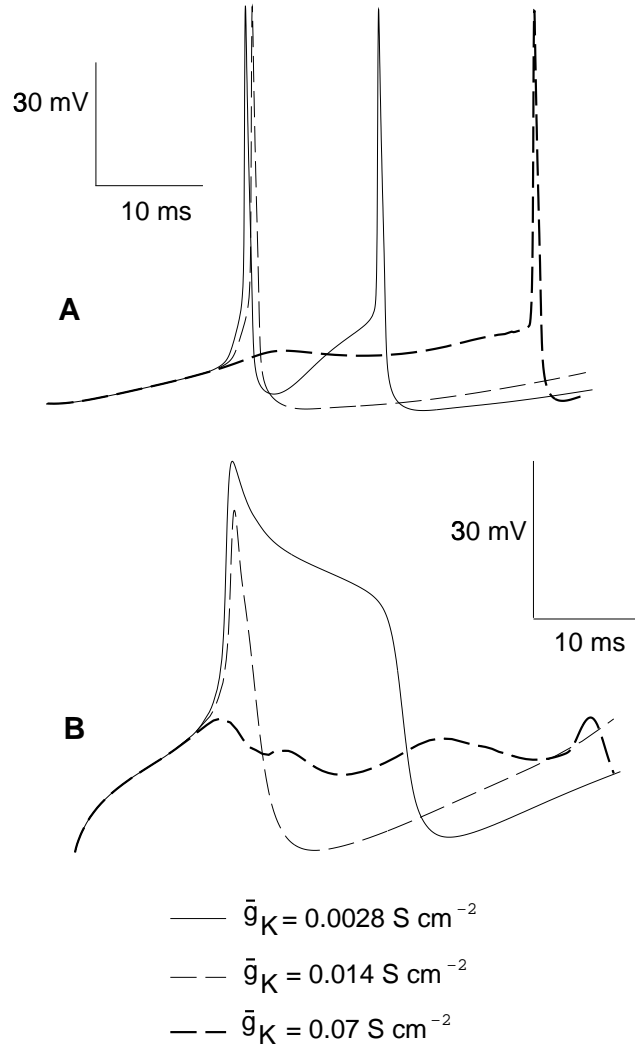


Figure 2.1: Response of the full model to a total constant current of 0.4 nA to the glomerulus, divided evenly among the compartments (~ 4.3 pA per compartment). (A) Somatic membrane potential trace and (B) Membrane potential trace at base of glomerular tuft, for varying \bar{g}_K in the tuft. These figures show the double somatic spike and extended dendritic calcium spike seen with low \bar{g}_K , that are removed by increasing the value of the parameter. Further increasing \bar{g}_K delays the somatic spike and abolishes the dendritic calcium spike.

The correspondence of these compartments to the parts of the real neurone is of course only approximate in such a reduced model. Bhalla and Bower used different conductances in the proximal and distal sections of the secondary dendrites. The secondary dendrite compartment in the reduced models includes only the distal dendrite conductances. The axon is not represented explicitly in my models. It may be considered to be subsumed into the soma compartment.

The current balance equations for the four compartments (soma, glomerulus, primary dendrite, secondary dendrite) are:

$$\begin{aligned} C_m V'_s &= -g_{\text{pas}}(V_s - E_{\text{rest}}) - g_{\text{Na}}(V_s - 45) - g_{\text{Kfast}}(V_s + 70) - g_{\text{K}}(V_s + 70) \\ &\quad - g_{\text{KA}}(V_s + 70) - g_{\text{KCa}}(V_s + 70) - g_{\text{LCa}}(V_s - 70) + (g_{\text{sd}}/p)(V_d - V_s) \\ &\quad + (g_{\text{sp}}/p)(V_p - V_s) + I_s/p \end{aligned} \quad (2.1)$$

$$\begin{aligned} C_m V'_g &= -g_{\text{pas}}(V_g - E_{\text{rest}}) - g_{\text{K}}(V_g + 70) - g_{\text{LCa}}(V_g - 70) + (g_{\text{pg}}/q)(V_p - V_g) \\ &\quad + I_g/q \end{aligned} \quad (2.2)$$

$$\begin{aligned} C_m V'_p &= -g_{\text{pas}}(V_p - E_{\text{rest}}) - g_{\text{Na}}(V_p - 45) - g_{\text{Kfast}}(V_p + 70) - g_{\text{K}}(V_p + 70) \\ &\quad - g_{\text{LCa}}(V_p - 70) + (g_{\text{sp}}/r)(V_s - V_p) + (g_{\text{pg}}/r)(V_g - V_p) \end{aligned} \quad (2.3)$$

$$\begin{aligned} C_m V'_d &= -g_{\text{pas}}(V_d - E_{\text{rest}}) - g_{\text{Na}}(V_d - 45) - g_{\text{Kfast}}(V_d + 70) \\ &\quad + (g_{\text{sd}}/s)(V_s - V_d) \end{aligned} \quad (2.4)$$

where V_s , V_g , V_p and V_d are the membrane potentials of the somatic, glomerular, primary dendritic and secondary dendritic compartments respectively and E_{rest} is the resting membrane potential (-65 mV). Currents and conductances are expressed as densities with units of $\mu\text{A cm}^{-2}$ and mS cm^{-2} respectively. Capacitance (C_m) has a value $1.0 \mu\text{F cm}^{-2}$ and time is in units ms. The Hodgkin-Huxley formalism is used for all channels. The gating equations for the channels are exactly as given by Bhalla and Bower [11]. p is the ratio of the surface area of the soma compartment to the total cell membrane area; q , r and s are the ratios of the glomerular, the primary dendrite and the secondary dendrite surface areas respectively to the total surface area ($p+q+r+s = 1$). g_{sd} , g_{sp} , g_{pg} are the conductances joining the soma and secondary dendrite, soma and primary dendrite, and primary dendrite and glomerular compartments respectively. The equations are similar for the two- and three-compartment models, but with g_{sg} instead of g_{sp} and g_{pg} . The maximum conductance values are given in Table 2.1. The sodium and calcium reversal potentials are the values used by Bhalla and Bower. They are somewhat low, although not entirely outside the range of what is seen experimentally. Similarly, the potassium reversal potential is not sufficiently negative. The

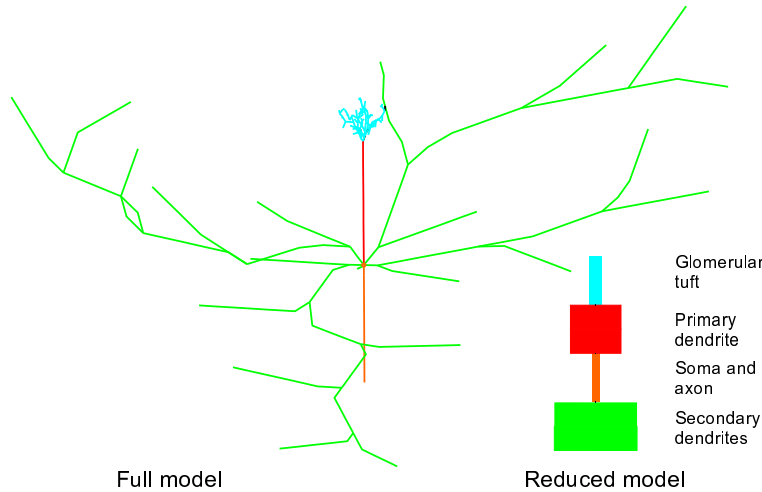


Figure 2.2: The 286-compartment and four-compartment mitral cell models, showing the approximate correspondence of the cell regions. The area of the blocks in the representation of the reduced model is proportional to the surface area of the compartments.

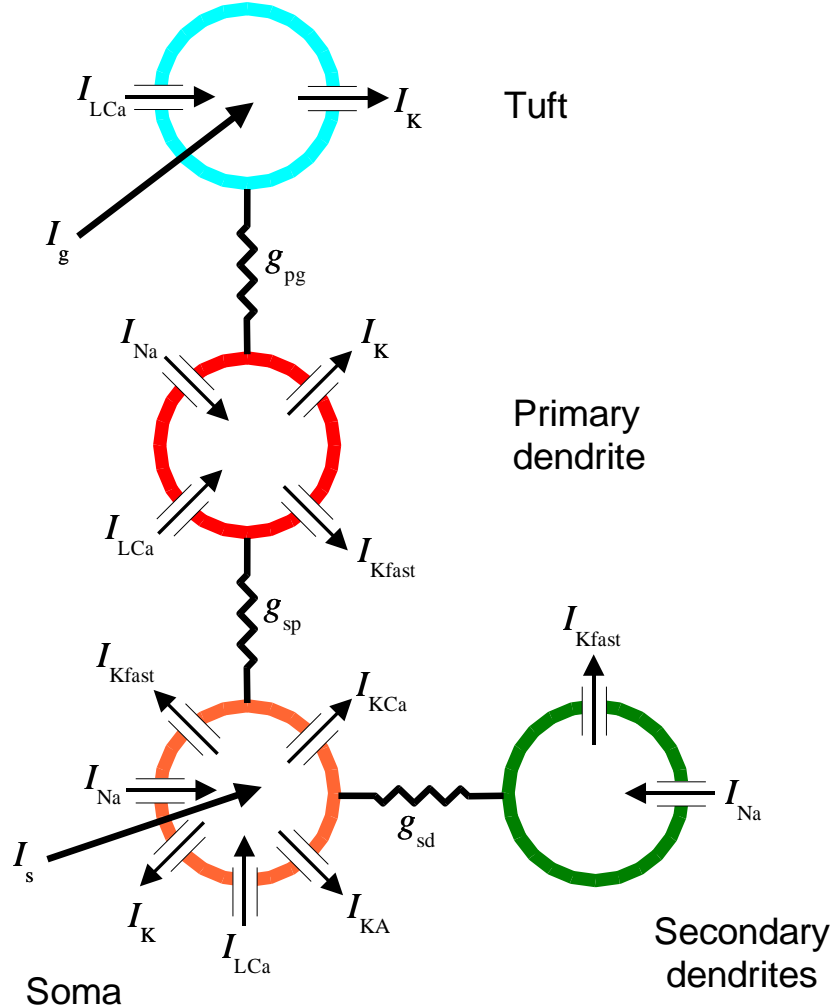


Figure 2.3: Schematic of the four-compartment model showing ion channels and points of stimulation. Currents are sodium (I_{Na}), slow potassium delayed rectifier (I_K), fast potassium delayed rectifier (I_{Kfast}), potassium anomalous rectifier (I_{KA}), calcium-dependent potassium (I_{KCa}) and L-type calcium (I_{LCa}). The conductances between soma and secondary dendrite, soma and primary dendrite, and primary dendrite and glomerulus are g_{sd} , g_{sp} and g_{pg} respectively. I_s and I_g are the currents injected into the soma and glomerular tuft respectively.

Compartment	Na	Kfast	LCa	K	KA	KCa
Soma/axon	1532	1956	40	28	58.7	142
Glomerular tuft	0	0	95	200	0	0
Primary dendrite	134	123	22	174	0	0
Secondary dendrites	226	330	0	0	0	0

Table 2.1: Channel distribution for the reduced mitral cell models. The values are the maximum conductance values in S m^{-2} .

exact values of the reversal potentials is not critical, as any change in their values could be compensated for by changing the experimentally-unknown values of the peak conductances.

The stimulating currents I_s and I_g are given by:

$$I_s = \alpha_s I_{\text{full}} \quad (2.5)$$

$$I_g = \alpha_g I_{\text{full}} \quad (2.6)$$

where I_{full} is the stimulating current applied to the soma or glomerular compartment of the full model and α_s and α_g are constant factors. These ‘current factors’ are intended to adjust for differences in the input resistance of the models. For each run the current inputs were set to zero for the first 50 ms then stepped up to I_s or I_g . A current step was used to stimulate the models to match the current clamp stimulation used by Bhalla and Bower. To test whether a current step is a good approximation to synaptic input in the glomerulus I modelled synaptic input with 940 AMPA and NMDA synapses, with equal maximum conductances (100 pS) receiving input from independent Poisson processes with mean rates from 4 to 200 Hz. I observed an approximately linear relationship between the constant current needed to produce a particular output firing rate and the synaptic input frequency needed to produce the same output rate (Figure 2.4). Therefore I concluded that constant current was a reasonable approximation to synaptic input in these cells.

2.2.1.3 Fitting the models

The maximum conductances of the voltage-gated currents and the membrane capacitance were all fixed to the values used in Bhalla and Bower [11]. The numbers of parameters are therefore four, six and eight for the two-, three- and four-compartment models respectively. It would of course be possible to vary the maximum conductances to obtain a better fit. However, this would add fourteen extra parameters for the four-compartment model, hence increasing the difficulty of fitting the model and increasing the possibility of over-fitting.

I used the Simplex algorithm [112] to fit the simplified models to the full model. The Simplex algorithm is a method for function minimization that does not require function derivatives or line minimizations. In an n -dimensional parameter space, a simplex is a geometric figure with $n + 1$ vertices, e.g. a triangle in two dimensions or a tetrahedron in three dimensions. Each vertex is a point in parameter space. The value of the error function (i.e. the goodness-of-fit of the reduced model to the full model) is evaluated at each vertex, and the vertex with the largest error is discarded. A new vertex is found using various transformations of the simplex, including reflections, expansions and contractions in one or more dimensions. The error function is then evaluated at the new vertex and the sequence repeated. In this way, the simplex ‘crawls’ about in parameter space, always discarding the point with the largest error. The Simplex method is slower than methods using line minimizations (e.g. Powell’s or Brent’s methods - see [112]) but has the advantage that it is less likely to get stuck in local minima, since the error function is evaluated at several points (the vertices), not just one.

I used two criteria for evaluating goodness of fit. The preliminary criterion was:

- the squared difference between voltage traces of simplified and full models over the first 200 ms for current injection to the soma of $I_{\text{full}} = 0.4 \mu\text{A cm}^{-2}$.

This criterion is referred to henceforth as ‘fit-to-shape’. It was hoped that fitting to spike shape, rather than simply to firing rate, would capture some of the important features of the full model dynamics, so

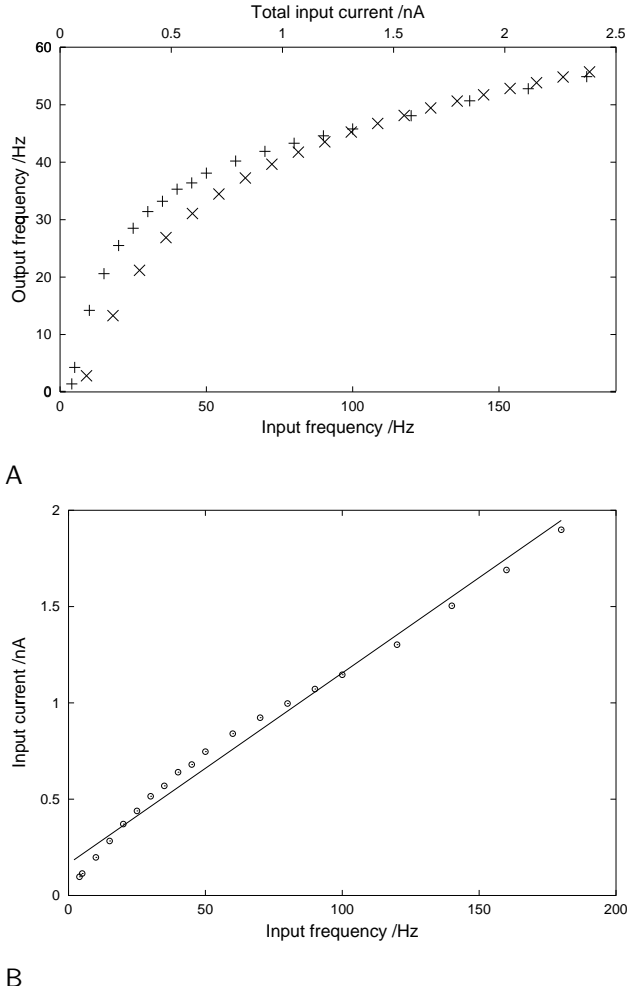


Figure 2.4: Comparison of Poisson process synaptic input with constant current approximation. (A) Mean output firing frequency (inverse of mean of nine inter-spike intervals) as a function of mean input frequency (+) and of input current (x). (B) Input current plotted against the mean input frequency which produces the same output frequency as the current. The ordinates come from fitting a logarithmic function to the graph of output frequency vs input current then reading off the equivalent current at each output frequency of the synaptic input data. The resulting function is clearly non-linear, but follows a linear function quite closely.

that fitting at one input level would give a good fit at all levels. This proved not to be the case (see Results), so a second criterion was used which explicitly averages over input levels and over somatic and ‘synaptic’ inputs:

- the squared proportional difference in spike time for the first four spikes, summed over current injections of $I_{\text{full}} = 0.2, 0.4, 0.8, 1.6 \mu\text{A cm}^{-2}$ to the soma and to the glomerulus, i.e., if t_k^{reduced} and t_k^{full} are the times of the peaks of the k th spikes in the reduced and full models, then

$$\text{error} = \sum_{\substack{\text{soma} \\ \text{glomerulus}}} \sum_{I_{\text{full}}} \sum_{k=1}^4 \left(\frac{t_k^{\text{reduced}} - t_k^{\text{full}}}{t_k^{\text{full}}} \right)^2 \quad (2.7)$$

This criterion is referred to henceforth as ‘fit-to-time’.

These criteria capture both the transient and steady state behaviour of the models, since the models settle down very quickly into regular firing (the difference between the firing rate calculated from the mean of the first three inter-spike intervals (ISIs) and that calculated from the mean of the fiftieth to the hundredth ISIs is 0.8% for 1.0 nA input and 0.2% for 0.1 nA input to the full model. The firing rates plotted in Figures 2.8 and 2.10 were calculated from the first three ISIs). The range of input currents used produces output firing over the range 10-100 Hz.

2.2.2 Granule cell models

2.2.2.1 Description of reduced models

The full Bhalla and Bower granule cell model has 944 compartments; I investigated simplifications with two or three compartments. The three compartment model has deep dendrite, soma and peripheral dendrite compartments. These correspond to the regions in the full model with uniform channel distributions, excepting the ‘trunk’ region which is not explicitly modelled here. The two compartment model lumps together the soma and deep dendrites. A schematic of the three compartment model is shown in Figure 2.5.

The current balance equations for the three compartments (soma, peripheral dendrite, deep dendrite) are:

$$\begin{aligned} C_m V'_s &= -g_{\text{pas}}(V_s - E_{\text{rest}}) - g_{\text{Na}}(V_s - 45) - g_{\text{KM}}(V_s + 70) - g_K(V_s + 70) \\ &\quad - g_{\text{KA}}(V_s + 70) + (g_{\text{sd}}/u)(V_d - V_s) + (g_{\text{sp}}/u)(V_p - V_s) + I_s/u \end{aligned} \quad (2.8)$$

$$C_m V'_p = -g_{\text{pas}}(V_p - E_{\text{rest}}) - g_{\text{Na}}(V_p - 45) - g_K(V_p + 70) + (g_{\text{sp}}/v)(V_s - V_p) \quad (2.9)$$

$$C_m V'_d = -g_{\text{pas}}(V_d - E_{\text{rest}}) + (g_{\text{sd}}/w)(V_s - V_d) \quad (2.10)$$

where V_s , V_p and V_d are the membrane potentials of the soma, peripheral dendrite and deep dendrite compartments respectively. Note that the latter two symbols are the same as for the mitral cell primary and secondary dendrites respectively. Which cell is being referred to will be made clear throughout. u , v and w are the ratios of the surface areas of the soma, peripheral dendrite and deep dendrite compartments respectively to the total cell membrane area ($u+v+w=1$). g_{sd} and g_{sp} are the conductances joining the soma and deep dendrite, and soma and peripheral dendrite compartments respectively. All other symbols are as for the mitral cell model. Note that the sodium channel is not the same as in the mitral cell model, but the K and KA channels are the same (see [11] for more details). The maximum conductances of the voltage-gated currents and the membrane capacitance were all fixed to the values used in Bhalla and Bower, as for the mitral cell model. The maximum conductances are summarised in Table 2.2.

2.2.2.2 Fitting the models

Because fitting to spike times rather than to spike shape was found to be of great advantage for the mitral cell model, only the former fitting method was used for the granule cell. At intermediate input levels, the full granule cell model shows spike time adaptation (probably due to the KM current), in contrast to the

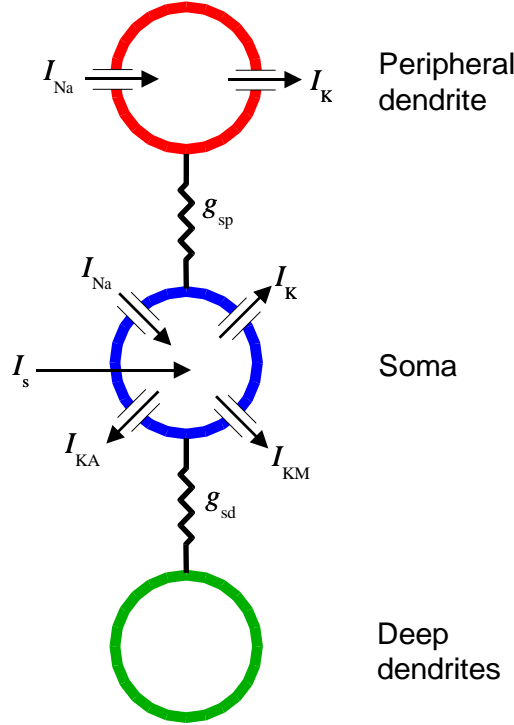


Figure 2.5: Schematic of the three compartment granule cell model showing ion channels and point of stimulation. Currents are sodium (I_{Na}), slow potassium delayed rectifier (I_K), potassium anomalous rectifier (I_{KA}) and muscarinic potassium (I_{KM}). The conductances between soma and peripheral dendrite and between soma and deep dendrites are g_{sp} and g_{sd} respectively. I_s is the current injected into the soma.

Compartment	Na	K	KM	KA
Soma	1611	1313	1334	88
Deep dendrites	0	0	0	0
Peripheral dendrite	1355	243	0	0

Table 2.2: Channel distribution for the reduced granule cell models. The values are the maximum conductance values in S m^{-2} .

mitral cell model (compare Figures 2.6 and 2.13), so six spikes were used for the error measure, rather than four, to better capture both the transient and steady-state behaviours. Five input levels were used: $I_{\text{full}} = 0.01, 0.03, 0.1, 0.3$ and $1.0 \mu\text{A cm}^{-2}$. In summary,

$$\text{error} = \sum_{I_{\text{full}}} \sum_{k=1}^6 \left(\frac{t_k^{\text{reduced}} - t_k^{\text{full}}}{t_k^{\text{full}}} \right)^2 \quad (2.11)$$

where the symbols are defined as for Eq.2.7.

2.2.3 Numerical methods

All models were simulated in NEURON Version 4.1. running on a Digital XP1000 workstation under Digital Unix. The integration method for the fit-to-time optimisations was the NEURON inbuilt global variable-time-step method with default parameters and for the fit-to-shape optimisations was the default fixed-time-step method with time step $25 \mu\text{s}$. The Simplex algorithm was taken from *Numerical Recipes* [112]. The NEURON scripts for the reduced models are given in Appendix B. As a check, the four-compartment mitral cell model was also simulated in XPP. The agreement between NEURON and XPP was very good (difference of 0.21 ms after five spikes/180 ms).

2.3 Results

2.3.1 Mitral cell model

2.3.1.1 Fitting to the spike shape

The fit-to-shape error measure has an important limitation, illustrated by the observation that a simplified model firing with the same frequency as the full model but out of phase with it has a larger error than a model which does not fire at all, although qualitatively it would be regarded as a better match. Nevertheless, using a manual search to obtain a coarse fit and the Simplex optimisation algorithm to refine this, fits were obtained for the two-, three- and four-compartment models. Figure 2.6 shows the response of the full model and reduced models to current injection of $I_{\text{full}} = 0.4 \mu\text{A cm}^{-2}$ to the soma. The parameter values are given in Table 2.3. The fit is poor for the two-compartment model, with a reset potential of -58 mV compared to -65 mV for the full model (Figure 2.6A). The fit is good for the three- and four-compartment models, with the four-compartment model coming closest to reproducing the rapid initial post-spike rebound followed by slower depolarisation exhibited by the full model. The rebound is interpreted as being due to current flow from the calcium channels in the glomerulus to the soma. This is borne out by an experiment in which these channels were removed from the glomerulus of the full model (data not shown). The addition of the primary dendrite compartment in going from three to four compartments is important in delaying the arrival of this current at the soma. The role of the secondary dendrite compartment is chiefly to slow the firing rate. The three-compartment model exhibits a kink in the down-slope of the action potential, which is due to delayed firing in the secondary dendrite.

A good fit under one input condition does not guarantee a good fit under all conditions. Figure 2.7 shows the discrepancy between the full model and the reduced models with the injected current amplitude doubled. In the three-compartment model, the delay in firing of the secondary dendrite is even more pronounced.

2.3.1.2 Fitting to spike times

The second error measure produces a closer fit in spike timing over a range of input currents (Figure 2.8). This is unsurprising since the error measure was designed with this aim in mind. In addition, this error measure is much smoother than the first, and gives greater confidence that the minimum found is close to the global minimum. Fitting to spike shape leads to differences of up to 32% in firing frequency and 76% in the latency of the first spike, for the four-compartment model in the frequency range 10-120 Hz with

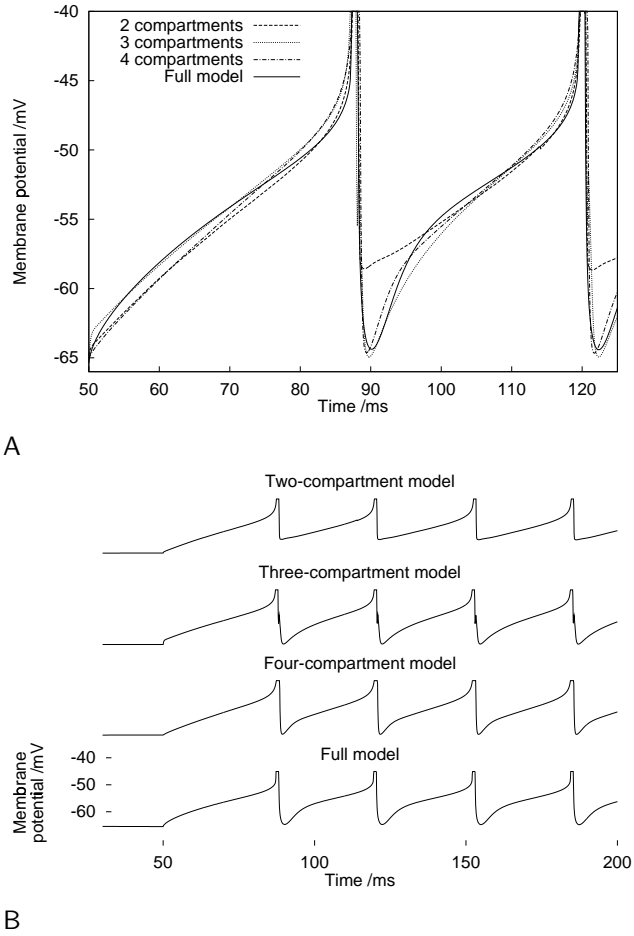


Figure 2.6: Somatic membrane potential trace for full and reduced models with $I_{\text{full}} = 0.4 \mu\text{A cm}^{-2}$ after fitting to spike shape. Both three- and four-compartment models give good fits to the full model. The two-compartment model has a markedly raised reset potential.

	Fit to spike shape			Fit to spike times		
	2	3	4	2	3	4
p	0.166	0.0500	0.0475	0.274	0.0845	0.0510
q	-	0.299	0.184	-	0.140	0.0840
r	-	-	0.216	-	-	0.328
g_{sg}	8.39×10^{-4}	4.87×10^{-5}	-	2.09×10^{-3}	4.44×10^{-5}	-
g_{sd}	-	1.85×10^{-4}	3.31×10^{-2}	-	3.13×10^{-4}	1.94×10^{-4}
g_{sp}	-	-	2.33×10^{-4}	-	-	5.47×10^{-5}
g_{pg}	-	-	4.08×10^{-4}	-	-	5.86×10^{-5}
α_s	1.43	1.35	1.44	2.60	1.78	1.37
α_g	-	-	-	3.02	1.84	1.85

Table 2.3: Best fit parameter values for 2-, 3- and 4-compartment reduced mitral cell models. Units of g_{sg} , g_{sd} , g_{sp} and g_{pg} are S cm^{-2} . Other parameters are dimensionless.

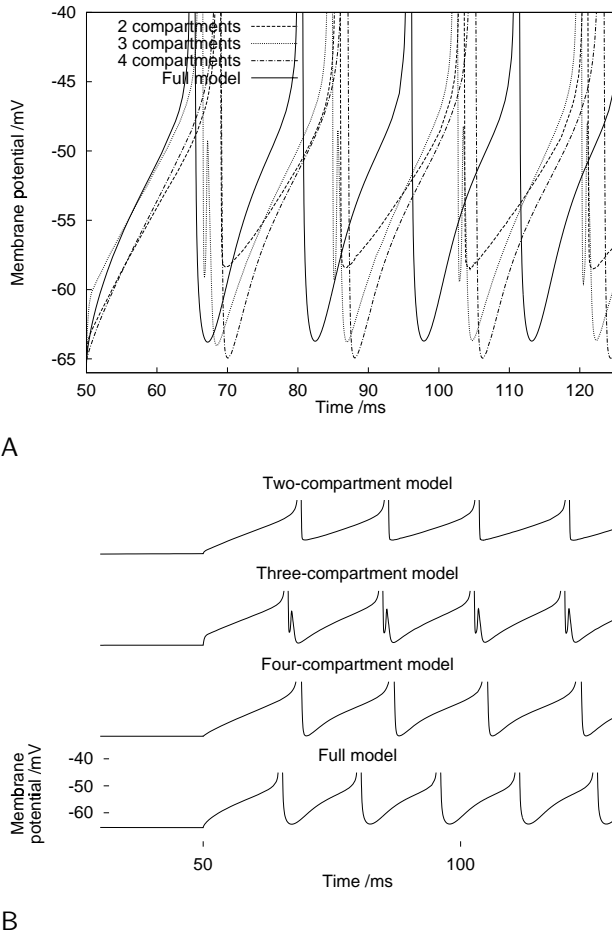


Figure 2.7: Somatic membrane potential trace for full and reduced models with $I_{\text{full}} = 0.8 \mu\text{A cm}^{-2}$ after fitting to spike shape with $I_{\text{full}} = 0.4 \mu\text{A cm}^{-2}$. The miniature spike on the down-slope of the action potential in the three-compartment model is due to the delay between spiking in the soma and in the secondary dendrite.

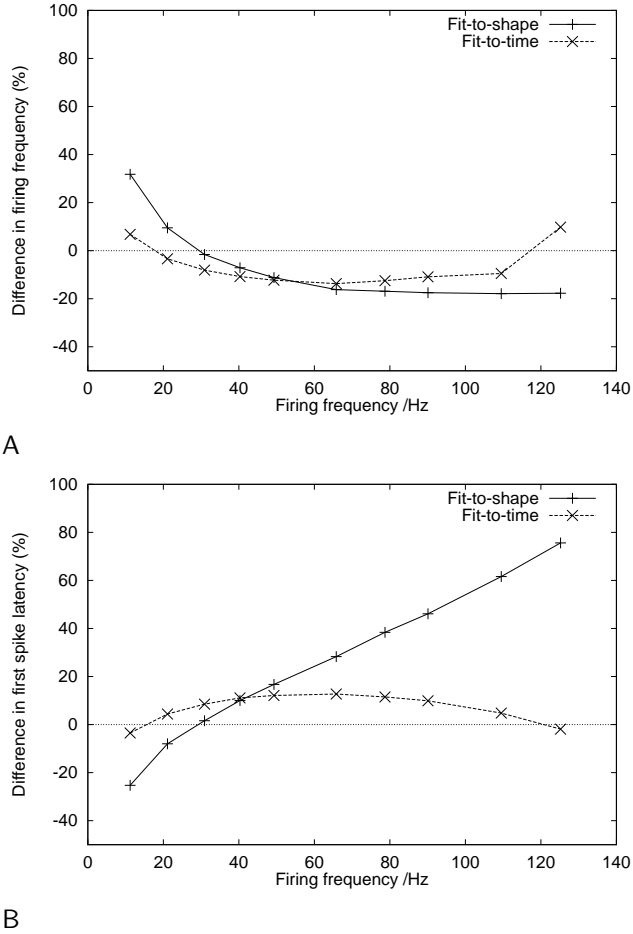


Figure 2.8: Comparing fit-to-shape to fit-to-time for the four-compartment model. (A) Firing frequency, (B) Latency of first spike. Current was injected in the soma compartment. The four compartment model with fit-to-shape parameters shows almost zero deviation from the full model with current injection $0.4 \mu\text{A cm}^{-2}$, the level at which it was fitted, but large differences with higher or lower inputs. In contrast, the four-compartment model with fit-to-time parameters fits reasonably well over a wide range of input levels.

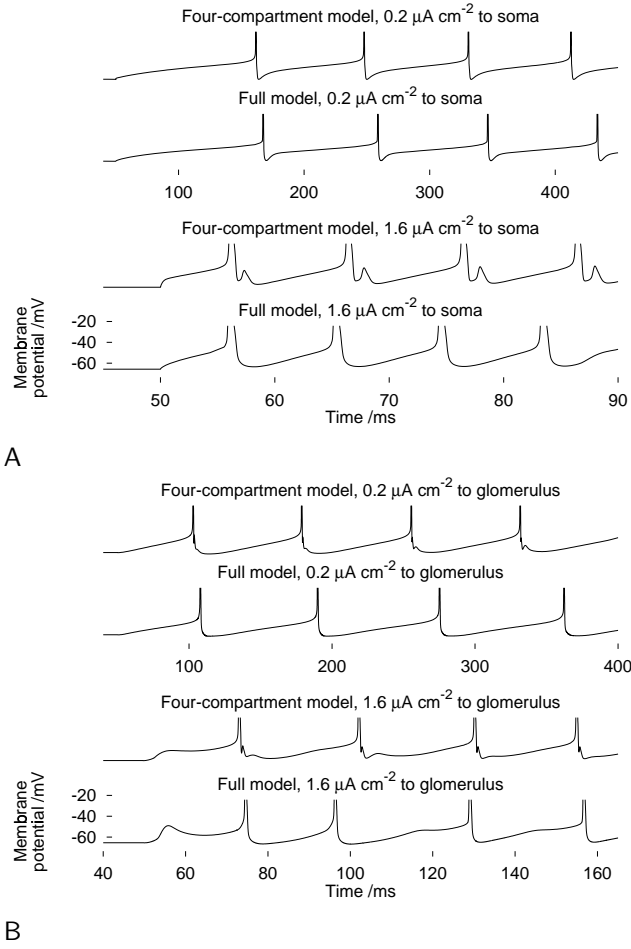


Figure 2.9: Somatic membrane potential trace for full and four-compartment models with $I_{\text{full}} = 0.2 \mu\text{A cm}^{-2}$ and $1.6 \mu\text{A cm}^{-2}$ after fitting to spike timing. (A) Current injection to soma. (B) Current injection to glomerulus. The models fit well in terms of first spike latency and firing frequency, but there are discrepancies in the detailed shape of the membrane potential traces. This illustrates one of the problems with very-reduced compartmental models.

current injection to the soma. The maximum differences are only 13% and 14% after fitting the same model to spike times. After fitting to spike times the spike shapes of the reduced models are similar to that of the full model but with a deeper hyperpolarisation after the spike and a kink in the down-slope of the action potential, due to delayed firing in the secondary dendrite (Figure 2.9).

For somatic current injection, all three reduced models have qualitatively the same behaviour as the full model, but the three- and four-compartment models have a much better quantitative fit to the full model than does the two-compartment model (Figures 2.10A,C).

Injecting current into the glomerulus leads to more complex behaviour than somatic injection. Above a certain level, about $1.1 \mu\text{A cm}^{-2}$ for the full model (giving a firing rate of 40 Hz), the first spike is suppressed by a large slow potassium current in the glomerulus (caused by a large calcium spike) (note the step in first spike latency in Figure 2.10D) and the steady-state firing rate is also depressed (Figure 2.10B). The three- and four-compartment models also exhibit this behaviour, although the threshold for the transition differs slightly. Discounting the large differences which occur near this transition, the largest difference in firing rate between reduced and full models for somatic or glomerular current injection is 14% for the four compartment model and 22% for the three-compartment model.

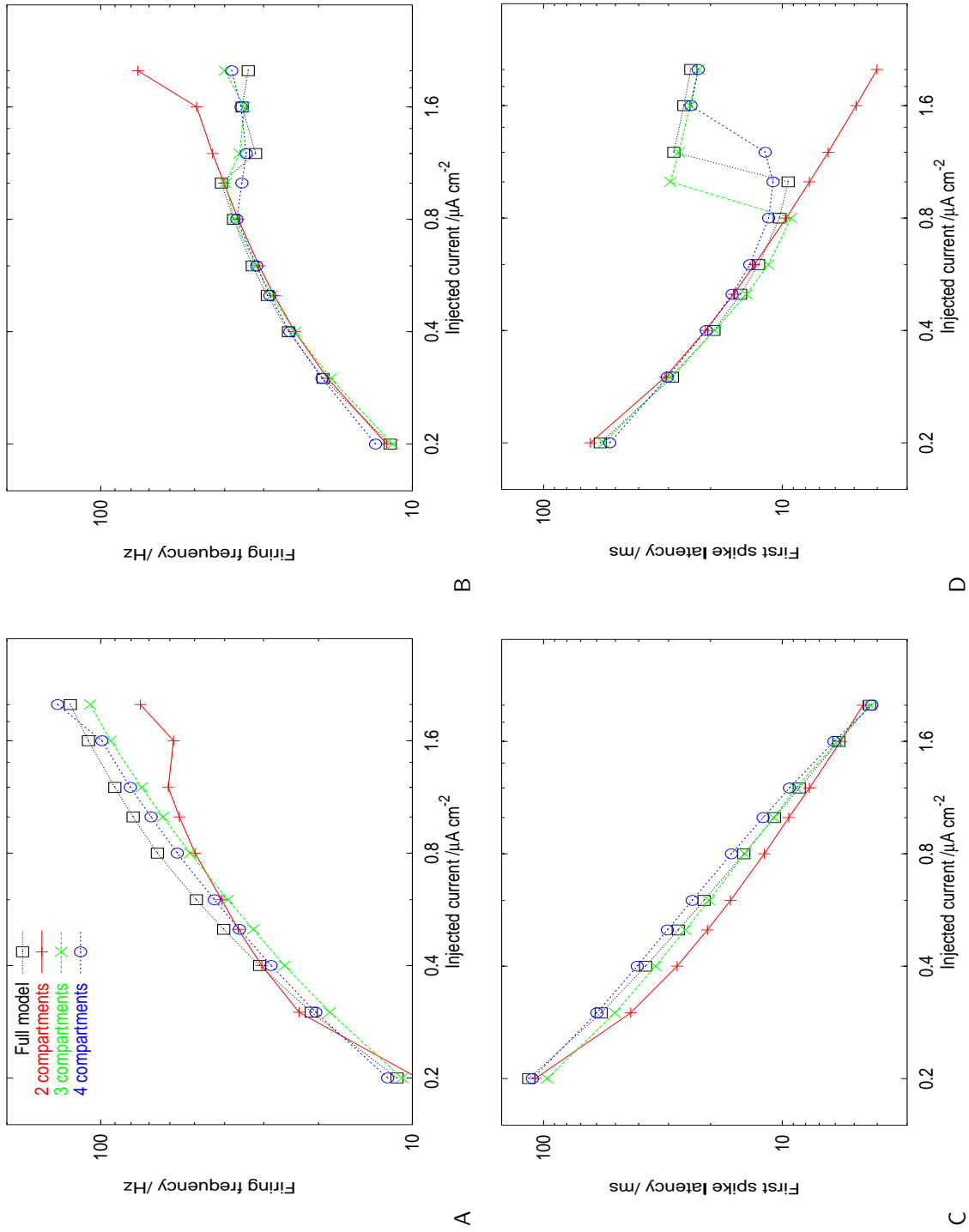


Figure 2.10: Comparing reduced models with two, three and four compartments, with fit-to-time parameters: (A) Firing frequency as a function of current for stimulation of soma; (B) as A for stimulation of glomerulus; (C) Latency of first spike as a function of current for stimulation of soma; (D) as C for stimulation of glomerulus. The three- and four-compartment models fit the full model closely for a wide range of input levels and for both somatic and glomerular inputs. The two- compartment model gives a tolerable fit for somatic input and for low glomerular input, but deviates considerably for high glomerular input.

	Number of compartments	
	2	3
u	0.0220	0.0136
v	-	0.308
g_{sp}	2.31×10^3	3.08×10^{-4}
g_{sd}	-	4.34×10^{-4}
α_s	0.950	0.625

Table 2.4: Best fit parameter values for reduced granule cell models. Units of g_{sd} and g_{sp} are S cm^{-2} . Other parameters are dimensionless.

2.3.1.3 Simulation time

The processor time taken to simulate one hundred spikes (using the variable time step integration method) with a current injection of $0.4 \mu\text{A cm}^{-2}$ to the soma is as follows: two-compartment model 1.8 seconds; three-compartment model 2.5 seconds; four-compartment model 2.9 seconds; full model 219 seconds. The four-compartment model gives a 75-fold reduction in simulation time over the full model and the two-compartment model a 120-fold reduction.

2.3.2 Granule cell model

2.3.2.1 Fitting to spike times

After fitting, the three-compartment granule cell model agrees closely with the full model in terms of firing frequency, first spike latency, and spike shape, over two orders of magnitude in input current (see Figures 2.11, 2.12 and 2.13). The two-compartment model is much less satisfactory (Figure 2.12). The fitted parameter values are shown in Table 2.4. The value of g_{sp} for the two-compartment model is very large, so the cell is effectively a single compartment. The deep dendrites (which have no active conductances) are clearly required to reproduce the full model behaviour.

2.3.2.2 Simulation time

The processor time taken to simulate one thousand spikes (using the variable time step integration method) with a current injection of $0.05 \mu\text{A cm}^{-2}$ to the soma is as follows: two-compartment model 17 seconds; three-compartment model 20 s; full model 1164 s. With a current of $0.6 \mu\text{A cm}^{-2}$, the processor times are 13 s, 15 s and 898 s. These currents were chosen to minimise the differences in firing

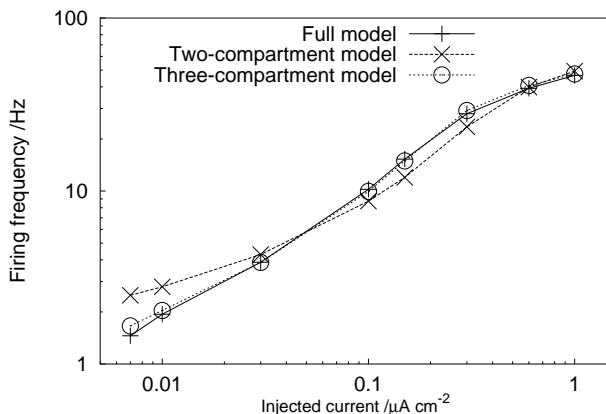


Figure 2.11: Comparing reduced and full granule cell models: firing frequency as a function of injected current. The three compartment model agrees closely with the full model over a broad range.

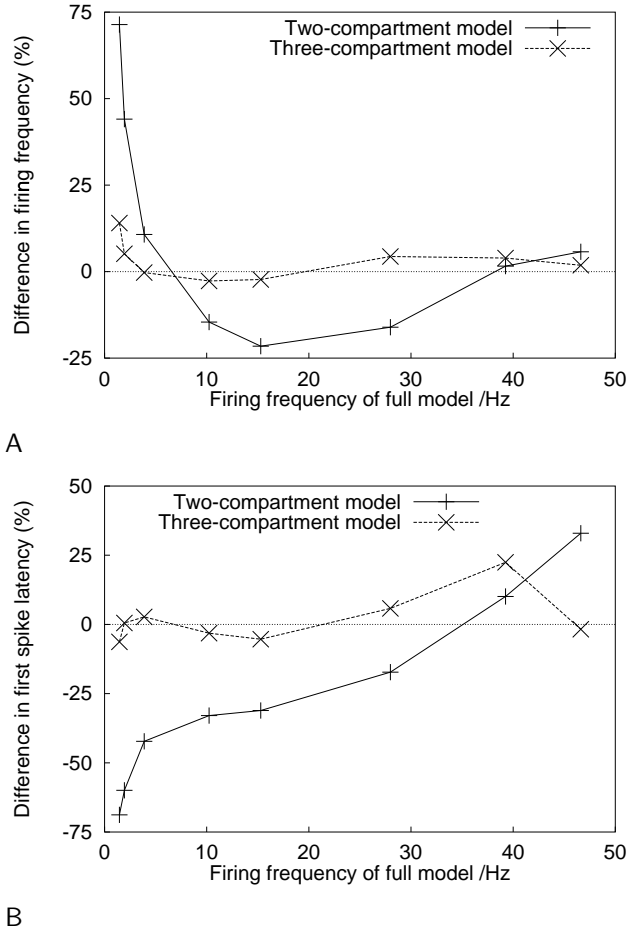


Figure 2.12: Comparing reduced granule cell models with two and three compartments: (A) Difference in firing frequency between the reduced and full models, (B) Difference in latency of first spike between the reduced and full models. Current was injected in the soma compartment. The three compartment model agrees closely with the full model over a broad range. The two-compartment model is much less satisfactory.

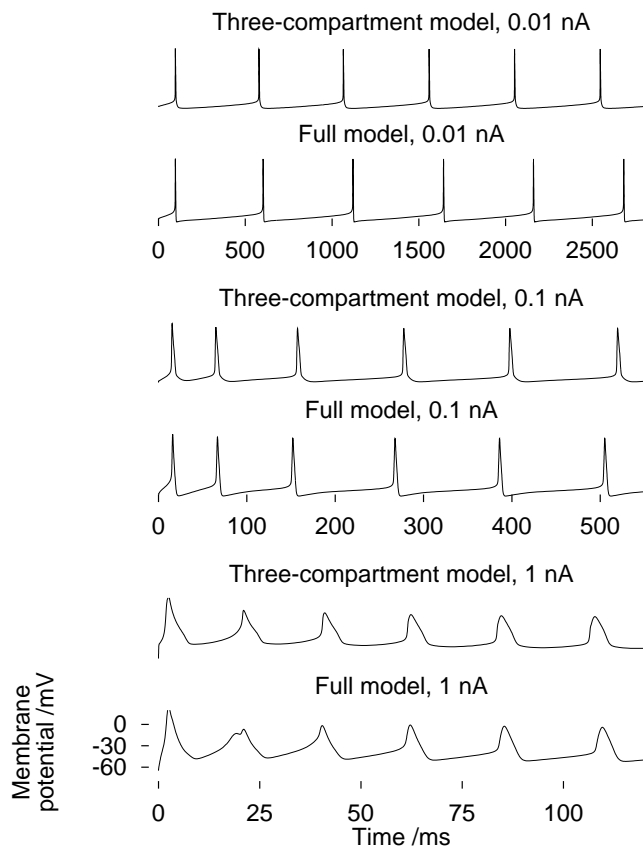


Figure 2.13: Somatic membrane potential trace for full and three-compartment granule cell models with $I_{\text{full}} = 0.01, 0.1$, and 1 nA . The reduced model fits the full model well both in quantitative spike times and in qualitative features of spike shape.

rate between the three models (see Figure 2.11). The three-compartment model gives a 60-fold reduction in simulation time over the full model and the two-compartment model a 70-fold reduction.

2.4 Discussion

The four- and three-compartment mitral cell models give good qualitative and quantitative fits to the fully-detailed model. In particular they exhibit the same rather complicated calcium channel-related behaviour at high input levels as the full model, in which a calcium spike in the glomerulus causes the opening of slow potassium channels which then suppress the sodium spike at the soma. This behaviour was not a criterion for fitting – it arises naturally from the model structure. Since the three-compartment model exhibits the correct qualitative behaviour, and adding a fourth compartment produces only a small quantitative increase in accuracy at the expense of increased simulation time, it was not thought necessary to test models with five or more compartments.

How do the fitted parameters of the reduced models compare to those of the full model? For the full model $p = 0.056$ (lumping soma and axon areas together), $q = 0.078$, $r = 0.11$ and $s = 0.75$. These are not very dissimilar to the area ratios of the three- and four-compartment models (see Table 2.3). The axial conductances are also similar in magnitude in the full model compared to the reduced models, although the current factors α_s and α_g are greater than 1, suggesting lower input resistance for the reduced models.

How unique are the fitted parameters? The optimisation procedure I used to fit the models can only ever guarantee to find a local minimum. By restarting the search many times from different points in parameter space I am reasonably confident that the parameters I have found are close to the global minimum.² Combining the Simplex algorithm with simulated annealing has been shown to be the best strategy for parameter fitting for small compartmental models [147]. My simpler strategy is less time consuming to implement and run, however. However there are certainly other minima which give good fits. For example, one local minimum for the four-compartment model has g_{sd} effectively zero, reducing the four-compartment model to a three- compartment one with only soma, primary dendrite and glomerulus. The most tightly constrained parameters are the areas of the soma and glomerulus. The area of the secondary dendrite compartment and the g_{sd} conductance have the widest margins of error.

This investigation has emphasised the importance of using a wide input range when fitting a model. The reduced models fit the full model well within the range of firing rates 10–120 Hz. The lower end of this range corresponds to the experimental mean rate of spontaneous firing in mammals [12, 53]; the higher end is seen experimentally during bursts [100]. It would be possible to re-fit the model to cover a lower range if the high input regime was not of interest.

The agreement between the three-compartment reduced and the full granule cell models is at least as good as the agreement for the mitral cell case. The range of firing rates over which the fit is good is shifted downwards compared to the mitral case, being about 2–50 Hz. Three compartments are optimum for the granule cell, compared to four for the mitral cell. This probably reflects the more complex morphology of the full mitral cell model.

The true test of any models such as these is their behaviour in a network. The greatly improved speed (and memory requirements) of these models compared to the fully-detailed models should allow network simulations with thousands of cells – still far fewer than the fifty thousand or so mitral cells and millions of granule cells in the real bulb [121], but potentially allowing realistic behaviour to be simulated and a bridge built between single cell and network level properties.

The models of Bhalla and Bower are anatomically and physiologically detailed and were carefully fitted to current clamp recordings, but they are by no means the last word in mitral and granule cell models. As new data and new models become available it will be important to adjust the reduced models to take account of these.

The next task is to assemble these reduced single cell models into a network model.

²The search was restarted about twenty times for each model. On average, about half of these converged to a minimum with an error within 1% of the lowest error. The others converged to higher local minima.

Much of the material in this chapter has previously been published in reference [32]

Chapter 3

Mitral cell interactions: phase locking in two-cell systems

3.1 Introduction

To approach an understanding of the olfactory bulb, an understanding of the interactions between different mitral/tufted cells is critical, as these are the cells that transmit olfactory information to the cortex. Mitral/tufted cells do not interact directly, but only indirectly via interneurones: granule and periglomerular cells (see §1.1.1).

The inhibition between the mitral cells may affect both the mean firing rate and the detailed temporal structure of firing. Both experimental and theoretical results motivate a particular consideration of synchronization between the mitral cells. Prominent oscillations in field potential responses in vertebrate olfactory bulb [1, 74] are suggestive of synchronization of neuronal firing [37], and recent intracellular recordings have shown close synchronization of spike firing times in about 25% of recorded mitral cell pairs [67]. In the antennal lobe of honeybees, synchronization of projection neurone spiking has been shown to have behavioural importance [138]. For more detail, see §1.1.3. Spike synchronization in pulse-coupled networks of spiking neurones has been extensively studied theoretically and using computer simulations (see, for example, [27, 46, 146]), with most emphasis on the case of homogeneous networks. Both excitatory and inhibitory connections frequently produce either synchrony or antisynchrony, depending on the conditions. This literature is reviewed further in the Discussion section of this chapter (§3.4).

In this chapter, I investigate the simplest possible system: just two mitral cells. This makes it easier to obtain analytical results and allows a more comprehensive evaluation of the system properties. The disadvantage is that results may not generalise to larger networks. Larger networks are considered in the next chapter.

I consider two systems: (a) a two-cell system consisting of two mitral cells with direct inhibitory contacts (Figure 3.1A); (b) a three-cell system consisting of two mitral cells and one interneurone (Figure 3.1B). The interneurone could be a granule cell or a periglomerular cell. Each mitral cell has an excitatory connection to the interneurone, and an inhibitory connection from it. All connections are pulse-coupled: a spike in the pre-synaptic cell is required to trigger an excitatory/inhibitory event in the post-synaptic cell. These two systems are equivalent when the mitral–interneurone excitatory connection is strong enough that a single mitral cell spike leads to an interneurone spike.

This chapter will proceed as follows: I begin by analysing the two-cell system with the leaky integrate-and-fire (LIF) model. This has the advantage that it is amenable to mathematical analysis. I show that the cells can synchronize or phase-lock their firing and derive the conditions for this to occur. I then analyze the possible states of the system when phase-locking breaks down: harmonic locking and suppression. This analysis is extended to more complex synaptic connections between the two cells. The biophysical models (Chapter 2) are more realistic than the LIF model, but are not amenable

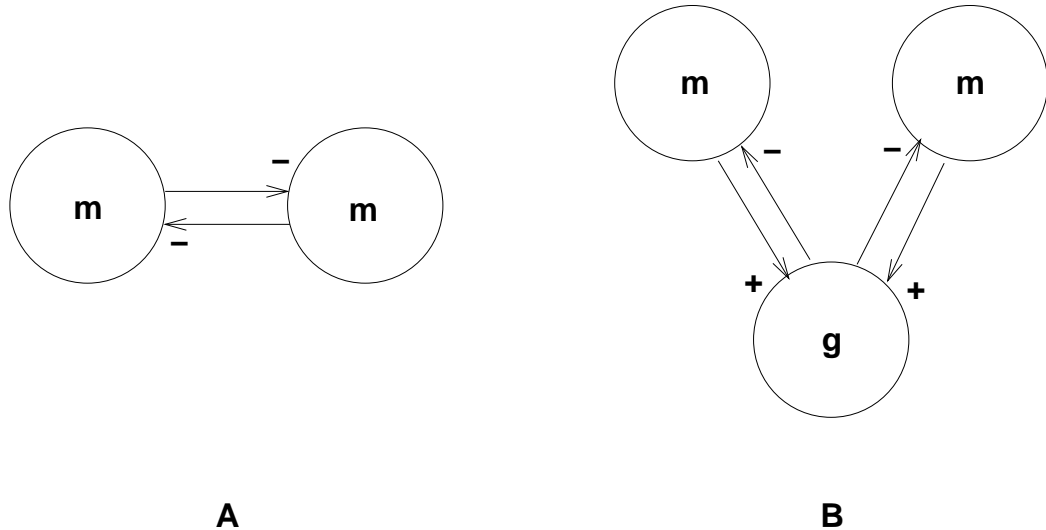


Figure 3.1: (A) Two mitral cell (m) system with direct inhibitory connections. (B) Two mitral cell system with inhibition mediated via an interneurone (g).

to mathematical analysis. I therefore use numerical simulation to study the network with the four-compartment mitral cells, and to compare its behaviour to the LIF network. I find that the LIF and biophysical networks have similar behaviours – both exhibit phase-locking, for example – but that there are some differences. I then study the three-cell system using first the LIF models and then the biophysical models (four-compartment mitral cell and three-compartment granule cell models). Mediating inhibition via an interneurone rather than directly can also produce phase-locking and harmonic locking, but more complex behaviour is also seen.

3.2 Direct mitral-mitral inhibition

3.2.1 The integrate-and-fire model

I consider the leaky integrate-and-fire model, in which the membrane potential V evolves in time according to the current balance equation:

$$C \frac{dV}{dt} = -\frac{V}{R} + I(t) \quad (3.1)$$

(where C is the cell membrane capacitance, R is the membrane resistance, and I is the current input) until V reaches some threshold value V_θ , at which point it is reset to some baseline value which can be taken to be zero with no loss of generality.

If $I(t)$ is a constant value, I , the solution to equation 3.1 is

$$V(t) = IR + (V(0) - IR)e^{-t/RC} \quad (3.2)$$

The natural firing period (that is, with no synaptic input) of the cell, T , may be obtained by setting $V(0) = 0$ and $V(T) = V_\theta$:

$$T = RC \ln \left(\frac{IR}{IR - V_\theta} \right) \quad (3.3)$$

I consider a system of two integrate-and-fire cells, with identical parameters except that Cell 1 receives a higher level of input than Cell 2. The cells interact as follows: when the membrane potential of either cell reaches threshold there is a delay of time t_d after which the membrane potential of the other cell is instantaneously reduced by a constant amount ΔV .

It will be convenient to define the following quantities:

$$\tau = RC$$

$$\theta = \frac{I_2 R - V_\theta}{I_2 R}$$

$$\delta = \frac{\Delta V}{V_\theta}$$

$$\alpha = \frac{I_1 - I_2}{I_2}$$

$I_2 R$ is the equilibrium level which the membrane potential of Cell 2 would reach if it did not reset. For the cell to fire at all requires $I_2 R > V_\theta$, hence $0 < \theta < 1$. The parameter θ controls the non-linearity of the system. If θ is large, V reaches threshold rapidly and approximately linearly; if θ is close to zero, V approaches the threshold slowly and non-linearly. α is a measure of the heterogeneity of the inputs. Cell 1 is defined to be the cell receiving the highest input, so $\alpha \geq 0$.

We may now rewrite equation 3.2 for the two cells as:

$$x_1(t) = \frac{1 + \alpha}{1 - \theta} + \left(x_1(0) - \frac{1 + \alpha}{1 - \theta} \right) e^{-t/\tau} \quad (3.4)$$

$$x_2(t) = \frac{1}{1 - \theta} + \left(x_2(0) - \frac{1}{1 - \theta} \right) e^{-t/\tau} \quad (3.5)$$

where $x(t) = V(t)/V_\theta$ varies between 0 and 1.

3.2.2 Existence of phase-locked solutions

Due to the different input levels to the cells, the cells have different ‘natural’ firing periods (the period between consecutive instances of the cell membrane reaching threshold, under conditions of no interactions between the cells). We wish to determine whether the cells will synchronize or phase-lock their firing and, if so, under what conditions. We will proceed as follows: first we derive the return map for the

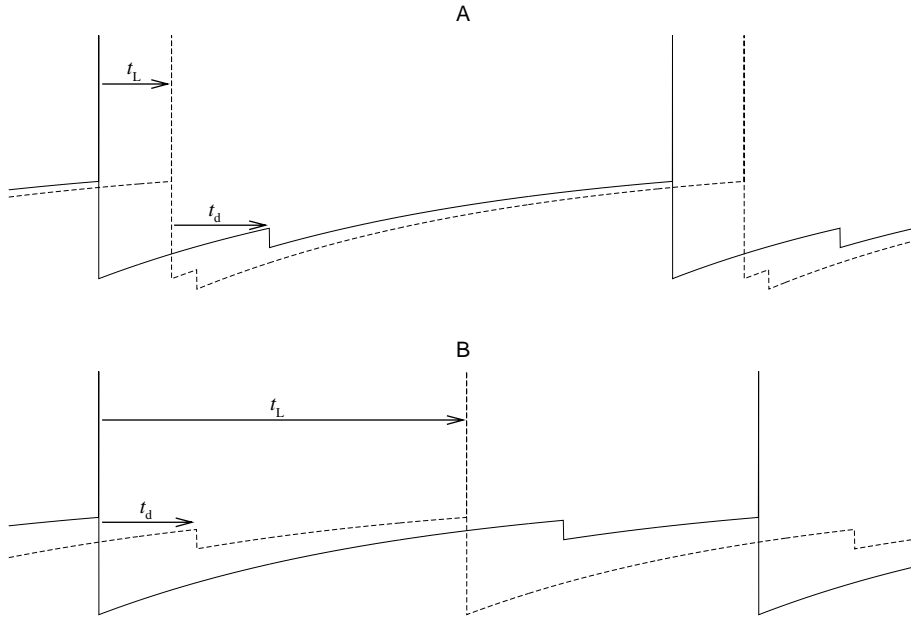


Figure 3.2: Possible firing patterns of two neurons with inhibitory connections: (A) Both cells fire before either is inhibited ($t_L < t_d$); (B) Cell 2 is inhibited earlier than it fires ($t_L > t_d$). Parameters: $\theta = 0.2$, $\delta = 0.2$, $\alpha = 0.02$, $t_d = 0.3\tau$. Solid line – Cell 1; dashed line – Cell 2

system, i.e. the $(n+1)$ th time lag, t_L^{n+1} , as a function of the n th time lag, t_L^n (§3.2.2.1). Then we assert that the condition for 1:1 phase-locking, $t_L^{n+1} = t_L^n$, is true and show that the return map equation has a solution in this case (§3.2.2.2). Finally we show that this solution is stable (§3.2.2.3). The assumptions made in deriving the return map can be used to determine the region of parameter space within which 1:1 phase-locking can stably exist (§3.2.2.4).

3.2.2.1 Derivation of return map

If Cell 1 fires at time t , and Cell 2 fires at time $t + t_L^n$ then there are two possibilities, for $t_d > 0$:

- A. $t_L^n < t_d$ - both cells fire within the delay time. (Figure 3.2A)
- B. $t_L^n > t_d$ - Cell 2 is inhibited before it fires. (Figure 3.2B)

I further make the assumption that α is sufficiently small that Cell 1 fires only once before Cell 2 fires – I shall later derive the conditions for this to be true (Equations 3.25, 3.26 and 3.27).

For case A we see from equation 3.4 that immediately before receiving the downward step in x_1 ,

$$x_1(t_L^n + t_d) = \frac{1 + \alpha}{1 - \theta} \left(1 - e^{-(t_L^n + t_d)/\tau} \right) \quad (3.6)$$

Denoting the time to threshold from this point as t^* ,

$$\begin{aligned} 1 &= x_1(t_L^n + t_d + t^*) \\ &= \frac{1 + \alpha}{1 - \theta} + \left[\frac{1 + \alpha}{1 - \theta} \left(1 - e^{-(t_L^n + t_d)/\tau} \right) - \delta - \frac{1 + \alpha}{1 - \theta} \right] e^{-t^*/\tau} \end{aligned} \quad (3.7)$$

and hence

$$t^* = \tau \ln \left(\frac{(1 + \alpha)e^{-(t_L^n + t_d)/\tau} + \delta(1 - \theta)}{\theta + \alpha} \right) \quad (3.8)$$

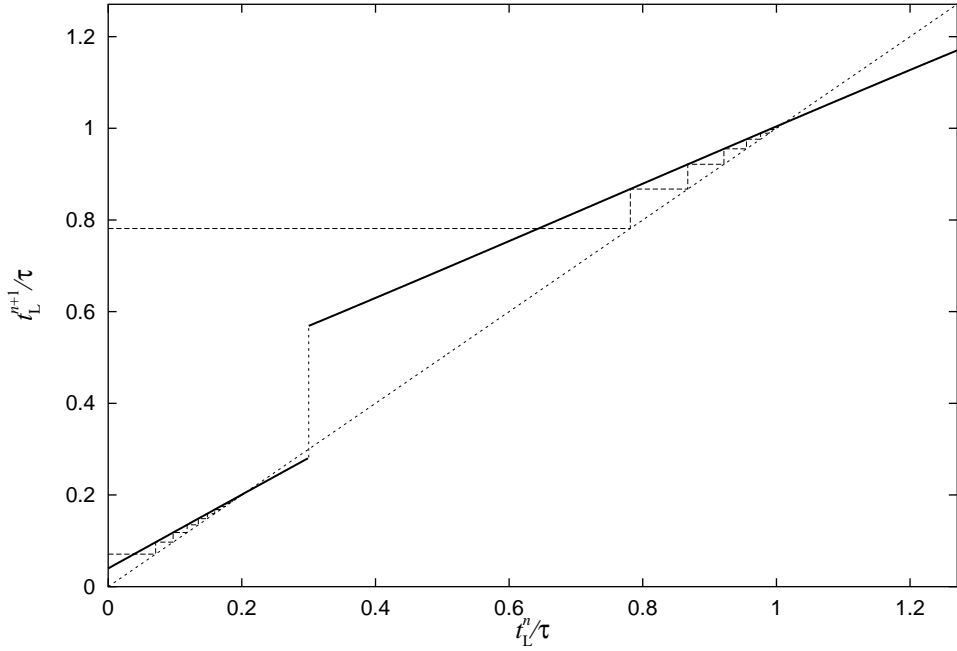


Figure 3.3: The return map for 1:1 firing (solid line) showing the convergence to t_L^E of trajectories from two different initial conditions (long-dashed lines). With the parameters used here $\alpha = 0.01$, $\delta = 0.1$, $\theta = 0.2$ and $t_d = 0.3\tau$, there are two stable equilibria, corresponding to cases A and B.

so Cell 1 fires next after an interval

$$T_1^n = t_L^n + t_d + t^* = \tau \ln \left(\frac{1 + \alpha + \delta(1 - \theta)e^{(t_L^n + t_d)/\tau}}{\theta + \alpha} \right) \quad (3.9)$$

Cell 2 receives the downward step a time $t_d - t_L^n$ since it last fired, and so fires next after an interval

$$T_2^n = \tau \ln \left(\frac{1 + \delta(1 - \theta)e^{(t_d - t_L^n)/\tau}}{\theta} \right) \quad (3.10)$$

The new time lag,

$$t_L^{n+1} = t_L^n + T_2^n - T_1^n \quad (3.11)$$

$$= t_L^n + \tau \ln \left(\frac{(\theta + \alpha)(1 + \delta(1 - \theta)e^{(t_d - t_L^n)/\tau})}{\theta(1 + \alpha + \delta(1 - \theta)e^{(t_d + t_L^n)/\tau})} \right) \quad (3.12)$$

For case B, (Figure 3.2B), Cell 1 receives the downward impulse after time $t_L^n + t_d$, as for case A, and T_1^n is given by equation 3.9 above. Cell 2 receives the impulse a time $T_1^n - t_L^n + t_d$ since it last fired, hence

$$T_2^n = \tau \ln \left(\frac{1 + \delta(1 - \theta)e^{(T_1^n - t_L^n + t_d)/\tau}}{\theta} \right) \quad (3.13)$$

and

$$t_L^{n+1} = t_L^n + \tau \ln \left(\frac{\theta + \alpha + \delta^2(1 - \theta)^2e^{2t_d/\tau} + \delta(1 + \alpha)(1 - \theta)e^{(t_d - t_L^n)/\tau}}{\theta(1 + \alpha + \delta(1 - \theta)e^{(t_d + t_L^n)/\tau})} \right) \quad (3.14)$$

Equations 3.12 and 3.14 define a return map which maps t_L^n onto itself. (Figure 3.3).

3.2.2.2 Equilibrium time lags

At equilibrium, $t_L^{n+1} = t_L^n = t_L^E$ and so, for case A,

(3.15)

$$\theta \left(1 + \alpha + \delta(1 - \theta) e^{(t_L^E + t_d)/\tau} \right) = (\theta + \alpha) \left(1 + \delta(1 - \theta) e^{(t_d - t_L^E)/\tau} \right) \quad (3.16)$$

$$\left(\theta \delta(1 - \theta) e^{t_d/\tau} \right) e^{t_L^E/\tau} - \alpha(1 - \theta) - \left((\theta + \alpha) \delta(1 - \theta) e^{t_d/\tau} \right) e^{-t_L^E/\tau} = 0 \quad (3.17)$$

$$\theta e^{2t_L^E/\tau} - \frac{\alpha}{\delta} e^{-t_d/\tau} e^{t_L^E/\tau} - (\theta + \alpha) = 0 \quad (3.18)$$

So

$$t_L^E = \tau \ln \left[\frac{1}{2\theta} \left(\frac{\alpha}{\delta} e^{-t_d/\tau} + \left[\left(\frac{\alpha}{\delta} e^{-t_d/\tau} \right)^2 + 4\theta(\theta + \alpha) \right]^{\frac{1}{2}} \right) \right] \quad (3.19)$$

t_L^E has a minimum of zero at $\alpha = 0$, increases monotonically with α and decreases monotonically with δ , with θ and with t_d , i.e.: increasing the difference in inputs increases the equilibrium lag time; increasing the ‘synaptic strength’ and ‘synaptic time delay’ decrease the lag; making the cell response more linear decreases the lag.

For case B:

$$t_L^E = \tau \ln \left[\frac{1}{2\theta} \left(\frac{\alpha}{\delta} e^{-t_d/\tau} + \delta(1 - \theta) e^{t_d/\tau} + \left[\left(\frac{\alpha}{\delta} e^{-t_d/\tau} + \delta(1 - \theta) e^{t_d/\tau} \right)^2 + 4\theta(1 + \alpha) \right]^{\frac{1}{2}} \right) \right] \quad (3.20)$$

In this regime, t_L^E is non-zero at $\alpha = 0$, increases monotonically with α and $1/\theta$, as for case A, but now t_L^E has a minimum in δ and in t_d . In the equal inputs limit ($\alpha = 0$), case A corresponds to the synchronous solution and case B to the anti-synchronous solution found by van Vreeswijk and Abbott [146] for fast synapses.

3.2.2.3 Stability of phase-locked solutions

To show that the equilibria derived above are stable it is sufficient to show that

$$\frac{dt_L^{n+1}}{dt_L^n} < 1 \quad (3.21)$$

for each section of the return map. For case A, equation 3.12 may be re-written as

$$z = y + \ln \left(\frac{J + e^{-y}}{K + e^y} \right) + c \quad (3.22)$$

where $y = t_L^n/\tau$, $z = t_L^{n+1}/\tau$, $J = e^{-t_d/\tau}/(\delta(1 - \theta))$, $K = (1 + \alpha)e^{-t_d/\tau}/(\delta(1 - \theta))$ and $c = \ln(1 + \alpha/\theta)$, and therefore

$$\begin{aligned} \frac{dt_L^{n+1}}{dt_L^n} &= \frac{dz}{dy} \\ &= 1 - \left(\frac{e^{-y}}{J + e^{-y}} + \frac{e^y}{K + e^y} \right) \\ &< 1 \end{aligned} \quad (3.23)$$

since $J, K > 0$ by the definitions of α , δ and t_d to be positive or zero and the definition that $0 < \theta < 1$. The proof proceeds similarly for case B.

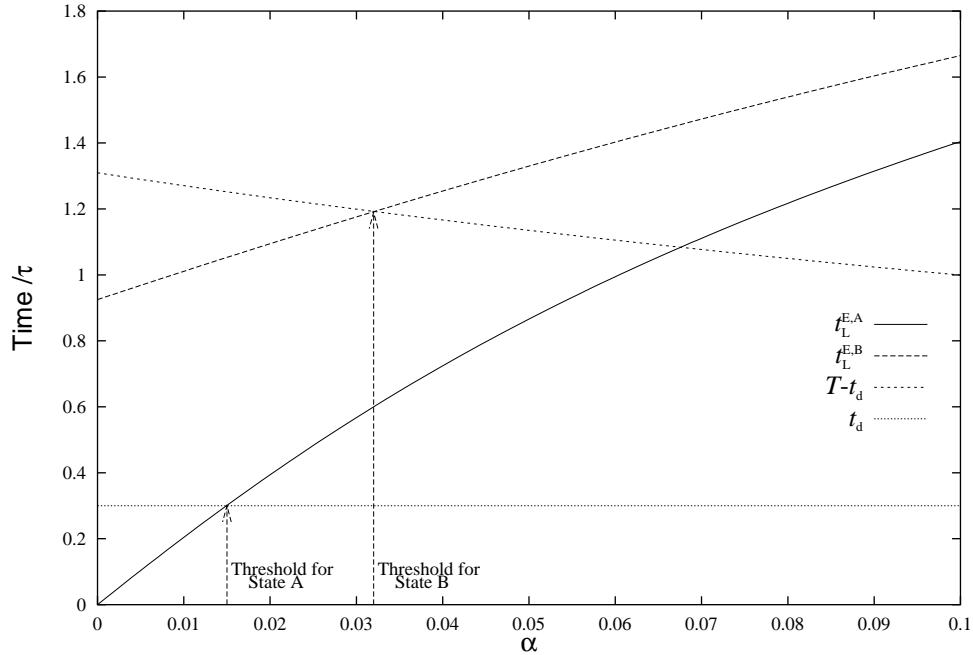


Figure 3.4: Time lags and firing periods for A and B types of 1:1 firing as functions of α , illustrating the thresholds for these firing types. Parameters: $\theta = 0.2$, $\delta = 0.1$, $t_d = 0.3\tau$.

3.2.2.4 Threshold of 1:1 firing

Figure 3.4 shows t_L^E as a function of α for $\theta = 0.2$, $\delta = 0.1$ and $t_d = 0.3\tau$. An equilibrium exists for case A provided $t_L^E < t_d$ and $t_d < T$, where

$$T = \tau \ln \left(\frac{1 + \alpha}{\theta + \alpha} \right) \quad (3.24)$$

is the natural firing period of Cell 1. An equilibrium exists for case B provided $t_L^E > t_d$ and $t_L^E + t_d < T$. For the case shown in Figure 3.4, both equilibria exist for $\alpha < 0.015$, while only the case B equilibrium exists for $0.015 < \alpha < 0.032$. For $\alpha > 0.032$ it is possible for Cell 1 to fire a second time before ever receiving an inhibitory pulse from Cell 2, and so 1:1 firing is no longer possible. Figure 3.5 shows transitions from A-type to B-type and from B-type to non-1:1 firing.

These conditions can be expressed in terms of the parameters α , δ , θ and t_d as follows:

$$t_L^{E,A} < t_d \quad \Rightarrow \quad \alpha < \frac{\theta(e^{2t_d/\tau} - 1)}{1 + \frac{1}{\delta}} \quad (3.25)$$

$$t_d < T \quad \Rightarrow \quad \alpha < \frac{1 - \theta e^{2t_d/\tau}}{e^{2t_d/\tau} - 1} \quad (3.26)$$

$$\begin{aligned} t_L^{E,B} + t_d < T \quad \Rightarrow \quad \alpha < & \frac{\delta + \theta}{1 + \delta e^{2t_d/\tau}} - \delta(1 - \theta) - 2\theta \\ & + \left[\left(\frac{\delta + \theta}{1 + \delta e^{2t_d/\tau}} - \delta(1 - \theta) - 2\theta \right)^2 \right. \\ & \left. + 4\delta\theta \left(1 - e^{2t_d/\tau} (\delta(1 - \theta) + \theta) \right) \right]^{\frac{1}{2}} \end{aligned} \quad (3.27)$$

Figure 3.6 shows the threshold values of α as functions of δ for A- and B-type firing ($\theta = 0.2$, $t_d = 0.3\tau$). B-type firing is favoured by intermediate values of δ and θ , and by small values of t_d . In

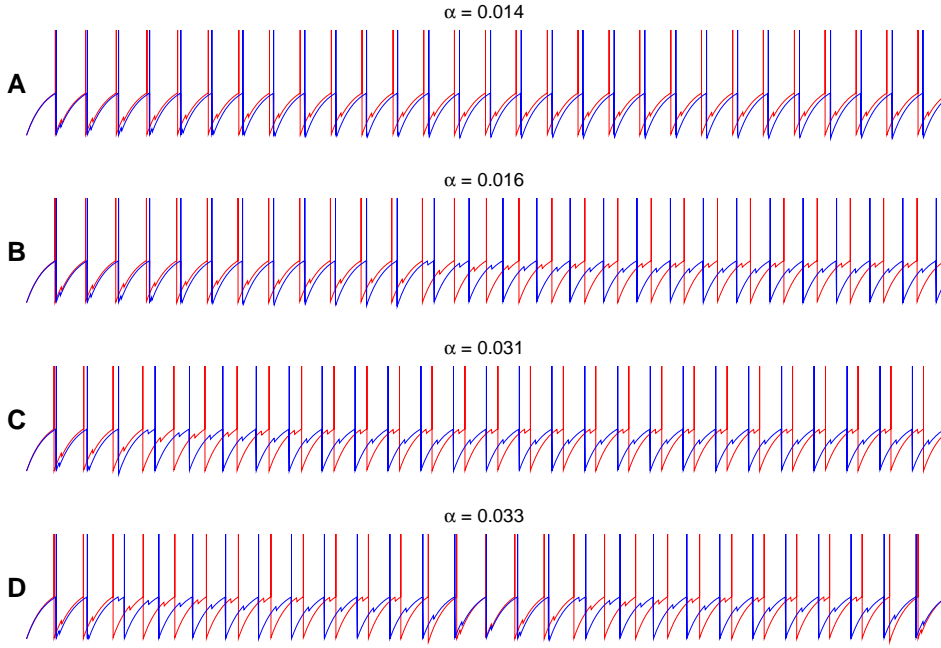


Figure 3.5: Transitions from Type A firing (A) to Type B firing (B) and from Type B firing (C) to harmonic locking (D) as α is increased.

contrast the range of α for which A-type firing is stable is increased by increasing all three parameters, up to the limit imposed by $t_d < T$, at which the α -threshold falls off rapidly.

3.2.3 Harmonic (mode) locking

When α is increased past the threshold for 1:1 firing, the possible states of the system are suppression (see §3.2.4) or harmonic locking. Harmonic locking (or mode locking) is used to describe the state where Cell 1 fires n_1 times and Cell 2 fires n_2 times ($n_1, n_2 \in \mathbb{Z}$, $n_1 > n_2 \geq 1$) before returning to the original phase lag.

We can derive the return maps for $1 < n_1/n_2 < 2$ in a similar manner to that used for the 1:1 return map (equations 3.12 and 3.14). The return map is discontinuous with five pieces:

- i. $t_L^n < t_d$
- ii. $t_L^n > t_d$, $t_L^n + t_d < T$, one inhibitory pulse within T_2^n
- iii. $t_L^n > t_d$, $t_L^n + t_d < T$, two inhibitory pulses within T_2^n
- iv. $t_L^n > t_d$, $t_L^n + t_d > T$, one inhibitory pulse within T_2^n
- v. $t_L^n > t_d$, $t_L^n + t_d > T$, two inhibitory pulses within T_2^n

An example for $n_1:n_2 = 8:7$ is shown in Figure 3.7.

The bifurcation diagrams for the inter-spike intervals T_1 and T_2 and the time lag t_L^n as functions of α (Figures 3.8, 3.9 and 3.10) clearly show the harmonic-locking. The structure of the locking is more clearly seen in plots of n_2 vs α (Figure 3.11). The fraction n_2/n_1 is always rational and irreducible and forms an infinite order Farey sequence. This has the property that between any two terms n_2/n_1 and n'_2/n'_1 there will be a term $(n_2 + n'_2)/(n_1 + n'_1)$. I have not proved the Farey sequence is infinite order, but calculations at finer and finer scales have revealed no upper limit to n_1 and n_2 . The behaviour is summarised in the following points:

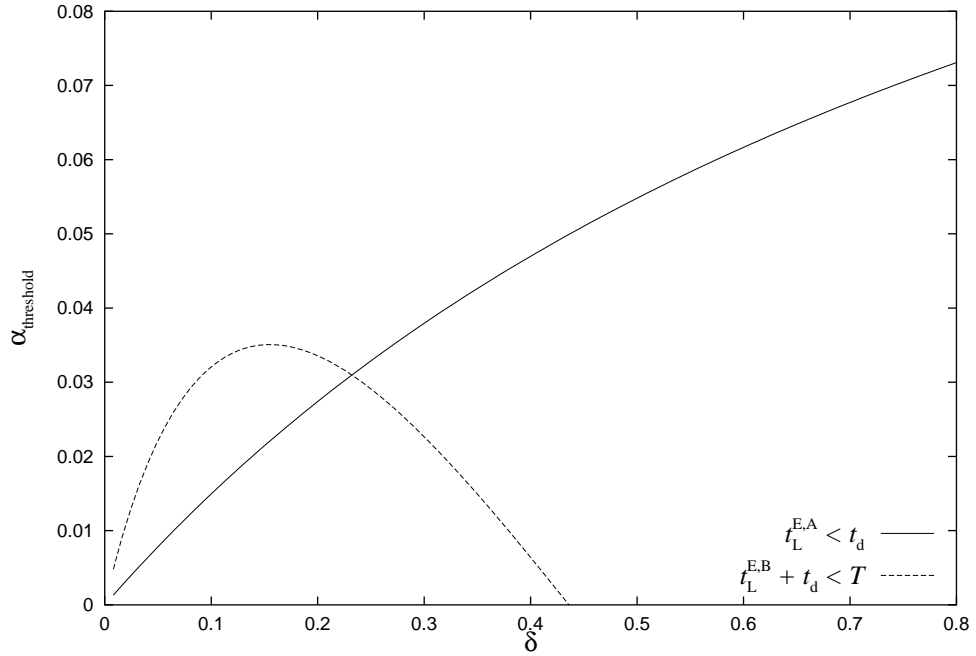


Figure 3.6: Thresholds of A- and B-type firing in terms of α , as functions of δ . Note that B-type firing has a higher α -threshold at small δ , and that the threshold for both types goes to zero as $\delta \rightarrow 0$. Parameters: $\theta = 0.2$, $t_d = 0.3\tau$

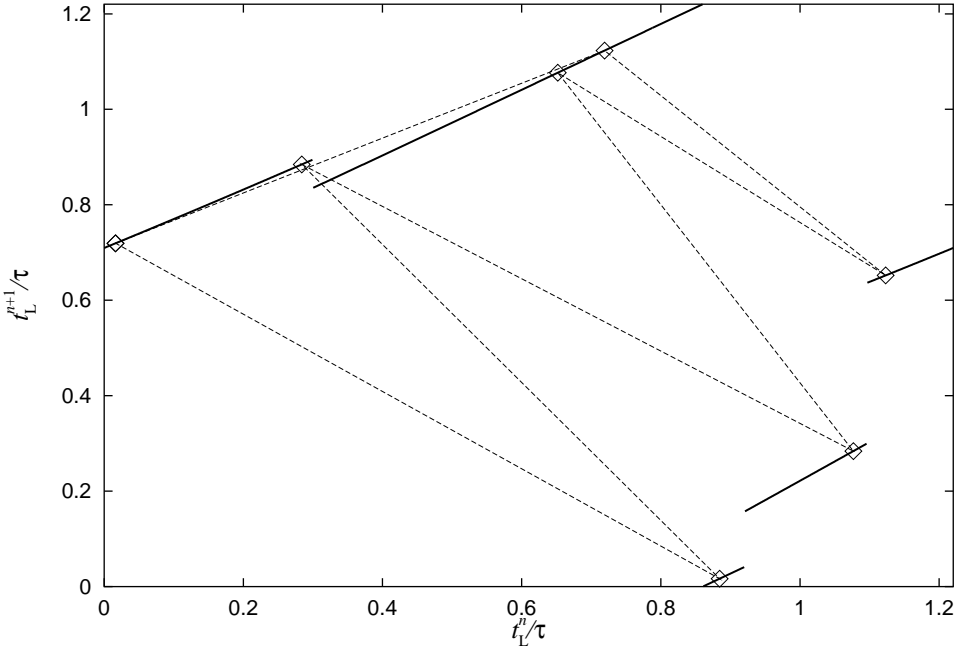


Figure 3.7: Return map for 8:7 firing. There is one stable orbit for any initial condition. Parameters: $\alpha = 0.135$, $\delta = 0.1$, $\theta = 0.2$, $t_d = 0.3\tau$

1. States for which n_1 and n_2 are small cover a larger region of α -space than states for which n_1 and n_2 are large (see Figure 3.11C). For example, for the parameters shown in Figure 3.8, the 2:1 firing state covers a range of ~ 0.1 , while the 12:11 firing state covers only ~ 0.001 .
2. There is a sharp boundary above which $n_2 = 0$ (see §3.2.4 below).
3. The parameter δ reduces the threshold for suppression and increases the effect noted in point 1 above. The parameter θ has an approximately opposing effect.

To express T_1 , T_2 and t_L^n as a function of α , θ , δ and t_d is difficult due to the discontinuous nature of the function. It may be more useful to simply calculate the envelopes within which all possible values of the inter-spike intervals must lie. This is done in Appendix A and an example of the T_2 envelope is shown in Figure 3.12. Taking the ratio of the mid-points of these envelopes gives an approximation of n_1/n_2 , which may be useful in relating the spiking model to a firing rate model.

3.2.4 Suppression

For a large enough discrepancy in the drive to the two cells and a large enough inhibitory voltage step, the firing of the cell with the smaller drive (Cell 2 here) can be completely suppressed (also known as ‘oscillator death’).

To derive the threshold for suppression, we note that if x_2 does not increase from $x_2 = 1 - \delta$ to $x_2 = 1$ during time T , Cell 2 will fire at most once (depending on the initial conditions) before being suppressed.

From equation 3.5,

$$\frac{1}{1-\theta} + \left(1 - \delta - \frac{1}{1-\theta}\right) e^{-T/\tau} < 1 \quad \text{for suppression}$$

$$1 - \delta - \frac{1}{1-\theta} < \frac{-\theta(1+\alpha)}{(\theta+\alpha)(1-\theta)}$$

$$\delta > \frac{\theta}{\theta+\alpha} \quad (3.28)$$

$$\text{or} \quad \alpha > \theta \left(\frac{1}{\delta} - 1 \right) \quad (3.29)$$

independent of t_d . For $\delta = 0.1$, $\theta = 0.2$ and $t_d = 0.3\tau$, the suppression threshold ($\alpha = 1.8$) is 56 times the threshold of 1:1 firing ($\alpha = 0.032$). Increasing δ to 0.8 moves the suppression threshold ($\alpha = 0.050$) below the 1:1 firing threshold ($\alpha = 0.073$), so the system goes directly from 1:1 firing to suppression.

3.2.5 Alternative synaptic models

In this section I consider elaborations of the simple ‘synaptic’ scheme analysed so far:

1. Self-inhibition. If Cell 1 fires then both Cells 2 and 1 receive a downward step in membrane potential after a time t_d .
2. Linear voltage step. Instead of being constant, the membrane potential step is linearly dependent on the current membrane potential, i.e. instead of $x \rightarrow x - \delta$, $x \rightarrow x - \delta x$. This is equivalent to the effect of the reversal potential in more realistic, conductance-based synaptic models.

Conductance-based synaptic models are considered in the next section. I have derived the forms of T_1 , T_2 , t_L^E and $\alpha_{\text{threshold}}$ for A- and B-type firing, for the two extensions described above and for the combination of the two extensions. They are listed in Appendix A together with the results for the original model.

The effect of the extensions to the original synaptic model can be seen in Figure 3.13. Using a voltage-dependent voltage step rather than a constant step considerably reduces the phase lag for a given α . Adding self-inhibition produces a small increase in the phase lag. The change in the phase lag in turn affects the ability of the system to sustain 1:1 firing with large α (Figure 3.14). In summary, no

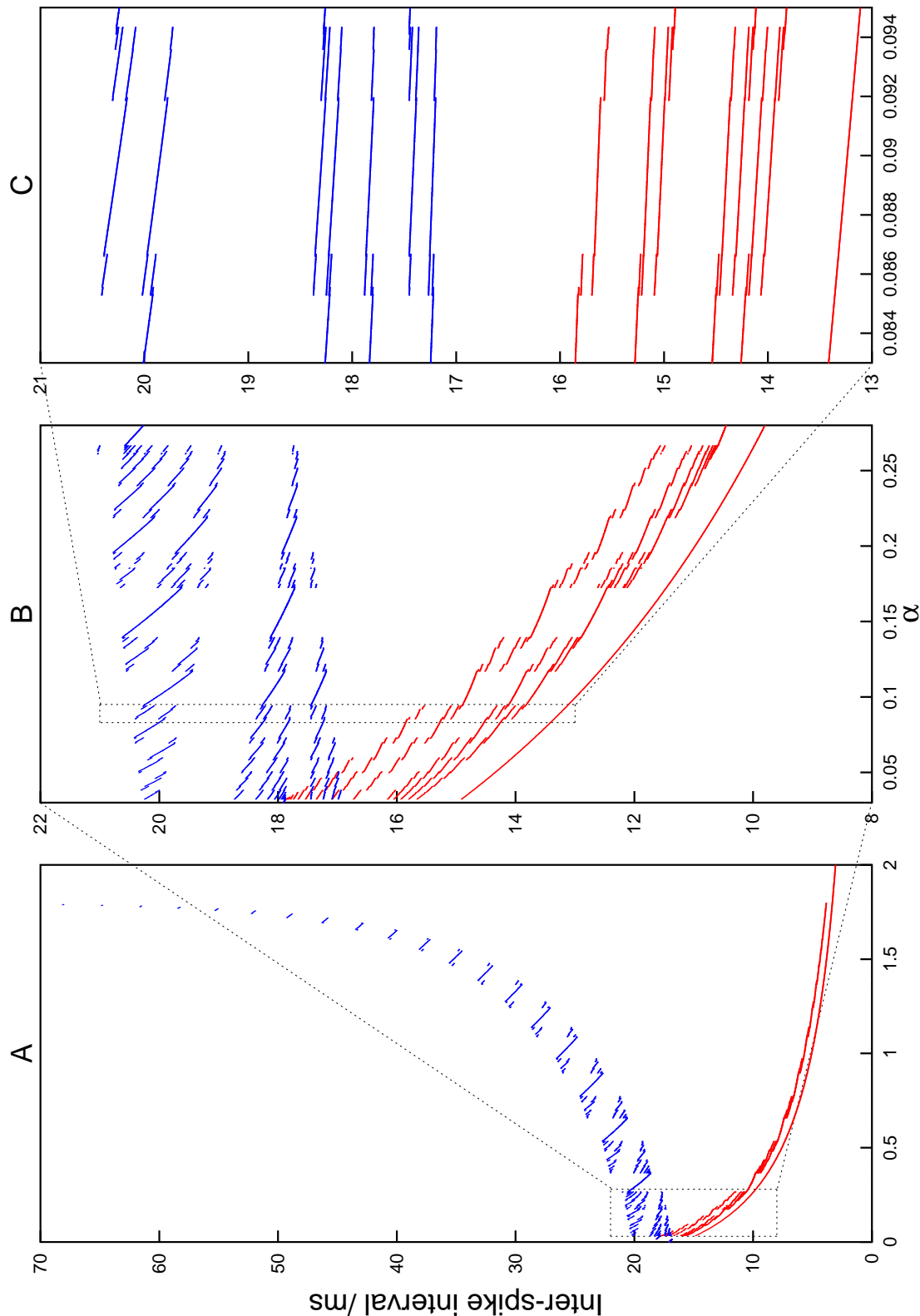


Figure 3.8: Bifurcation diagram for the equilibrium inter-spike intervals (ISIs) of Cell 1 (red) and Cell 2 (blue), as a function of α . Parameters: $\theta = 0.2$, $\delta = 0.1$, $t_d = 0.3\tau$. When the system is in a state of $n_1:n_2 = 3:2$ firing, for example, the ISI of Cell 2 has two values and the ISI of Cell 1 has three possible values.

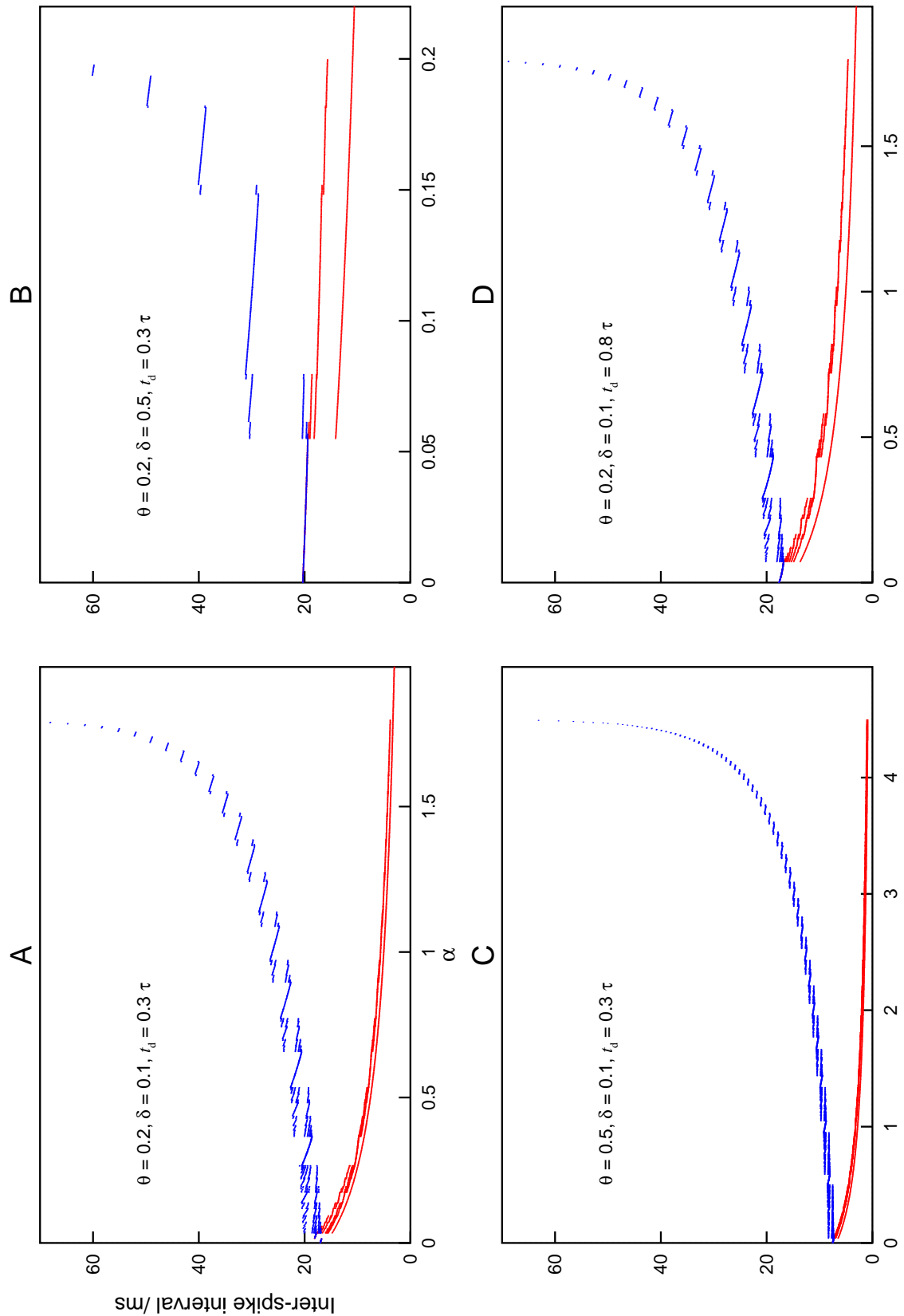


Figure 3.9: Bifurcation diagrams of T_1 and T_2 for various parameter values.

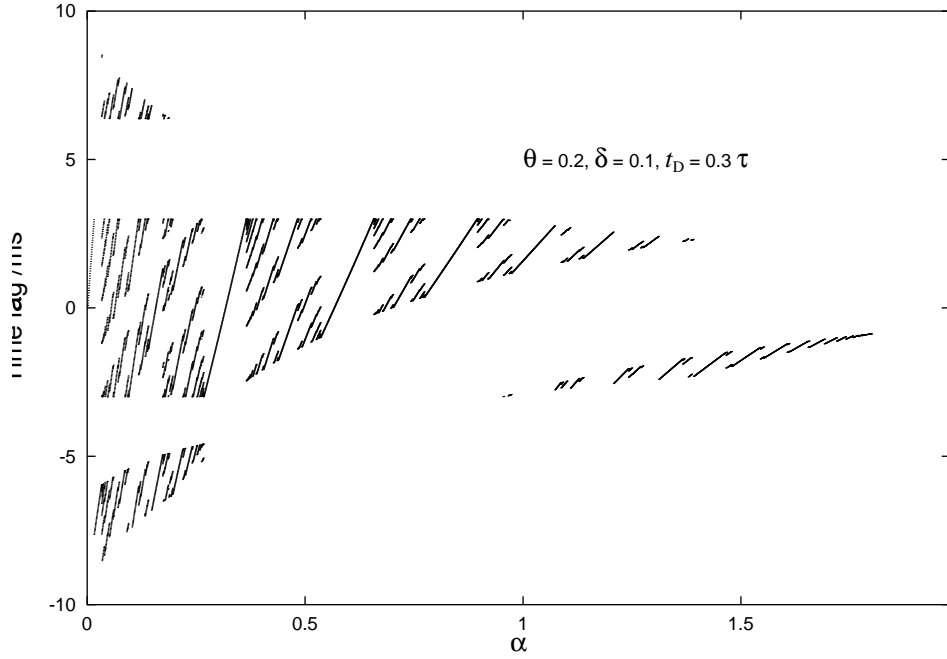


Figure 3.10: Bifurcation diagram of time lag t_L^n as a function of α . Parameters: $\theta = 0.2$, $\delta = 0.1$, $t_d = 0.3\tau$.

self-inhibition and a voltage-dependent voltage step increase the range of α within which the system will fire with 1:1 phase locking.

The threshold for suppression with the voltage-dependent voltage step is the same as for the original case with a constant step (Equation 3.28). The threshold for the self-inhibitory case with constant step is

$$\delta > \frac{\theta}{\alpha - \theta(e^{t_d/\tau} - 1)} \quad \text{for } \alpha > \theta(e^{t_d/\tau} - 1) \quad (3.30)$$

Cell 1 cannot suppress Cell 2 if $\alpha < \theta(\exp(t_d/\tau) - 1)$. The threshold for self-inhibition with variable voltage step is

$$\delta > \frac{\theta}{\alpha + \theta \left(1 - \frac{\theta(1+\alpha)}{1-\theta} (e^{t_d/\tau} - 1) \right)} \quad \text{for } \alpha > 1 - \frac{\theta(1+\alpha)}{1-\theta} (e^{t_d/\tau} - 1) \quad (3.31)$$

The suppression thresholds are plotted in Figure 3.15, for $\theta = 0.2$ and $t_d = 0.3\tau$. With self-inhibition, suppression requires a much larger disparity in the inputs to the two cells, and/or a much larger inhibitory step. Adding a voltage-dependent voltage step reduces these requirements somewhat.

3.2.6 Conductance-based synapses

All the connections considered so far have been instantaneous steps in membrane potential. A more realistic synaptic model uses a change in membrane conductance with a finite rise and decay time.

It is difficult to repeat the previous analysis for synaptic models with non-zero rise and decay times (e.g. alpha-function synapse). However, we can gain a qualitative idea of what the effects are likely to be. For a fast rise and decay (decay much less than the firing period), the solutions will be only a little perturbed from the instantaneous case if the charge-transfer is normalised to be the same. The largest effect will be nearest threshold, when the more-spread-out inhibition will not delay firing so much. For fast rise and slow decay times, there will be a membrane potential change during the current period (the effective δ), and a steady-state contribution equivalent to increasing θ . This will reduce the thresholds for 1:1

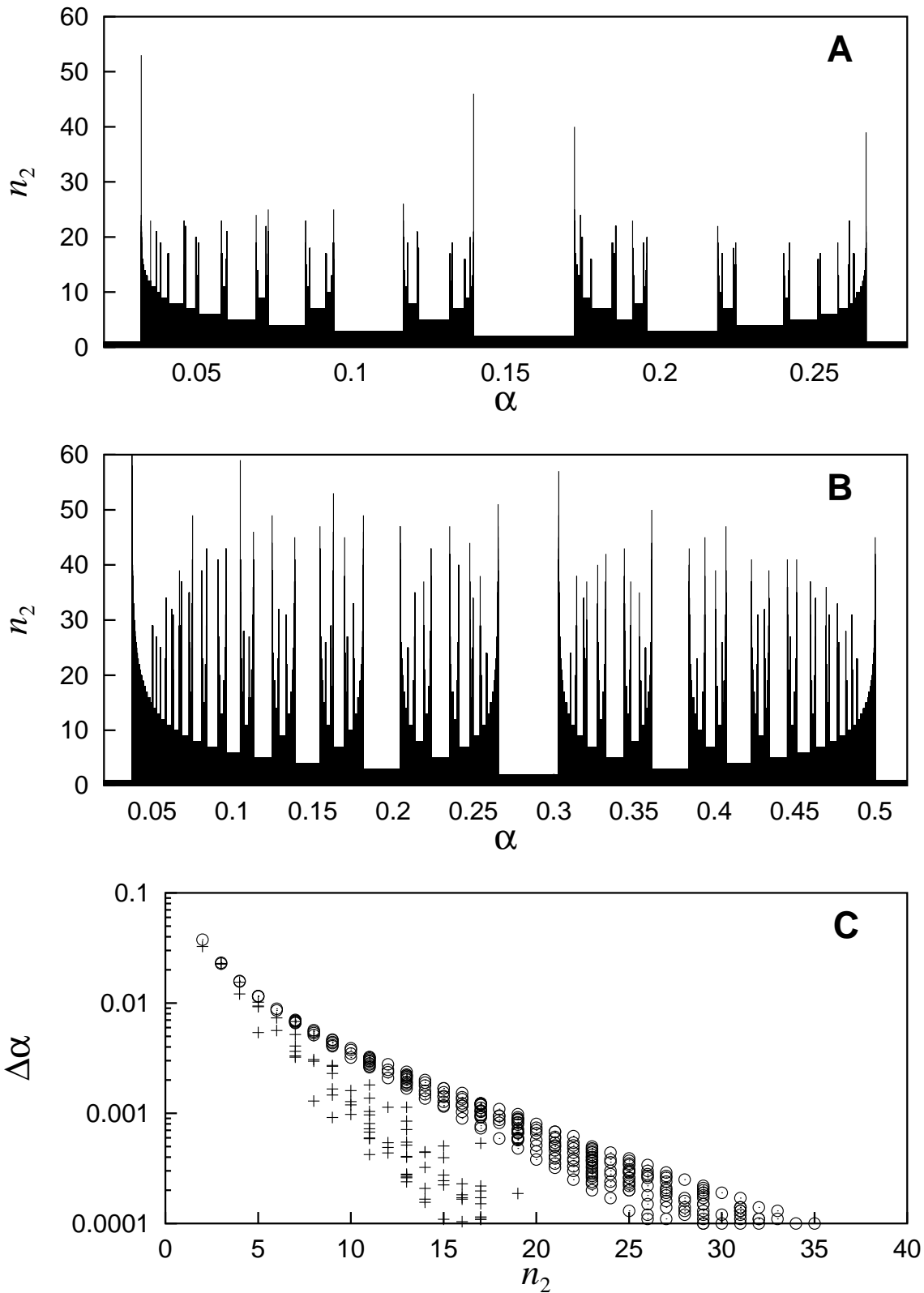


Figure 3.11: A. The number of spikes in Cell 2 in one repeat period (n_2) as a function of α for $\theta = 0.2$, $\delta = 0.1$, $t_d/\tau = 0.3$. B. same parameters as A, except $\theta = 0.5$. C. A plot of $\Delta\alpha(n_2)$, the range of α within which the rotation number n_2 is constant, for the two cases shown in A and B. + $\theta = 0.2$, $\odot \theta = 0.5$.

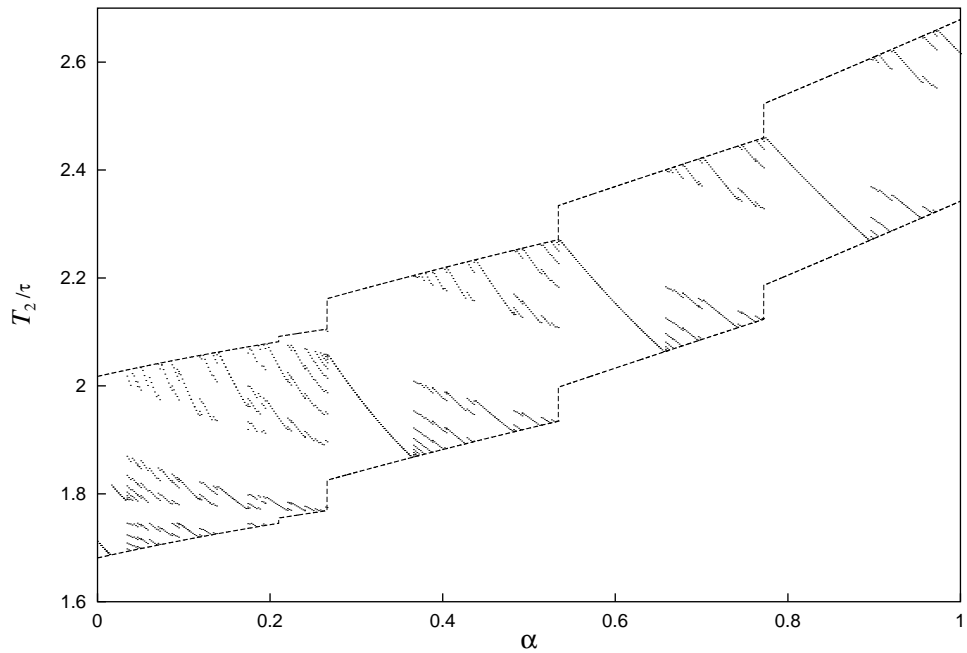


Figure 3.12: The bifurcation diagram from Figure 3.8 together with the calculated maximum- and minimum- T_2 envelope

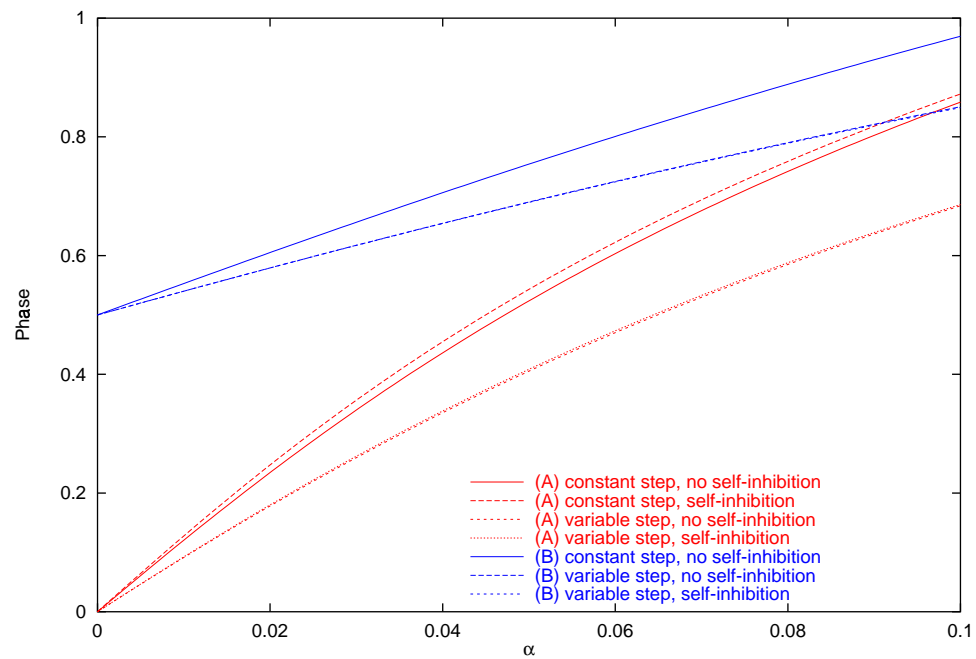


Figure 3.13: Equilibrium phase lags for A- and B-type 1:1 firing, as functions of α , for various forms of synaptic interaction. Parameters: $\theta = 0.2$, $\delta = 0.1$, $t_d = 0.3\tau$.

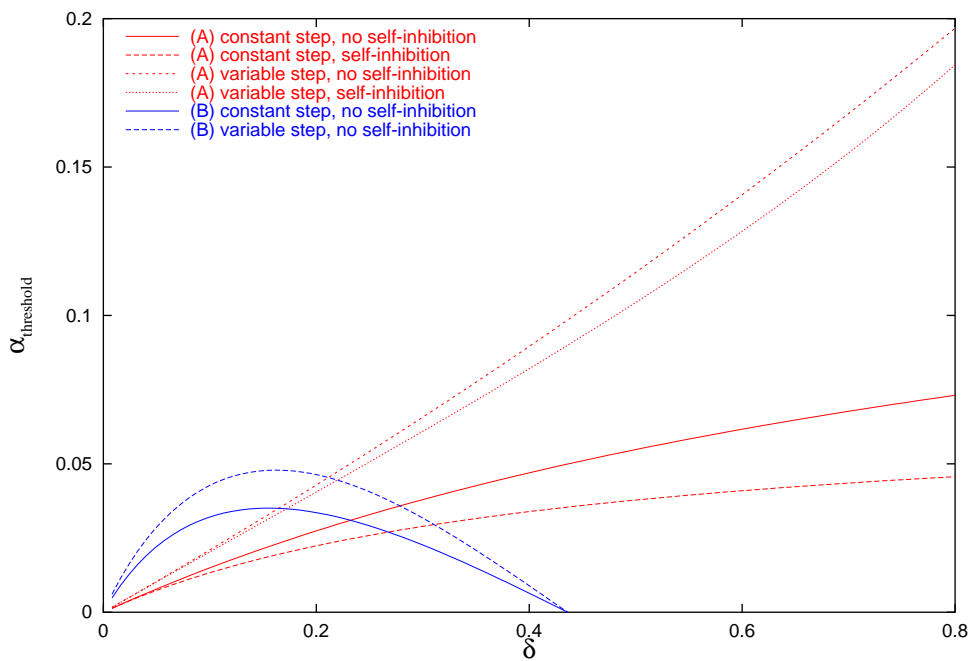


Figure 3.14: α -thresholds for A- and B-type 1:1 firing, as functions of δ , for various forms of synaptic interaction. Parameters: $\theta = 0.2$, $t_d = 0.3\tau$.

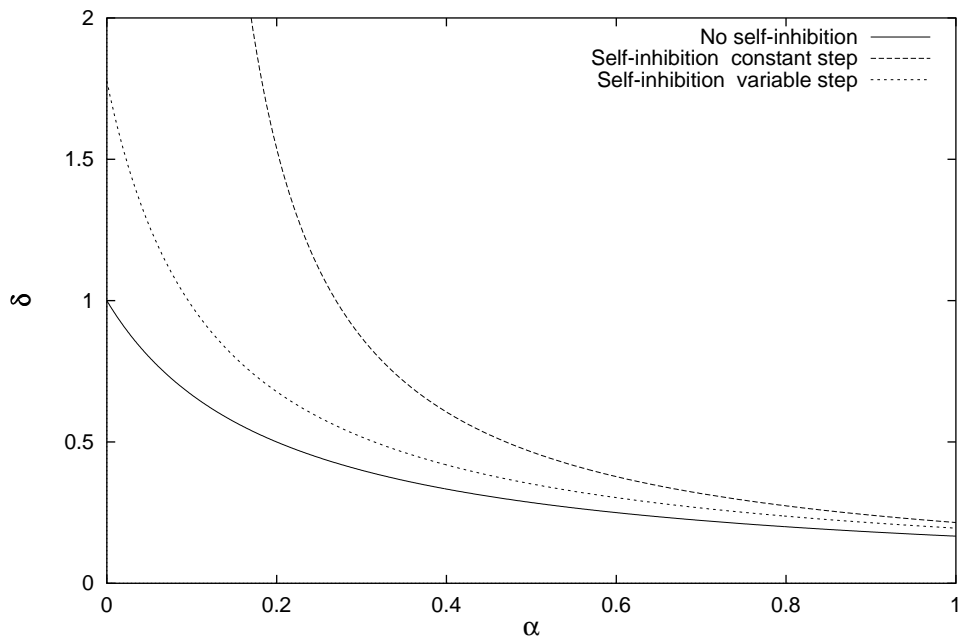


Figure 3.15: Thresholds for suppression in δ -space, as functions of α . Parameters: $\theta = 0.2$, $t_d = 0.3\tau$.

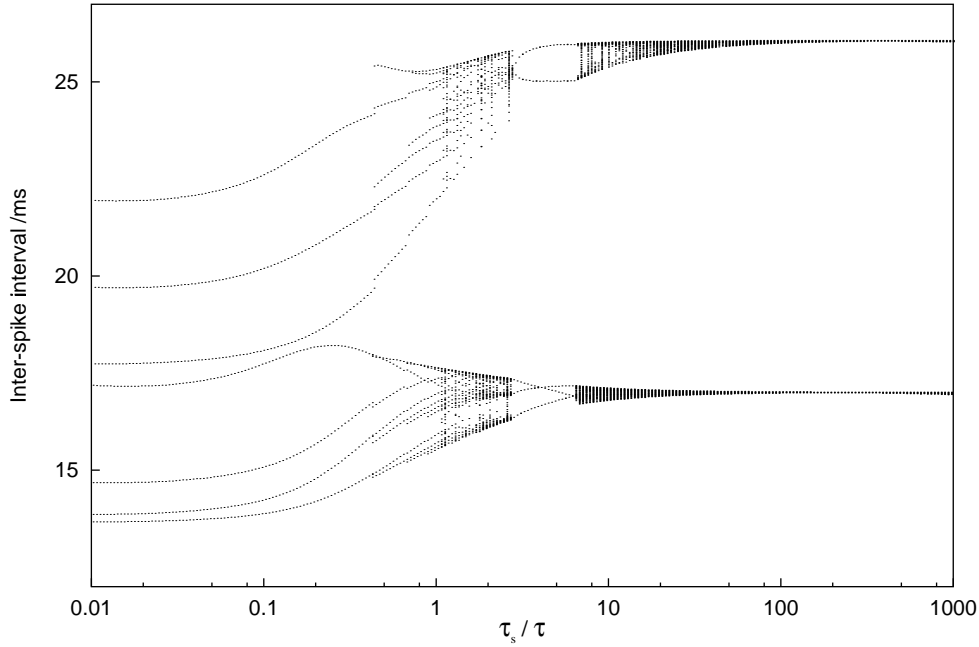


Figure 3.16: Effect of varying synaptic decay time τ_s on firing patterns of Cell 1 (bottom) and Cell 2 (top). The network was simulated for 5000 spikes in Cell 1, and only those inter-spike intervals (measured to a precision of 0.01 ms) that occurred more than 50 times are shown here, to ensure there are no transient effects. Parameters: $\theta = 0.2$, $\alpha = 0.1$, $\bar{g}_s = 20$ pS, $t_d = 0.3\tau$.

locking and produce higher order mode locking (reduce the slope of the function $\Delta\alpha(n_2)$). Additionally, the effect of a synaptic event can carry over into the next period. Since inhibition occurs later during the period of the faster firing cell, the carry-over will be most pronounced for this cell, which will be slowed still further. This is likely to work in opposition to the summation effect.

Figure 3.16 shows the bifurcation diagrams for T_1 and T_2 for synapses with a step-increase in conductance and exponential decay, as functions of τ_s , the time-constant of the decay. Initially, the firing period gradually increases, while still retaining harmonic locking at the same ratio. Around $\tau_s = 0.3\tau$ the harmonic ratio begins to increase. At certain values of τ_s , small-integer harmonic locking is again stable, but then the size of the integers in the harmonic ratio increases again until the state of the system is indistinguishable from asynchrony.

Figure 3.17A compares the bifurcation diagram for step changes in membrane potential (with ‘reversal potential’) to the diagram for a conductance-based model with $\tau_s = \tau$. It is clear that high-order mode locking occurs for a larger range of α in the large τ_s case, but Figure 3.17B makes it clear that n_1/n_2 still follows a Farey sequence and hence is not asynchronous.

Therefore, finite synaptic decay time, unlike finite rise time [146], does not lead to asynchronous firing, although high-order harmonic locking may be indistinguishable from asynchrony over a short time-scale.

3.2.7 Reduced biophysical mitral model

I now ask whether the results obtained for the leaky integrate-and-fire model also apply to the biophysical, reduced mitral cell model (Chapter 2).

I simulated two instances of the four-compartment mitral cell model with the parameters given in Table 2.3. The synaptic model was an exponential synapse (instantaneous rise time, exponential decay with time constant $\tau_s = 18$ ms). The synaptic current is given by:

$$I_s(t) = \bar{g}_s e^{-t/\tau_s} (V(t) - E_s) \quad (3.32)$$

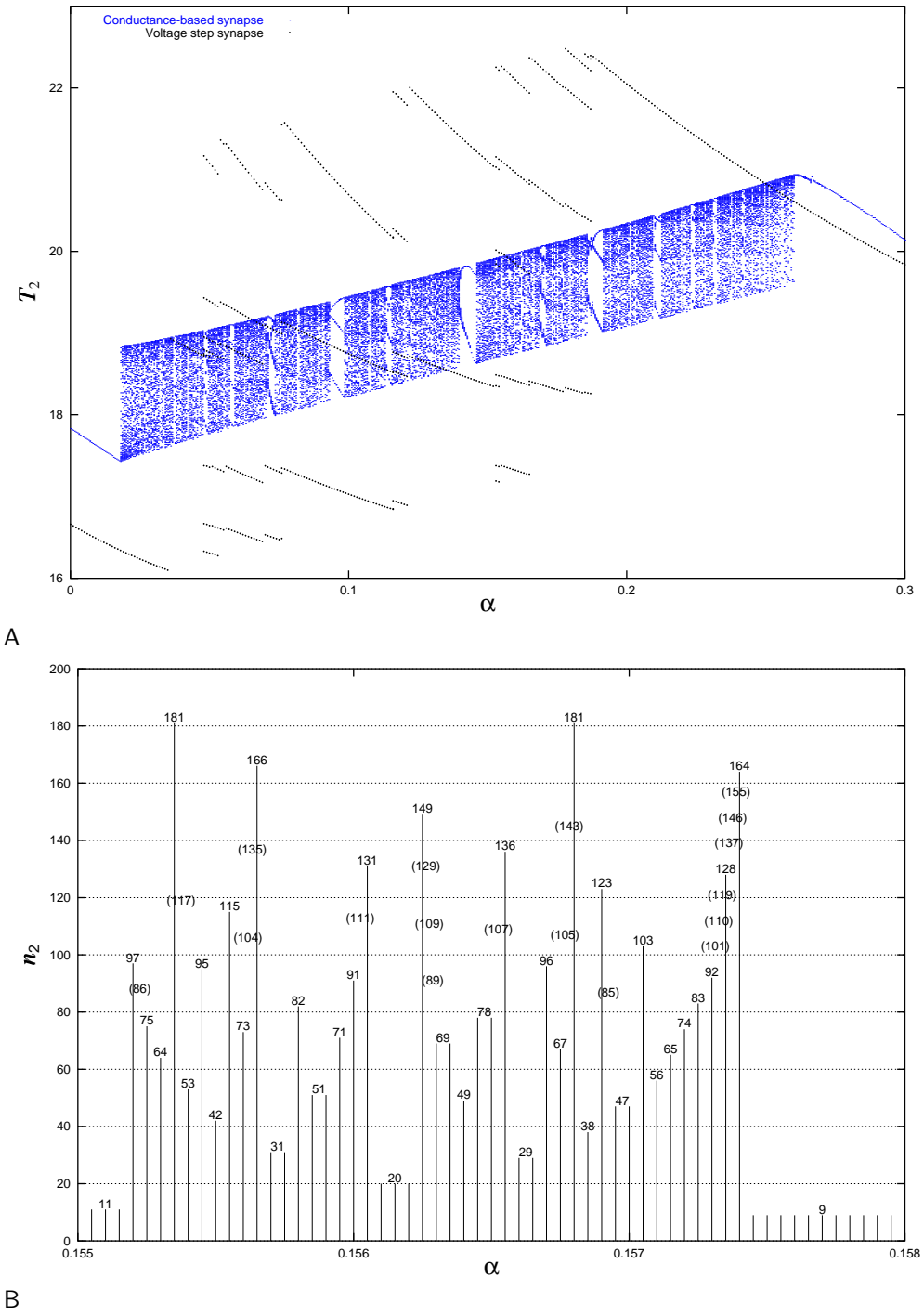


Figure 3.17: (A) Bifurcation diagram for synaptic connections modelled as either a voltage-dependent step in membrane potential or as a decaying exponential conductance-based synapse with τ_s . $\theta = 0.2$, $t_d/\tau = 0.3$, $\delta = 0.167$, $\bar{g}_s = 13.1$ pS. δ and \bar{g}_s were chosen so that the suppression threshold was the same for both systems. (B) n_2 as a function of α for the conductance-based synapse, demonstrating that the conductance-based model also follows a Farey sequence. The bars are labelled with the value of n_2 . Numbers in brackets are members of the sequence which have not been resolved at this resolution.

where \bar{g}_s is the maximum synaptic conductance and E_s is the synaptic reversal potential (taken as -70 mV here). The synaptic time delay was 3 ms. There was no self-inhibition.

For ‘small’ \bar{g}_s ($\bar{g}_s \lesssim 0.07 \mu\text{S}$), the pattern of harmonic locking is similar to that for the LIF model (compare Figure 3.18 to Figures 3.9 and 3.10). There are some notable differences, however. First, within regions of $p:q$ locking, the firing periods bifurcate to give $2p:2q$ locking (the bifurcation arises from the spike initiation zone alternating between the soma and the glomerular tuft). Second, the bifurcations do not all have the same character: note the direct change from 7:6 to 6:5 locking at $\alpha = 0.079$, with no intermediate higher-order harmonic lockings as are always found for the LIF model. Thirdly, there appear to be some regions of chaotic firing.

For large \bar{g}_s the pattern is qualitatively different (Figure 3.19). Time lags are generally small (< 20 ms), so there is an approximate synchronization but no mode-locking except for a few, narrow regions of low-order locking. A possible reason is that Cell 2 (the less strongly stimulated cell) is able sometimes to suppress Cell 1 (see Figure 3.19D), whereas this is not the case for the LIF model.

The transition between these two regions as \bar{g}_s is increased is not sharp (Figure 3.20).

Because of the non-linear nature of the biophysical models, it cannot be assumed that the response is independent of the drive to Cell 2 (in contrast to the LIF system). To test this, the current input to Cell 2 was increased from 0.28 nA to 1.9 nA. For small α , the high-input response was qualitatively similar to the low-input response (inset to Figure 3.21), but different behaviour – multiple high-order harmonics co-existing – was seen at large α (main part of Figure 3.21).

In conclusion, the LIF model is a reasonable approximation to the biophysical model for weak coupling but not for strong coupling. In the weak coupling regime the biophysical model shows precise phase- and mode-locking. In the strong coupling regime there is no high-order mode locking (the dynamics are apparently chaotic), but phase lags are small, which can be regarded as approximate synchronization.

3.3 Inhibition via an interneurone

In the olfactory bulb, mitral cells do not inhibit each other directly, but via interneurons. In this section I compare the effects of direct and interneurone-mediated inhibition.

3.3.1 The model

Like the mitral cells, the interneurone is modelled with a leaky integrate-and-fire model, with membrane time constant τ_g . The interneurone receives no constant current input; the only input to the interneurone is excitatory synaptic input from the mitral cells: when either mitral cell fires, x_g (membrane potential as a fraction of the threshold) is incremented by an amount δ_g . When the interneurone fires, both x_1 and x_2 are decremented by an amount δ . The sum of the synaptic delays from mitral cell–interneurone and from interneurone–mitral cell is written t_d . It does not matter how this delay is apportioned between the two directions.

3.3.2 Perfect integrator

The simplest case is where the firing of either mitral cell is sufficient to fire the interneurone ($\delta_g \geq 1$). This is identical to the two-cell system with self-inhibition described earlier (§3.2.5).

For $0.5 \geq \delta_g < 1$ and the interneurone a ‘perfect integrator’ ($\tau_g = \infty$), exactly two mitral cell firings are required to fire the interneurone and produce inhibition. There are two possible states of 1:1 firing:

1. if the firing of Cell 1 causes the interneurone to fire, then

$$t_L^E = \tau \ln \left[\frac{\theta + \alpha}{\theta - \frac{\alpha}{\delta} e^{-t_d/\tau}} \right] \quad (3.33)$$

There are two conditions for this state to exist and be stable:

$$\theta - \frac{\alpha}{\delta} e^{-t_d/\tau} > 0 \quad \text{and} \quad t_L^E < t_d \quad (3.34)$$

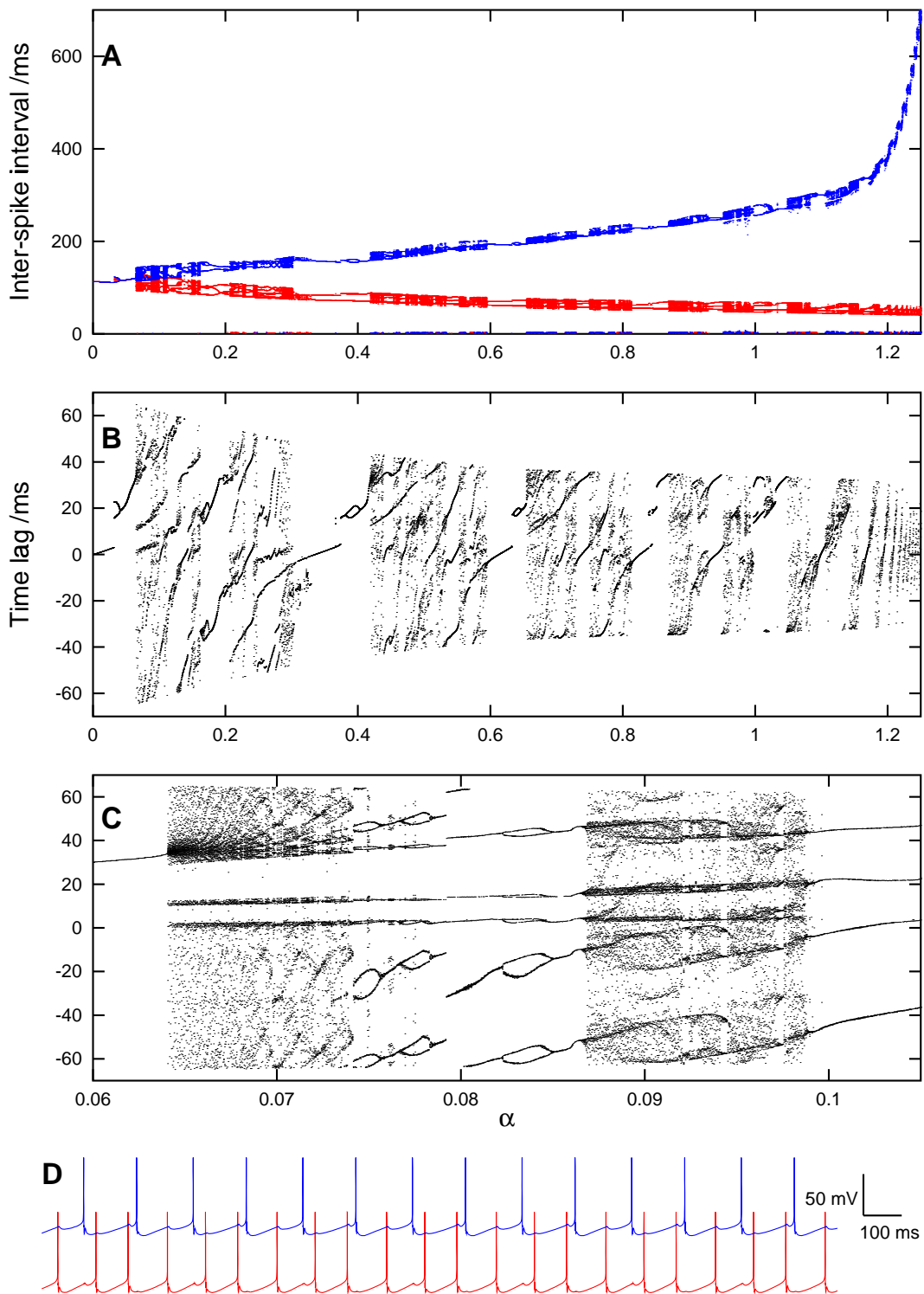


Figure 3.18: (A) Bifurcation diagram of inter-spike intervals vs. α for the two-cell model with the four-compartment reduced mitral cells and weak coupling. For each value of α the model was simulated for 20 s and the first 5 s discarded to remove transient effects. Synaptic parameters: $\tau_s = 18$ ms, $\bar{g}_s = 5 \times 10^{-2}$ μS . (B) Bifurcation diagram of time lags vs. α . (C) The same model simulated over a shorter rage of α to show fine detail. (D) An example of 3:2 harmonic locking, for $\alpha = 0.18$. Upper trace: Cell 2, Lower trace: Cell 1.

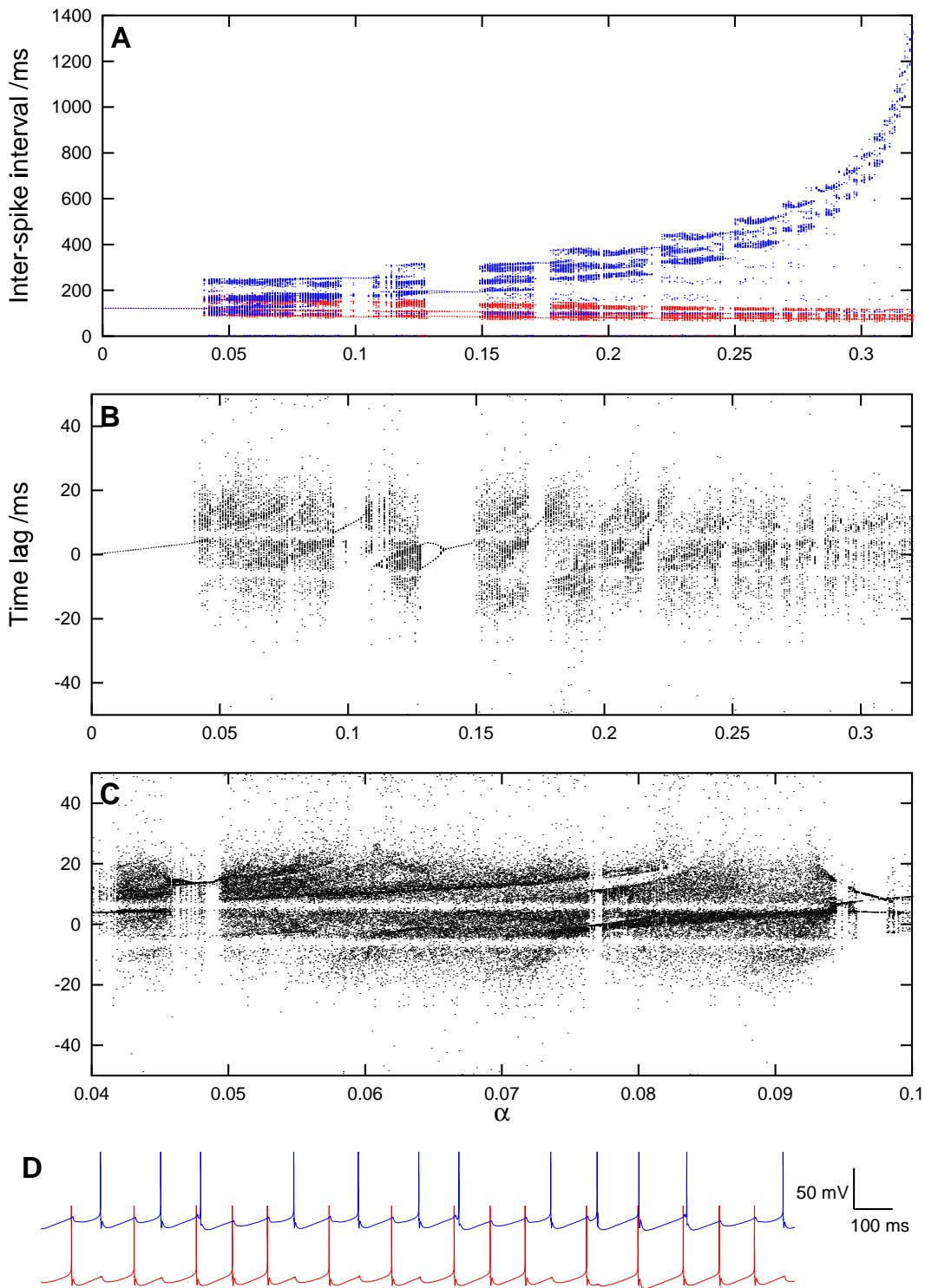


Figure 3.19: (A) Bifurcation diagram of inter-spike interval vs. α for the two-cell model with the four-compartment reduced mitral cells with strong coupling. For each value of α the model was simulated for 20 s and the first 5 s discarded to remove transient effects. Synaptic parameters: $\tau_s = 18$ ms, $\bar{g}_s = 10 \times 10^{-2}$ μS . (B) Bifurcation diagram of time lag vs. α . (C) The same model simulated over a shorter rage of α to show fine detail. (D) Membrane potential traces for $\alpha = 0.05$. There is no phase locking. *cf* Figure 3.18C. Upper trace: Cell 2, Lower trace: Cell 1.

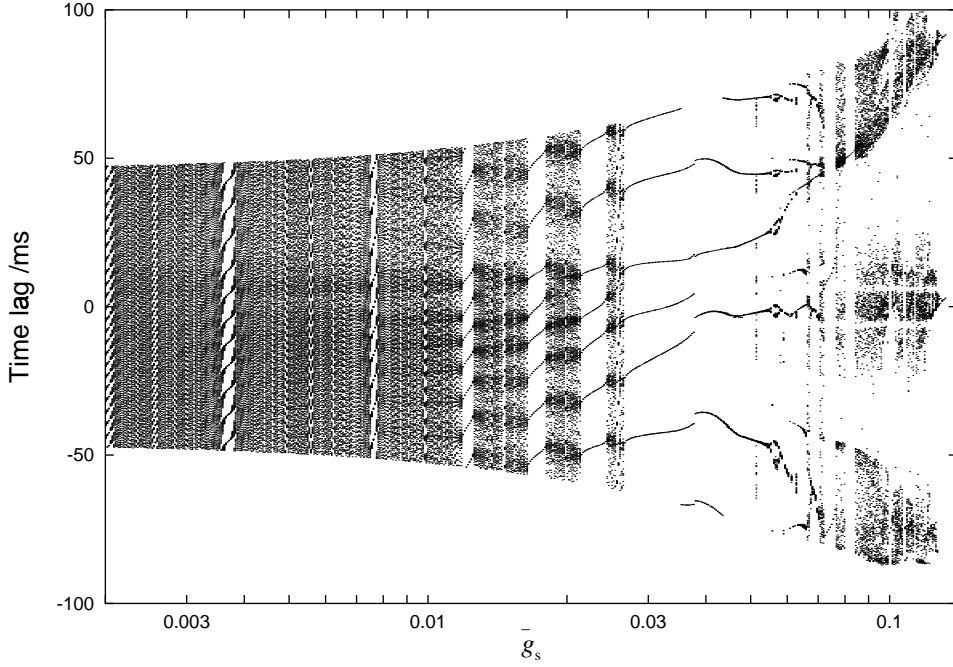


Figure 3.20: Bifurcation diagram of time lag vs. \bar{g}_s for the two-cell model with the four-compartment reduced mitral cells. For each value of \bar{g}_s the model was simulated for 30 s and the first 10 s discarded to eliminate transient effects. Note the transition to lower-order harmonic locking as \bar{g}_s is increased, then the transition to apparently chaotic firing above $\bar{g}_s \simeq 0.07$. Parameters: $\tau_s = 18$ ms, $\alpha = 0.1$.

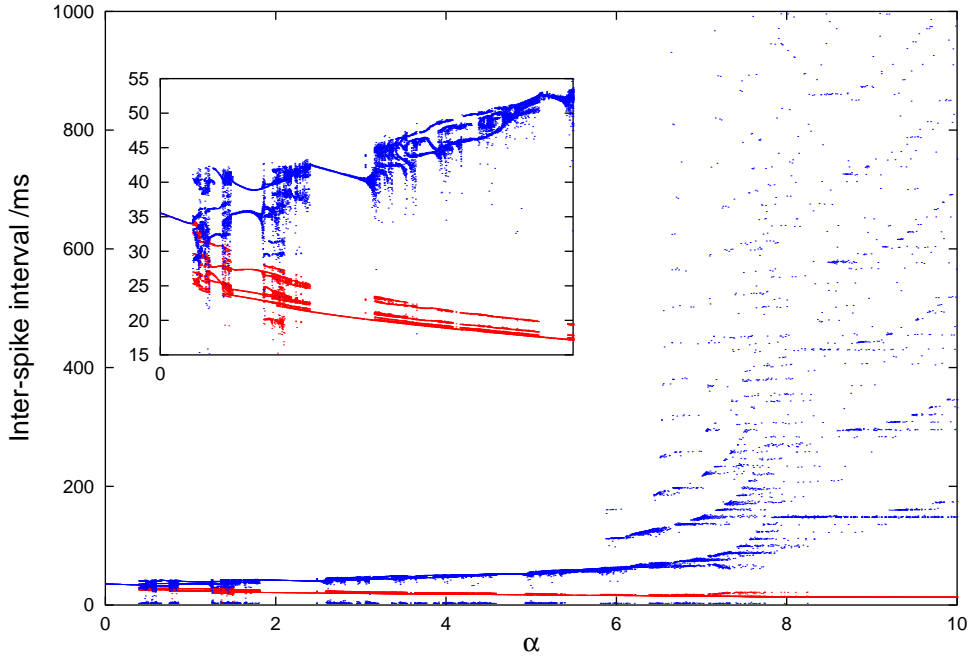


Figure 3.21: Bifurcation diagram of inter-spike interval vs. α for a high level of input to Cell 2. Compare to Figure 3.18A. The inset shows a close-up of the low- α region.

The first condition is satisfied if the second one is, but not vice versa. The second condition gives a threshold of

$$\alpha < \frac{\theta(e^{t_d/\tau} - 1)}{1 + \frac{1}{\delta}} \quad (3.35)$$

2. if the firing of Cell 2 causes the interneurone to fire, then

$$t_L^E = \tau \ln \left[\frac{1}{\theta} \left(\frac{\alpha}{\delta} e^{-t_d/\tau} + \theta + \alpha \right) \right] \quad (3.36)$$

The condition for this state to exist and be stable is

$$t_L^E + t_d < T' \quad (3.37)$$

giving a threshold of

$$\alpha < \frac{1 + e^{t_d/\tau} (\delta(1 - \theta) - \theta)}{1/\delta + e^{t_d/\tau}} \quad (3.38)$$

The α -threshold for the second state (Cell 2 fires the interneurone) is always higher than the threshold for the first state. Where both are stable, initial conditions will determine which state is reached. The threshold for the three-cell model (with an interneurone) is higher than the threshold for the two-cell model (direct inhibition) for small θ , large δ and small t_d .

If $\delta_g < 0.5$, 1:1 firing is only possible if s , the number of steps required to fire the interneurone, is even. Figure 3.22 shows the bifurcation diagram for $s = 5$. The threshold for suppression is raised since the amount of inhibition received by the mitral cells is reduced. For $\alpha \gtrsim 2$, the pattern of harmonic locking is the same as for the two cell model, except that the ratios $n_1:n_2$ are larger, for example the first three $n_1:1$ regions are 4:1, 9:1 and 14:1 (note these are $(s-1):1$, $(2s-1):1$ and $(3s-1):1$), rather than 1:1, 2:1 and 3:1 for the two-cell model. For $\alpha \lesssim 2$, we still observe harmonic locking, but the slope of the function $\Delta\alpha(n_2)$ is smaller than in the region above $\alpha \gtrsim 2$, and appears to vary with α . n_2/n_1 no longer follows a Farey sequence.

3.3.3 Leaky integrator

The effect of making the interneurone a leaky integrator is that s , the number of mitral spikes needed to fire the interneurone and produce inhibition, is no longer constant.

In the bifurcation diagram for the leaky interneurone model (Figure 3.23A), at least five regions of different behaviour may be distinguished:

I	$n_g = 0$	$\frac{n_1+n_2}{n_g} = \infty$
II	$n_g < n_2$	$\frac{n_1+n_2}{n_g} \geq s_{\min} + 1$
III	$n_g = n_2$	$\frac{n_1+n_2}{n_g} \geq s_{\min} + 1$
IV	$n_g > n_2$	$\frac{n_1+n_2}{n_g} \geq s_{\min}$
V	$n_g > n_2$	$\frac{n_1+n_2}{n_g} = s_{\min}$

In Region I there is no interaction between the mitral cells and hence no phase locking. In Regions II and III phase locking does occur, but the repeat period is large and the range of α for which $n:1$ locking is seen is very small. In a larger network, or with noise in the network, it would be very hard to distinguish this behaviour from Region I. In Regions IV and V, the pattern is like that seen when $\tau_g = \infty$, which in turn is similar to the two-cell model.

In summary, the three-cell model, in the general case, switches from no or poor phase locking when the input to Mitral Cell 1 is small (so that the mitral cell firing rates are low compared to the granule cell membrane time constant) to good phase locking when the input to Mitral Cell 1 is large. In a larger network, it might be expected that synchronization/phase-locking would only be seen when the total input to the network exceeded some threshold.

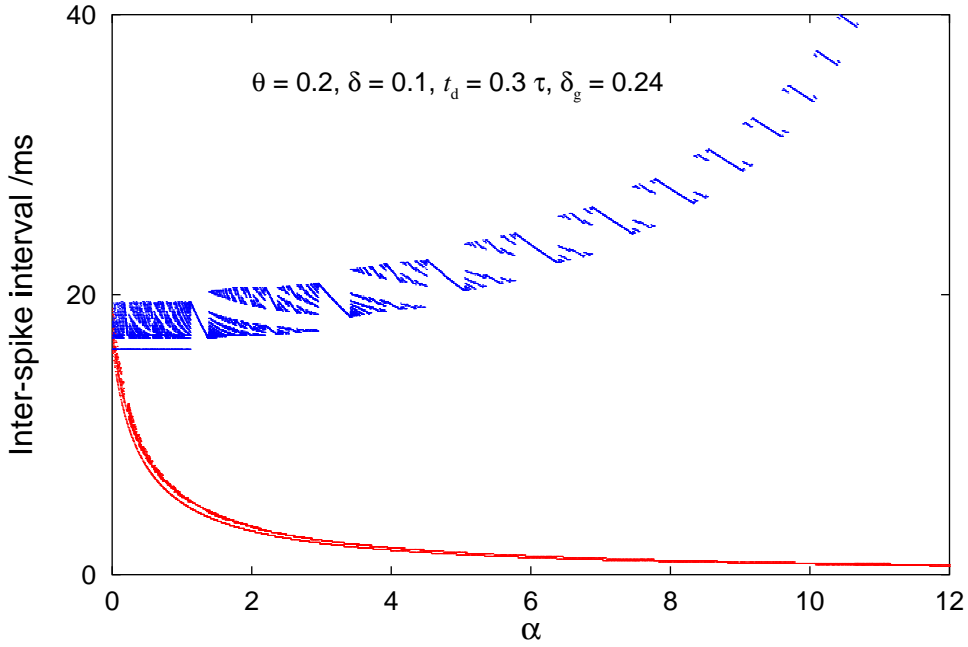


Figure 3.22: Bifurcation diagram for T_1 and T_2 as functions of α for the three-cell system with $\tau_g = \infty$ and $s = 5$. The other parameters are the same as for the two-cell system bifurcation diagram in Figure 3.8.

3.3.4 Biophysical interneurone model

As for the two-cell system, I now ask whether the three-cell system with LIF neurones is a good approximation to the three-cell system with biophysical mitral cells and a biophysical interneurone (the three-compartment granule cell model). The excitatory synaptic current in the granule cell is given by:

$$I_E(t) = \bar{g}_E e^{-t/\tau_E} (V_g(t) - E_E) \quad (3.39)$$

and the inhibitory synaptic current in the mitral cells by:

$$I_I(t) = \bar{g}_I e^{-t/\tau_I} (V_m(t) - E_I) \quad (3.40)$$

where \bar{g}_E, \bar{g}_I are the maximum synaptic conductances; τ_E, τ_I are time constants; V_g and V_m are the membrane potentials of the granule and mitral cells respectively; and E_E, E_I are the synaptic reversal potentials. The values of the fixed parameters are: $\tau_E = 5.5$ ms, $\tau_I = 18$ ms, $E_E = 0$ mV, $E_I = -70$ mV. The time delay of the excitatory synapse was set to zero; the delay of the inhibitory synapses was 3 ms.

If \bar{g}_E is large enough, then the firing of either mitral cell will be sufficient to fire the granule cell (compare to $\delta_g \geq 1$ for the LIF system), and the system should behave like two directly-coupled mitral cells. With $\bar{g}_E = 8 \times 10^{-3}$ μ S and $\bar{g}_I = 0.05$ μ S, this expectation is borne out for $\alpha \lesssim 1$ (compare Figures 3.18 and 3.24). Above this level the similarity breaks down: the three-cell system now exhibits non-periodic behaviour, although the bifurcation diagram for inter-spike intervals suggests ‘almost-mode-locked’ behaviour in which the inter-spike interval has preferred values, but the sequence of values is not repeated. The model was simulated for 10 seconds with the parameters used for Figure 3.24D (40 spikes in Cell 2) but no repeat was seen. The bifurcation diagram for time lag vs. \bar{g}_I (Figure 3.25), with small α , shows considerable similarity to the same diagram for the two-cell system (Figure 3.20), except that the breakdown of mode-locking at high \bar{g}_s is not seen at high \bar{g}_I .

With larger \bar{g}_I , the behaviour is more like the LIF system (Figure 3.26A) with well-defined mode-locking and suppression. Increasing the drive to Mitral Cell 2 (Figure 3.26B) has an effect similar to that of increasing δ or decreasing θ in the two-cell, LIF model – the size of the regions of small-integer mode-locking are increased.

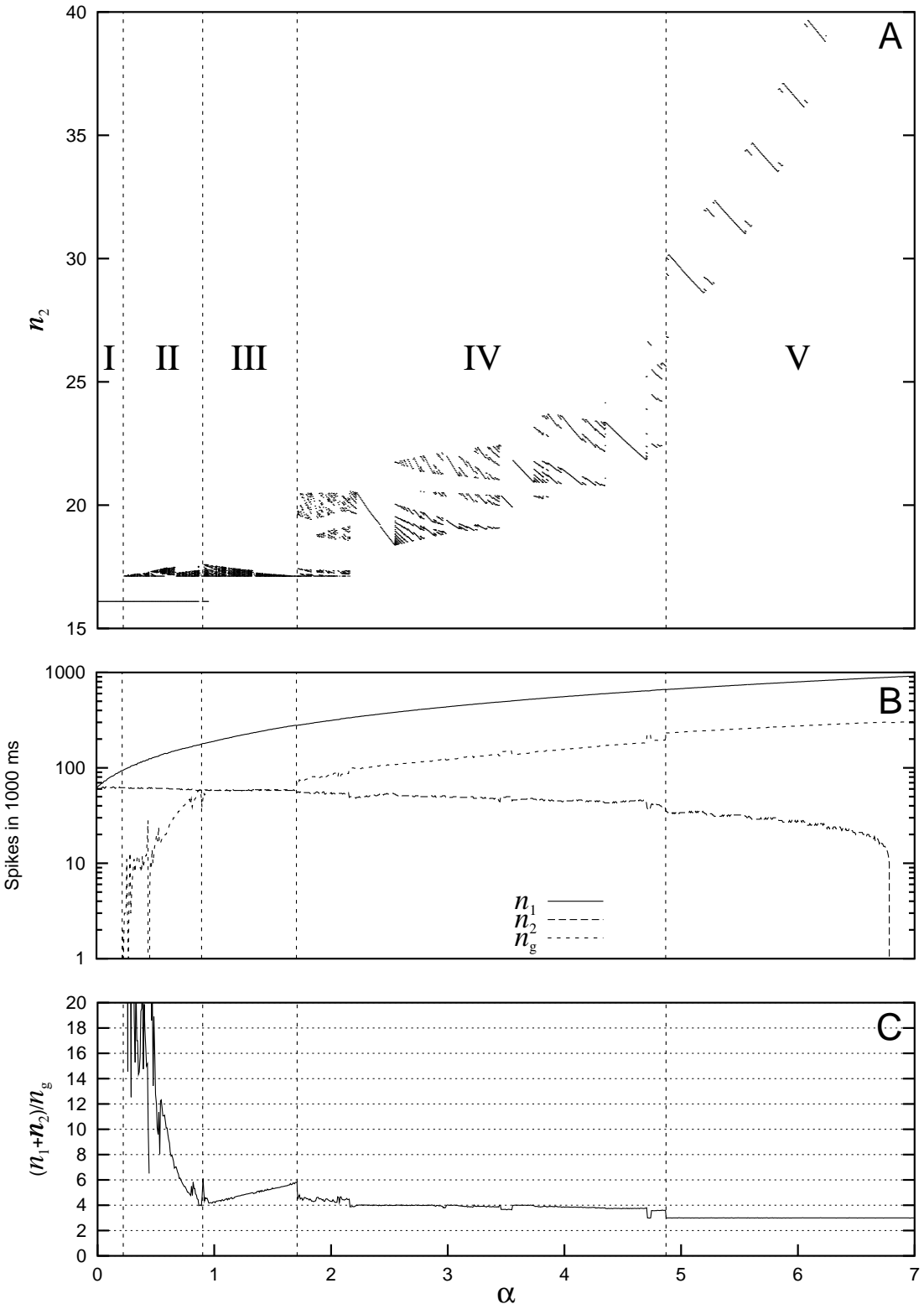


Figure 3.23: (A) Bifurcation diagram for n_2 as a function of α for the three-cell model with a leaky integrator interneurone. $\theta = 0.2$, $\delta = 0.1$, $t_d/\tau = 0.3$, $\delta_g = 0.4$, $\tau_g/\tau = 0.8$. Regions I to V are explained in the text. (B) Firing rate as a function of α for the three cells. (C) Ratio of summed mitral cell spikes to interneurone spikes. This is equivalent to the average value of s , the number of mitral cell spikes needed to fire the interneurone.

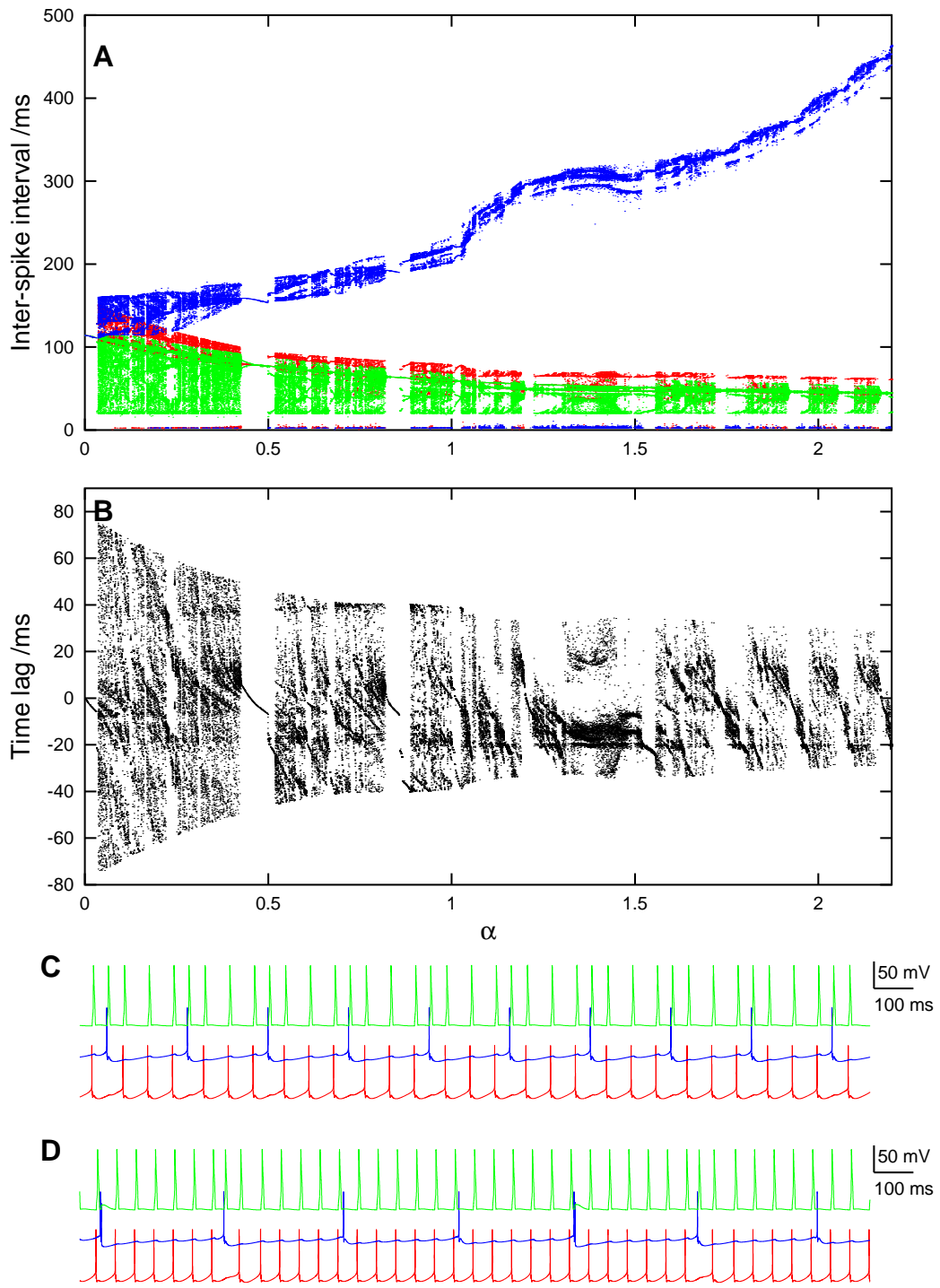


Figure 3.24: Three-cell, biophysical model with large \bar{g}_E : (A) Bifurcation diagram of inter-spike intervals vs. α . For each value of α the model was simulated for 20 s and the first 5 s discarded to remove transient effects. Synaptic parameters: $\bar{g}_I = 5 \times 10^{-2} \mu\text{S}$, $\bar{g}_E = 8 \times 10^{-3} \mu\text{S}$. (B) Bifurcation diagram of time lags vs. α . (C) Membrane potential traces for $\alpha = 0.88$ showing 3:1 mode-locking. Upper trace (green): Granule cell; Middle trace (blue): Mitral Cell 2; Lower trace (red): Mitral Cell 1. (D) Membrane potential traces for $\alpha = 1.3$ – locking is not seen.

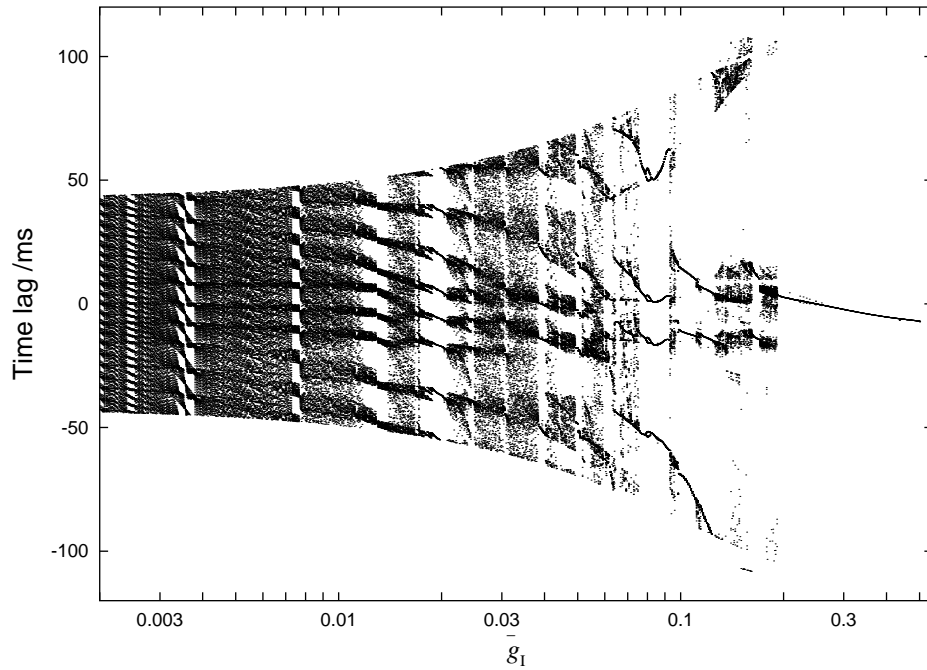


Figure 3.25: Three-cell, biophysical model with large \bar{g}_E : Bifurcation diagram of time lags vs. \bar{g}_I . For each value of \bar{g}_I the model was simulated for 20 s and the first 5 s discarded to remove transient effects. Parameters: $\alpha = 0.1$, $\bar{g}_E = 8 \times 10^{-3} \mu\text{S}$.

If \bar{g}_E is reduced, multiple mitral cell spikes are required to cause the granule cell to fire. The bifurcation diagrams for $\bar{g}_E = 1.6 \times 10^{-3} \mu\text{S}$ are shown in Figure 3.27. The region stimulated appears to correspond to Region II in Figure 3.23: the firing rate of Mitral Cell 2 is approximately constant; the firing rate of the granule cell is below that of Mitral Cell 2. Increasing α further will not move the response into Region III, since the biophysical mitral cell model, unlike the LIF model, has an upper limit of firing frequency.

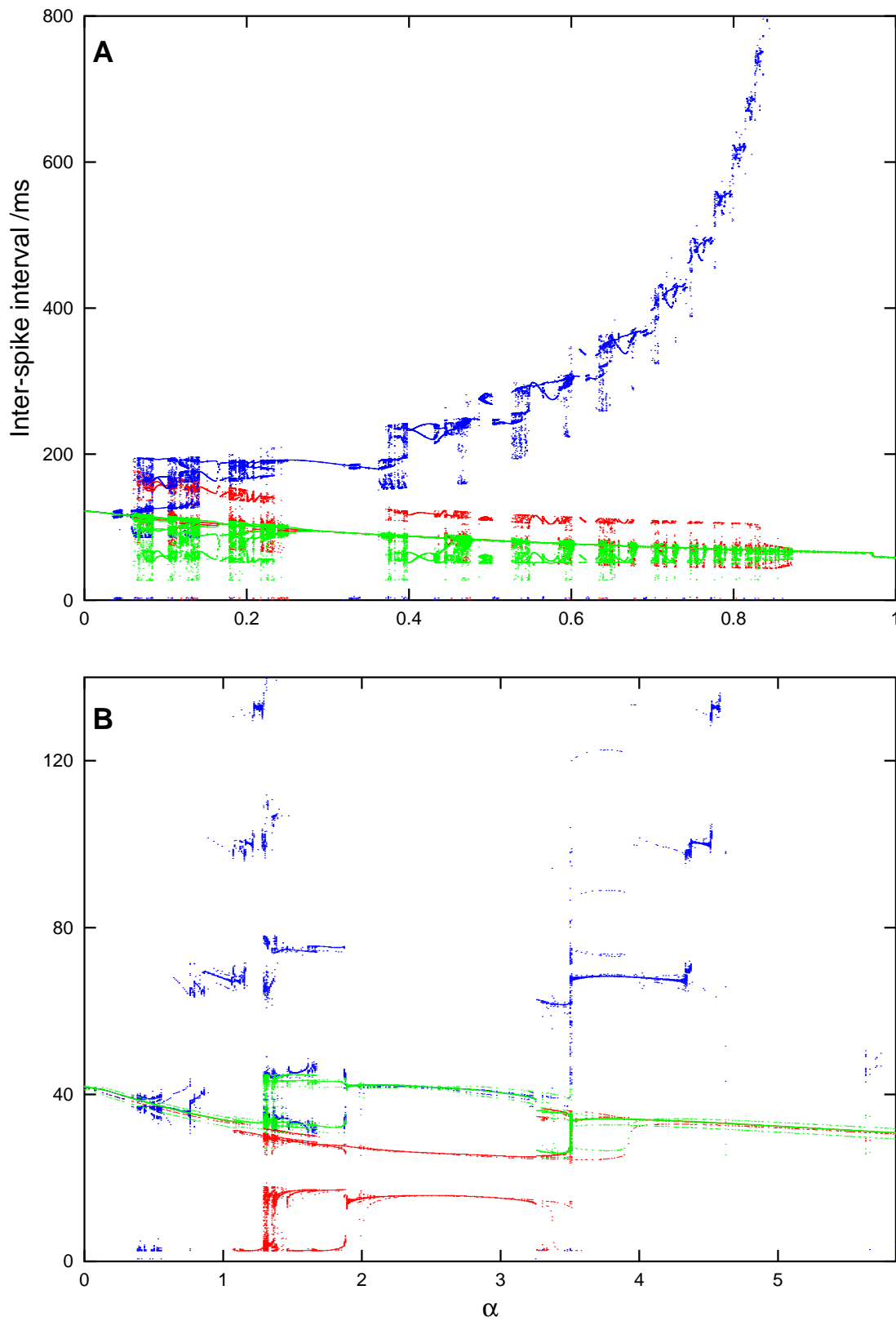


Figure 3.26: Three-cell, biophysical model with large \bar{g}_E and large \bar{g}_I : (A) Bifurcation diagram of inter-spike intervals vs. α . For each value of α the model was simulated for 20 s and the first 5 s discarded to remove transient effects. Synaptic parameters: $\bar{g}_I = 9 \times 10^{-2} \mu\text{S}$, $\bar{g}_E = 8 \times 10^{-3} \mu\text{S}$. (B) same as (A), but with larger driving current (1.9 nA to Cell 2 compared to 0.28 nA in (A)).

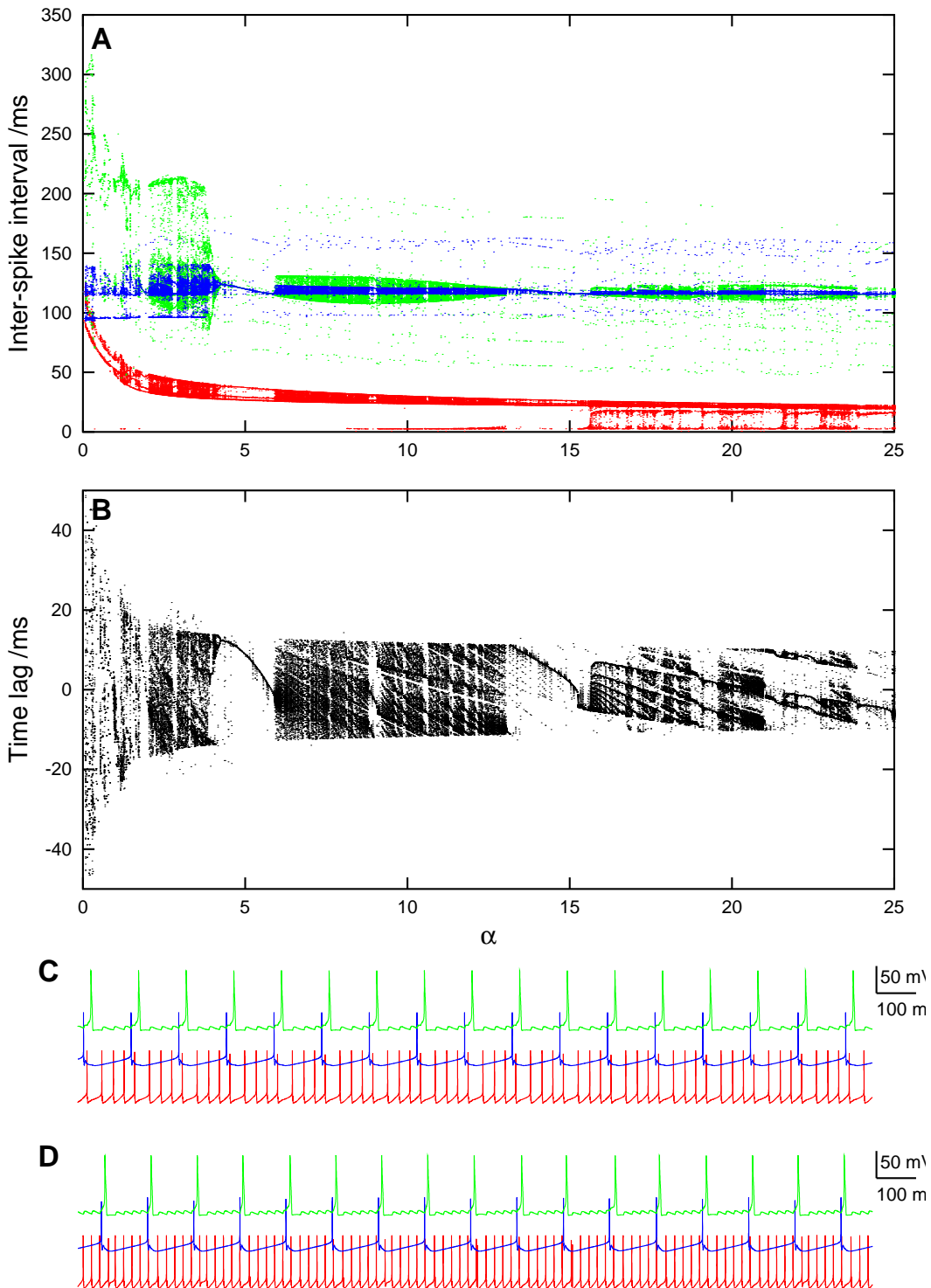


Figure 3.27: Three-cell, biophysical model with small \bar{g}_E : (A) Bifurcation diagram of inter-spike intervals vs. α . For each value of α the model was simulated for 20 s and the first 5 s discarded to remove transient effects. Synaptic parameters: $\bar{g}_I = 5 \times 10^{-2} \mu\text{S}$, $\bar{g}_E = 1.6 \times 10^{-3} \mu\text{S}$. (B) Bifurcation diagram of time lags vs. α . (C) Membrane potential traces for $\alpha = 5.0$ showing 4:1 mode-locking. Upper trace (green): Granule cell; Middle trace (blue): Mitral Cell 2; Lower trace (red): Mitral Cell 1. (D) Membrane potential traces for $\alpha = 20.0$ – no locking.

3.4 Discussion

In this first part of this chapter I have used mathematical analysis and computer simulation to study the properties of pairwise mitral cell interactions. I have proven the existence and stability of phase-locked solutions in a two-cell system with reciprocal, inhibitory connections based on instantaneous voltage steps, and have derived expressions for the equilibrium time lag between the cells, and for the limit of input heterogeneity beyond which 1:1 phase locking breaks down. I have studied the region of harmonic or mode locking in more detail than has been done previously [27], and derived an expression for the minimum-maximum inter-spike interval envelope, which allows an approximation of the spiking model in terms of a firing-rate model. I have shown by simulation that modelling the connections with more realistic, conductance-based synapses with instantaneous rise but finite decay time does not qualitatively affect the system behaviour – the same harmonic locking sequence structure is seen. Finally, I have shown that the integrate-and-fire model is a reasonable approximation to the biophysical, reduced mitral cell model for synaptic conductances below an approximate threshold, but not above this threshold.

In the second part of this chapter I have studied the more biologically realistic system of two mitral cells interacting via an interneurone. For this system, analytical solutions are much more difficult except for a few simple cases. Phase-locking is less robust for the three-cell than for the two cell system. (I define ‘robust’ phase-locking to mean that 1:1 and other low-order mode-locked solutions cover large ranges of α : the slope of the graph of $\Delta\alpha(n_2)$ is steep (see Figure 3.11C)). In general, for robust phase-locking to occur in the three-cell system requires that the interneurone fires faster than the slower-firing mitral cell. This in turn requires either a large disparity in the inputs to the two mitral cells (large α), or large maximum synaptic conductances. The system with biophysical neurone models shows qualitatively similar behaviour to the system with LIF neurones, but as for the two-cell system, the behaviour is more complex and apparently chaotic behaviour is often seen.

Most previous reports on analytical treatments of spike synchronization/phase locking in pulse-coupled networks with inhibitory connections focus on homogeneous networks [146, 46] (i.e. all the cells in the network receive identical inputs, and all synaptic weights are the same). Van Vreeswijk, Abbott and Ermentrout [146] considered two cells with inhibitory, zero-delay synaptic connections, and receiving identical, constant inputs. For integrate-and-fire models with general coupling, and for the Hodgkin-Huxley model with weak coupling (allowing a phase-coupled model description), they prove that for slow synapses only the synchronous state is stable, while for fast synapses both synchronous and anti-synchronous states are stable. Gerstner, van Hemmen and Cowan [46] present a ‘unifying framework’ for the results of van Vreeswijk *et al* and for other reports on synchronization of pulse-coupled oscillators. They consider a spatially homogeneous network of neurons, and use the spike response model (a generalisation of the integrate-and-fire model) to prove the following ‘locking theorem’:

‘In a spatially homogeneous network of spiking neurons with standard dynamics, a necessary and, in the limit of a large number n of presynaptic neurons ($n \rightarrow \infty$), also sufficient condition for a coherent oscillation to be asymptotically stable is that firing occurs when the postsynaptic potential arising from all previous spikes is increasing in time.’

They apply this theorem using a geometric method to construct and determine the stability of a coherent oscillation. For purely inhibitory synapses, their conclusion is that coherent oscillations are always stable, provided the delay is less than some upper bound.

Chow [27] generalises the results of Gerstner *et al* to the case of weak heterogeneity in the inputs to the neurons. For a network of neurons with all-to-all coupling, coherent oscillations are stable with weak-enough heterogeneity if the corresponding state in the homogeneous case is also stable, e.g. if the homogeneous case has synchronous and anti-synchronous states, the heterogeneous state has near-synchronous (constant phase difference near to zero) and near-anti-synchronous (constant phase-difference near to 1/2) states. When phase-locking is broken by increasing heterogeneity, the possible states are asynchrony, harmonic locking and suppression.

There has been very little detailed consideration of the effects of *strong* heterogeneity, i.e. of the states that arise when 1:1 phase-locking is broken. Coombes and Bressloff [31] have analysed a system of two synaptically-coupled integrate-and-fire neurones and show that mode-locked states can exist. They derive

a set of integral equations that may be solved to obtain the phases and the repeat period. Their analysis focuses on a system with mixed excitatory and inhibitory coupling and in the limit of weak coupling, and so is of limited relevance to the system I consider with purely inhibitory coupling and strong synaptic coupling.

The bifurcation sequences of the inter-spike intervals and time lags (see Figure 3.8, for example), which are related to the Farey sequence, are very similar to those seen in studies of periodically stimulated integrate-and-fire neurones [30], which is unsurprising since the cells in the two-cell system receive *almost-periodic* stimulation.

As far as I am aware, there are no published analyses of systems in which inhibition is mediated via an interneurone.

In summary, indirect inhibition produces phase/mode-locking as does direct inhibition, but in general the regions of 1:1 or low-order locking are smaller, and the system may be in one of several qualitatively different regimes depending on the input disparity. We may ask then why, if synchronization is important in olfactory processing, biological olfactory systems use interneurones to mediate inhibition, rather than the more effective solution of having mitral cells inhibit one another directly? This question has a number of possible answers. One is to conclude that synchronization is *not* functionally important in olfactory processing. Another is to invoke Dale's Principle [134] – the mitral cell must release the same neurotransmitter at all its synapses, and since it must be excitatory at the axon terminal, it must be excitatory at the dendrodendritic synapses. A third answer is that mediating inhibition via an interneurone allows modulation of the inhibition by other cortical areas, and this outweighs the disadvantage of indirect inhibition. A fourth answer is that interneurone-mediated inhibition has some advantage in large networks which is not apparent in the two-mitral cell system. All these answers, except possibly the first, are plausible. The possibility of an advantage in large networks seems particularly likely considering the large excess of granule over mitral cells.

To assess the value of this work for studying 'real' mitral-granule cell interactions we must consider the realism of the models. This chapter has shown that the details of the single cell models are not critical; however, the details of the synaptic models are more important. The synaptic models used in this chapter are simple: either instantaneous voltage steps or instantaneous conductance steps with fast exponential decay. At the mitral–granule cell synapse in the olfactory bulb the NMDA receptor, which has a long time constant, plays an important role [63, 125]. The presence of the NMDA receptor could oppose or promote robust phase-locking. As Figure 3.16 shows, longer synaptic decay times generally lead to less robust phase-locking. On the other hand, it is conceivable that NMDA receptor currents summate over time to produce a general increase in granule cell excitability and hence faster firing, with the fast AMPA receptor currents controlling the precise timing of granule cell firing. It has been shown in this chapter that faster interneurone firing leads to more robust phase-locking and therefore the NMDA receptor could promote robust phase-locking. Further work to resolve this question is required.

It is easy to conceive how 1:1 and $n:1$ phase-locking might be useful computationally for a neural system, for example in binding signals from different receptors into a single representation. Whether more general phase-locking modes could be useful is questionable, since in general the spikes of different cells would not occur close together in time. Furthermore, harmonic locking would surely be difficult to obtain, or even to recognize in experimental recordings, in larger networks than two cells. The presence of noise in the network activity would tend to make high-order harmonic locking indistinguishable from asynchrony.

If temporal features such as synchronization are not used in olfactory computation, and only the average rate of firing is important, then the tendency of mutually inhibitory elements to phase lock will tend to quantize the mitral cell firing rates. This may have some value in rejecting noise, but could also reduce the information carrying capacity of the system.

It is difficult to extrapolate results from the simple system of two interacting mitral cells to a large network of mitral and granule cells. The existence and properties of synchronization and phase-locking in large networks are investigated, by simulation, in the next chapter.

Chapter 4

An olfactory bulb network model

4.1 Introduction

Having developed reduced, biophysical models of olfactory bulb neurones (Chapter 2) and studied the interactions of these neurones in minimal networks of two or three cells (Chapter 3), the next step is to develop a large network model with hundreds or thousands of neurones, which can begin to approach the complexity of the real bulb.

The strategy for modelling is to use a level of detail such that the number of unknown parameters is as small as possible. As discussed in Chapter 2, the single cell models were simplified from detailed compartmental models [11] which had been fitted to experimental data. The amplitudes, time constants and transmission delays of the synapses are also obtained from the literature. Some experimental data about the statistics of connections between neurones in the bulb is available. The problem is that available computational power is not sufficient to simulate a network with as many neurones as the real bulb, and once the size of the network is reduced the connection statistics are changed. A simple method for specifying the synaptic connections is therefore adopted, and the effects of varying connection statistics can be investigated by simulation experiments. Modelling electrical stimulation of the bulb is straightforward. Modelling odour stimulation is difficult, as the relationship between odorant identity and the spatio-temporal pattern of inputs to the bulb is only partially understood (see §1.1.3 and §1.1.4). A simple model of olfactory inputs is therefore used, which captures some qualitative aspects of odour inputs but which is not necessarily quantitatively accurate.

As a test of the model, a series of simulation experiments with electrical stimulation were performed and the results compared to published experimental data which were not used in developing the model (§4.4). This gives confidence that the model is capturing some features of network interactions in the real olfactory bulb.

Simulation experiments with ‘odour’ stimulation were then performed to investigate (i) how the model response (in terms of phase-locking/synchronization and the spatial distribution of activity) is affected by stimulus intensity, (ii) how the response depends on connectivity parameters and (iii) whether the network makes it easier to discriminate between similar odour inputs.

4.2 Description of the model

4.2.1 Cells

The neurone types that have been described in the olfactory bulb are mitral cells, tufted cells, periglomerular cells, granule cells and short-axon cells (see §1.1.1). The decision as to which of these cell types should be included in a model is based primarily on the contribution each is thought to make to the network behaviours of interest (i.e. a cell type which makes a large contribution must be included, while one which makes a minor contribution may be excluded), secondarily on the information that is available

about each cell type (i.e. little is gained by including a poorly characterised cell type in the model). In summary, there must be a trade-off between completeness and simplicity.

The mitral/tufted cells and the granule cells are thought to form the fundamental circuit of the olfactory bulb. Detailed models of these cell types have been published [11], and in Chapter 2 I have simplified these detailed models so they are fast enough to be used in large networks. Therefore these cell types have been included in the model.

The short-axon cells are present in very small numbers compared to the other cell types, which suggests that their role in the processing carried out by the bulb may be small, and almost nothing is known about their physiology; therefore I have not included these cells in the model.

The decision whether or not to include periglomerular neurones is difficult. The population of periglomerular cells is large and their synaptic connections are fairly well understood. Less is known about the physiology of these cells than about mitral and granule cells, although there have been recent measurements of sodium and potassium channel kinetics in frogs [6, 7] and rats [116, 117]. Detailed reconstructions of the cell morphology for compartmental modelling have not been made. In evolutionary terms, periglomerular cells appeared late [38] – they are not present at all in fish and are most numerous in mammals. This suggests that PG cells provide a refinement of the bulb’s fundamental computations, which are performed by the mitral/tufted–granule cell system. On balance, I have decided not to include PG cells in this model, although future extensions of the model could include these cells.

Is it necessary to model mitral and tufted cells separately? Both types are output neurones and have similar morphology – glomerular tuft and extensive lateral dendrites – but there are also many differences between them: in size, in orthodromic response properties [42, 124], in axonal projection patterns to central olfactory areas, in the distribution of secondary dendrites [94, 106] and of local axon collaterals [70]. Moreover there is a functional separation of sub-layers [70], with less communication between the mitral and tufted cell populations than within them. I conclude that tufted cells need not be modelled explicitly to gain basic insights into olfactory bulb function, although they must be included as the model is developed and we gain a fuller picture.

In summary, the cell models used are the four-compartment mitral cell model and the three-compartment granule cell model developed in Chapter 2.

4.2.2 Synapses

4.2.2.1 Which synapses to include

Within the glomerulus Since periglomerular cells are not included in this model, the only intra-glomerular synapses are the ORN–mitral cell synapses. For simplicity, sensory inputs to the mitral cells are modelled as constant currents rather than with a synaptic model. This simplification proved to be reasonably accurate for a single mitral cell model (see Chapter 2).

Dendrodendritic mitral–granule cell synapses As discussed in §1.1.1, mitral/ tufted cells have GABA_A receptors and granule cells have both NMDA and AMPA/kainate receptors at the dendrodendritic synapses in the EPL. There is a consensus that these synapses are fundamental to the function of the bulb [119, 135, 158], so they must be included in any model.

Mitral cell autoexcitation Immunocytochemical studies have demonstrated the presence of NMDA[109] and metabotropic (mGluR1 α) [145] glutamate receptors on mitral cell secondary dendrites. This suggests that mitral cells can produce self-excitation, and this has been demonstrated physiologically for both the metabotropic [145] and NMDA receptors [62]. The NMDA-current is much smaller than the GABA-mediated inhibitory current. The metabotropic receptor has been shown to produce increases in intracellular calcium [145], but its effect on membrane potential appears to be negligible compared to that of the NMDA receptor [62]. It is possible that activation of the metabotropic receptor is associated with longer-term processes such as synaptic plasticity, rather than short-term processing.

Further, paired recordings from neighbouring mitral cells have demonstrated that glutamate diffusion

can produce weak, short-range mitral-mitral cell excitatory coupling (lateral excitation about 1.5% of self-excitation) [62]. It has been suggested that this could promote synchronization of mitral cell firing [62].

Mitral cell auto- and lateral-excitation have not been included in this model because of the small size of the currents compared to the GABA_A current and because of the lack of experimental data on mitral cell NMDA and metabotropic glutamate receptors.

Granule to granule cell synapses It has been demonstrated that granule cells receive GABAergic synaptic input [152]. However, the identity of the presynaptic cells is not known – they could be other interneurons, centrifugal fibres and/or other granule cells.

There is morphological evidence for gap junctions between clusters of granule cells [120]. If these junctions represent functional electrical synapses, this would tend to synchronize granule cell firing. I have not modelled gap junctions, but one consequence of synchronization is that close neighbours would fire as a single cell, and so the effect could be approximated by reducing the ratio of granule:mitral cells.

Mitral/tufted cell axon collaterals Although mitral and tufted cell axon collaterals terminate in the granule cell layer [70], very little is known about their physiological effect, so I have not included them here.

4.2.2.2 Synaptic models

In a large network model with many thousands of synapses, the model of a single synapse must inevitably be highly simplified. For the fast synapses in this model (AMPA and GABA_A), an action potential in the presynaptic compartment at time t_0 (detected by a simple threshold-crossing method) produces a step change in the post-synaptic conductance, after a time delay t_d to account for transmitter release and diffusion, which then decays exponentially. The postsynaptic currents are given by:

$$I_{\text{AMPA}}(V, t) = \bar{g}_{\text{AMPA}} e^{-t'/\tau_{\text{AMPA}}} (V(t) - E_E) \quad t' > 0 \quad (4.1)$$

and

$$I_{\text{GABA}_A}(V, t) = \bar{g}_{\text{GABA}_A} e^{-t'/\tau_{\text{GABA}_A}} (V(t) - E_I) \quad t' > 0 \quad (4.2)$$

where $t' = t - t_0 - t_d$, \bar{g}_{AMPA} and \bar{g}_{GABA_A} are the maximal conductances for the AMPA and GABA_A synapses, E_E and E_I are the reversal potentials for the excitatory and inhibitory synapses respectively, and $V(t)$ is the postsynaptic membrane potential. t_d is different for the mitral–granule and granule–mitral directions. For the AMPA and NMDA synapses, $t_d = t_d^E$ and for the GABA_A synapses, $t_d = t_d^I$.

For the NMDA receptor, the rise time is too long to be modelled by an instantaneous change in conductance. Therefore I use the simple, but computationally efficient, model described by Destexhe *et al* [34, 35]. A presynaptic action potential produces a pulse of neurotransmitter of constant concentration, duration t_{dur} , at the postsynaptic site. The postsynaptic response is modelled with a two-state kinetic model. The constant neurotransmitter concentration allows the kinetic equation to be solved analytically, giving:

$$I_{\text{NMDA}}(V, t, [\text{Mg}]) = \bar{g}_{\text{NMDA}} B(V, [\text{Mg}]) r(t') (V(t) - E_E) \quad (4.3)$$

where

$$r(t') = \begin{cases} (1 - e^{-t'/\tau_{\text{NMDA}}^\alpha}) & 0 < t' < t_{\text{dur}} \\ r(t_{\text{dur}}) e^{-(t' - t_{\text{dur}})/\tau_{\text{NMDA}}^\beta} & t' > t_{\text{dur}} \end{cases} \quad (4.4)$$

where \bar{g}_{NMDA} is the maximal NMDA conductance, $\tau_{\text{NMDA}}^\alpha$ and τ_{NMDA}^β are the time constants for the rise and decay phases respectively, $[\text{Mg}]$ is the extracellular Mg²⁺ concentration, $B(V, [\text{Mg}])$ is the voltage-dependent magnesium block, and all other parameters are as previously defined. The magnesium block is taken from Jahr and Stevens [64]:

$$B(V, [\text{Mg}]) = \frac{1}{1 + \frac{e^{-0.062V} [\text{Mg}]}{3.57}} \quad (4.5)$$

\bar{g}_{AMPA}	1.0 nS	\bar{g}_{NMDA}	0.593 nS
\bar{g}_{GABA_A}	0.6 nS	τ_{AMPA}	5.5 ms
$\tau_{\text{NMDA}}^\alpha$	52 ms	τ_{NMDA}^β	343 ms
τ_{GABA_A}	18 ms	t_{dur}	30 ms
t_d^E	1.8 ms	t_d^I	0.6 ms
$[\text{Mg}^{2+}]$	1.0 mM	E_{Na}	45 mV
E_{Ca}	70 mV	E_K	-70 mV
E_E	0 mV	E_I	-70 mV

Table 4.1: Summary of network model parameters

A second spike which arrives during the rise time t_{dur} extends t_{dur} rather than adding to the conductance. Otherwise, multiple inputs summate. Full details of this are given in reference [35].

4.2.2.3 Synaptic parameters

Values of the maximal conductances and synaptic time constants are obtained from the literature:

Excitatory synapses The rise time of the fast component is very short [125]. For simplicity it is taken to be zero, and the AMPA component is described by an instantaneous rise and exponential decay. The decay time constant of the fast component of the EPSC has been measured as 5.5 ± 1.2 ms [125]; The rise time of the NMDA current is about 30 ms with a rise time constant of $\tau_{\text{NMDA}}^\alpha = 52 \pm 10$ ms [125]. The decay time constant, $\tau_{\text{NMDA}}^\beta = 343 \pm 48$ ms [125].

The peak of the fast (AMPA) component of the EPSC recorded in granule cells is approximately 60 pA [63, 125]. Assuming a driving force of about 60 mV gives $\bar{g}_{\text{AMPA}} = 1 \times 10^{-3} \mu\text{S}$ per synapse. The peak amplitude of the NMDA current is 0.26 ± 0.05 times that of the AMPA current in magnesium-free conditions [125], giving $g_{\text{NMDA}}^{\text{peak}} = 2.6 \times 10^{-4} \mu\text{S}$, but due to the non-zero rise time, this is not the same as \bar{g}_{NMDA} :

$$\bar{g}_{\text{NMDA}} = \frac{g_{\text{NMDA}}^{\text{peak}}}{1 - e^{-t_{\text{dur}}/\tau_{\text{NMDA}}^\alpha}} \quad (4.6)$$

from eq. 4.4, which gives $\bar{g}_{\text{NMDA}} = 5.9 \times 10^{-4} \mu\text{S}$.

A summary of the parameters is given in Table 4.1.

Inhibitory synapses Unitary inhibitory post-synaptic currents (IPSCs) recorded in mitral cells have a peak amplitude of about 40 pA, and decay time constant of 18 ± 1 ms [125], with the chloride reversal potential maintained near 0 mV and the holding potential at -70 mV. This gives $\bar{g}_{\text{GABA}_A} = 6 \times 10^{-4} \mu\text{S}$ per synapse. The rise time is about 4 ms [125] and as for the AMPA synapse an instantaneous rise is used.

Synaptic time delays The ideal way to determine the synaptic time delays is to record simultaneously from mitral and granule cells and measure the time between a mitral cell spike and the onset of the EPSP in the granule cell, and the time between a granule cell spike and the onset of the IPSP in the mitral cell. To my knowledge, such a recording has not been carried out, so we must rely on more indirect data. Mori and Takagi [98] measured the time between the arrival of an antidromic spike at the mitral cell soma (inferred from field potential recordings) and the onset of an EPSP in a granule cell (from intracellular recording), obtaining a value of 1.8 ± 0.3 ms (mean \pm standard deviation, $n = 23$). This time delay includes the conduction time from the soma along the secondary dendrite to the synapse, but this is appropriate for the model, since the spike time is measured at the soma. The time between the arrival of the antidromic spike and the onset of an IPSP in mitral cells was 2.4 ± 0.4 ms ($n = 102$), giving a time delay for the granule-mitral synapse of at most 0.6 ms.

The synaptic parameters are summarised in Table 4.1.

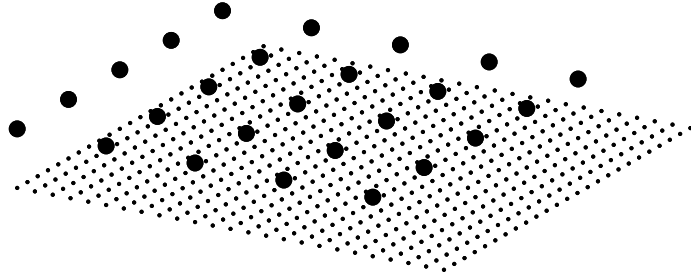


Figure 4.1: The mitral (large circles) and granule (small circles) cell arrays. Connections between cells can wrap round from one side of the array to the opposite side.

4.2.3 Connections

4.2.3.1 Connection statistics

The pattern of connections within a neural system can strongly influence its function. This presents a major challenge to modelling, since many connectivity parameters are not known and may change with the size of the network that is modelled.

Important factors include the size (both number of cells and spatial extent) and shape of the network, the number of synapses per cell, and the frequency of synapses as a function of distance and direction from the cell soma. These determine the degree of interaction between any two cells, i.e. how many synapses there are in the shortest path between two cells, or, more comprehensively, the distribution of path lengths between any two cells.

Topology of the network As the olfactory bulb is laminar, it is natural to describe it by a two-dimensional network. To represent the actual shape of the OB the network topology should be defined by the surface of some ellipsoid. A planar network, however, makes calculation of location and distance much easier. Therefore the mitral and granule cells are arranged in square arrays of equal ‘physical’ size (although there are more granule cells than mitral cells, the distance between granule cells is less than the distance between mitral cells), as shown in Figure 4.1. Edge effects are dealt with by using wrap-round connections in both dimensions.

Number of connections The number of synapses per mitral cell, n_{syn} , has not been experimentally determined. However, it can be estimated from other measurements. The number of synapses in the EPL of adult mice has been estimated by electron microscopy as $(1.1 \pm 0.3) \times 10^9$ [111]. It is unclear whether this estimate is of reciprocal synapses or of individual synapses (a reciprocal synapse consists of an excitatory-inhibitory pair). In the latter case, the number of reciprocal synapses will be half the above estimate. An indirect estimate gives a very similar result: the number of spines on the peripheral dendrites of a single granule cell has been measured as 144–297 in mice [156] and 158–420 in rabbits [94]. Assuming 200 spines per cell and one reciprocal synapse per spine, taking the number of mitral cells per mouse OB as 38400 [121] and the ratio of granule:mitral cells as 150 [133], then the number of synapses in the EPL = $200 \times 38400 \times 150 = 1.15 \times 10^9$.

Assuming a constant density of synapses on mitral/tufted cell dendrites, it would be expected that mitral cells, which are larger, would have more synapses than tufted cells. The total secondary dendrite lengths for mitral and middle tufted cells have been measured as $15016 \mu\text{m}$ and $4050 \mu\text{m}$ respectively [94]. Therefore, taking the ratio of tufted:mitral cells as 2.5 [133],

$$\text{Synaptic density} = \frac{1.1 \times 10^9}{38400(15016 + 2.5 \times 4050)} \simeq 1.14 \mu\text{m}^{-1} \quad (4.7)$$

so the number of synapses per mitral cell is approximately $1.14 \times 15016 = 17000$ and the number per tufted cell is 4600.

These calculations assume that all synapses involve a mitral/tufted cell, and so they ignore centrifugal inputs onto interneurones in the EPL. Therefore these are probably slight overestimates.

Distribution of connections There are a number of ways to specify the connections between cells in a model. The only practical ones assume that connections are formed randomly, dependent only on the relative positions of the two cells, and not on the individual identity of the cell, or on the other connections of the cell. In fact, use-dependent formation and pruning of synapses during development is likely to result in just such non-random connectivity, but we do not currently have any information which would allow connections to be specified in this way. One method for specifying connections in a semi-random fashion is to randomly generate a dendritic morphology for each cell based on statistical data (from [94], for example), and then to generate a synapse whenever two dendrites come within a certain distance of one another. This method can potentially capture the connectivity rather accurately, in a statistical sense, but is rather computationally intensive. A simpler method is to suppose that each mitral cell has a probability density field $p(r, \phi)$ (polar coordinates in the plane of the secondary dendrites), such that the probability of forming a synaptic connection within a region of size $r\delta r\delta\phi$ at point (r, ϕ) is

$$P(r, \phi) = p(r, \phi)r\delta r\delta\phi \quad (4.8)$$

The identity of the granule cell to which the connection is made could also be determined by such a probabilistic method. However, since the radius of the granule cell dendritic field is much smaller than that of the mitral cell, it is simplest to make the connection to the granule cell whose soma is nearest to the point (r, ϕ) .

I make the simplifying assumption that the probability of a mitral cell forming a synapse at a point depends only on the radial distance of the point from the soma, and not on the direction, i.e.

$$p(r, \phi) = p(r) \quad (4.9)$$

This is an approximation, since of course synapses must occur on dendrites, and these project in definite directions from the cell. However, the dendrites branch copiously, so the approximation appears reasonable.

What is $p(r)$? First, I assume that synapses are approximately evenly spaced along the dendrites. If the dendrites have no branches, then $p(r) \propto 1/r$ (i.e. the average *number* of synapses at any given radial distance is constant, so the *density* of synapses declines with distance). If the dendrites branch copiously such that dendritic density is constant within the arbour, then $p(r) = \text{constant}$. In practice, $p(r)$ is likely to lie somewhere within these limits. For any single cell, $p(r)$ will have a discontinuity at each branch point, but these can be smoothed out by taking an ensemble average from many cells. For simplicity I have used $p(r) \propto 1/r$ in all the simulations shown in this chapter, but it would be of interest in future to examine the effect of the $p(r)$ distribution on the network behaviour.

In summary, the connections are specified as follows: The number of synapses per mitral cell is fixed. For each synapse, a direction ϕ and radius r are chosen at random from uniform distributions, and a connection made to the granule cell whose soma is located closest to the point (r, ϕ) . Therefore the number of synapses per granule cell is not constant, but follows some distribution.

Calculation of connectivity parameters We require some metric to quantify the connection statistics of the real and the modelled olfactory bulb. The two metrics I have chosen to use are:

1. the proportion of the granule cells within its arbour to which a mitral cell is connected – the ‘connection fraction’;
2. the fraction of the granule cells connected to one mitral cell which are also connected to any other given, neighbouring, mitral cell – the ‘mutual connection fraction’.

These are obviously related, and together give some idea of the degree of communication between different elements of the network. These have the advantage that they are easy to calculate. I have not considered more sophisticated metrics such as the fraction of mutual connections as a function of the distance between two cells (not only for neighbouring cells).

4.2.3.2 The scaling problem

Simulating large, highly connected networks in which the individual elements are themselves complex is extremely computationally intensive. To simulate a model of a mammalian olfactory bulb with the same number of cells and connections as the real bulb may just be possible on today's supercomputers; it is certainly not possible on anything less powerful. Therefore it is desirable to simulate smaller networks and to infer the behaviour of the full-scale network from the behaviour of the smaller simulations.

In principle there are two ways to shrink a network: it can be made smaller in extent or be made more sparse. A smaller network, which may represent a sub-region of the bulb, has the same connectivity within the sub-region, but ignores any inputs from outside. Given the very large extent of mitral cell dendrites, this may have a significant influence on the behaviour. However, with focal electrical stimulation or weak odour stimulation, only one or a small number of glomeruli are activated, and so only the mitral cells connected to those few glomeruli, and the granule cells to which they connect, need be simulated. The other mitral cells receive no input and therefore produce no output and therefore have no influence on the stimulated mitral cells (this ignores background activity, which could be simulated by a small, constant drive to the granule cells).

A sparser network does not suffer from edge effects, but will have different connectivity to the full-scale network: either the number of connections per cell will be reduced or the connection fraction and mutual connection fraction will be increased.

I have chosen a mixed strategy: both reducing the number of cells and decreasing the network size relative to the range of connections. A network smaller than the range of the secondary dendrites allows the number of synapses per mitral cell to be reduced, since many connections will be to granule cells outside the simulated region.

4.2.4 Input

The input to the olfactory bulb is from two sources: (i) the olfactory nerve (sensory inputs from ORNs or electrical stimulation of the nerve); (ii) the medial and lateral olfactory tracts (centrifugal inputs/feedback from higher levels of cortex or electrical stimulation of the tracts).

4.2.4.1 Sensory input

Considering first the sensory input, there are two considerations: the spatial distribution of input intensity; and the temporal structure – the statistics and modulation of the ORN spike train.

Spatial structure In one sense, modelling the spatial distribution of inputs is easy: each ORN-type projects to one or a pair of glomeruli and each glomerulus receives input from only one ORN-type [18, 93, 149]. However, any given receptor responds to a broad range of odorants, and any given odorant activates receptors of more than one type. There is as yet no satisfactory model for this, although features of the odour molecule such as shape and chemical identity appear to be important [66, 96]. There is some evidence that receptors which respond to chemically-similar odorants project to nearby glomeruli [45, 61] but it is not established that this arrangement has a functional purpose [76].

I chose to model 10 odour ‘features’ and 36 receptor types/glomeruli (in a 6×6 array). Let a_{ij} be the degree of activation of each receptor type j by each odour feature (OF) i ($0 \leq a_{ij} \leq 1$). All the a_{ij} 's form a 10×36 matrix, \mathbf{A} . An odour is then represented by a 10 element vector \mathbf{x} . Applying odour \mathbf{x} to the bulb model produces a receptor-activation vector \mathbf{y} :

$$\mathbf{y} = \mathbf{Ax} \quad (4.10)$$

This assumes no interaction between odour features at the receptor level and so is a simplification of the real situation [73]. The current applied to the glomerular compartment of mitral cell j is then proportional to the element y_j of the receptor activation vector. The proportionality includes a scaling for odour intensity.

There are no good statistical data available which would allow determination of the matrix \mathbf{A} . In developing a procedure to specify \mathbf{A} , I adopted the criterion that a large minority of the elements should

be zero (no response), and that a small minority should have strong responses. This criterion is based on imaging studies of glomerular activation (e.g. [44, 45, 122]). \mathbf{A} is generated as follows:

- each element a_{ij} is picked independently from a normal distribution with mean 0.0 and variance 0.5. Then \mathbf{A} is transformed as follows: each column vector j of \mathbf{A} is mapped onto the two-dimensional glomerular space to form a matrix \mathbf{S}^j . Each element s_{lm}^j of \mathbf{S}^j is convolved with a kernel

$$\begin{pmatrix} e^{-2\sqrt{2}} & e^{-2} & e^{-2\sqrt{2}} \\ e^{-2} & e^0 & e^{-2} \\ e^{-2\sqrt{2}} & e^{-2} & e^{-2\sqrt{2}} \end{pmatrix} = \begin{pmatrix} 0.059 & 0.135 & 0.059 \\ 0.135 & 1.000 & 0.135 \\ 0.059 & 0.135 & 0.059 \end{pmatrix} \quad (4.11)$$

i.e. each element is transformed to a weighted sum of itself and its close neighbours. The elements are then normalised to be between 0 and 1. The modified \mathbf{S}^j is then mapped back onto column vector j of \mathbf{A} . This acts to introduce a dependence between the activations of nearby glomeruli.

Temporal structure The inputs to a given mitral/tufted cell can be modelled as continuous currents or as spike trains activating synapses. The neurotransmitter released by ON axon terminals is glutamate [10] and mitral cells have both NMDA and AMPA receptors [41].

The presence of the long-duration NMDA current suggests that a constant-current approximation may be valid for odour stimulation (see the results in §2.2). On the other hand, odour-elicited field-potential oscillations in vertebrate olfactory epithelium, which are abolished by tetrodotoxin [37], suggest that ORN firing may be synchronized, which would invalidate the constant-current approximation. The stimulus amplitude may be also have periodic modulation due to sniffing or breathing.

For simplicity, I have used the constant-current approximation for odour input.

4.2.4.2 Centrifugal connections

Much less is known about the centrifugal inputs than about the sensory inputs. The origins and neurochemistry of the centrifugal fibres are discussed in Section §1.1.1.

Centrifugal innervation can be divided into two categories: external effects which are not induced by olfactory input, e.g. the noradrenergic and cholinergic input in ewes, caused by stimulation of the vagina and cervix during parturition, which leads to the formation of own-lamb-specific olfactory memories [69]; and feedback effects in which an olfactory signal transmitted from bulb to cortex causes centrifugal input. The ‘external’ inputs are likely to be spatially homogeneous in their effect and to have a global effect – perhaps changing the system from one state or condition to another, e.g. from a non-learning to a learning state. The feedback inputs may have local effects, in that feedback could be targeted to the region of the specific neurones which caused the feedback, or may also have global effects. The time delay for feedback is unknown. In a single mitral cell recorded by Fischer and Zippel [43], a suppression of firing beginning 2.5 s after odour presentation was abolished by cryogenic blockade of the olfactory tract, suggesting that some feedback can have time delays of several seconds. The spike latency of piriform cortex neurones following olfactory bulb electrical stimulation is on average 18 ms [101], so a lower bound for feedback delay is about 40 ms. In practice it is likely to be longer, since some intra-cortical processing must occur before the feedback signal is generated. Therefore, just after presentation of a novel stimulus, feedback can be ignored. Centrifugal inputs can be ignored entirely when considering experiments performed in bulb slices, since bulbar-cortical connections are not preserved in this preparation.

I have chosen not to include centrifugal inputs in the model at this stage.

4.3 Numerical methods

The model was simulated in NEURON version 4.1 running on a Digital XP1000 workstation under Digital Unix and in NEURON version 5.0 running on a Dell Precision 330 workstation under Linux. NEURON allows the use of fixed time step and variable time step integration methods. The fixed time step methods are backward Euler and Crank-Nicholson. The variable time step method is multi-order, and may be used

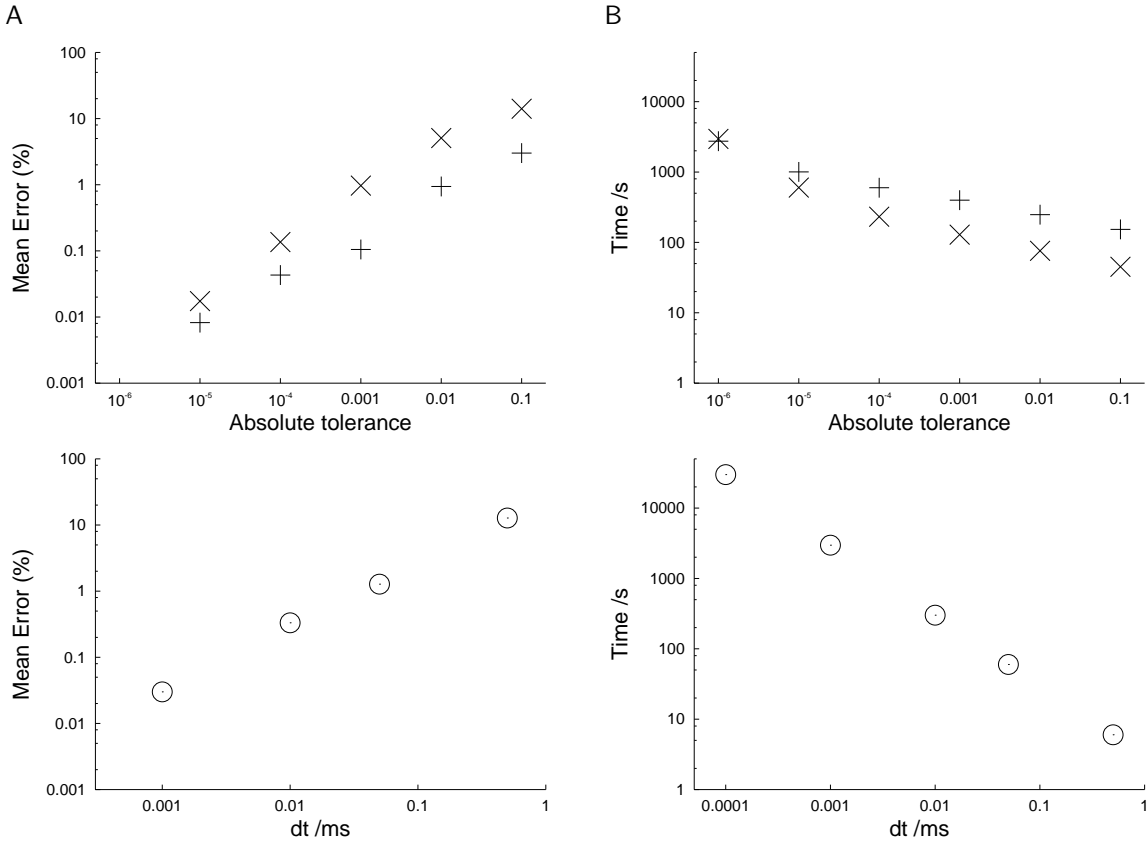


Figure 4.2: The effect of integration parameters on accuracy. (A) Mean absolute error (%) in inter-spike intervals. See text for details of error calculation. (B) Time taken to integrate for 300 ms. \times local variable time step; $+$ global variable time step; \odot fixed time step.

globally (the same time step is used for all elements of the model) or locally. In order to determine the most suitable method, I simulated a small network of 16 mitral cells and 256 granule cells using (a) fully implicit backward Euler (FIBE), (b) global variable time step (GVTS) and (c) local variable time step (LVTS). For the FIBE method, the time step (dt) was varied. For the variable time step methods, the local absolute error tolerance ($atol$) was varied. The model was simulated for 300 ms with 50 synapses per mitral cell and the input current for each mitral cell chosen at random from a uniform distribution in the range 0–2 nA. For each integration method and for each value μ of the integration parameter ($atol$ or dt), the inter-spike intervals, T_i^μ , were calculated (63 ISIs in total, ranging from 22.2 to 96.5 ms), and an error value was calculated:

$$E_\mu = \frac{1}{63} \sum_{i=1}^{63} \left| \frac{T_i^\mu - T_i^\nu}{T_i^\nu} \right| \quad (4.12)$$

where ν is the smallest value of the integration parameter for each integration method ($\nu = 10^{-6}$ for both variable time step methods; $\nu = 0.1 \mu\text{s}$ for the FIBE method). The time taken to run the simulation was also recorded. The results for the XP1000 workstation are shown in Figure 4.2. Note that some of the parameter values were different from those used in the rest of this chapter¹ but a partial repeat of these simulations with both sets of parameters confirmed that the effect on the results is negligible. The LVTS method always requires a smaller absolute tolerance to achieve the same accuracy as the GVTS method, but it is faster for all error levels above 0.01%. The FIBE method is slower than the LVTS method for error levels below about 0.5%.

¹ $E_E = 45 \text{ mV}$, $\bar{g}_{\text{NMDA}} = 0.312 \text{ nS}$ and $\bar{g}_{\text{AMPA}} = 0.6 \text{ nS}$

The error between the most accurate runs of each method was also calculated as above. Comparing LVTS with GVTs gave an error of 0.009%, while comparing LVTS with FIBE gave a much larger error of 1.4%.

For most of the simulations reported in this chapter I have used the LVTS method with $\text{atol}=0.01$. This gives an error level of about 5%. Some results were checked with $\text{atol}=10^{-4}$.

4.4 Response to olfactory nerve shock

4.4.1 Introduction and Methods

The dendrodendritic reciprocal synapse has a central role in olfactory bulb function, and therefore it is desirable to test this aspect of the model with reference to experimental results. Schoppa *et al* [125] recorded synaptic currents in mitral and granule cells in response to focal electrical stimulation of one glomerulus, giving a detailed picture of dendrodendritic function. In this experiment the bulb model was simulated with the same conditions, as far as possible, as used by Schoppa *et al*.

The somata of mitral cells innervating a single glomerulus are likely to be distributed within a small area (one study found that 96% of mitral cells connected to the same glomerulus were separated by less than 120 μm [21]). For simplicity in determining connections, the model assumes that the somata are located at a single point, and therefore the range of connections can be set to the entire extent of the cell array.

The size of the mitral cell array was 5×5 . To reduce synchronization of cell firing, some heterogeneity was added to the network by picking \bar{g}_{NMDA} for each cell from a normal distribution with standard deviation equal to half the mean. This method of adding heterogeneity was chosen arbitrarily to obtain the desired effect. One mitral cell was voltage clamped at -70 mV with a series resistance of $2 \text{ M}\Omega$ and the chloride reversal potential set to 0 mV. All mitral cells were simultaneously stimulated in the glomerular compartment with a current pulse of amplitude 20 nA and duration 5 ms. The extracellular magnesium concentration $[\text{Mg}^{2+}]$ was set to 0 mM. The model was simulated for 3000 ms using the LVTS method with absolute tolerance 0.01. Other model parameters are given in Table 4.1 or in the text.

4.4.2 Results

The network model responds to glomerular shock with a single action potential in each mitral cell (Figure 4.3A) and a train of action potentials in granule cells (e.g. Figure 4.3B). The duration and frequency of this spike train depends on the number of synaptic inputs each granule cell receives. The granule cell population response is an initial, synchronized burst followed by unsynchronized firing (Figure 4.3D) with an exponentially-decaying spike-time histogram (STH) (Figure 4.3E). The prolonged granule-cell firing produces a long-duration IPSC in the voltage-clamped mitral cell. This IPSC was fitted between 50 and 2000 ms with a single exponential function (time constant 296 ms) and with the sum of two exponentials (time constants 55 ms and 367 ms). This IPSC is similar in amplitude and time-course to that seen experimentally by Schoppa *et al* [125] (Figure 4.3F), except that the model time constant is shorter than the experimental time constant.

4.4.2.1 Contributions of AMPA and NMDA receptors

In order to separate out the contributions of the AMPA and NMDA receptors to the network response, the model was simulated with the conductances for these synapses set in turn to zero. The results are shown in Figure 4.4. It is apparent that the NMDA receptor is needed to generate prolonged spike trains in the granule cell population (Figure 4.4B,D) and hence to generate prolonged IPSCs in the mitral cells (Figure 4.4C). The main effect of removing the AMPA current is to increase the rise time of the mitral cell IPSC. A second effect is to increase the amplitude of the prolonged granule cell population response: the peak of the baseline spike time histogram is 42 spikes per second while the peak of the no-AMPA histogram is 67 spikes per second (Figure 4.4D).

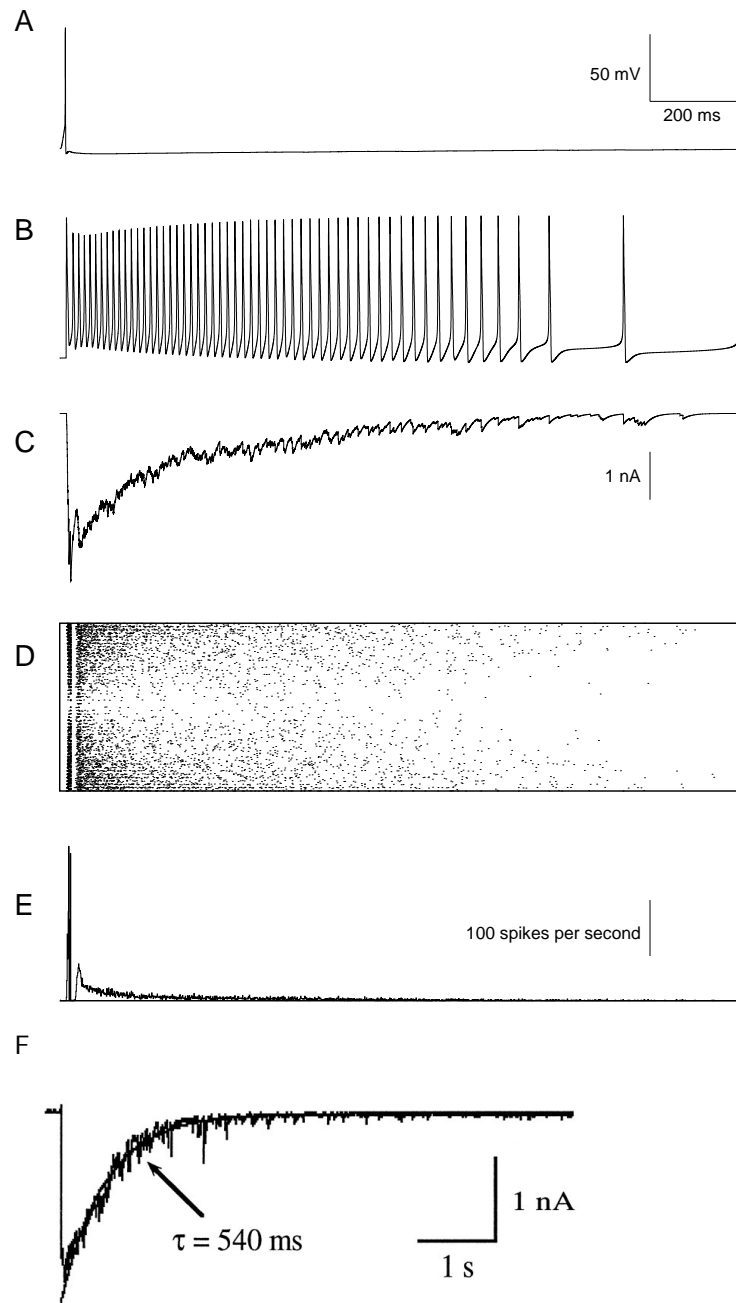


Figure 4.3: Glomerular stimulation produces a single spike in all mitral cells (A), and prolonged firing in some granule cells (B). The overall granule cell response is a brief, synchronized burst, seen in the raster plot (D) and post-stimulus spike histogram (E), followed by unsynchronized firing which decays exponentially (E). The granule cells produce a prolonged IPSC in mitral cells (C), which is similar to that seen experimentally (F), although the decay is faster. Parameters: $n_{\text{gran}}/n_{\text{mit}} = 100$; $n_{\text{syn}} = 200$; $[\text{Mg}^{2+}] = 0 \text{ mM}$. Figure (F) was reproduced from reference [125].

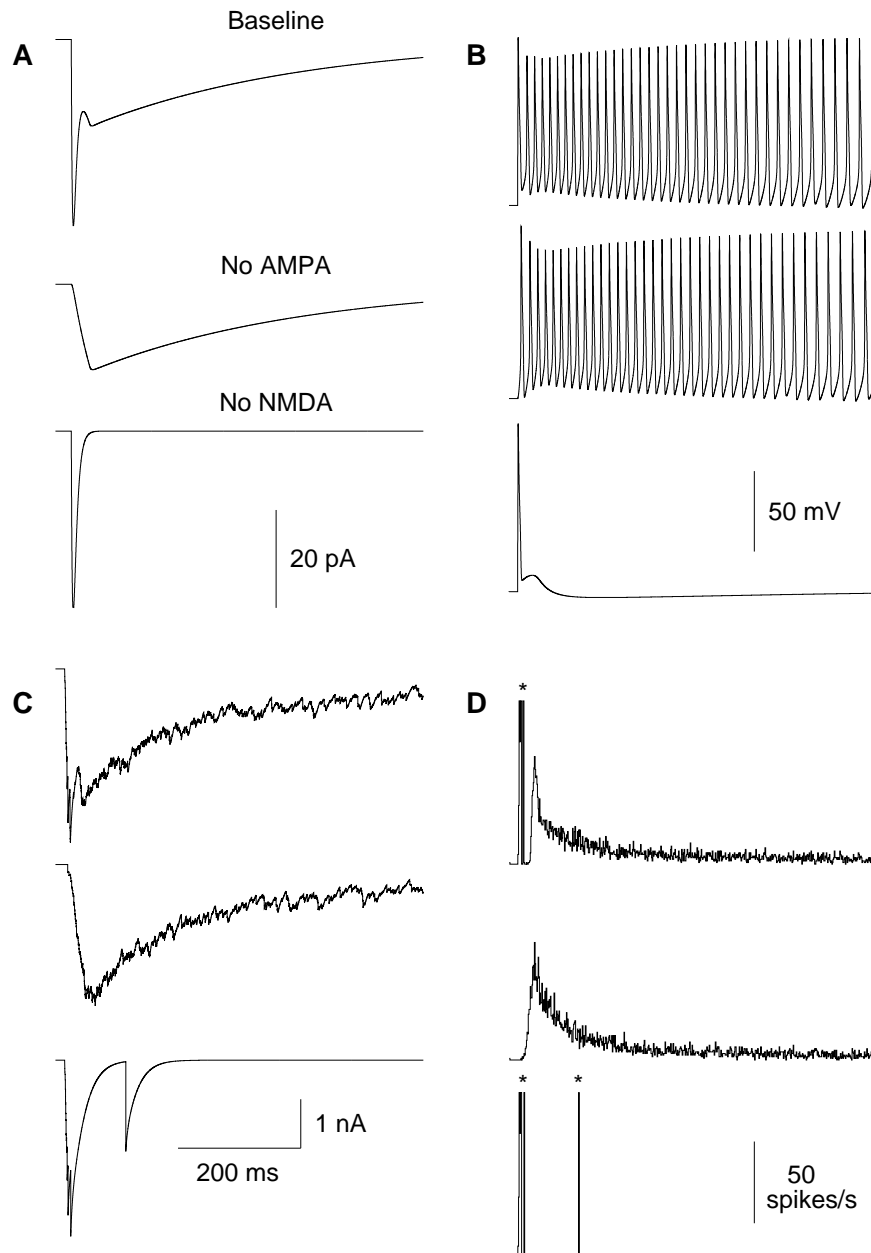


Figure 4.4: The separate contributions of fast AMPA and slow NMDA currents to the granule cell EPSC (A) in response to glomerular stimulation are clearly seen. While the presence of NMDA receptors alone is sufficient to produce a prolonged train of action potentials in granule cells (B and D), AMPA-receptors alone produce only one or two spikes per cell, leading to a greatly-reduced duration of the IPSC in the mitral cells (C). Note that removing AMPA receptors increases the amplitude of the broad peak in the granule cell population STH (D), compared to baseline. In (D), * indicates that the bin has been truncated at 100 spikes.

	Increasing n_{syn}	Increasing n_{gran}	Increasing n_{syn} and n_{gran}
Granule cell firing rate	↑	↓	↑
IPSC amplitude	↑	↓	↑
IPSC decay time	↑	↓	—
STH amplitude	↑	↑	↑
STH decay time	↑	↓	—

Table 4.2: Summary of the effects of changing network parameters on the model response to a glomerular shock stimulus. ↑ denotes an increase, ↓ denotes a decrease and — denotes no change in the quantity in the leftmost column.

4.4.2.2 Effect of $[\text{Mg}^{2+}]$

All the previous simulations were carried out with $[\text{Mg}^{2+}] = 0 \text{ mM}$. To investigate the effect of magnesium ion concentration on the model, a number of simulations were performed with varying values of $[\text{Mg}^{2+}]$. Figure 4.5A shows the mitral cell IPSCs for different values of $[\text{Mg}^{2+}]$. The effect of increasing $[\text{Mg}^{2+}]$ is to shorten the prolonged component of the IPSC, with little or no effect on the early component. The total charge transferred to the mitral cell may be found by integrating the IPSC curve over time. Figure 4.5B shows the total charge (as a fraction of the total charge at $[\text{Mg}^{2+}] = 0 \text{ mM}$) as a function of $[\text{Mg}^{2+}]$, for the simulations and for Schoppa *et al.*'s experimental results. The total charge decreases exponentially as a function of $[\text{Mg}^{2+}]$. The model is more sensitive to small Mg^{2+} concentrations than is the experimental preparation.

4.4.2.3 Extended stimulus

In response to an extended current clamp stimulus (amplitude 2 nA, duration 300 ms) the mitral cells fire a series of action potentials interspersed with some ‘almost spikes’, when the action potential appears to be suppressed (Figure 4.6A). Each mitral cell spike produces a burst of granule cell firing (Figure 4.6C), which in turn leads to pulsed inhibition of the mitral cells (Figure 4.6B).

4.4.2.4 Influence of network connectivity

The easily-characterised response to glomerular shock provides a good opportunity to examine the effects of changing network connectivity parameters. The number of mitral cells, n_{mit} , was fixed throughout. The number of granule cells, n_{gran} , was first fixed at 2500 while the number of synapses per mitral cell, n_{syn} , was set at 50, 200 or 500. The results are shown in Figure 4.7. Increasing n_{syn} increases the average number of synapses per granule cell, leading to faster and more prolonged granule cell firing in a larger number of cells. In turn, this decreases the rate of decay of the mitral cell IPSC. Increasing n_{syn} also increases the amplitude of the mitral cell IPSC.

Fixing n_{syn} at 200 while decreasing n_{gran} ($n_{\text{gran}} = 4900, 2500$ or 1225) (Figure 4.8) has a similar effect to fixing n_{gran} and increasing n_{syn} (Figure 4.7): the durations of the granule cell response and the mitral cell IPSC are increased. The main differences are (i) with fixed n_{syn} the peak of the granule cell spike time histogram decreases and (ii) the reduction in IPSC amplitude is much less pronounced.

Increasing n_{syn} and decreasing n_{gran} both have the same effect: to increase the average number of synapses per granule cell. These effects were offset against each other by increasing both parameters so as to keep the average number of synapses per granule cell constant at 2.0. The results are shown in Figure 4.9, and are similar to the results for increasing n_{syn} with fixed n_{gran} (Figure 4.7) with the exception that the decay time constants of the granule cell STH and the mitral cell IPSC remain approximately constant as n_{syn} is increased.

The results shown in Figures 4.7, 4.8 and 4.9 are summarised in Table 4.2. This table makes it clear that n_{syn} has the dominant effect on the firing rate of the most strongly-activated granule cell and on the amplitude of the mitral cell IPSC, but that n_{syn} and n_{gran} have approximately equal and opposite effects on the time course of the response; the most important factor affecting the time course is the average number of synapses per granule cell.

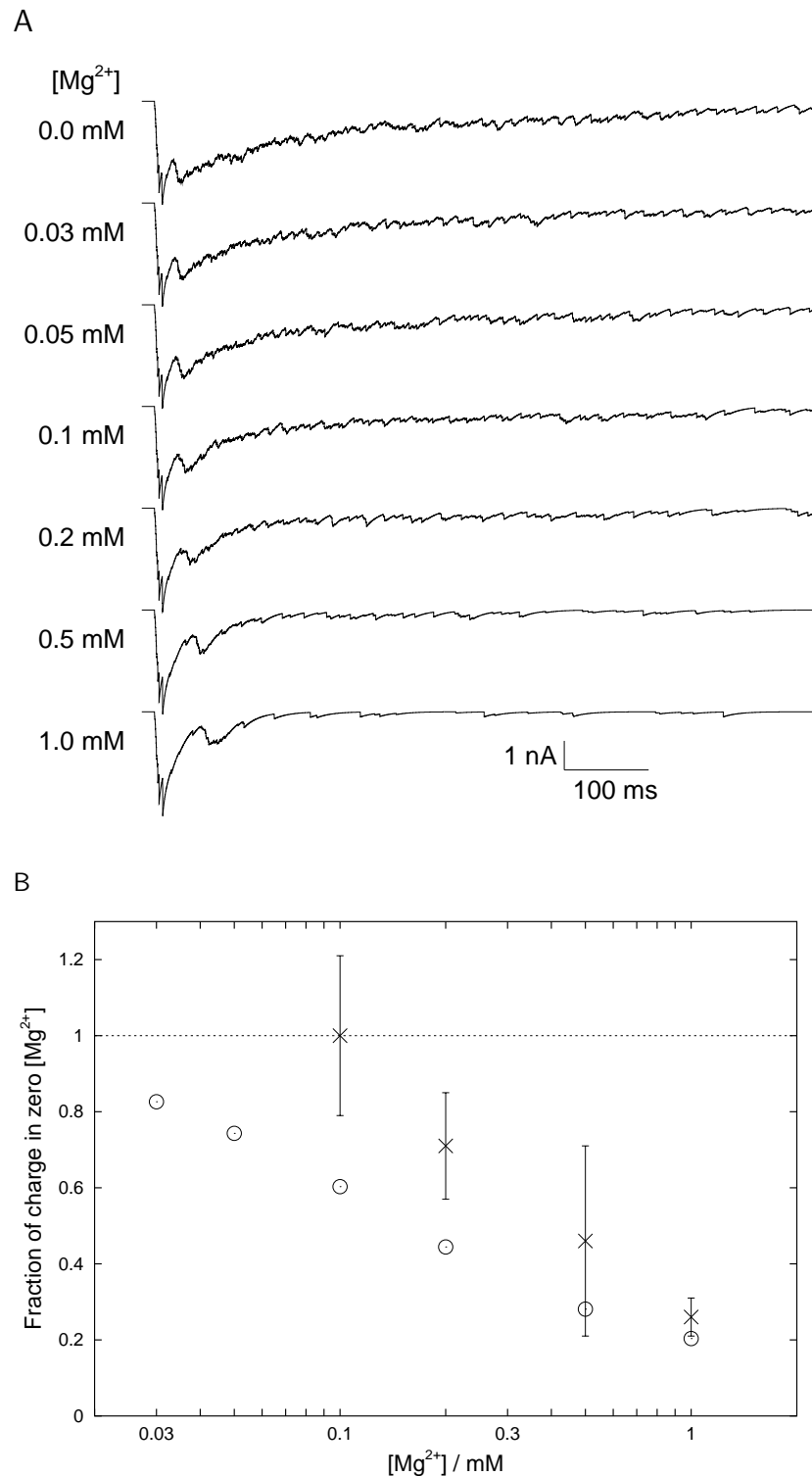


Figure 4.5: (A) Increasing the external magnesium ion concentration, $[Mg^{2+}]$, reduces the duration of the mitral cell IPSC while having little effect on the peak current. (B) The total charge transferred to the cell (found by integrating the IPSC curve) is reduced exponentially by increasing $[Mg^{2+}]$. The sensitivity of the model (\circ) to $[Mg^{2+}]$ is greater than is found experimentally (\times).

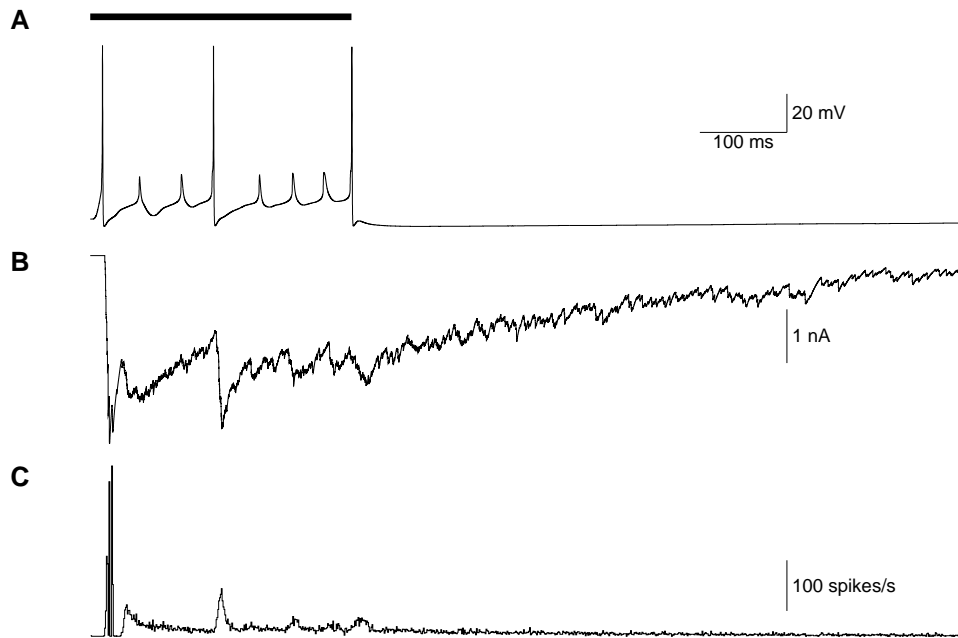


Figure 4.6: The mitral cells respond to a 300 ms current clamp stimulus by firing several action potentials (A), each of which produces a burst of firing in the granule cell population (C – STH), leading to pulsed inhibition of the mitral cell (B – mitral cell IPSC). The solid bar indicates the duration of the stimulus.

4.4.3 Discussion

The simulated IPSC in a voltage-clamped mitral cell in response to a glomerular shock stimulus is similar to that measured experimentally by Schoppa *et al* [125] (Figure 4.3). The amplitude is approximately the same; the time constant of the decay is somewhat shorter.

Compared to NMDA receptors, AMPA receptors make very little contribution to the model response (see Figure 4.4). Without NMDA receptors, granule cells fire only one or two action potentials, and the IPSC in mitral cells is of much shorter duration. This is in good agreement with experimental findings that, in zero Mg^{2+} , dendrodendritic inhibition is governed almost entirely by NMDA receptors [63, 125]. An unexpected result is that the population response of granule cells is enhanced in both amplitude and duration by removal of AMPA receptors (Figure 4.4D). This suggests that the initial, AMPA-mediated phase of the EPSP may inhibit subsequent firing. It would be interesting to test for this effect experimentally.

The effect of increasing the external magnesium ion concentration is to reduce the duration but not the amplitude of the mitral cell IPSC (Figure 4.5). This is not surprising due to the presence of the magnesium-block in the NMDA conductance model. The model is more sensitive to low Mg^{2+} concentrations than the experimental preparation: experimentally, no reduction in IPSC size is seen below 0.1 mM Mg^{2+} [125] whereas the total charge is reduced to 60% of baseline in the model at the same concentration. At 1 mM, the simulation and experimental responses are about the same. The magnesium block function used in the model was obtained from recordings of hippocampal neurones [64], not olfactory granule cells; it is uncertain whether the discrepancy here between model and experiment is due to this or to the differences in network connectivity.

Increasing the number of synapses per mitral cell increases the amplitude of the mitral cell IPSC, unsurprisingly. 200 synapses per mitral cell gives an amplitude of about 2 nA, which is a typical value seen experimentally [63, 125]. This is many fewer than the total number of synapses calculated for each mitral cell (see §4.2.3.1). Increasing the number of synapses also increases the duration of the IPSC and of the granule cell population response, although the principal factor appears to be the mean number

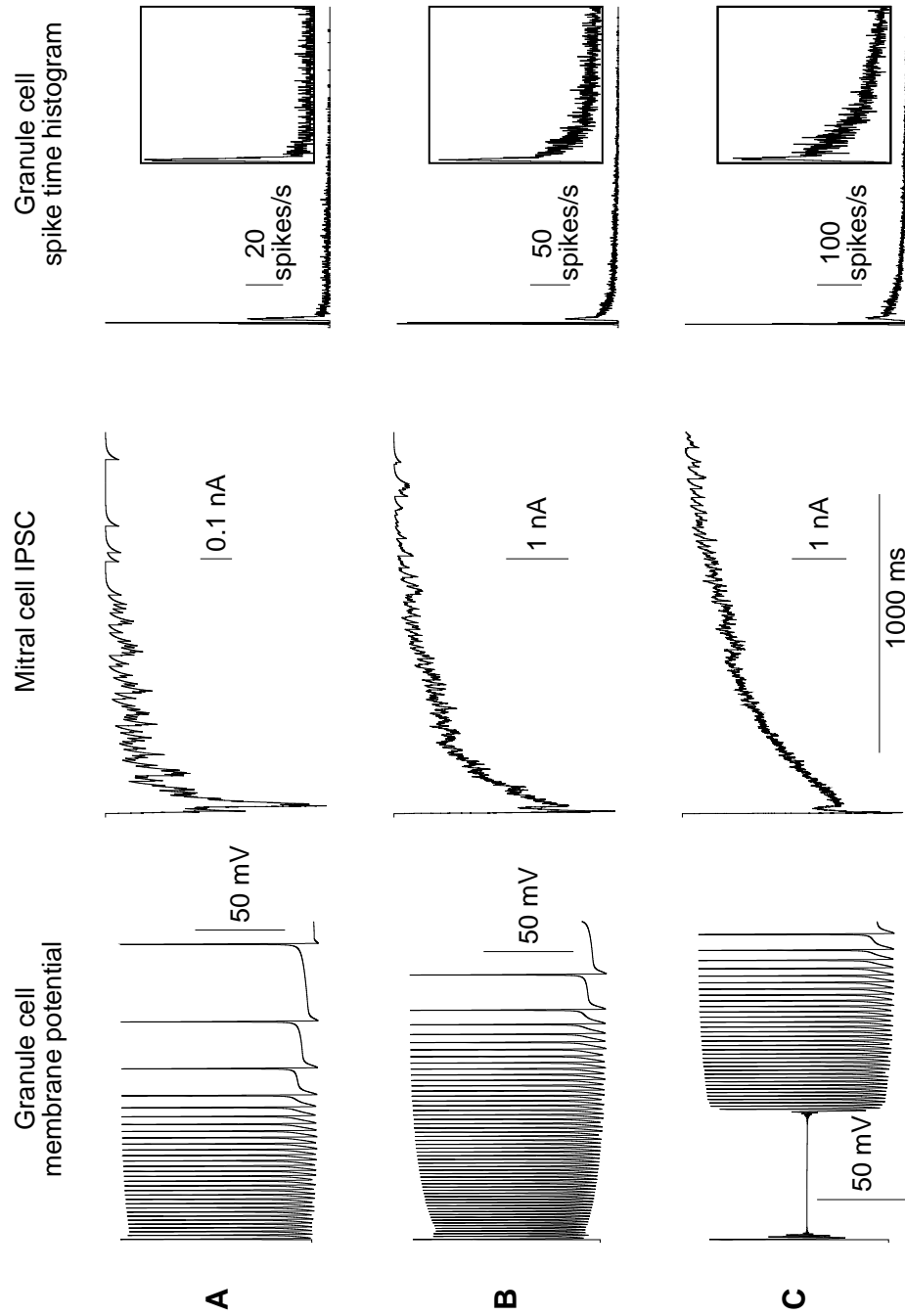


Figure 4.7: Effect on the response to glomerular stimulation of changing the number of synapses with a fixed number of granule cells. (A) $n_{syn} = 50$; (B) $n_{syn} = 200$; (C) $n_{syn} = 500$. Increasing n_{syn} increases the average number of synapses per granule cell, leading to faster and more prolonged granule cell firing. Note the extreme behaviour in (C) where the granule cell is initially driven so hard that it cannot sustain action potentials. The rate of decay of the granule cell response is decreased by increasing n_{syn} (see the spike time histograms). The insets show a more detailed view of the first 600 ms of the response), and this in turn leads to slower decay of the mitral cell IPSC. For (C) the chloride reversal potential was changed from 0 mV to -40 mV, reducing the driving force for the GABA_A current, in order to prevent space-clamp breakdown.

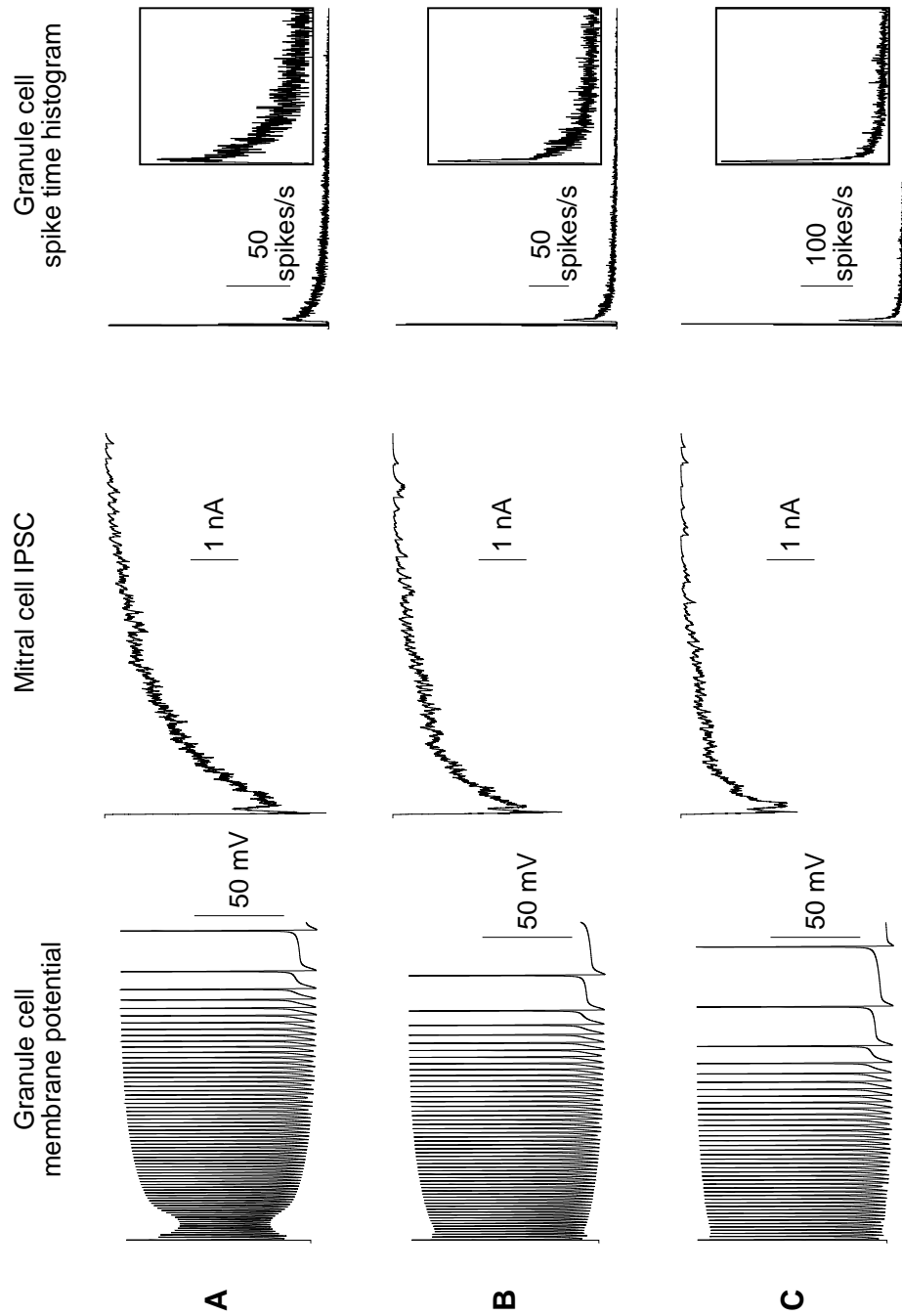


Figure 4.8: Effect on response to glomerular stimulation of changing the number of granule cells while keeping the number of synapses per mitral cell constant at 200. (A) $n_{\text{gran}} = 1225$; (B) $n_{\text{gran}} = 2500$; (C) $n_{\text{gran}} = 4900$.

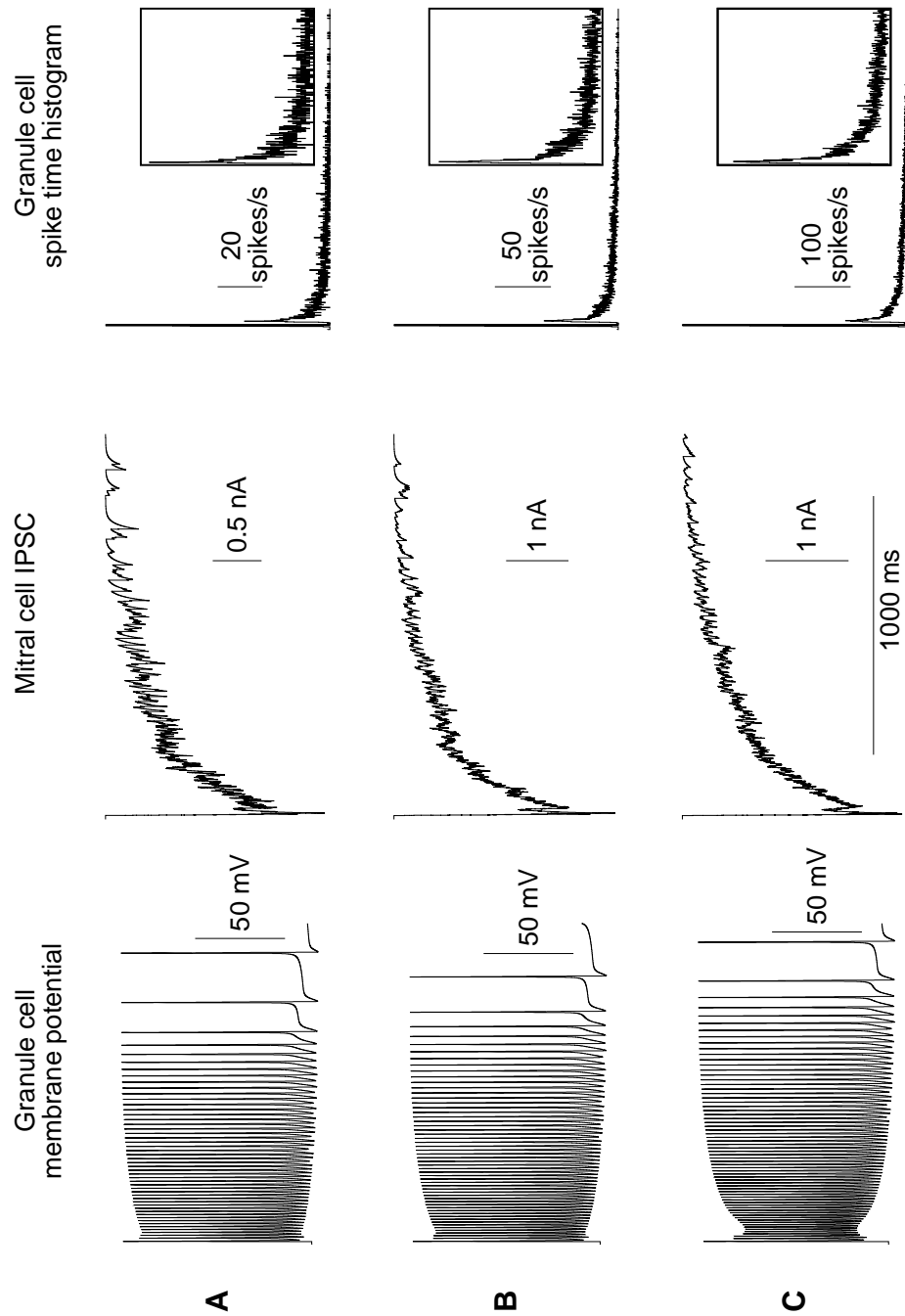


Figure 4.9: Effect on response to glomerular stimulation of changing the number of granule cells and the number of synapses per mitral cell to keep the average number of synapses per granule cell constant. (A) $n_{\text{gran}} = 1225$, $n_{\text{syn}} = 98$; (B) $n_{\text{gran}} = 2500$, $n_{\text{syn}} = 200$; (C) $n_{\text{gran}} = 4900$, $n_{\text{syn}} = 392$. When the number of granule cells is changed to compensate, the effect of increasing the number of synapses is less pronounced than when the number of granule cells is fixed (*cf* Figure 4.7). The decay rate of the population response is approximately constant, only the amplitude of the response is changed. For (C) the chloride reversal potential was changed from 0 mV to -40 mV, reducing the driving force for the GABA_A current, in order to prevent space-clamp breakdown.

of synapses per granule cell, since increasing the number of granule cells proportional to the number of synapses considerably reduces the effect. An interesting aspect of Schoppa *et al*'s results is that the decay time constant of the IPSC is longer than that of the NMDA conductance. I had speculated that this was due to the presence of some long time-constant calcium-dependent process in the granule cell or to recurrent excitation of the mitral cell secondary dendrite. For most of the simulations, the IPSC was shorter than the NMDA current. However, in the simulations with a higher number of synapses per granule cell, the IPSC was longer than the NMDA current, showing that the intrinsic membrane properties of the granule cell model are sufficient to produce this effect.

How realistic is the network model? The models of the individual cells are based on experimental data (see Chapter 2); the ratio of granule:mitral cells is biologically realistic [133]; the synaptic time constants and maximum conductances were derived from experimental data (§4.2.2). The principal difference between the model and the real bulb is in the connectivity of the network. The available computational power limited the number of cells to about 5000 and the total number of synapses to about 12000. In the model, 200 synapses per mitral cell was found to produce a similar response to the experimental recordings. In contrast, a real mitral cell makes about 17000 dendrodendritic synapses (see §4.2.3.1). In the simulations I found that a granule cell receiving only a single synaptic input from a mitral cell will not usually fire an action potential, and so some of the 17000 synapses will not receive reciprocal inhibition. Also, in general, synapses have a small probability of being activated by any given pre-synaptic action potential, whereas the synapses in the model are always activated. Both these factors will tend to reduce the number of functional synapses in a mitral cell, but there still seems to be a discrepancy between model and experiment which it would be worthwhile to investigate further in future.

The representation of synaptic transmission used in this model is very simple: a pre-synaptic spike triggers a post-synaptic conductance. However, several studies have demonstrated that dendrodendritic inhibition can be induced in the presence of sodium-channel blocker TTX [63, 125], which suggests that granule cell action potentials are not necessary for GABA release. More detailed studies of GABA release from granule cells show that GABA release is evoked by calcium influx through both voltage-dependent calcium channels (VDCCs) and NMDA channels [26, 49]. Simple spike-triggering is an approximation of the VDCC-dependent mechanism, since the channels will be most strongly activated during spikes. In contrast, granule cell spikes will reduce the calcium influx through NMDA channels by reducing the driving force for calcium entry. The location of dendrodendritic synapses on granule cell spines reduces the need for action potentials for reciprocal inhibition, since larger depolarisations can be generated within spines than on dendritic shafts; however, action potentials may still be needed for lateral inhibition.

The simple spike-triggering model reproduces many of the features of dendrodendritic inhibition, including the amplitude and time-course of the mitral cell IPSC, and the effects of AMPA- and NMDA-receptor blockers on the IPSC. Recordings of spike-trains from granule cells during glomerular shock stimulation would help to test the adequacy of the current model, since some granule cells in the model fire at high rates (peak instantaneous firing rate up to 90 Hz). Future elaborations of the current model, incorporating granule cell spines and calcium-dependent transmitter release, would help to elucidate the effects of calcium-entry through NMDA receptors and suggest a computational role for this arrangement.

A number of predictions can be made based on this study. First, only a small proportion of synapses on mitral cell secondary dendrites are activated by any given action potential. This could be tested by measuring vesicle release probability and channel opening probabilities at these synapses. Second, changing the number of active reciprocal synapses or the number of granule cells has predictable effects on the mitral cell IPSC and on the granule cell population response (see Table 4.2). Testing this set of predictions would be challenging, due to the difficulty of manipulating the relevant parameters and measuring the relevant quantities in experimental preparations as opposed to a computer model. To change n_{syn} it may be possible to use low concentrations of GABA and glutamate channel blockers, which would block some but not all synapses. To change the number of granule cells the thickness of the slice in an olfactory bulb slice preparation could be varied, or the deep part of the granule cell layer could be surgically removed in a slice. A measurement of the granule cell population activity could perhaps be performed by multi-electrode extracellular recording in the granule cell layer.

In general, these results indicate that the measurement of synaptic conductances which are dependent on the activity and topography of the network, such as performed by Schoppa *et al* [125], is a powerful

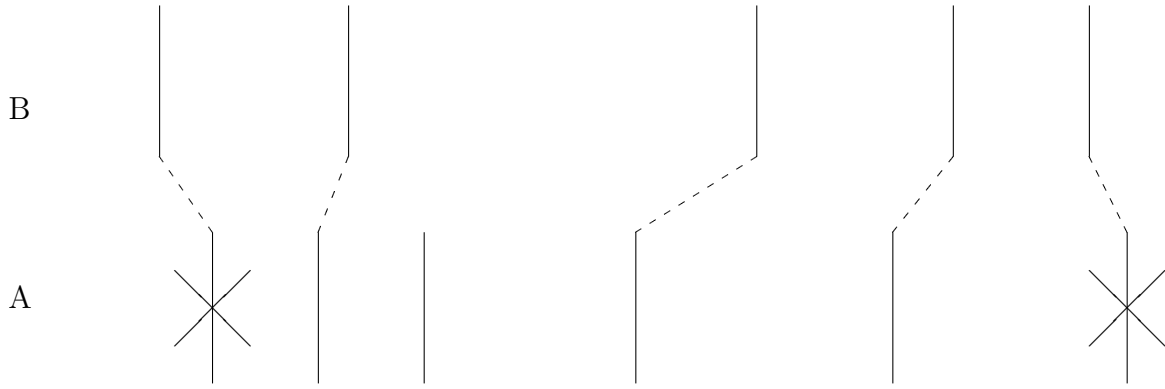


Figure 4.10: Determination of time lags. For each spike time t_i^A in cell A , find the closest spike time t_j^B in cell B , provided that spike is within half the inter-spike interval (e.g. the third spike in cell A has no time lag as there is no spike that is closer to it than to its neighbours). Then the time lag, $\ell_i^{AB} = t_j^B - t_i^A$. The first and last spike times for cell A are discarded, since the inter-spike interval is not defined before the first spike or after the last spike.

way of testing network models.

4.5 Response to odour stimulation

4.5.1 Introduction and Methods

The aim of this experiment was to simulate the bulb network model with an ‘odour-like’ input, in order to answer the following questions: will the large network exhibit synchronization of mitral cell firing, as did the two-mitral cell network studied in Chapter 3? How are differences in odour intensity represented? How will the behaviour scale to larger networks?

Many figures in this section show smoothed spike-time histograms. These are generated by summing Gaussian curves of area 1 centered on each spike time of each cell. This has the advantage over a normal histogram of not imposing arbitrary bins. The variance of the Gaussian functions was set to 1/4 of the mean ISI of the fastest firing cell.

Perfect or near-perfect synchrony can easily be recognised in the spike time raster plots of the cell population. Phase-locking and partial synchronization are much more difficult to discern. Therefore, a numerical index is necessary to identify and quantify synchronization and phase-locking.

I use two indices, one of which is sensitive to synchronization (phase-locking with zero phase difference), the other to phase-locking in general. Both are based on statistics of the phase-lag between spikes in different cells. The phase-lags are calculated as follows: for each mitral cell k ($k = 1, \dots, n$) in the network, for each spike time t_i^k ($i = 2, \dots, N_k - 1$ where N_k is the number of spikes in cell k) of that cell except the first and last, we find the closest spike time t_j^l in every other cell l ($l = 1, \dots, n; l \neq k$), provided that spike is within half the inter-spike interval (see Figure 4.10). The time lag for spike time t_i^k with respect to cell l is then defined by $\ell_i^{kl} = t_j^l - t_i^k$. The phase lag ϕ_i^{kl} is defined by

$$\phi_i^{kl} = \begin{cases} \ell_i^{kl} / (t_i^k - t_{i-1}^k) & \ell_i^{kl} < 0 \\ 0 & \ell_i^{kl} = 0 \\ \ell_i^{kl} / (t_{i+1}^k - t_i^k) & \ell_i^{kl} > 0 \end{cases} \quad (4.13)$$

The synchronization index, σ_1 , is then defined by

$$\sigma_1 = \frac{1}{\sum_k \sum_l N'_{kl}} \sum_{k=1}^n \sum_{\substack{l=1 \\ l \neq k}}^n |\phi_i^{kl}| \quad (4.14)$$

where N'_{kl} is the number of time lags for cell k with respect to cell l . N'_{kl} will be less than the number of spikes N_k since the phase-lag is not defined for the first and last spikes of a cell and some spikes in cell k may not have a spike in cell l within half the inter-spike interval.

The phase-locking index, σ_2 , is defined by

$$\sigma_2 = \left(\frac{1}{n(n-1)} \sum_{k=1}^n \sum_{\substack{l=1 \\ l \neq k}}^n \text{Var}(\phi_i^{kl}) \right)^{\frac{1}{2}} \quad (4.15)$$

where $\text{Var}(\phi_i^{kl})$ is the variance of the phase lags ϕ_i^{kl} of cell k with respect to cell l .

To thoroughly investigate such a complex model as that described here is a very large project. Therefore I have carried out a few preliminary experiments which address some questions of interest. The first two experiments examine the effects of odour intensity (§4.5.2.1) and of connectivity parameters (§4.5.2.2) on the network response in terms of spatial patterns of firing rates and of spike synchronization/phase-locking. The third experiment (§4.5.2.3) begins to address the question of how the network might improve the ability of the olfactory system to discriminate similar odorants. Except where noted, the network size was 6×6 mitral cells and 72×72 granule cells. The range of synaptic connections was $1/2$ the size of the granule cell array. The specific details of each experiment are given in the relevant section of the Results.

4.5.2 Results

The response of the network model to a simulated odour stimulus which activates all glomeruli is shown in Figure 4.11. For the first 1000 ms the mitral cells received weak, ‘background’ stimulation which did not cause those mitral cells that are activated to synchronize their firing, although there is some evidence of synchronization in the granule cell raster plot (Figure 4.11C), which is not surprising due to the large ‘fan-out’ from mitral to granule cells. Once the odour stimulus is added, both mitral and granule cells rapidly synchronize their firing. Due to the synchronization of firing, mitral cell firing rates appear to be quantized, with most cells firing at the population response oscillation frequency of about 15 Hz or at some rational fraction of the population frequency. Because of this the variability in output firing rates is less than the variability in input currents. However, the differences in output between neighbouring cells can be much greater than the differences in input. The fastest-firing granule cells fire at the same rate as the fastest mitral cells but the majority of granule cells fire at lower rates.

4.5.2.1 Effect of odour intensity

Odorants are presented to olfactory systems with a wide range of intensities, yet the identity of the odorant is recognised almost independent of intensity. In imaging studies, the number of activated glomeruli increases as the stimulus intensity is increased [44, 45, 65] and individual ORNs and mitral cells fire faster. How then is the constancy of identity achieved by the olfactory system?

Two versions of the model were simulated with the same odour input but at different intensities, i.e. the input currents to different mitral cells were in the same ratio but the absolute magnitudes of the currents were changed. In one version there were no connections between mitral cells ($n_{\text{syn}} = 0$); in the other, $n_{\text{syn}} = 500$.

The results are shown in Figure 4.12 (mitral cell raster plots and mean firing rates) and Figure 4.13 (smoothed spike-time histograms). As the global input intensity is raised, for the same ‘odour’ at different ‘concentrations’, the number of activated mitral cells is increased, and the firing rate of activated mitral

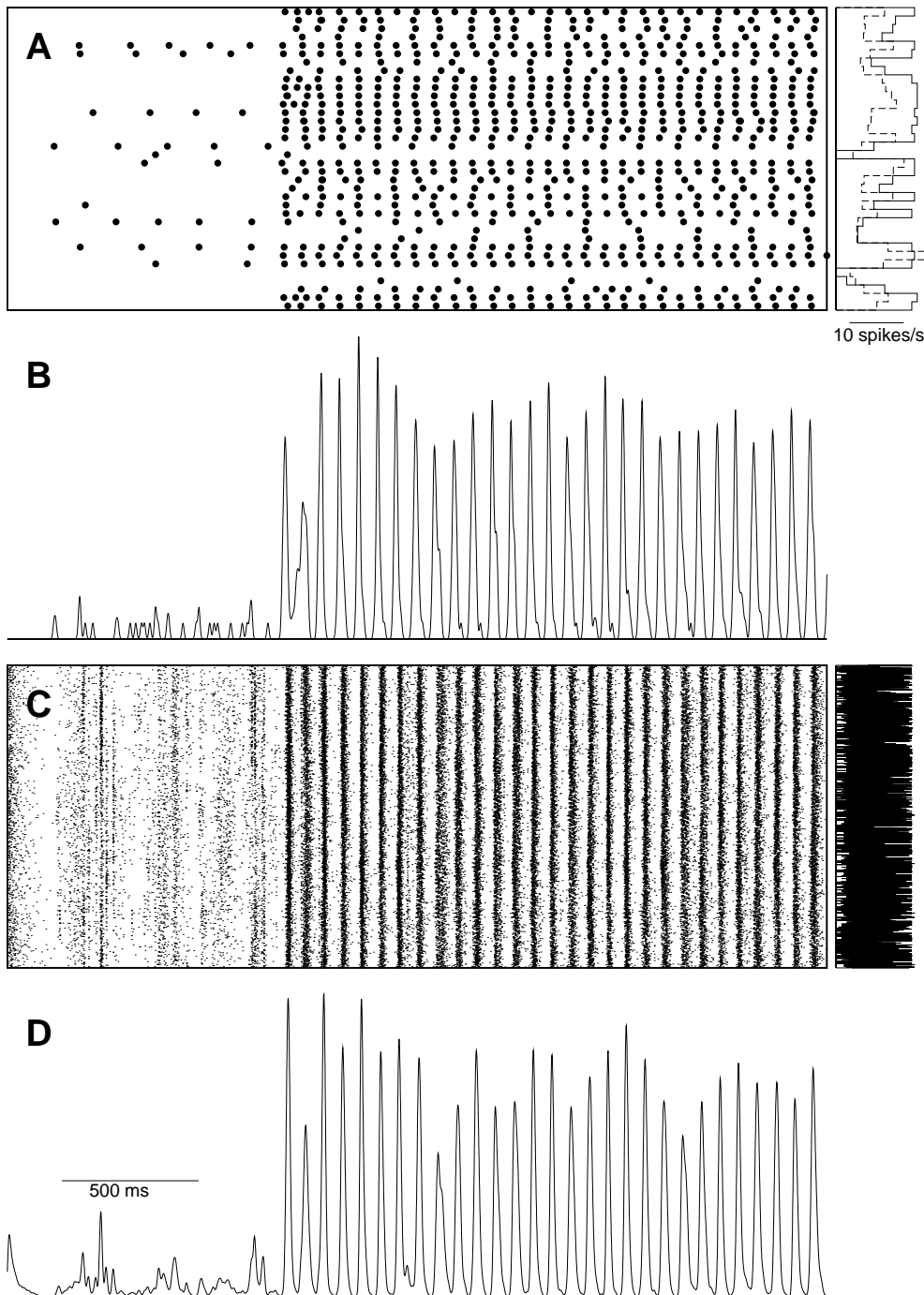


Figure 4.11: Response of the mitral-granule network to a simulated odour stimulus. (A) Mitral cell raster plot and bar graph showing input currents (dashed line) and output firing rates (solid line). In the raster plot each dot represents a spike and each row of dots is a different cell. The two-dimensional structure of the network cannot be represented in this plot: the network is laid out row by row into a one dimensional array. Therefore neighbouring lines in the plot do not necessarily represent neighbouring cells in the array. (B) Mitral cell population smoothed spike time histogram. (C) Granule cell raster plot and bar graph showing output firing rates. (D) Granule cell population smoothed spike time histogram. Initially the network received weak, ‘background’ stimulation. At time 1000 ms the strong odour stimulus is added. The odour is one that activates all glomeruli. Both mitral and granule cells rapidly synchronize their firing at a rate of about 15 Hz.

$n_{\text{gran}}:n_{\text{mit}}$	n_{syn}	$\bar{g}_{\text{GABA}_A} / \text{nS}$
4	14	21.6
9	31	9.60
25	87	3.46
49	170	1.76
100	347	0.864
169	587	0.511

Table 4.3: Parameters used to assess effect of number of granule cells on network synchronization

cells is increased, although this saturates at high input levels. Compared to the no-connections case, firing rates are lower with mitral–granule connections, and the responses saturate at lower levels. Synchronization of the responses is apparent in the raster plots and in the smoothed spike-time histograms for maximum input levels of 0.8–1.0 nA and upwards.

The graph of synchronization and phase-locking indices against maximum input confirms this: the indices begin to depart significantly from the no-connections baseline between 0.8 and 1.0 nA (Figure 4.14).

To determine whether there is a significant difference at 0.8 nA, each model was simulated six times with different seeds for the random number generator, giving $\sigma_1 = 0.2126 \pm 0.0007$ and $\sigma_2 = 0.1250 \pm 0.0002$ (mean \pm standard error, $n=6$) with no connections, $\sigma_1 = 0.2128 \pm 0.0018$ and $\sigma_2 = 0.1240 \pm 0.0005$ with connections. For each index, an F-test was carried out to determine whether the no-connections distribution had the same variance as the with-connections distribution. For the synchronization index σ_1 , $P = 0.03$; for the phase-locking index σ_2 , $P = 0.01$. Therefore for both indices the distributions have unequal variances. This was expected because the only source of variability in the no-connections network is different inputs, whereas the with-connections network also has variability from different connections. I next carried out a one-tailed t-test assuming unequal variances: for σ_1 , $P = 0.47$; for σ_2 , $P = 0.06$. Therefore the differences in the phase-locking and synchronization indices between the no-connections network and the with-connections network are not significant at the 5% level at 0.8 nA. All statistical tests were carried out in Gnumeric v0.54.

4.5.2.2 Effect of varying the ratio of granule:mitral cells

As discussed in §4.2.3.2, as the size of the network is changed, so are the network properties. Since it is not possible to simulate a full-sized network, I was interested in whether simulating networks of different sizes would reveal some trend which would allow extrapolation of results to large networks.

Therefore, I changed the number of granule cells in the network while adjusting n_{syn} and \bar{g}_{GABA_A} to keep the total input to granule and mitral cells approximately constant:

$$\text{synapses per granule cell (mean)} = \frac{n_{\text{mit}}}{n_{\text{gran}}} n_{\text{syn}} = 3.472 \quad (4.16)$$

$$\text{peak mitral cell inhibition} = n_{\text{syn}} \bar{g}_{\text{GABA}_A} = 0.3 \mu\text{S} \quad (4.17)$$

(see Table 4.3 for the parameter sets used).

This change in the number of granule cells appears to have no consistent effect on the firing rate (Figure 4.15A) or synchronisation/phase-locking indices (Figure 4.15B) of the mitral cells.

4.5.2.3 Responses to similar odorants

One possible function of the olfactory bulb is to increase the difference between the representations of two similar odours in order to make it easier to discriminate between them. I conducted a preliminary, limited investigation to test whether the current network could carry out this function for two arbitrarily chosen inputs. More extensive studies will be needed to determine the generality of these results.

In this experiment I stimulated the network with the following two odour vectors:

Odour A (0.0, 0.0, 0.0, 1.0, 0.0, 0.4, 0.2, 0.0, 0.0, 0.0)

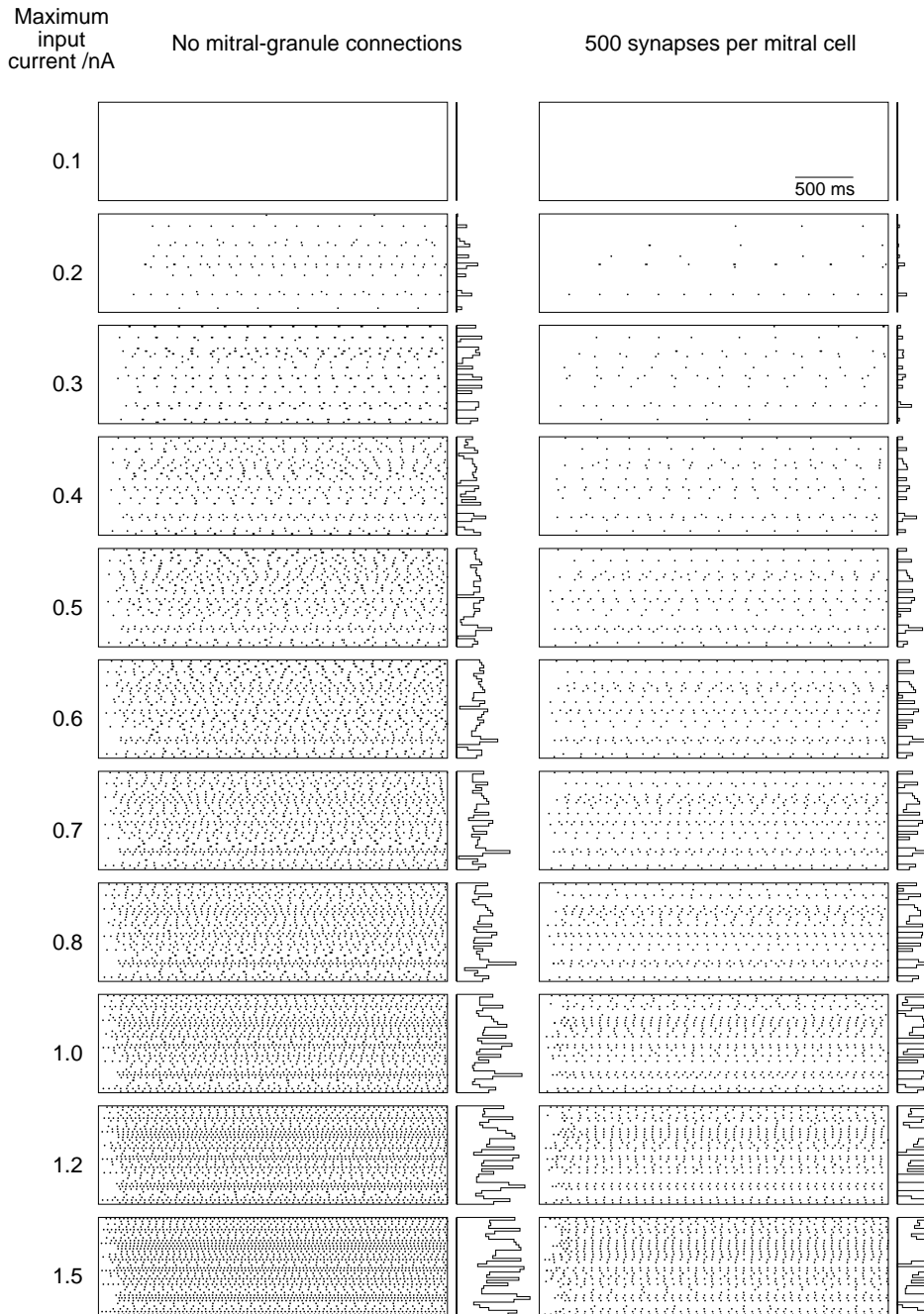


Figure 4.12: The effect of input intensity on mitral cell response. Mitral cell raster plots with no mitral–granule connections and with 500 synapses per mitral cell, for different values of maximum current (leftmost column, units nA; see text for more detail). The bar graphs next to each raster plot show the number of spikes in each line of the raster in the final 2000 ms of the simulation.

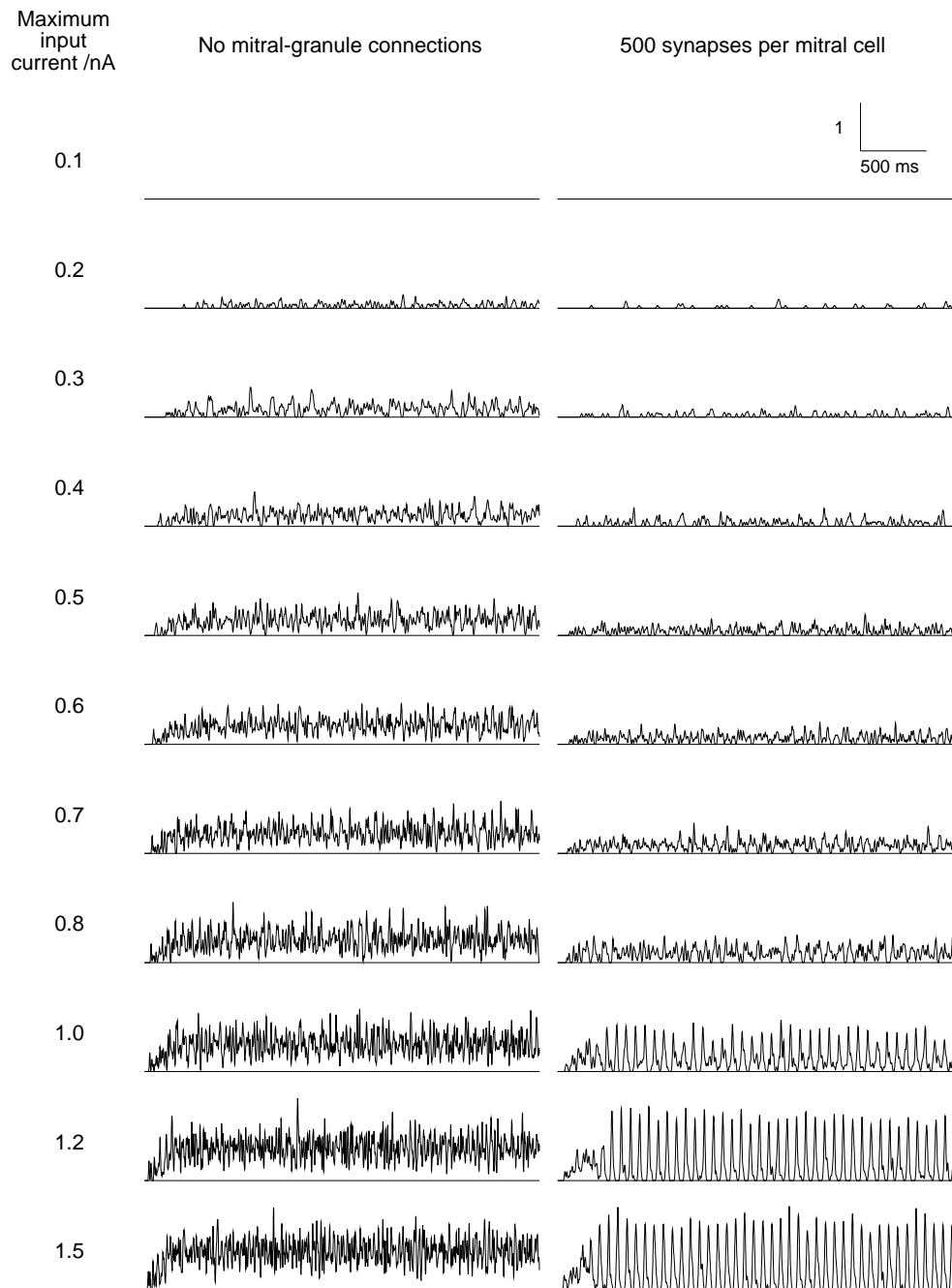


Figure 4.13: Effect of input intensity on mitral cell response – smoothed spike time histograms for the raster plots shown in Figure 4.12.

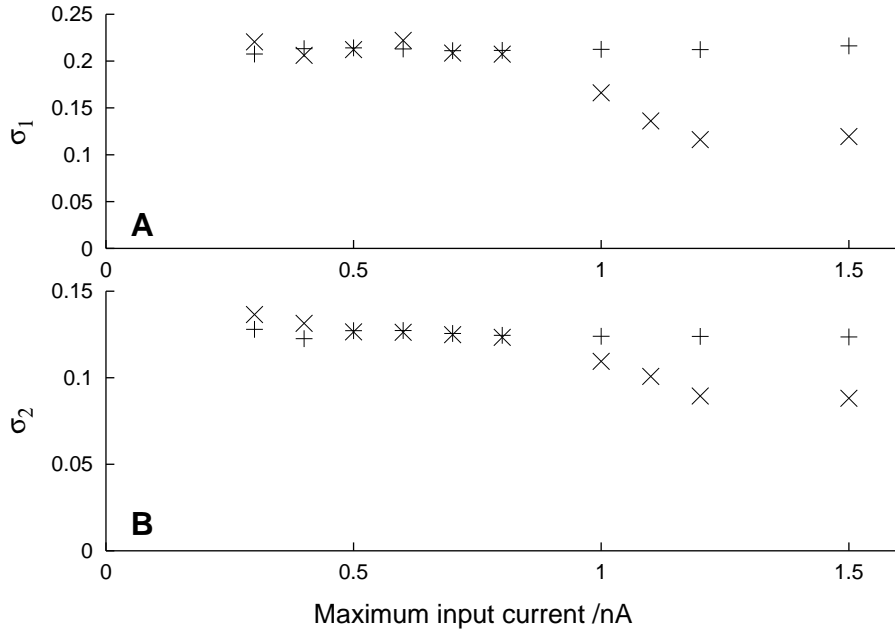


Figure 4.14: Effect of input intensity on (A) phase-locking index and (B) synchronization index. \times no connections; $+$ 500 synapses per mitral cell.

Odour *B* (0.0, 0.0, 0.1, 0.9, 0.0, 0.5, 0.1, 0.0, 0.0, 0.0)

The vectors were chosen to have small differences in a few of the elements. This represents my definition of ‘similar’ for the purposes of this experiment. To generate the input vectors from the odour vectors I used two versions of the odour transformation matrix \mathbf{A} (see §4.2.4.1 for definitions), one generated from a Gaussian distribution with mean 0.0 and variance 0.5 (the *dense mapping*), the other from a uniform distribution over the range (-3,1) (the *sparse mapping*). The main difference is that the sparse mapping leads to more not-activated and weakly-activated inputs than does the dense mapping.

For these experiments a larger mitral cell array was used than in the previous experiments (8×8 instead of 6×6) in order to more clearly resolve spatial effects.

Figure 4.16 shows the input vectors and output firing rate vectors for Odours *A* and *B*, with the dense mapping, under three different experimental conditions. Each pair of vectors is normalised by the maximum element from both vectors, to have elements between 0 and 1. To quantify the difference between the (normalised) vector for Odour *A*, \mathbf{y}^A , and the vector for Odour *B*, \mathbf{y}^B , we calculate

$$\Delta = \frac{1}{n} \sum_{k=1}^n |y_k^A - y_k^B| \quad (4.18)$$

where y_k^A is the k th element of \mathbf{y}^A , etc. For the input vectors, $\Delta = 0.024$. For the output vectors, $\Delta = 0.038$ (Figure 4.16B), $\Delta = 0.050$ (Figure 4.16C) and $\Delta = 0.008$ (Figure 4.16D). Except in the low-current case, for which Δ is skewed by the large number of inactive cells, the difference between the output vectors is greater than between the input vectors, which would presumably make it easier to discriminate between the outputs than between the inputs. The larger values of Δ in the outputs compared to the inputs are due to a small number of cells with very large differences in output firing rate.

Similar results are seen with the sparse mapping (Figure 4.17). Here, for the input vectors, $\Delta = 0.026$. For the output vectors, $\Delta = 0.031$ (Figure 4.17B) and $\Delta = 0.034$ (Figure 4.17C).

The changes in Δ do not appear to be related to the degree of synchronization, which is very different for the different mappings and different parameter sets (Figure 4.18). However, temporal factors could

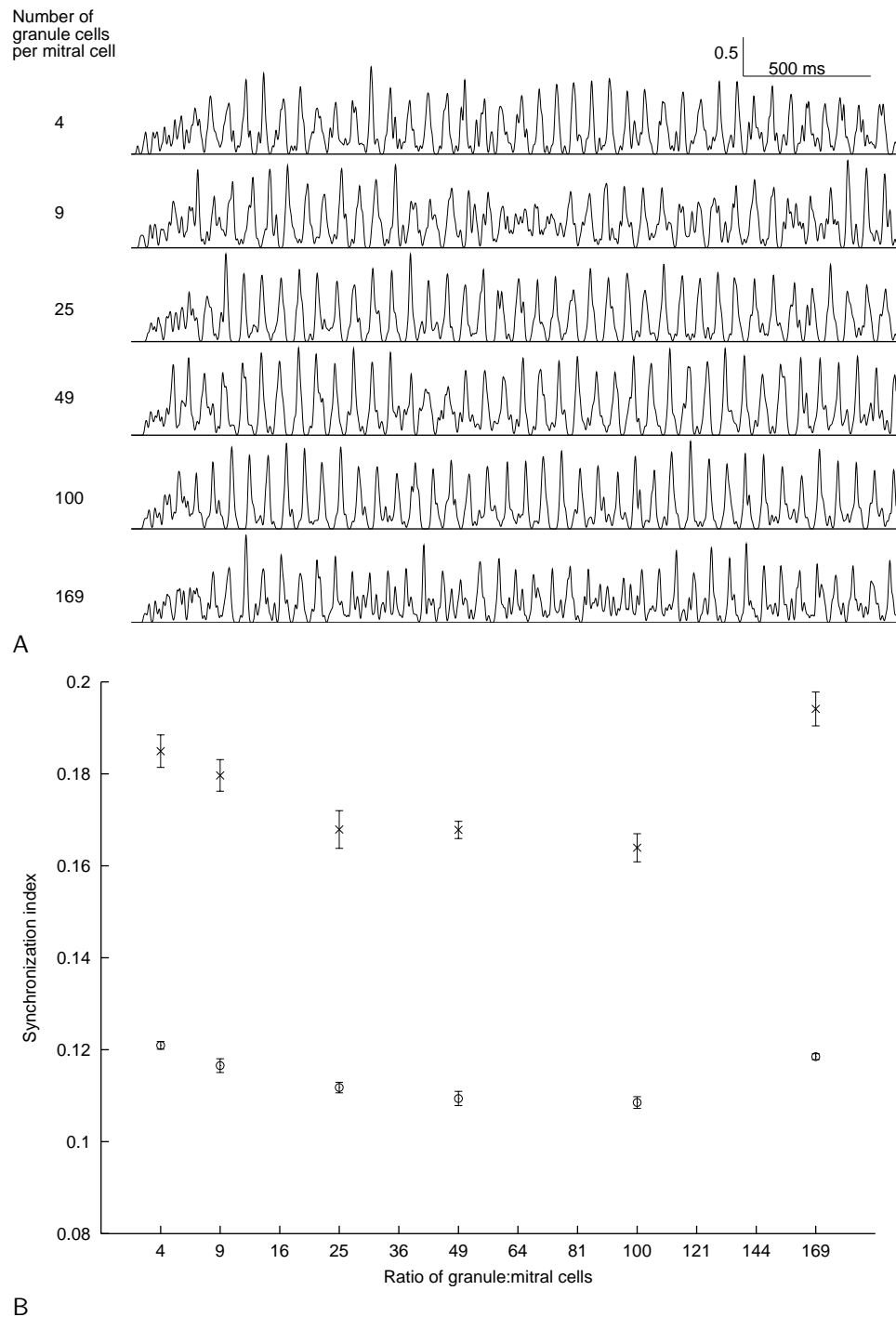


Figure 4.15: Effect on synchronization of changing the ratio of granule:mitral cells. (A) Smoothed mitral cell spike histograms with different numbers of granule cells. (B) Synchronization (\times) and phase-locking (\circ) indices as a function of the number of granule cells (error bars show standard error of the mean, $n=6$).

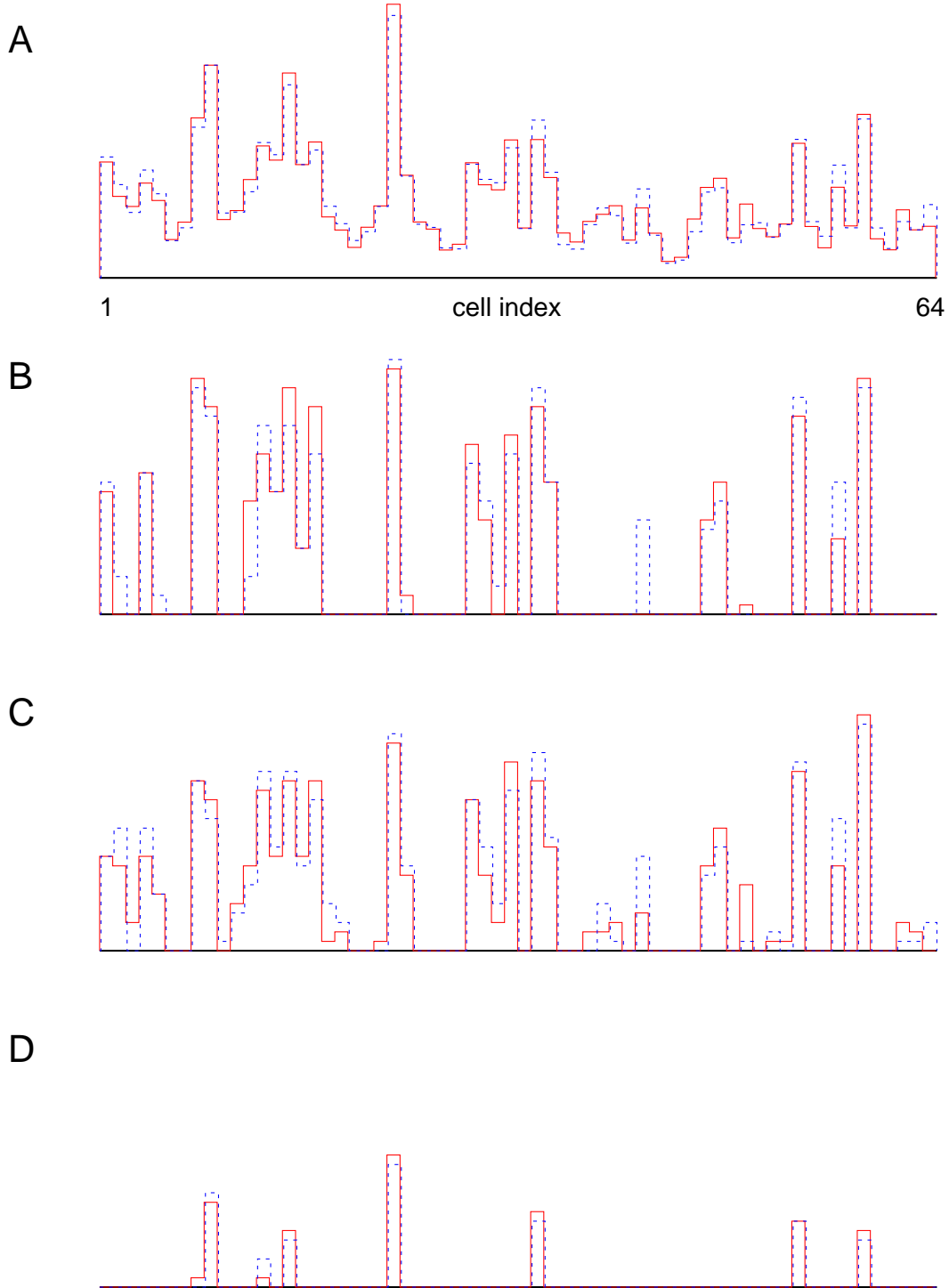


Figure 4.16: Comparison of inputs and outputs for two similar odours, with a dense odour mapping. In each graph, the solid red line is Odour A, the dashed blue line is Odour B. (A) Input currents. (B) Output firing rates with connection range one-quarter the size of the cell array. (C) Output firing rates with connection range one-tenth the size of the cell array. (D) Output firing rates with input currents one-third of those in (B) and (C), connection range one-quarter the size of the cell array.

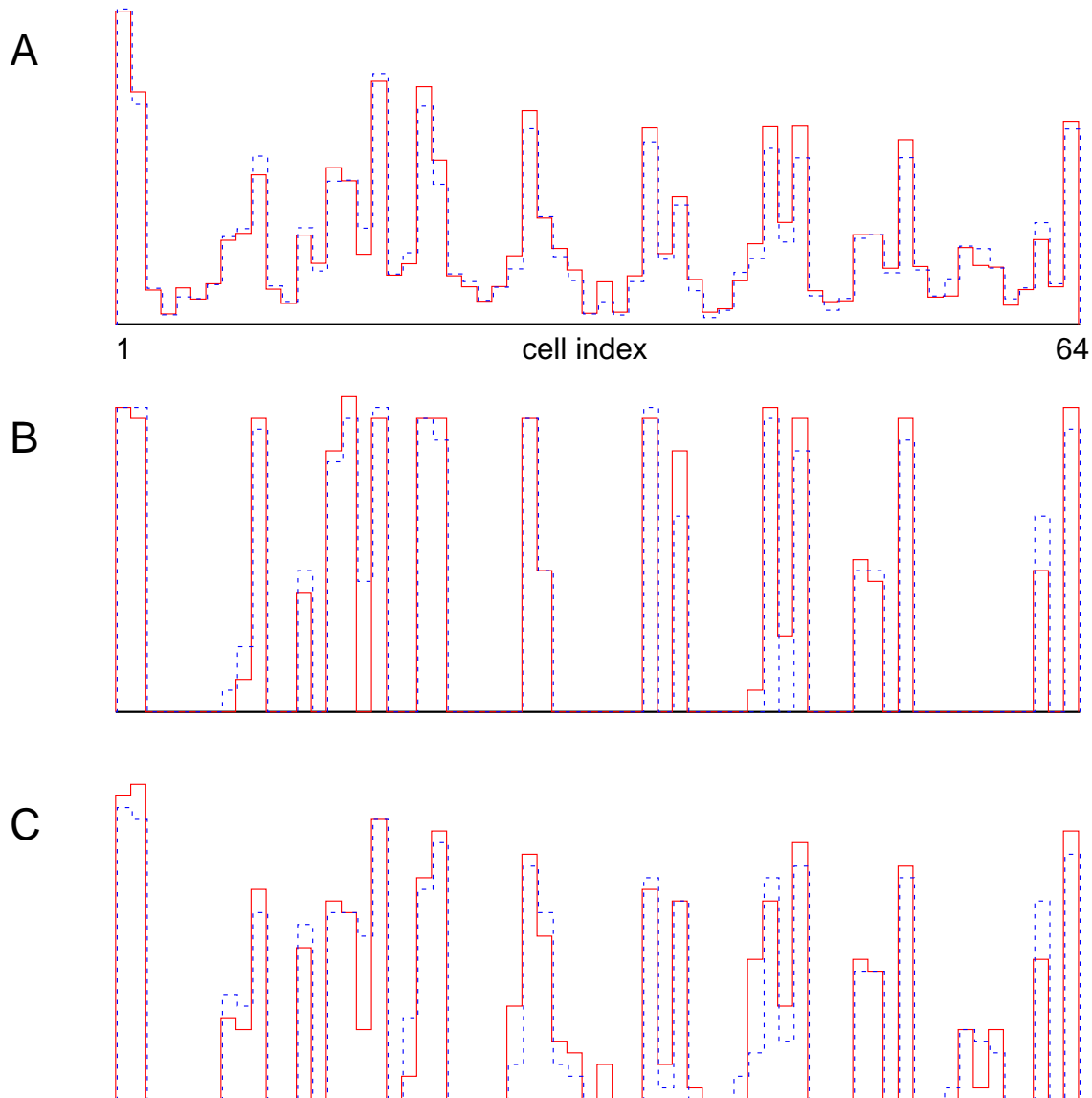


Figure 4.17: Comparison of inputs and outputs for two similar odours, with a sparse odour mapping. In each graph, the solid red line is Odour A, the dashed blue line is Odour B. (A) Input currents. (B) Output firing rates with connection range one-quarter the size of the cell array. (C) Output firing rates with connection range one-tenth the size of the cell array.

be used to discriminate between similar odours. Figure 4.19 shows granule cell raster plots and smoothed spike-time histograms for stimulation with the two similar odours. With Odour *B*, there are two distinct phases of global oscillation interspersed with a period of asynchrony, whereas with Odour *A*, global oscillation develops more slowly but persists. These features (together with the differences in time-averaged firing rates) could theoretically be used to discriminate between the odours.

4.5.3 Discussion

Global synchronization of mitral and granule cell firing was seen in Figure 4.11 ('synchronization' is an approximate term, since slower-firing cells tend to fire with a small phase-lag compared to the fast-firing cells). Does this predict that synchronization should be easily found in experimental olfactory bulb preparations? An important difference is that the current model has many fewer cells than the real olfactory bulb, and hence the connectivity is higher in the model. High connectivity means that distant cells communicate easily and so synchronization is more likely to occur.

The 'connection fraction' (CF) and 'mutual connection fraction' (MCF) were defined in §4.2.3.1. It is possible to estimate these metrics for the rabbit olfactory bulb. The surface area of the mitral cell layer in rabbit is about 20 mm^2 [119]. The volume of the entire bulb is 87.7 mm^3 [121], giving a surface area of 95.5 mm^2 if we assume spherical geometry. Mitral cell dendrites ramify in the external plexiform layer, the surface area of which must be between the above values. Since the mitral cell dendrites tend to ramify in the deep portion of the EPL, the effective surface area for connections will be nearer to the smaller value. 30 mm^2 would seem a reasonable value.

The radius of the mitral cell secondary dendrite arbour in rabbit is $850 \mu\text{m}$, giving a field area of approximately 2.3 mm^2 . Therefore

$$\frac{\text{area of dendrite arbour}}{\text{effective surface area of EPL}} = \frac{2.3}{30} = 0.08 \quad (4.19)$$

i.e. one cell covers approximately $\frac{1}{13}$ th of the EPL 'surface area'. This same area contains the dendrites of approximately $0.08 \times (5 \times 10^6) = 4 \times 10^5$ granule cells.

The number of synapses formed by one mitral cell was earlier calculated to be approximately 17000. Therefore, assuming each mitral cell never forms more than one synapse with any granule cell, $\text{CF} = 17000/400000 = 0.043$, i.e. a mitral cell contacts about 4% of the granule cells within its arbour.

A simple estimate of the number of granule cells having connections to both members of any given pair of neighbouring mitral cells is then $0.043 \times 0.043 \times 4 \times 10^5 \simeq 720$, assuming that the distance between the cells is much smaller than the radius of the arbour. This gives $\text{MCF} = 720/17000 \simeq 4\%$, and corresponds to copious branching ($p(r) = \text{constant}$). This is a lower limit since $p(r)$ is likely to fall with distance from the soma, so nearby mitral cells will have a higher proportion of common contacts.

So we have a lower limit of 4% for the mutual connection fraction in the rabbit olfactory bulb, and a value of 4% for the connection fraction. In the network model, for the experiments varying odour intensity and the ratio $n_{\text{gran}}:n_{\text{mit}}$, $\text{CF} = 0.12$ and $\text{MCF} \geq 0.15$. In summary, the connectivity of the network is only about three times as high as in the real bulb. Since synchronization is robustly seen in the network, it should also be seen in the bulb, although perhaps less easily. As mentioned in the Introduction, synchronization was seen in about 25% of cell pairs recorded in the rabbit olfactory bulb *in vivo* [67]. Synchronization is less likely to be seen in the slice preparation, since much of the mitral cell secondary dendrite arbour is not preserved.

Increasing input intensity increases synchronization/phase-locking. This result can be understood by reference to the results of Chapter 3, where it was shown that $n:1$ phase-locking is promoted by strong inhibition of the mitral cells, which of course requires strong activation of the granule cells. Figure 3.23 shows that for small values of α , the drive to the most strongly activated cell, granule cells fire at low rates or not at all, inhibition of the mitral cells is therefore weak, and the regions of parameter space in which $n:1$ phase-locking is seen are very small. Only at high values of α are large regions of $n:1$ phase-locking seen. This effect should be seen in any neural system which has principal neurones mutually inhibiting one another via interneurones. It would be very interesting to search for this effect in the vertebrate

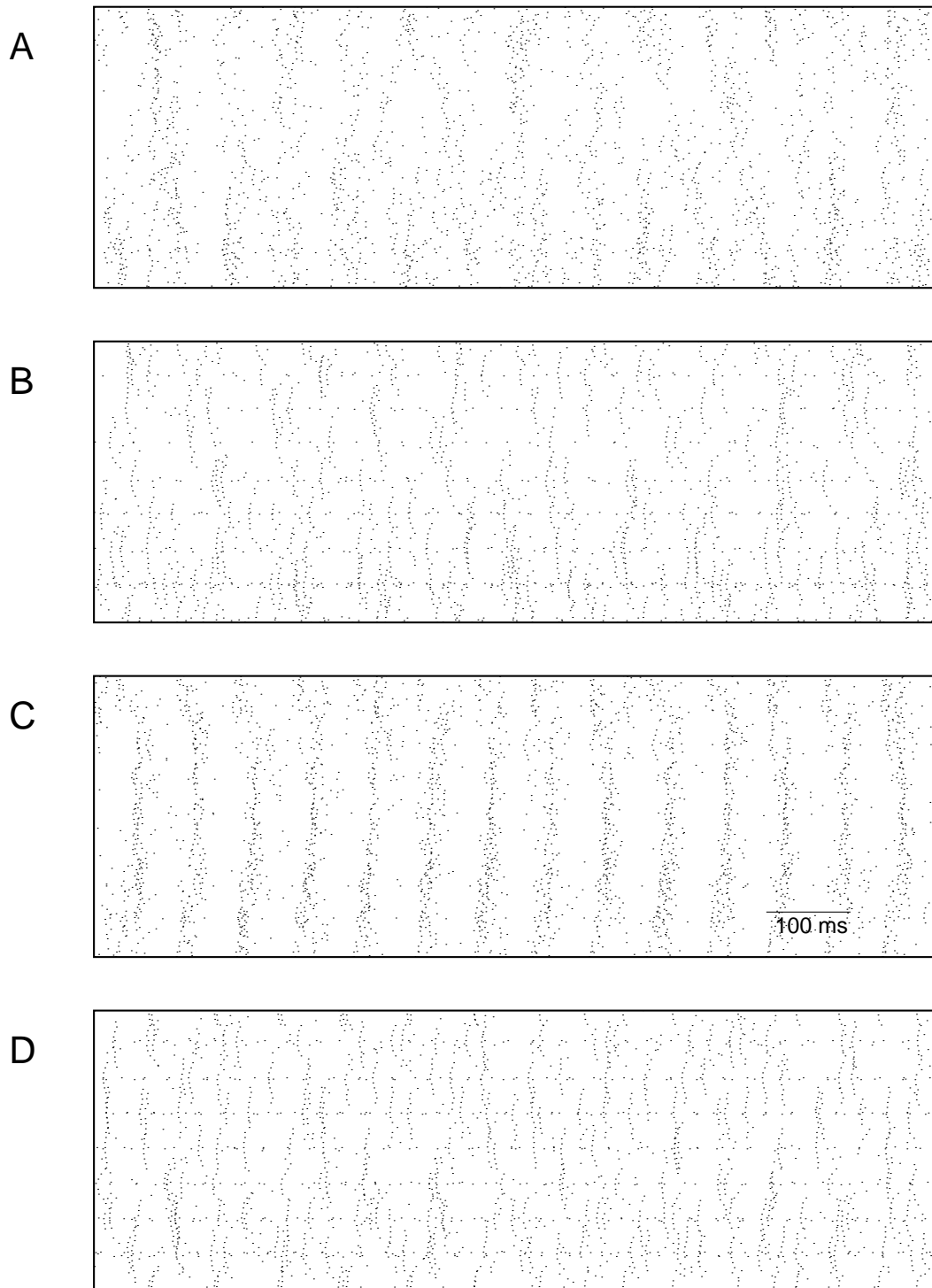


Figure 4.18: Granule cell raster plots for stimulation with Odour *A*, with different odour → input mappings and different connection ranges. (A) and (B) use the dense mapping (see text); (C) and (D) use the sparse mapping. For (A) and (C) the range of connections was one-quarter the size of the cell array; for (B) and (D) the range was one-tenth the size of the array. Good global synchronization occurs only in (C). Local synchronization can be seen in the other plots.

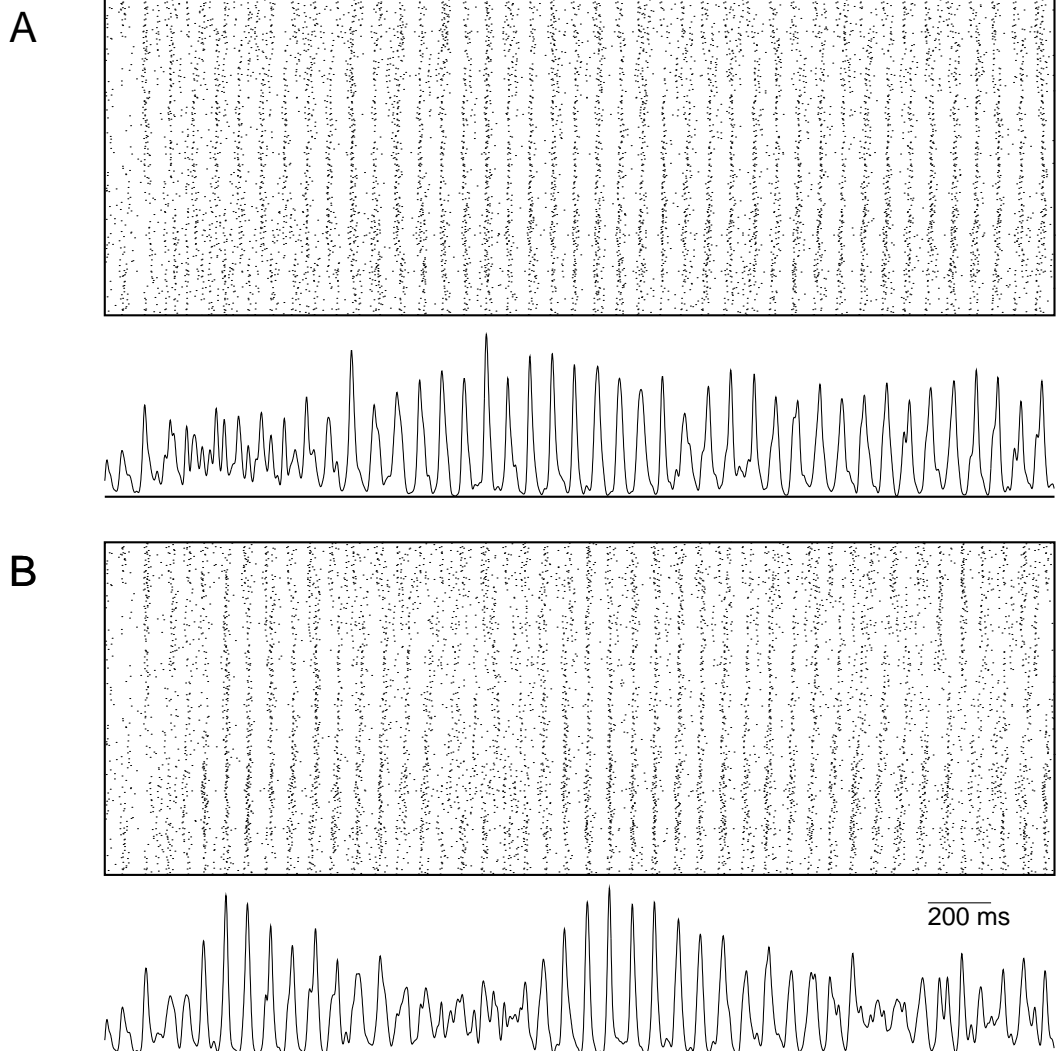


Figure 4.19: Granule cell raster plots and smoothed spike-time histograms for stimulation with (A) Odour A and (B) Odour B. The slow temporal changes in the power of the global oscillation are quite different in the two cases. The parameters are the same as for Figure 4.16B.

olfactory bulb or insect antennal lobe. A secondary prediction is that the firing rate of the granule cells should be comparable to or greater than that of the mitral/tufted cells when synchronization is seen.

A secondary effect of synchronization is that mitral cell firing rates become quantized, which is likely to reduce the effectiveness of using firing rates as part of the olfactory code. This suggests that the discriminatory ability of the olfactory system may be maximized at intermediate input intensities.

Over almost two orders of magnitude, the ratio of mitral:granule cells has no consistent effect on the firing rates or synchronization of the network provided other parameters are adjusted to maintain constant average input to the individual cells. This is very convenient for modelling, since if fewer granule cells need be simulated, more mitral cells can be added to the network.

The question of how the olfactory bulb processes its inputs, and how this might contribute to discrimination of different odours is a complex one, which will not be answered quickly. Here I have carried out some preliminary experiments which suggest that a bulb-like network can enhance the differences between the representations of similar inputs. However, the enhancement is not dramatic, and the question of how the cortex might use this enhancement is not addressed. These experiments do not address how the temporal structure of the response may be used in odour processing, but this model could now be used to examine hypotheses about this problem.

Chapter 5

Discussion and Conclusions

In this final chapter I discuss the behaviour of the olfactory bulb network model in relation to experimental recordings from the olfactory bulb, to other models of the bulb and to theories of olfactory bulb function. I then discuss the strengths and limitations of the model, and how the approximations made in developing the model may affect the validity of the results. Finally I lay out a program of future work, building upon the results of this dissertation, to further investigate the processing of sensory information in the olfactory bulb.

5.1 Comparison of the model with the real bulb

The model was compared closely to one particular set of experimental data [125], obtained from electrical stimulation of the glomerular layer. Very similar experimental results have been obtained independently [26, 63]. The agreement between simulation and experimental results was good, although with fewer synapses in the model than are calculated to exist in the real bulb. A number of predictions regarding the effect of network connectivity on the synaptic response were made, which may be experimentally testable (see §4.4.3).

In the response to inputs mimicking odour stimulation, the model behaviour showed much less temporal variation in firing rates than is seen experimentally [52, 53]. This may be due to the lack of noise in the model inputs and to the heterogeneity of synaptic strengths throughout the network. It could also reflect the lack of periglomerular cells in the model. The model clearly shows temporal oscillations in network activity and synchronization of spikes between different neurones, both of which are seen experimentally (see §1.1.3.4). The analysis in Chapter 3 demonstrated that synchronization and phase-locking should be seen in any similarly-connected network provided the input levels and synaptic strengths are sufficiently strong.

This model is more detailed and biologically realistic than any previously-published olfactory bulb network model. It is most comparable to the models of White *et al* [153] and of Linster [81, 82].

As mentioned in the Introduction, the intention of White *et al* [153] was ‘*to investigate whether available data are sufficient for formulating a simulated bulb circuit that can generate realistic mitral cell output.*’ This was also one of the intentions of the current study, but the available data and available computer power are both much greater now than then, and I have been able to go considerably beyond that study. In particular, White *et al* were limited to qualitative comparisons of mitral cell voltage traces, whereas I have been able to compare synaptic currents as well as voltage traces, which gives a stronger constraint on the configuration of the network. I have also used my model to begin to address questions about olfactory bulb ensemble behaviour, such as properties of stimulus-evoked synchronization.

The models of Linster and her collaborators [81, 82] are more schematic than either White *et al*’s model or the model presented here, but they are used to address the role of lateral inhibition in tuning the odour response. In the model of Linster and Gervais [81] the OB network acts to reduce the overlap between the representations of different odorants. This is similar to my finding in §4.5.2.3. I have not

fully explored the range of parameters within which this tuning occurs for my model, but it would be interesting in future to compare my results in more detail with those of Linster, and to attempt to tune the parameters of Linster's simple model to reproduce the behaviour of my detailed model.

Other abstract models to which my detailed model could be linked are the associative memory models of Hendin, Horn and Tsodyks [56] and Hoshino, Kashimori and Kambara [60]. This would first require a physiologically-realistic implementation of synaptic plasticity in my model, however.

The results presented here are consistent with most of the hypotheses about olfactory bulb function discussed in the Introduction (§1.1.4). Regarding the first hypothesis, the model does appear to reduce the overlap between representations of similar odorants, although further work on this is required. Regarding the second hypothesis, the bulb circuitry does introduce temporal correlations, in the form of phase-locking, between signals from different receptors. Whether these correlations are computationally useful remains to be demonstrated. Regarding the third hypothesis, the bulb appears to be able to encode information about stimulus strength in the degree of synchronization, which may allow this information to be separated from information about stimulus identity. The remaining hypotheses, regarding associative memories and the transformation of odour space, require different synaptic weights at different synapses and so are beyond the scope of the current work.

5.2 Validity of the model

5.2.1 Validity of detailed single-cell models

In Chapter 2 I developed simple biophysical, compartmental models of the olfactory mitral and granule cells based on the morphologically-detailed models published by Bhalla and Bower [11]. These simplified models were used as the basis of further studies. It is important to ask how valid the original models are as representations of real cells.

5.2.1.1 Morphology

The sizes of mitral, tufted and granule cells vary between species and within an individual olfactory bulb, but the general shape is constant within mammals, and presumably the cells fulfill the same or a very similar function in different species. The models of Bhalla and Bower [11] use ‘average’ morphologies based primarily upon data from rabbit, but also mouse and rat [47, 94, 113, 114]. It would be interesting to investigate the effect of heterogeneity in cell morphology on the responses of the single cells and of the network. In particular, the model could be easily extended to include both mitral and tufted cells and all three types of granule cell.

5.2.1.2 Active channel properties

In Bhalla and Bower’s models, ‘*The identities of the channels included in each model were inferred from the published effects of specific channel blockers on the electrical properties of each cell.*’ At the time their model was published, no detailed descriptions of channel kinetics were available for the mitral cell, so model parameters were based on known values for similar channels in other cell types. The model contains a fast sodium channel (Na), four potassium channels – two potassium delayed rectifier channels (K and K_{fast}), an anomalous rectifier channel (KA) and a calcium-dependent channel (KCa) – and an L-type calcium channel (LCa). More recent publications are largely consistent with this scheme. Chen and Shepherd [25] suggest that there may be two types of A-family potassium currents, the rapidly inactivating classical A-current and a slowly inactivating potassium current (or D-current). Wang *et al* [150] found and partially characterised an A-type potassium current and a delayed rectifier, although both channel types are activated at considerably more depolarised potentials than the channels used in Bhalla and Bower’s model (Table 5.1). They found two distinguishable calcium-dependent potassium currents.

Subthreshold membrane potential oscillations have been observed recently in mitral/tufted cells [25, 33] and demonstrated to be an intrinsic membrane property dependent on a voltage-dependent sodium

channel rather than a synaptic phenomenon [33]. One suggested mechanism for such oscillations is an interaction between a persistent sodium current and a slowly inactivating potassium current [25], although lowering the external potassium concentration affects neither the amplitude nor frequency of oscillations [33].

The distribution of L-type calcium channels has been investigated using imaging methods [15, 123], in cultured tadpole OB neurones. The observed density was highest on somata and decreased with distance along the dendrites. This is in reasonable agreement with the best-fit distribution of Bhalla and Bower. An N-type calcium current is also found in cultured OB neurones, mainly on dendrites [15].

Conductance densities of sodium and potassium channels have now been measured in rat mitral cell primary dendrites [14]. The experimental values of $\bar{g}_{\text{Na}} = 90 \text{ pS } \mu\text{m}^{-2}$ and $\bar{g}_{\text{K}} = 513 \text{ pS } \mu\text{m}^{-2}$ compare to the values of $\bar{g}_{\text{Na}} = 13.4 \text{ pS } \mu\text{m}^{-2}$ and $\bar{g}_{\text{K}} = 29.7 \text{ pS } \mu\text{m}^{-2}$ found by Bhalla and Bower [11] by model fitting and $\bar{g}_{\text{Na}} = 260 \text{ pS } \mu\text{m}^{-2}$ and $\bar{g}_{\text{K}} = 42 \text{ pS } \mu\text{m}^{-2}$ obtained by Shen *et al* [132], also by model fitting. There are large discrepancies here, with Bhalla and Bower's sodium conductance being an order of magnitude smaller than the other two values, and the experimental potassium current an order of magnitude larger than the two model values. A partial explanation for the former may be that the Bhalla and Bower model has a much larger sodium conductance in the soma than in the primary dendrite, whereas the experimental study found uniform sodium conductance throughout the soma and primary dendrite, and this is modelled in Shen *et al*. Regarding the second discrepancy, Shen *et al* suggest it may be attributed to the very large variance of the experimental data set [14].

At the time Bhalla and Bower's model was published, knowledge about granule cell active channels was considerably more sketchy than for mitral cells. The model includes a sodium channel (Na_{gran}) and three potassium channels: delayed rectifier (K), A-type (KA) and non-inactivating muscarinic (KM). Schoppa and Westbrook [126] have recently measured some properties of sodium, delayed rectifier and KA conductances in rat granule cells. There are considerable differences between the measured parameters and those used by Bhalla and Bower, except in the case of the K channel (Table 5.2). Of particular note are the differences in the KA conductances (Figure 5.1). In addition, the I_{A} current was measured to be much larger in comparison to I_{K} in the dendrites than in the soma. This is in contrast to the Bhalla-Bower model in which there are no dendritic KA channels. In light of the crucial role the KA current appears to play in regulating mitral–granule synaptic communication [63, 125, 126], it is very probable that the Bhalla-Bower granule cell model will prove to be inadequate for bulb modelling.

In summary, at the time this work was begun, the models of Bhalla and Bower were the only ones available, and there was little available data to allow improvement of them. The models are constrained by their morphological detail and unknown parameters were obtained by fitting to experimental recordings. On this basis it is reasonable to use them as the basis of network modelling of the olfactory bulb, and I am confident that my main conclusions in Chapters 3 and 4 would be unchanged by using an updated model.

However, new data have become available which may have a bearing on studies of information processing in the bulb, particularly the subthreshold membrane potential oscillations in mitral/tufted cells [25, 33] and the granule cell KA current. It will therefore be important in future to update the detailed models of Bhalla and Bower, incorporating recent experimental data about ion channels and fitting to recordings from the primary and secondary dendrites as well as to recordings from the soma. To repeat the process of reducing the full models to few-compartment models would be straightforward, and then the differences

			Wang <i>et al</i>	Bhalla and Bower
I_{A}	Mid-point voltage /mV	activation	7.6	-42
		inactivation	-47.4	-110
Time constant /ms		activation	3.1–12.2	1.4
		inactivation	43.4–51.2	150
I_{K}	Mid-point voltage /mV	activation	21	-10

Table 5.1: Comparison of mitral cell channel parameters from Bhalla and Bower [11] and Wang, McKenzie and Kemm [150].

		Schoppa and Westbrook	Bhalla and Bower
I_A	midpoint voltage for steady-state inactivation /mV	-66 ± 4	-110
	activation threshold /mV	-44 ± 2	-100
	inactivation time constant /ms	24 ± 5	150
I_K	activation threshold /mV	-33 ± 5	-38
	activation threshold /mV	-41 ± 3	-70
I_{Na}	midpoint voltage for steady-state inactivation /mV	-63	-52
	inactivation time constant at -18 mV /ms	0.9 ± 0.11	3

Table 5.2: Comparison of granule cell channel parameters from Bhalla and Bower [11] and Schoppa and Westbrook [126].

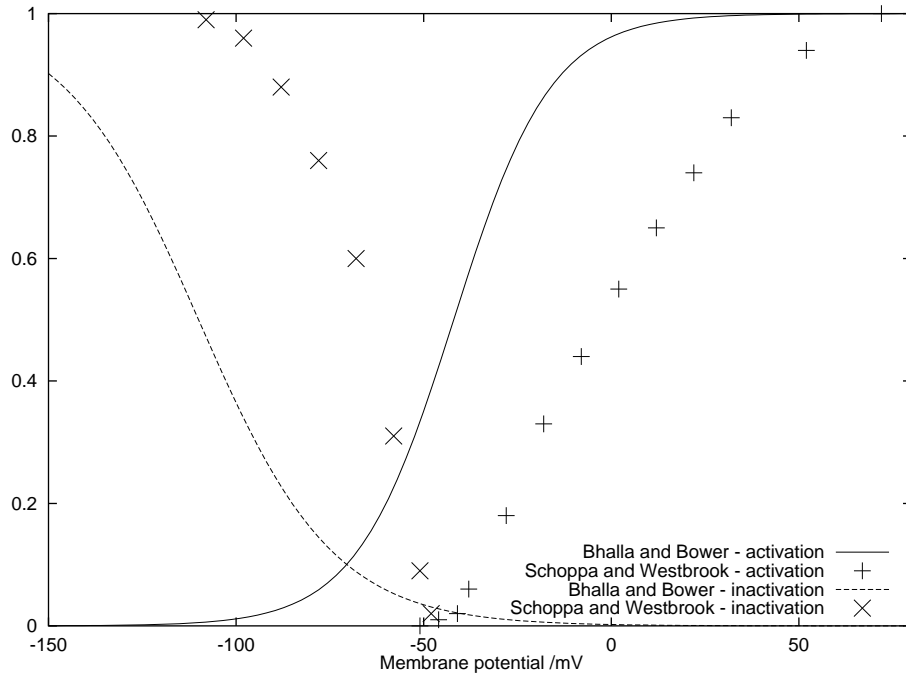


Figure 5.1: The activation and steady-state inactivation curves for the granule cell KA channel, as measured by Schoppa and Westbrook [126] (points), compared to those used by Bhalla and Bower [11] (lines)

in network behaviour due to the different single-cell properties could be investigated.

5.2.2 Validity of simplified models

As well as the validity of the original, morphologically-detailed models it is important to assess the validity of the simplified models.

In terms of the times at which action potentials occur (and therefore of firing rates) the reduced models fit the full models closely. In a network in which neurones communicate via spike-triggered synapses these reduced models are therefore a valid substitute for the full models.

However, these morphologically-simple models ignore most of the information processing which may be occurring within dendrites and spines. The reduced mitral cell model separates the inhibitory inputs to the secondary dendrites from the excitatory inputs to the primary dendrite tuft and from the zone of spike initiation, but interactions within the secondary dendrites or within the tuft cannot be represented. Therefore, the current models must be considered a first approximation, and morphologically-detailed models or simplified models which take account of dendritic processing should be introduced to obtain a fuller picture.

5.2.3 Validity of the network model

The most important simplifications and approximations made in the network model are:

- i. Only mitral and granule cells are included. Tufted cells are assumed to be equivalent to mitral cells, or to be involved in a largely separate, functionally-independent circuit. Periglomerular cells are not included. A more detailed justification for this simplification is given in §4.2.1.
- ii. Synapses are spike-triggered. No membrane depolarisation short of a full action potential is sufficient to cause a post-synaptic potential. How well this represents the synaptic properties found experimentally is discussed in the previous chapter, §4.4.3.
- iii. The procedure for specifying connections between mitral and granule cells assumes, effectively, no branching of the mitral cell secondary dendrites. The effects of specifying connections more realistically will be complex; one effect is likely to be an increase in the effective communication range of the mitral cells.
- iv. The number of cells in the network is 100-1000 times fewer than in the real olfactory bulb. This is not a problem when simulating a limited region such as a single glomerulus (§4.4), and may be compensated for by scaling other parameters when simulating larger regions.

Finally, I should like to note that although many simplifications and approximations have had to be made in developing the single-cell and network models, this is an advantage since it avoids too many assumptions about unknown elements. On the other hand, to simplify further would have risked throwing out many experimentally-measured parameters. This model can be considered a base upon which more detailed models can be built, and with which they can be compared.

5.3 Conclusions

The principal aim of this project has been to develop a detailed, biologically-realistic model of the olfactory bulb to integrate data from different experimental approaches and to provide a link between detailed experimental data and more abstract theories of information processing in the olfactory system. To what extent has this aim been achieved?

In the Introduction I suggested that the model should have explanatory value, predictive value and an integrative function. All of these have, to some extent, been achieved.

Explanatory value. Experiments with the model have given insight into the origin of oscillations and synchronization in the olfactory bulb and how the pattern of connections can affect the behaviour. Explanations of higher-level issues such as the role of the olfactory bulb in olfactory coding have not yet been addressed.

Predictive value. I have been able to make a number of predictions, for example that increasing the average number of synapses per granule cell will increase the duration of the reciprocal IPSC in the mitral cell, and that increasing odour concentration will increase the tendency of the cells to synchronize their firing. To what extent these predictions are (i) experimentally testable and (ii) correct remains to be seen.

Integrative function. The parameters of the model have been taken from various reports in the literature. In general, the different sources are consistent. The most obvious discrepancy is between the indirect calculations of mitral cell synaptic density in §4.2.3.1 and the synaptic density needed for the model to reproduce the experimental results of Schoppa *et al* (§4.4). Resolution of this discrepancy could provide much information about synaptic integration by the granule cell.

In the Introduction I also listed some biological and computational problems I wished to address using the model. The first question was whether oscillations and/or spike synchronization should occur in the olfactory bulb, how they arose and what was their computational function. My conclusion is that spike synchronization, which leads to oscillations in the population activity, should indeed be found in the olfactory bulb, and that the synchronization arises from the mutual inhibition of mitral cells mediated via the reciprocal synapses with granule cells. The question about the computational role of synchronization remains to be addressed.

The second question was how the properties of individual cells and synapses influence the network behaviour. This question was not directly addressed in the network, but in the two- and three-cell systems (Chapter 3) the influence of synaptic delays, synaptic time constants and the properties of the cell membrane on the firing rates and phase-locking behaviour of the cells was analysed in detail for the simple integrate-and-fire model. The more complex biophysical model was shown to behave similarly provided the system was not driven too hard.

The third problem was to elucidate the role of lateral inhibition in the olfactory bulb. One aspect of its role is to support synchronization, as discussed above. The second aspect of its role, to affect the spatial representation of odours within the bulb, was not investigated in such detail, although the preliminary experiments in §4.5.2.3 support the hypothesis that lateral inhibition enhances the differences between the representations of similar odorants.

The last problem was methodological rather than biological. How well can a model with ten thousand cells approximate the real bulb with millions of cells? Two approaches were taken. The first was to study a sub-region of the bulb – a single glomerulus – for which the model can have almost as many cells as in the real system. This is useful for studying how single cells behave in the network context, but cannot address questions about the representation of odours. To approach the modelling of the entire bulb, simulation experiments were carried out to show that the ratio of granule:mitral cells did not have a large or consistent effect on the network behaviour, provided other parameters were scaled to keep the level of input to individual cells constant. This opens the door to simulating much larger networks representing a large fraction of the bulb. By reducing the number of granule cells, thousands of mitral cells, grouped in dozens or hundreds of glomeruli, can be simulated.

5.4 Further work

The work presented in this dissertation is only a beginning. The model presented here can serve as the foundation of an extensive project to investigate how information is processed in the olfactory bulb.

Particular components of that project are as follows:

- A detailed study of the spatial and temporal distribution of activity in the olfactory bulb during odour stimulation, with particular reference to the binding hypothesis, building on the results

reported in §4.5. Experimental techniques are starting to become available which can track activity in many cells in real time, for example high-resolution optical imaging based on voltage-sensitive dyes or intrinsic signals, and multi-electrode arrays which can record simultaneously from dozens of cells. A model such as the one presented here is needed to make sense of the complex data available in such experiments.

- Refinement and extension of the model. The most important refinements/extensions are: (i) updating the single cell models and including details of information processing in dendrites and spines; (ii) incorporating periglomerular neurones; (iii) distinguishing between mitral and tufted cells; and (iv) modelling the dendrodendritic synapses in more detail, particularly the role of calcium in neurotransmitter release. The results presented here can serve as a baseline against which the effects of adding and refining elements can be measured.
- Studying plasticity and learning in the olfactory system. How the behaviour of the model is affected by changing synaptic strengths will shed light on how the real olfactory bulb is changed by experience, and the effects of that on olfactory perception.

The use of models in neuroscience is an iterative process. It is hoped that this model may be used to guide experimental investigations, which will then feed back into better models, suggesting further experiments and so on until the path from smelling a rose to remembering the childhood garden is no longer so mysterious.

Appendix A

Mathematical appendix

This appendix has two sections. The first is an extension of §3.2.3. The envelopes of possible values of the inter-spike interval are derived for the case of harmonic locking in the two-cell integrate-and-fire system. The second section contains some expressions which are plotted in Chapter 3 but which are not given there. The derivations of these expressions are not given here, but in each case the derivation proceeds similarly to one which is given in Chapter 3.

A.1 Calculation of inter-spike-interval envelope for harmonic locking

In order to relate the spiking model to a firing rate model it would be useful to be able to calculate the ratio T_2/T_1 as a function of the four parameters α , θ , δ and t_d . As a first step, we can calculate, for Cell 1, the envelope within which all possible values of the inter-spike interval must lie, and the same for Cell 2. Taking the ratio of the mid-points of these envelopes gives an approximation of n_1/n_2 .

Calculation of the envelope for T_1 is straightforward. Trivially, $T_1^{\min} = T$. T_1^{\max} arises when Cell 1 is inhibited just before it reaches threshold. Using equation 3.4 it is simple to show that

$$T_1^{\max} = T + \tau \ln \left(1 + \frac{\delta(1-\theta)}{\theta+\alpha} \right) \quad (\text{A.1})$$

The envelope for T_2 is discontinuous. First consider the range within which $1 < n_1/n_2 < 2$. The shortest T_2 will be a period receiving only a single downward step, and in which that step occurs earliest. Let t^* be the time from the last firing to the downward step. For small t_d , $T_2^{\min} = t^* + T$ (see Figure A.1A). It can be easily shown from equation 3.5 that

$$t^* = -\tau \ln \left[\theta e^{T/\tau} - \delta(1-\theta) \right] \quad (\text{A.2})$$

and therefore

$$T_{2,1 < n_1/n_2 < 2}^{\min,A} = \tau \ln \left[\frac{1+\alpha}{\theta(1+\alpha) - \delta(1-\theta)(\theta+\alpha)} \right] \quad (\text{A.3})$$

For larger t_d , a shorter T_2^{\min} is obtained (Figure A.1B):

$$T' = \tau \ln \left[\frac{1+\alpha + \delta(1-\theta)e^{(2t_d-t^*)/\tau}}{\theta+\alpha} \right] \quad (\text{A.4})$$

where T' is a period of Cell 1 during which it receives one inhibitory step.,

$$T_{2,1 < n_1/n_2 < 2}^{\min,B} = \tau \ln \left[\frac{1}{\theta} \left(1 + \delta(1-\theta)e^{t^*/\tau} \right) \right] = t^* + T' \quad (\text{A.5})$$

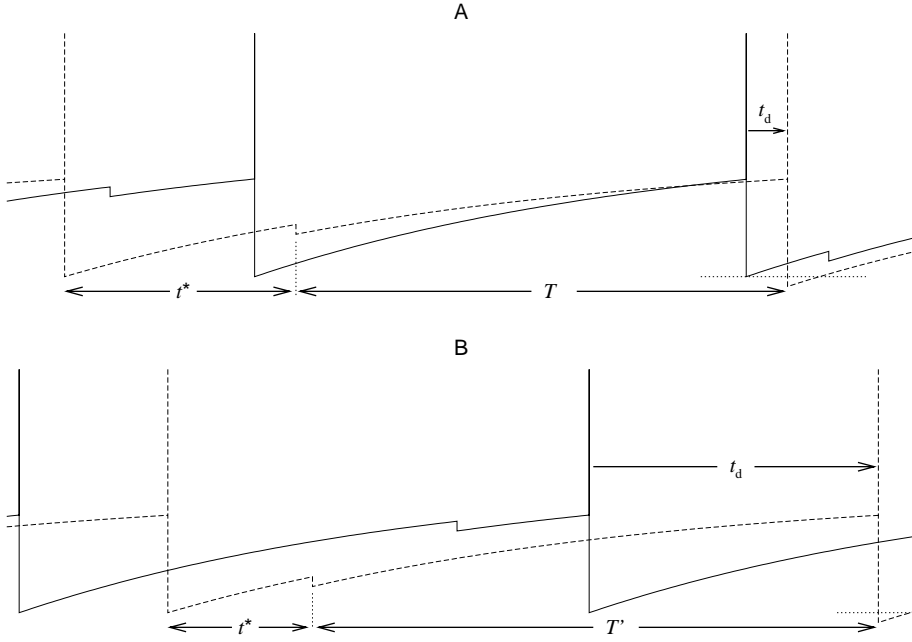


Figure A.1: Illustration of the minimum firing period for Cell 2, for a given α . (A) small t_d , (B) large t_d . Solid line = Cell 1, dashed line = Cell 2.

$$\Rightarrow t^* = \tau \ln \left[\frac{\theta + \alpha - \delta\theta(1 - \theta)e^{2t_d/\tau}}{\theta(1 + \alpha) - \delta(1 - \theta)(\theta + \alpha)} \right] \quad (\text{A.6})$$

$$T_{2,1 < n_1/n_2 < 2}^{\min,B} = \tau \ln \left[\frac{1 + \alpha - \delta^2(1 - \theta)^2 e^{2t_d/\tau}}{\theta(1 + \alpha) - \delta(1 - \theta)(\theta + \alpha)} \right] \quad (\text{A.7})$$

The threshold between these two occurs when t^* (from eq. A.6) = $2t_d$ and is

$$t_d = \frac{\tau}{2} \ln \left[\frac{\theta + \alpha}{\theta(1 + \alpha) - \alpha\delta(1 - \theta)} \right] \quad (\text{A.8})$$

Now consider the range within which $2 < n_1/n_2 < 3$. Now the shortest T_2 will be a period receiving only two downward steps, and in which those steps occur earliest. For small t_d , $T_2^{\min} = t^* + 2T$ and it is easily shown that

$$T_{2,2 < n_1/n_2 < 3}^{\min,A} = \tau \ln \left[\frac{(1 + \alpha)^2}{[\theta(1 + \alpha) - \delta(1 - \theta)(\theta + \alpha)] (1 + \alpha) - \delta(1 - \theta)(\theta + \alpha)^2} \right] \quad (\text{A.9})$$

cf equation A.3. For larger t_d , $T_2^{\min} = t^* + T' + T$ and so

$$T_{2,2 < n_1/n_2 < 3}^{\min,B} = \tau \ln \left[(1 + \alpha) \left(\frac{1 + \alpha - \delta^2(1 - \theta)^2 e^{2t_d/\tau}}{[\theta(1 + \alpha) - \delta(1 - \theta)(\theta + \alpha)] (1 + \alpha) - \delta(1 - \theta)(\theta + \alpha)^2} \right) \right] \quad (\text{A.10})$$

cf equation A.7.

There is possibly a further solution with still higher t_d , for which $T_2^{\min} = t^* + T + T'$, but I have not calculated this because it will rarely or never occur. Expressions for T_2^{\min} can be obtained for the ranges $3 < n_1/n_2 < 4$, $4 < n_1/n_2 < 5$, etc., similarly.

The expressions for $T_2^{\min, A}$ (Equations A.3 and A.9) may be re-expressed in terms of T as:

$$T_{2,1 < n_1/n_2 < 2}^{\min} = -\tau \ln \left(\theta - \delta(1-\theta)e^{-T/\tau} \right) \quad (\text{A.11})$$

$$T_{2,2 < n_1/n_2 < 3}^{\min} = -\tau \ln \left(\theta - \delta(1-\theta)e^{-T/\tau} - \delta(1-\theta)e^{-2T/\tau} \right) \quad (\text{A.12})$$

respectively, which suggests that

$$T_{2,m < n_1/n_2 < m+1}^{\min} = -\tau \ln \left(\theta - \delta(1-\theta) \sum_{j=1}^m e^{-jT/\tau} \right) \quad (\text{A.13})$$

$$= -\tau \ln \left(\theta - \delta(1-\theta) \left(\frac{1 - e^{-mT/\tau}}{1 - e^{-T/\tau}} - 1 \right) \right) \quad (\text{A.14})$$

by summing the geometric series. This expression makes it very easy to calculate T_2^{\min} for any m .

In every case,

$$T_2^{\max} = T_2^{\min} + \tau \ln \left(\frac{1 - (1-\delta)(1-\theta)}{\theta} \right) \quad (\text{A.15})$$

The next stage in calculating of the envelope within which all possible values of the inter-spike interval must lie, is to derive the boundaries in α at which $n_1/n_2 = 2, 3, 4$, etc. Consider Figure A.1A. As α is increased, t^* increases relative to T until the starting spike collides with the previous spike in Cell 1 (Figure A.2). At this point,

$$T' = \tau \ln \left[\frac{1 + \alpha + \delta(1-\theta)e^{2t_d/\tau} t_\theta}{\theta + \alpha} \right] \quad (\text{A.16})$$

and

$$t^* = -\tau \ln \left[\theta \left(\frac{1 + \alpha}{\theta + \alpha} \right) - \delta(1-\theta) \right] = T' - \tau \ln(t_\theta) \quad (\text{A.17})$$

where $t_\theta = (1 - (1 - \delta)(1 - \theta)) / \theta$ from which we obtain

$$\alpha = \frac{1}{\theta + \delta(1 + \theta)} \left(-K_1 + [K_1^2 + 4(\theta + \delta(1 + \theta))K_2]^{\frac{1}{2}} \right) \quad (\text{A.18})$$

where

$$K_1 = \delta \left(e^{2t_d/\tau} (\theta^2 - \delta^2(1-\theta)^2) - \theta(\theta+3) \right) \quad (\text{A.19})$$

$$K_2 = \theta \left(\theta(1-2\delta) + \delta e^{2t_d/\tau} (\delta(1-\delta)(1-\theta)^2 + \theta) \right) \quad (\text{A.20})$$

This is the boundary at which $n_1/n_2 = 2$. The other boundaries can be calculated similarly. An example of the resulting envelope for T_2 is shown in Figure 3.12.

The equations for the minimum-maximum inter-spike interval envelope could now be used to obtain an approximate value for n_1/n_2 as a function of α, θ, δ and t_d .

A.2 Periods and time lags for alternative synaptic models

Type A firing

Constant step, no self-inhibition

$$T_1^A = \tau \ln \left[\frac{1 + \alpha + \delta(1-\theta)e^{(t_L^E + t_d)/\tau}}{\theta + \alpha} \right] \quad (\text{A.21})$$

$$T_2^A = \tau \ln \left[\frac{1 + \delta(1-\theta)e^{(t_d - t_L^E)/\tau}}{\theta} \right] \quad (\text{A.22})$$

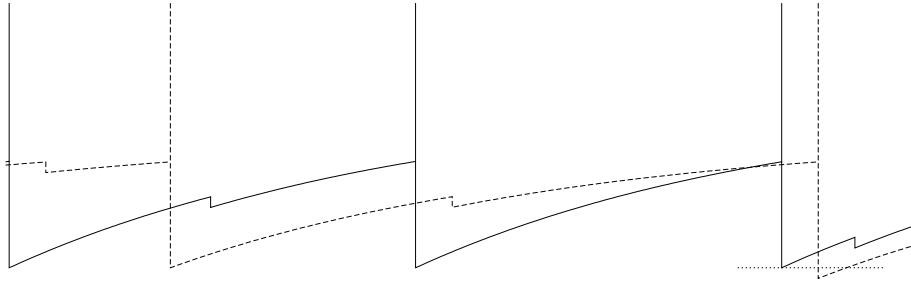


Figure A.2: Illustration of T_2^{\min} when n_1/n_2 is just less than 2.00. Increasing α beyond this point will cause the firing time of Cell 2 to jump back in time so that Cell 2 receives two inhibitory pulses, and there is a discontinuous change in T_2^{\min} . Solid line = Cell 1, dashed line = Cell 2.

$$t_L^E = \tau \ln \left[\frac{1}{2\theta} \left(\frac{\alpha}{\delta} e^{-t_d/\tau} + \left[\left(\frac{\alpha}{\delta} e^{-t_d/\tau} \right)^2 + 4\theta(\theta + \alpha) \right]^{\frac{1}{2}} \right) \right] \quad (\text{A.23})$$

$$\alpha_{\text{threshold}} = \frac{\theta (e^{2t_d/\tau} - 1)}{1 + \frac{1}{\delta}} \quad (\text{A.24})$$

Variable step, no self-inhibition

$$T_1^A = \tau \ln \left[\frac{1 + \alpha}{\theta + \alpha} \left(1 - \delta + \delta e^{(t_L^E + t_d)/\tau} \right) \right] \quad (\text{A.25})$$

$$T_2^A = \tau \ln \left[\frac{1 - \delta + \delta e^{(t_d - t_L^E)/\tau}}{\theta} \right] \quad (\text{A.26})$$

$$t_L^E = \tau \ln \left[\frac{1}{2\theta(1 + \alpha)} \left(\frac{\alpha}{\delta} e^{-t_d/\tau} + (1 - \delta)(1 - \theta) \right. \right. \\ \left. \left. + \left[\left(\frac{\alpha}{\delta} e^{-t_d/\tau} + (1 - \delta)(1 - \theta) \right)^2 + 4\theta(1 + \alpha)(\theta + \alpha) \right]^{\frac{1}{2}} \right) \right] \quad (\text{A.27})$$

$$\alpha_{\text{threshold}} = \frac{\theta (e^{2t_d/\tau} - 1)}{1 + \frac{(1-\delta)(1-\theta)}{\delta} - \theta e^{2t_d/\tau}} \quad (\text{A.28})$$

Constant step, self-inhibition

$$T_1^A = \tau \ln \left[\frac{1 + \alpha + \delta(1 - \theta)e^{t_d/\tau} + \delta(1 - \theta)e^{(t_L^E + t_d)/\tau}}{\theta + \alpha} \right] \quad (\text{A.29})$$

$$T_2^A = \tau \ln \left[\frac{1 + \delta(1 - \theta)e^{t_d/\tau} + \delta(1 - \theta)e^{(t_d - t_L^E)/\tau}}{\theta} \right] \quad (\text{A.30})$$

$$t_L^E = \tau \ln \left[\frac{1}{2\theta} \left(\alpha \left(1 + \frac{e^{-t_d/\tau}}{\delta} \right) + \left[\alpha^2 \left(1 + \frac{e^{-t_d/\tau}}{\delta} \right)^2 + 4\theta(\theta + \alpha) \right]^{\frac{1}{2}} \right) \right] \quad (\text{A.31})$$

$$\alpha_{\text{threshold}} = \frac{\theta(e^{2t_d/\tau} - 1)}{1 + \frac{1}{\delta} + e^{t_d/\tau}} \quad (\text{A.32})$$

Variable step, self-inhibition

$$T_1^A = \tau \ln \left[\frac{1+\alpha}{\theta+\alpha} \left((1-\delta)^2 + \delta(1-\delta)e^{t_d/\tau} + \delta e^{(t_L^E+t_d)/\tau} \right) \right] \quad (\text{A.33})$$

$$T_2^A = \tau \ln \left[\frac{1}{\theta} \left((1-\delta)^2 + \delta(1-\delta)e^{t_d/\tau} + \delta e^{(t_d-t_L^E)/\tau} \right) \right] \quad (\text{A.34})$$

$$\begin{aligned} t_L^E = \tau \ln & \left[\frac{1}{2\theta(1+\alpha)} \left(\alpha(1-\theta)(1-\delta) \left(\frac{1-\delta}{\delta} e^{-t_d/\tau} + 1 \right) \right. \right. \\ & \left. \left. + \left[\left(\alpha(1-\theta)(1-\delta) \left(\frac{1-\delta}{\delta} e^{-t_d/\tau} + 1 \right) \right)^2 + 4\theta(1+\alpha)(\theta+\alpha) \right]^{\frac{1}{2}} \right) \right] \quad (\text{A.35}) \end{aligned}$$

$$\alpha_{\text{threshold}} = \frac{\theta(e^{2t_d/\tau} - 1)}{1 + (1-\delta)(1-\theta)(e^{t_d/\tau} + \frac{1+\delta}{\delta} - \theta e^{2t_d/\tau})} \quad (\text{A.36})$$

Type B firing

Constant step, no self-inhibition

$$T_1^B = T_1^A \quad (\text{A.37})$$

$$T_2^B = \tau \ln \left[\frac{1}{\theta - \delta(1-\theta)e^{(t_d-t_L^E)/\tau}} \right] \quad (\text{A.38})$$

$$t_L^E = \tau \ln \left[\frac{1}{2\theta} \left(\frac{\alpha}{\delta} e^{-t_d/\tau} + \delta(1-\theta)e^{t_d/\tau} + \left[\left(\frac{\alpha}{\delta} e^{-t_d/\tau} + \delta(1-\theta)e^{t_d/\tau} \right)^2 + 4\theta(1+\alpha) \right]^{\frac{1}{2}} \right) \right] \quad (\text{A.39})$$

$$\begin{aligned} \alpha_{\text{threshold}} = \frac{1}{2(\frac{1}{\delta} + e^{2t_d})} & \left(\theta \left(1 - \frac{1}{\delta} \right) - e^{2t_d/\tau} (2\theta + \delta(1-\theta)) \right. \\ & + \left[\left(\theta \left(1 - \frac{1}{\delta} \right) - e^{2t_d/\tau} (2\theta + \delta(1-\theta)) \right)^2 \right. \\ & \left. \left. + 4\theta \left(\frac{1}{\delta} + e^{2t_d/\tau} \right) \left(1 - (\delta - \delta\theta + \theta) e^{2t_d/\tau} \right) \right]^{\frac{1}{2}} \right) \quad (\text{A.40}) \end{aligned}$$

Variable step, no self-inhibition

$$T_1^B = T_1^A \quad (\text{A.41})$$

$$T_2^B = \tau \ln \left[\frac{1-\delta}{\theta - \delta e^{(t_d-t_L^E)/\tau}} \right] \quad (\text{A.42})$$

$$t_L^E = \tau \ln \left[\frac{1}{2\theta} \left(\frac{\alpha(1-\delta)(1-\theta)e^{-t_d/\tau}}{\delta(1+\alpha)} + \delta e^{t_d/\tau} \right. \right. \\ \left. \left. + \left[\left(\frac{\alpha(1-\delta)(1-\theta)e^{-t_d/\tau}}{\delta(1+\alpha)} + \delta e^{t_d/\tau} \right)^2 + 4\theta(1-\delta) \right]^{\frac{1}{2}} \right) \right] \quad (\text{A.43})$$

$$\alpha_{\text{threshold}} = \frac{1}{2 \left(\theta - \frac{(1-\delta)(1-\theta)}{\delta} - e^{2t_d/\tau} \right)} \left(\frac{\theta(1-\theta)(1-\delta)}{\delta} + (\delta(1-\theta) + 2\theta) e^{2t_d/\tau} - 2\theta \right. \\ \left. - \left[\left(\frac{\theta(1-\theta)(1-\delta)}{\delta} + (\delta(1-\theta) + 2\theta) e^{2t_d/\tau} - 2\theta \right)^2 \right. \right. \\ \left. \left. - 4\theta \left(\theta - \frac{(1-\delta)(1-\theta)}{\delta} - e^{2t_d/\tau} \right) \left(1 - (\delta(1-\theta)) e^{2t_d/\tau} \right) \right]^{\frac{1}{2}} \right) \quad (\text{A.44})$$

Variable step, self-inhibition

$$T_1^B = T_1^A \quad (\text{A.45})$$

$$T_2^B = \tau \ln \left[\frac{(1-\delta) \left[(1 - e^{-t_d/\tau}) (1 - \delta) - 1 \right]}{\delta e^{-t_L^E/\tau} - \theta e^{t_{-D}/\tau}} \right] \quad (\text{A.46})$$

$$t_L^E = \tau \ln \left[\frac{1}{2\theta} \left(\frac{\alpha(1-\delta)(1-\theta)}{1+\alpha} \left(\frac{1-\delta}{\delta} e^{-t_d/\tau} + 1 \right) + \delta e^{t_d/\tau} \right. \right. \\ \left. \left. + \left[\left(\frac{\alpha(1-\delta)(1-\theta)}{1+\alpha} \left(\frac{1-\delta}{\delta} e^{-t_d/\tau} + 1 \right) + \delta e^{t_d/\tau} \right)^2 + 4\theta(1-\delta) \left(1 - \delta + \delta e^{t_d/\tau} \right) \right]^{\frac{1}{2}} \right) \right] \quad (\text{A.47})$$

Appendix B

Program listings

Note that some lines have been split to fit on the page.

B.1 Mitral cell model

```

// mitral.tem
// Template for mitral cell model
// Andrew Davison, The Babraham Institute
// 25th June 1999

begintemplate Mit
public soma, glom, prim, dend, AMPA, GABA, spiketest,
        spiketimes, spikecount, lastspikecount
create soma, glom, prim, dend, s2d, s2p, p2g
objref AMPA, GABA, spikecount, spiketimes

proc init() { local Len, Erest, RM, p, q, r, Atotal, gsp, gsd, gpg,
             AMPAtau, AMPArev, GABAAtau, GABAArev
create soma, glom, prim, dend, s2d, s2p, p2g
spiketimes = new Vector()
lastspikecount = 0

Len      = 100
RM       = 100000
Erest    = -65          // mV
Atotal   = 100000        // um2
gsp      = 5.47e-11      // S/cm2
gpg      = 5.86e-11
gsd      = 1.94e-10
RM       = 100000        // ohm.cm2
p        = 0.051
q        = 0.084
r        = 0.328
AMPAtau = 10            // ms
MPArev  = 0              // mV
GABAAtau = 18            // from Sc&98
GABAArev = -70

soma {
    insert pas
    insert nafast
    insert kfasttab
    insert kslowtab
    insert kA
    insert kca3
    insert lcafixed
    insert cad
    depth_cad = 8
    L         = Len
    diam     = p*Atotal/(PI*Len)
    Ra       = PI*diam*diam/(4*Len*Atotal)
    e_pas    = Erest
    g_pas    = 1/RM
    gcabar_lcafixed = 0.0095
    AMPA = new ExpSyn(0.5)
    AMPA.tau = AMPAtau
    AMPA.e   = AMPArev
}

prim {
    insert pas
    insert nafast
    insert kfasttab
    insert kslowtab
    insert lcafixed
    insert cad
    depth_cad = 8
    L         = Len
    diam     = r*Atotal/(PI*Len)
    Ra       = PI*diam*diam/(4*Len*Atotal)
    e_pas    = Erest
    g_pas    = 1/RM
    gbar_kfasttab = 0.00123
    gbar_nafast = 0.00134
    gbar_kslowtab = 0.00174
    gcabar_lcafixed = 0.0022
}

dend {
    insert pas
    insert kfasttab
    insert nafast
    L         = Len
    diam     = (1-p-q-r)*Atotal/(PI*Len)
    Ra       = PI*diam*diam/(4*Len*Atotal)
    e_pas    = Erest
    g_pas    = 1/RM
    gbar_kfasttab = 0.0330
    gbar_nafast = 0.0226
    GABA = new ExpSyn(0.5)
    GABA.tau = GABAAtau
    GABA.e   = GABAArev
}

s2d {
    diam   = 1
    Ra     = PI*diam*diam/(4*Len*Atotal) * ( 1/gsd )
    L     = 1
}
s2p {
    diam   = 1
    Ra     = PI*diam*diam/(4*Len*Atotal) * ( 1/gsp )
    L     = 1
}
p2g {
    diam   = 1
    Ra     = PI*diam*diam/(4*Len*Atotal) * ( 1/gpg )
    L     = 1
}

soma connect s2p(0),0
s2p connect prim(0),1
prim connect p2g(0),1
p2g connect glom(0),1
some connect s2d(0),1
s2d connect dend(0),1

```

```

// set reversal potentials, etc.
forall if (ismembrane("ca_ion")) {
    eca = 70          // mV
    cai = 0.00001    // mM
    cao = 2           // mM
    ion_style("ca_ion",3,2,0,0,1)
}
forall if (ismembrane("na_ion")) {
    ena = 45          // mV
}
forall if (ismembrane("k_ion")) {
    ek = -70          // mV
}

}
}

proc spiketest() {
    if (spikecount.n > lastspikecount) { // check for spike occurring
        spiketimes.append(spikecount.time)
        lastspikecount = spikecount.n
    }
}

endtemplate Mit

```

2

B.2 Granule cell model

```

// granule.tem
// Template for granule cell model
// Andrew Davison, The Babraham Institute
// 25th June 1999
// NMDA synapse added 15th April 2000
// Synaptic parameters changed 6th September 2000

begintemplate Gran
public soma, periph, deep, AMPAr, NMDAr, spiketest,
    spiketimes, spikecount, lastspikecount
create soma, periph, deep, s2d, s2p
objref AMPAr, NMDAr, spiketimes, spikecount

proc init() { local Len, Erest, RM, p, q, Atotal, gsp, gsd, AMPAtau,
    NMDAlpha, NMDAbeta, Erev, rsd, rsp
create soma, periph, deep, s2d, s2p

spiketimes = new Vector()
lastspikecount = 0

Erest      = -65          // mV
Atotal     = 8353         // um^2
gsp        = 3.08e-10     // S/cm^2
gsd        = 4.34e-10
RM         = 120000        // ohm.cm^2
Len         = 50
p          = 0.0136
q          = 0.308
rsd        = 1/(gsd*Atotal)
rsp        = 1/(gsp*Atotal)
NMDAlpha   = 0.0163        // ms^-1
NMDAbeta   = 0.00292       // ms^-1 from Sc&98
AMPAtau    = 5.5           // ms
Erev        = 0             // mV

soma {
    L          = Len
    diam      = p*Atotal/(PI*Len)
    Ra        = PI*diam*diam/(4*Len*Atotal)
    insert pas
    e_pas     = Erest          // mV
    g_pas     = 1/RM           // S/cm^2 (= 120000 ohm/cm^2)
    insert nagrantab
    insert kslowtab
    insert KM
    insert KA
    gnabar_nagrantab = 0.1611 // siemen-cm^-2
    gkbar_kslowtab  = 0.1313
    gkbar_KM       = 0.1334
    gkbar_KA       = 0.0088
}

periph {
    L          = Len
    diam      = q*Atotal/(PI*Len)
    Ra        = PI*diam*diam/(4*Len*Atotal)
    insert pas
    e_pas     = Erest
}

deep {
    L          = Len
    diam      = (1-p-q)*Atotal/(PI*Len)
    Ra        = PI*diam*diam/(4*Len*Atotal)
    insert pas
    e_pas     = Erest
    g_pas     = 1/RM
}

s2d {
    diam      = 1
    Ra        = PI*diam*diam/(4*Len*Atotal) * ( 1/gsd )
    L          = 1
}

s2p {
    diam      = 1
    Ra        = PI*diam*diam/(4*Len*Atotal) * ( 1/gsp )
    L          = 1
}

soma connect s2p(0), 0
s2p connect periph(0), 1
soma connect s2d(0), 1
s2d connect deep(0), 1

// set reversal potentials, etc.
forall if (ismembrane("na_ion")) {
    ena = 45 // mV
}
forall if (ismembrane("k_ion")) {
    ek = -70 // mV
}

}

proc spiketest() {
    if (spikecount.n > lastspikecount) { // check for spike occurring
        spiketimes.append(spikecount.time)
        lastspikecount = spikecount.n
    }
}

endtemplate Gran

```

2

B.3 Olfactory bulb network model

```

// bulb.hoc
// Olfactory bulb network model
// Andrew Davison, The Babraham Institute
// 14th May 2000, 24th May 2000, 25th August 2000
// =====
// == A. Parameters ==
// =====

nmity      = 6
nglom      = nmity*nmity
g2m        = 12
ngranx    = nmity*g2m
ngrany    = nmity*g2m
mitsep    = 1
gransep   = mitsep/g2m
seed       = 0
rmax      = ngranx*0.5
synpermit  = 500
thresh     = -10          // mV

```

```

edelay    = 1.8      // ms
conducedel = 0
idelay   = 0.6      // ms (from MoTa78)
AMPAweight = 1e-3    //          } based
NMDAweight = 7e-4    // uS      } on
iweight   = 6e-4    //          } Sc&#98
risetime  = 30       // ms approx. rise time of NMDA EPSC from Sc&#98
mgconc   = 1         // mM
maxinput  = 1.5
nof      = 10        // number of 'odour features'

// -----
// == B. Initialisation -----
// -----

xopen("$(NEURONHOME)/lib/hoc/noload.hoc") // standard run tools
xopen("grantabchannels.hoc") // data for channel tables
xopen("mitral.tem") // mitral cell template
xopen("granule.tem") // granule cell template
xopen("mymaths.hoc") // miscellaneous maths
                                // procedures and functions

objref cvode
cvode = new CVode(0) // start with CVode inactive
objref random
random = new Random(seed)
objref mit[nmitx][nmity]
objref gran[ngranax][ngrany]
objref m2gAMPAlist, m2gNMDAlist, g2mlist
m2gAMPAlist = new List()
m2gNMDAlist = new List()
g2mlist = new List()
objref input[nmitx][nmity], inputarray, outputarray
inputarray = new Matrix(nmitx,nmity)
outputarray = new Matrix(nmitx,nmity)
objref isi, lags
isi = new Vector()
lags = new Vector()
objref outfile
outfile = new File()
strdef filename, fileroot, odourfile, inputfile
objref work, work2
work = new Vector()
work2 = new Vector()
objref hist
objref odour
odour = new Vector(nof)

// -----
// == C. Procedures -----
// -----

// C.1. Create cells, specify co-ordinates, set cell parameters ----

proc create_cells() { local i,j
  printf("<<< Creating cells ...")
  for i = 0, nmitx-1 {
    for j = 0, nmity-1 {
      mit[i][j] = new Mit()
      mit[i][j].position(i*mmitsep,j*mmitsep)
    }
  }
  for i = 0, ngranax-1 {
    for j = 0, ngrany-1 {
      gran[i][j] = new Gran()
      gran[i][j].position(i*gransep,j*gransep)
    }
  }
  access mit[0][0].soma
  printf(" Cells created >>>\n")
}

// C.2. Connect cells, set synaptic parameters ----

func wrap() {
  if ($1 < 0) {
    return $2+$1
  } else {
    if ($1 < $2) {
      return $1
    } else {
      return $1-$2
    }
  }
}

proc connect_cells() { local i,j,phi,r,ii,jj,dg,edel
  // 2 arguments - dg, fileroot
  dg = $1 // "different glomeruli"
  printf("<<< Connecting cells ...")
  m2gAMPAlist.remove_all()
  m2gNMDAlist.remove_all()
  g2mlist.remove_all()
  sprint(filename,"%s.connect",$s2)
  outfile.wopen(filename)
  // Note: here it is possible for a mitral cell to have more than one
  // synaptic contact with any particular granule cell.
  for i = 0, nmitx-1 {
    for j = 0, nmity-1 {
      for k = 1, synpermit {
        phi = random.uniform(0,2*PI)
        r = random.uniform(0,rmmax)
        x = dg*i*g2m + r*sin(phi)
        y = dg*j*g2m + r*cos(phi)
        ii = wrap( nint(x),ngranax )
        jj = wrap( nint(y),ngrany )
        edel = edelay + r/rmax*conducedel
        mit[i][j].dend m2gAMPAlist.append( new NetCon(&v(0.5),
                                                       gran[ii][jj].AMPA,thresh,edel,AMPAweight) )
        mit[i][j].dend m2gNMDAlist.append( new NetCon(&v(0.5),
                                                       gran[ii][jj].NMDA,thresh,edel,NMDAweight) )
        gran[ii][jj].periph g2mlist.append( new NetCon(&v(0.5),
                                                       mit[i][j].GABA,thresh,idelay,iweight) )
      }
    }
  }
  outfile.close()
  printf(" Cells connected >>>\n")
}

proc set_GABA_weights() { local i // 1 argument - weight
  for i = 0,g2mlist.count()-1 {
    g2mlist.object(i).weight = $1
  }
}

proc set_AMPA_weights() { local i // 1 argument - weight
  for i = 0,m2gAMPAlist.count()-1 {
    m2gAMPAlist.object(i).weight = $1
  }
}

proc set_NMDA_weights() { local i // 1 argument - weight
  for i = 0,m2gNMDAlist.count()-1 {
    m2gNMDAlist.object(i).weight = $1
  }
}

// C.3. Specify inputs ----

proc insert_iclamps() { local i,j // 2 arguments - del, dur
  // if $1 is negative, delay is randomly chosen
  // in the uniform interval 0,$1
  for i = 0, nmitx-1 {
    for j = 0, nmity-1 {
      mit[i][j].glom input[i][j] = new IClamp(0.5)
      input[i][j].dur = $2
      input[i][j].del = abs($1)
    }
  }
  random.uniform(0,abs($1))
  if ($1 < 0) {
    for i = 0, nmitx-1 {
      for j = 0, nmity-1 {
        input[i][j].del = random.repick()
      }
    }
  }
}

proc set_no_input() { local i,j
  for i = 0, nmitx-1 {
    for j = 0, nmity-1 {
      inputarray.x[i][j] = 0.0
      input[i][j].amp = inputarray.x[i][j]
    }
  }
}

// Odour input
objref A, X, S

proc generate_odour_matrix() { local i,j,r,ix,iy,k,l,min,max
  A = new Matrix(nghlom,nof) // A is set here and should
                                // not be changed elsewhere
  S = new Matrix(nmitx,nmity) // X and S are local
  X = new Vector(nghlom) // matrices
  r = random.normal(0.0,0.5)

  // Generate original matrix
  for i = 0,nghlom-1 for j = 0,nof-1 {
    r = random.repick()
    if (r < 0) {r = 0}
    A.x[i][j] = r
  }

  // Average to obtain similar responses of nearby glomeruli
  blur = 2
  for j = 0,nof-1 {
    X = A.getcol(j)
    for ix = 0,nmitx-1 for iy = 0,nmity-1 {
      S.x[ix][iy] = X.x[ix*nmity+iy]
    }
    for ix = 0,nmitx-1 for iy = 0,nmity-1 {
      X.x[ix*nmity+iy] = 0
      for k = -1,1 for l = -1,1 {
        kx = mod(ix+k,nmitx)
        ly = mod(iy+l,nmity)
        X.x[ix*nmity+iy] += ( S.x[kx][ly] * exp(-blur*sqrt(k^2+l^2)) )
      }
    }
    A.setcol(j,X)
  }

  max = arraymax(A)
  min = arraymin(A)
  print "min, max ",min,max
  for i=0,nghlom-1 for j=0,nof-1 {
    A.x[i][j] += -min
  }
  A.muls(1/(max-min))
}

```

```

}

proc read_odour_file() { local i // 1 argument - id number of odour
    sprint(odourfile,"odour%d",$1)
    fopen(odourfile)
    for i = 0,nof-1 {
        odour.x[i] = fscanf()
    }
    fopen()
    printf("Odour %d loaded:\n",$1)
    odour.printf("%e.3f")
}

proc map_odour_to_input() { local i,j
    // 2 arguments - odour vector and odour intensity
    X = A.mulv($0i)
    for i = 0, nmity-1 {
        for j = 0, nmixt-1 {
            inputarray.x[i][j] += $2 * X[i*nmity+j]
            input[i][j].amp = inputarray.x[i][j]
        }
    }
}

// C.4. Procedures for processing spike times and writing out data -------

xopen("calcislag.hoc")

proc print_params() { // 1 argument - filename
    sprint(filename,"%s.param",$1)
    outfile.wopen(filename)
    outfile.printf("nmixt:      %d\n",nmixt)
    outfile.printf("nmity:      %d\n",nmity)
    outfile.printf("g2m:        %d\n",g2m)
    outfile.printf("mitsep:     %f\n",mitsep)
    outfile.printf("gransep:    %f\n",gransep)
    outfile.printf("seed:        %d\n",seed)
    outfile.printf("rmax:        %f\n",rmax)
    outfile.printf("synpermit:   %f\n",synpermit)
    outfile.printf("thresh:      %f\n",thresh)
    outfile.printf("edelay:       %f\n",edelay)
    outfile.printf("conducdel:  %f\n",conducdel)
    outfile.printf("idelay:      %f\n",idelay)
    outfile.printf("AMPAweight:  %f\n",AMPAweight)
    outfile.printf("NMDAweight:  %f\n",NMDAweight)
    outfile.printf("iweight:     %f\n",iweight)
    outfile.printf("maxinput:    %f\n",maxinput)
    outfile.printf("tstop:       %f\n",tstop)
    outfile.printf("ttrans:      %f\n",ttrans)
    outfile.printf("rtol:        %f\n",cvode.rtol())
    outfile.printf("atol:        %f\n",cvode.atol())
    outfile.printf("cvode:        %d\n",cvode.active())
    outfile.printf("local:       %d\n",cvode.use_local_dt())
    outfile.printf("risetime:    %f\n",risetime)
    outfile.printf("mgconc:     %f\n",mgconc)
    outfile.close()
}

// C.5. Procedures for running the model -------

proc random_init() { local i,j
    random.normal(-65,25)
    for i = 0,nmixt-1 {
        for j = 0, nmity-1 {
            mit[i][j].soma.v(0.5) = random.repick()
            mit[i][j].dend.v(0.5) = mit[i][j].soma.v(0.5)
            mit[i][j].prim.v(0.5) = mit[i][j].soma.v(0.5)
            mit[i][j].glom.v(0.5) = mit[i][j].soma.v(0.5)
        }
    }
    for i = 0,ngranz-1 {
        for j = 0, ngrany-1 {
            gran[i][j].soma.v(0.5) = random.repick()
            gran[i][j].deep.v(0.5) = gran[i][j].soma.v(0.5)
            gran[i][j].periph.v(0.5) = gran[i][j].soma.v(0.5)
        }
    }
}

proc advance() { local i,j
    fadvance()
    for i = 0,nmixt-1 {
        for j = 0, nmity-1 {
            mit[i][j].spiketest()
        }
    }
    for (i = 0; i <= ngranz-1; i+=1) { // testing for granule cell spikes
        for (j = 0; j <= ngrany-1; j+=1) { // seems to slow the simulation
            gran[i][j].spiketest() // way down, so comment this
            // out for faster running.
        }
    }
}

// =====
// == D. Running the model =====
// =====

// D.1. Set numerical parameters -------

tstop = 3000          // ms
ttrans = 1000          // ms - ignore spikes before this time
cvode.rtol(0)
cvode.atol(1e-2)
cvode.active(1)
cvode.use_local_dt(1)

// D.2. Set or read-in model parameters -----
Cdur_NMDA = risetime
mg_NMDA = mgconc
sprint(fileroot,"bulbdata001")
printf("Filename: %s\n",fileroot)

// D.3. Initialise the model -------

create_cells()
connect_cells(1,fileroot) // 1=different glomeruli
insert_iclamps(-200,tstop)
generate_odour_matrix()
set_no_input()
read_odour_file(1) // read in odour #1
map_odour_to_input(odour,maxinput)

set_AMPA_weights(AMPAweight)
set_NMDA_weights(NMDAweight)
set_GABA_weights(iweight)

print_params(fileroot)

// D.4. Run the model -------

startsw()
init()
random_init()
print "<<< Starting run >>>"
while (t < tstop) {
    advance()
}
print "Time: ",stopsw()

// D.5. Print-out results -------

print_raster(fileroot)
print_gran_raster(fileroot)
print_smooth_hist(minisi()/4,fileroot)
print_gran_smooth_hist(minisi()/4,fileroot)
print_isi_stats(fileroot)
print_si(fileroot,0)

// calcislag.hoc
// Opened by bulb.hoc
// Procedures for calculating interspike interval and
// time lag statistics and printing them out
// Andrew Davison, The Babraham Institute
// 7th September 2000

// Procedures for processing spike times -------

proc calc_isis() { local i,j,k,n
    // 3 arguments - indices of mitral cell, transient time
    if ($1 > nmixt || $2 > nmity) {
        print "Sorry - index out of range. Please try again."
        return
    }
    i = int($1)
    j = int($2)
    isi.resize(0)
    n = mit[i][j].spiketimes.size()
    if (n > 1) {
        for k = 1,n-1 {
            if (mit[i][j].spiketimes.x[k-1] > $3) {
                isi.append(mit[i][j].spiketimes.x[k]-mit[i][j].spiketimes.x[k-1])
            }
        }
    }
}

proc calc_gran_isis() { local i,j,k,n
    // 3 arguments - indices of granule cell, transient time
    if ($1 > ngranz || $2 > ngrany) {
        print "Sorry - index out of range. Please try again."
        return
    }
    i = int($1)
    j = int($2)
    isi.resize(0)
    n = gran[i][j].spiketimes.size()
    if (n > 1) {
        for k = 1,n-1 {
            if (gran[i][j].spiketimes.x[k-1] > $3) {
                isi.append(gran[i][j].spiketimes.x[k]-gran[i][j].spiketimes.x[k-1])
            }
        }
    }
}

proc calc_phase_lags() { local i1,j1,i2,j2,k,minidx,min
    // 5 arguments - indices of mitral cells, transient time
    if ($1 > nmixt || $2 > nmity || $3 > nmixt || $4 > nmity) {
        print "Sorry - index out of range. Please try again."
        return
    }
    i1 = int($1)
    j1 = int($2)
    i2 = int($3)
    j2 = int($4)
    lags.resize(0)
    // for each spiketime in cell 1, find closest spike in cell 2
    // Note: first and last spikes ignored since can't calculate previous ISI
    if (mit[i2][j2].spiketimes.size > 0) {

```

```

for k = 1,mit[i1][j1].spiketimes.size()-2 {
    if (mit[i1][j1].spiketimes.x[k] > $5) {
        work = mit[i2][j2].spiketimes.c.add(-mit[i1][j1].spiketimes.x[k])
        minidx = work.c.abs.min.ind()
        min = work.x[minidx]
        isiprev = mit[i1][j1].spiketimes.x[k-1]-mit[i1][j1].spiketimes.x[k]
        isinext = mit[i1][j1].spiketimes.x[k+1]-mit[i1][j1].spiketimes.x[k]
        if ((min > isiprev/2 && min < isinext/2) {
            if (min < 0) {
                lags.append(min/isiprev)
            } else {
                lags.append(min/isinext)
            }
        }
    }
}

proc time_hist() { local i,j // 1 argument - time step
    work.resize(0)
    for i = 0, nmitx-1 {
        for j = 0, nmity-1 {
            work.append(mit[i][j].spiketimes)
        }
    }
    hist = work.histogram(0,tstop,$1)
    hist.printf("%d\n")
}

func synch_index2a() { local n,ii,j1,i2,j2
    synchindex = 0
    n = 0
    for ii = 0, nmitx-1 {
        for jj = 0, nmity-1 {
            if (mit[ii][jj].spiketimes.size() > 0) {
                for i2 = 0, nmitx-1 {
                    for j2 = 0, nmity-1 {
                        if (i1 != i2 || jj != j2) {
                            calc_phase_lags(ii,j1,i2,j2,ttrans)
                            if (lags.size() > 1) {
                                synchindex += lags.var()
                                n += 1
                            }
                        }
                    }
                }
            }
        }
    }
    synchindex = sqrt(synchindex/n)
    return synchindex
}

func synch_index3a() { local ii,j1,i2,j2,n
    synchindex = 0
    n = 0
    for ii = 0, nmitx-1 {
        for jj = 0, nmity-1 {
            if (mit[ii][jj].spiketimes.size() > 0) {
                for i2 = 0, nmitx-1 {
                    for j2 = 0, nmity-1 {
                        if (i1 != i2 || jj != j2) {
                            calc_phase_lags(ii,j1,i2,j2,ttrans)
                            n += lags.size()
                            synchindex += lags.reduce("abs",0)
                        }
                    }
                }
            }
        }
    }
    return synchindex/n
}

// Procedures for writing out data -----
proc print_smooth_hist() { local i,j
    // 2 arguments - variance, filename root
    work.resize(0)
    for i = 0, nmitx-1 {
        for j = 0, nmity-1 {
            work.append(mit[i][j].spiketimes)
        }
    }
    hist = work.sumgauss(0,tstop,1,$1)
    sprint(filename,"%s.smhist",$s2)
    outfile.wopen(filename)
    outfile.printf("# Mitral cell smoothed histogram\n")
    hist.print(outfile,"%8.3f\n")
    outfile.close()
    work.resize(0)
    hist.remove(0,ttrans)
    work.spcrm(hist)
    sprint(filename,"%s.pow",$s2)
    outfile.wopen(filename)
    outfile.printf("# Power spectrum of Mitral cell smoothed histogram\n")
    work.print(outfile,"%9.5f\n")
    outfile.close()
}

proc print_gran_smooth_hist() { local i,j
    // 2 arguments - variance, filename root
    work.resize(0)
    for i = 0, ngranz-1 {
        for j = 0, ngrany-1 {
            work.append(gran[i][j].spiketimes)
        }
    }
    hist = work.sumgauss(0,tstop,1,$1)
    sprint(filename,"%s.gran.smhist",$s2)
    outfile.wopen(filename)
    outfile.printf("# Granule cell cell smoothed histogram\n")
    hist.printf(outfile,"%8.3f\n")
    outfile.close()
    work.resize(0)
    hist.remove(0,ttrans)
    work.spcrm(hist)
    sprint(filename,"%s.gran.pow",$s2)
    outfile.wopen(filename)
    outfile.printf("# Power spectrum of Granule cell smoothed histogram\n")
    work.print(outfile,"%9.5f\n")
    outfile.close()
}

proc print_raster() { local i,j,k // 1 argument - filename root
    sprint(filename,"%s.ras",$s1)
    outfile.wopen(filename)
    outfile.printf("# Mitral cell raster plot\n")
    for i = 0, nmitx-1 {
        for j = 0, nmity-1 {
            for k = 0, mit[i][j].spiketimes.size()-1 {
                outfile.printf("%d %d %d %10.3f\n",i,j,
                              i*nmity+j,mit[i][j].spiketimes.x[k])
            }
        }
    }
    outfile.close()
}

proc print_gran_raster() { local i,j,k // 1 argument - filename root
    sprint(filename,"%s.gran.ras",$s1)
    outfile.wopen(filename)
    outfile.printf("# Granule cell raster plot\n")
    for i = 0, ngranz-1 {
        for j = 0, ngrany-1 {
            for k = 0, gran[i][j].spiketimes.size()-1 {
                outfile.printf("%d %d %d %10.3f\n",i,j,
                              i*ngrany+j,gran[i][j].spiketimes.x[k])
            }
        }
    }
    outfile.close()
}

proc print_isi_stats() { local i,j // 1 argument - filename root
    sprint(filename,"%s.stats",$s1)
    outfile.wopen(filename)
    outfile.printf("#Interspike interval statistics for mitral cells\n")
    outfile.printf("# i j n mean median stdev \n")
    for i = 0, nmitx-1 {
        for j = 0, nmity-1 {
            calc_isis(i,j,ttrans)
            outfile.printf("%3d%3d%4d",i,j,isi.size())
            if (isi.size() > 0) {
                outfile.printf("%8.2f%8.2f",isi.mean(),isi.median())
                if (isi.size() > 1) {
                    outfile.printf("%8.2f\n",isi.stdev())
                }
            } else { outfile.printf("\n") }
        }
    }
    outfile.printf("#Interspike interval statistics for granule cells\n")
    outfile.printf("# i j n mean median stdev \n")
    for i = 0, ngranz-1 {
        for j = 0, ngrany-1 {
            calc_gran_isis(i,j,ttrans)
            outfile.printf("%3d%3d%4d",i,j,isi.size())
            if (isi.size() > 0) {
                outfile.printf("%8.2f%8.2f",isi.mean(),isi.median())
                if (isi.size() > 1) {
                    outfile.printf("%8.2f\n",isi.stdev())
                }
            } else { outfile.printf("\n") }
        }
    }
    outfile.close()
}

proc print_si() { // 1 argument - fileroot
    print "<<< Calculating synchronization indices >>>"
    sprint(filename,"%s.synch",$s1)
    outfile.wopen(filename)
    outfile.printf("Phase-locking index:      %10.5f\n",synch_index2a())
    outfile.printf("Synchronization index:   %10.5f\n",synch_index3a())
    outfile.close()
}

```


References

- [1] ADRIAN, E. D. (1942). Olfactory reactions in the brain of the hedgehog. *Journal of Physiology (London)* **100**:459–473.
- [2] ANTÓN, P. S., GRANGER, R. AND LYNCH, G. (1993). Simulated dendritic spines influence reciprocal synaptic strengths and lateral inhibition in the olfactory bulb. *Brain Research* **628**:157–165.
- [3] ANTÓN, P. S., LYNCH, G. AND GRANGER, R. (1991). Computation of frequency-to-spatial transform by olfactory bulb glomeruli. *Biological Cybernetics* **65**:407–414.
- [4] ARADI, I. AND ÉRDI, P. (1996). Signal generation and propagation in the olfactory bulb: multi-compartmental modelling. *Computers Math. Applic.* **32**:1–27.
- [5] ARONIADOU-ANDERJASKA, V., ENNIS, M. AND SHIPLEY, M. T. (1999). Current-source density analysis in the rat olfactory bulb: laminar distribution of kainate/AMPA- and NMDA-receptor-mediated currents. *Journal of Neurophysiology* **81**:15–28.
- [6] BARDONI, R., MAGHERINI, P. C. AND BELLUZZI, O. (1995). Sodium current in periglomerular cells of frog olfactory bulb in vitro. *Brain Research* **703**:19–25.
- [7] BARDONI, R., PUOPOLI, M., MAGHERINI, P. C. AND BELLUZZI, O. (1996). Potassium currents in periglomerular cells of frog olfactory bulb in vitro. *Neuroscience Letters* **210**:95–98.
- [8] BELLUSCIO, L., KOENTGES, G., AXEL, R. AND DULAC, C. (1999). A map of pheromone receptor activation in the mammalian brain. *Neuron* **97**:209–220.
- [9] BERKOWICZ, D. A. AND TROMBLEY, P. Q. (2000). Dopaminergic modulation at the olfactory nerve synapse. *Brain Research* **855**:90–99.
- [10] BERKOWICZ, D. A., TROMBLEY, P. Q. AND SHEPHERD, G. M. (1994). Evidence for glutamate as the olfactory receptor cell neurotransmitter. *Journal of Neurophysiology* **71**:2557–2561.
- [11] BHALLA, U. S. AND BOWER, J. M. (1993). Exploring parameter space in detailed single cell models: simulations of the mitral and granule cells of the olfactory bulb. *Journal of Neurophysiology* **69**:1948–1965.
- [12] BHALLA, U. S. AND BOWER, J. M. (1997). Multiday recordings from olfactory bulb neurons in awake freely moving rats: spatially and temporally organised variability in odorant response properties. *Journal of Computational Neuroscience* **4**:221–256.
- [13] BHATNAGAR, K. P., KENNEDY, R. C., BARON, G. AND GREENBERG, R. A. (1987). Number of mitral cells and the bulb volume in the aging human olfactory bulb: a quantitative morphological study. *Anatomical Record* **218**:73–87.
- [14] BISCHOFBERGER, J. AND JONAS, P. (1997). Action potential propagation into the presynaptic dendrites of rat mitral cells. *Journal of Physiology (London)* **504**:359–365.

- [15] BISCHOFBERGER, J. AND SCHILD, D. (1995). Different spatial patterns of $[Ca^{2+}]$ increase caused by N- and L-type Ca^{2+} channel activation in frog olfactory bulb neurones. *Journal of Physiology (London)* **487**:305–317.
- [16] BONINO, M., CANTINO, D. AND SASSOÈ-POGNETTO, M. (1999). Cellular and subcellular localization of γ -aminobutyric acid_B receptors in the rat olfactory bulb. *Neuroscience Letters* **274**:195–198.
- [17] BRENNAN, P. A. AND KEVERNE, E. B. (1997). Neural mechanisms of mammalian olfactory learning. *Progress in Neurobiology* **51**:457–481.
- [18] BUCK, L. B. (1996). Information coding in the vertebrate olfactory system. *Annual Review of Neuroscience* **19**:517–544.
- [19] BUCK, L. B. AND AXEL, R. (1991). A novel multigene family may encode odorant receptors: a molecular basis for odor recognition. *Cell* **65**:175–187.
- [20] BUONVISO, N., CHAPUT, M. A. AND BERTHOMMIER, F. (1992). Temporal pattern analyses in pairs of neighboring mitral cells. *Journal of Neurophysiology* **68**:417–424.
- [21] BUONVISO, N., CHAPUT, M. A. AND SCOTT, J. W. (1991). Mitral cell-to-glomerulus connectivity - an HRP study of the orientation of mitral cell apical dendrites. *Journal of Comparative Neurology* **307**:57–64.
- [22] BUSH, P. C. AND SEJNOWSKI, T. J. (1993). Reduced compartmental models of neocortical pyramidal cells. *Journal of Neuroscience Methods* **46**:159–166.
- [23] CASTILLO, P. E., CARLETON, A., VINCENT, J. D. AND LLEDO, P. M. (1999). Multiple and opposing roles of cholinergic transmission in the main olfactory bulb. *Journal of Neuroscience* **19**:9180–9191.
- [24] CHEN, W. R., MIDTGAARD, J. AND SHEPHERD, G. M. (1997). Forward and backward propagation of dendritic impulses and their synaptic control in mitral cells. *Science* **278**:463–467.
- [25] CHEN, W. R. AND SHEPHERD, G. M. (1997). Membrane and synaptic properties of mitral cells in slices of rat olfactory bulb. *Brain Research* **745**:189–196.
- [26] CHEN, W. R., XIONG, W. AND SHEPHERD, G. M. (2000). Analysis of relations between NMDA receptors and GABA release at olfactory bulb reciprocal synapses. *Neuron* **25**:625–633.
- [27] CHOW, C. C. (1998). Phase-locking in weakly heterogeneous neuronal networks. *Physica D* **118**:343–370.
- [28] CIOMBOR, K. J., ENNIS, M. AND SHIPLEY, M. T. (1999). Norepinephrine increases rat mitral cell excitatory responses to weak olfactory nerve input via alpha-1 receptors *in vitro*. *Neuroscience* **90**:595–606.
- [29] CLYNE, P. J., WARR, C. G., FREEMAN, M. R., LESSING, D., KIM, J. AND CARLSON, J. R. (1999). A novel family of divergent seven-transmembrane proteins: candidate odorant receptors in *Drosophila*. *Neuron* **22**:327–338.
- [30] COOMBES, S. (1999). Liapunov exponents and mode-locked solutions for integrate-and-fire dynamical systems. *Physics Letters A* **255**:49–57.
- [31] COOMBES, S. AND BRESSLOFF, P. C. (1999). Mode-locking and Arnold tongues in integrate-and-fire neural oscillators. *Physical Review E* **60**:2086–2096.
- [32] DAVISON, A. P., FENG, J. AND BROWN, D. (2000). A reduced compartmental model of the mitral cell for use in network models of the olfactory bulb. *Brain Research Bulletin* **51**:393–399.

- [33] DESMAISONS, D., VINCENT, J. D. AND LLEDO, P. M. (1999). Control of action potential timing by intrinsic subthreshold oscillations in olfactory bulb output neurons. *Journal of Neuroscience* **19**:10727–10737.
- [34] DESTEXHE, A., MAINEN, Z. F. AND SEJNOWSKI, T. J. (1994). An efficient method for computing synaptic conductances based on a kinetic model of receptor binding. *Neural Computation* **6**:14–18.
- [35] DESTEXHE, A., MAINEN, Z. F. AND SEJNOWSKI, T. J. (1998). Kinetic models of synaptic transmission. In: C. Koch and I. Segev (editors), *Methods in Neuronal Modeling: From Ions to Networks*, pp. 1–25. MIT Press, Cambridge, Massachusetts, 2nd edition.
- [36] DODD, J. AND CASTELLUCCI, V. F. (1991). Smell and taste: The chemical senses. In: E. R. Kandel, J. H. Schwartz and T. M. Jessel (editors), *Principles of Neural Science*, chapter 34, pp. 512–529. Appleton and Lange, East Norwalk, Connecticut, 3rd edition.
- [37] DORRIES, K. M. AND KAUER, J. S. (2000). Relationships between odor-elicited oscillations in the salamander olfactory epithelium and olfactory bulb. *Journal of Neurophysiology* **83**:754–765.
- [38] DRYER, L. AND GRAZIADEI, P. P. C. (1994). Mitral cell dendrites – a comparative approach. *Anatomy and Embryology* **189**:91–106.
- [39] DUCHAMP-VIRET, P., DUCHAMP, A. AND CHAPUT, M. A. (2000). Peripheral odor coding in the rat and frog: quality and intensity specification. *Journal of Neuroscience* **20**:2383–2390.
- [40] EISTHEN, H. L. (1997). Evolution of vertebrate olfactory systems. *Brain, Behaviour and Evolution* **50**:222–233.
- [41] ENNIS, M., ZIMMER, L. A. AND SHIPLEY, M. T. (1996). Olfactory nerve-stimulation activates rat mitral cells via NMDA and non-NMDA receptors in-vitro. *NeuroReport* **7**:989–992.
- [42] EZEH, P. I., WELLIS, D. P. AND SCOTT, J. W. (1993). Organization of inhibition in the rat olfactory bulb external plexiform layer. *Journal of Neurophysiology* **70**:263–274.
- [43] FISCHER, T. AND ZIPPEL, H. P. (1989). The effects of cryogenic blockade of the centrifugal, bulbopetal pathways on the dynamic and static response characteristics of goldfish olfactory-bulb mitral cells. *Experimental Brain Research* **75**:390–400.
- [44] FRIEDRICH, R. W. AND KORSCHING, S. I. (1997). Combinatorial and chemotopic odorant coding in the zebrafish olfactory bulb visualized by optical imaging. *Neuron* **18**:737–752.
- [45] FRIEDRICH, R. W. AND KORSCHING, S. I. (1998). Chemotopic, combinatorial and noncombinatorial odorant representations in the olfactory bulb revealed using a voltage-sensitive axon tracer. *The Journal of Neuroscience* **18**:9977–9988.
- [46] GERSTNER, W., VAN HEMMEN, J. L. AND COWAN, J. D. (1996). What matters in neuronal locking? *Neural Computation* **8**:1653–1676.
- [47] GREER, C. A. (1987). Golgi analyses of dendritic organization among denervated olfactory-bulb granule cells. *Journal of Comparative Neurology* **257**:442–452.
- [48] GUTHRIE, K. M., ANDERSON, A. J., LEON, M. AND GALL, C. (1993). Odor-induced increases in *c-fos* mRNA expression reveal an anatomical “unit” for odor processing in olfactory bulb. *Proceedings of the National Academy of Sciences of the USA* **90**:3329–3333.
- [49] HALABISKY, B., FRIEDMAN, D., RADOJICIC, M. AND STROWBRIDGE, B. W. (2000). Calcium influx through NMDA receptors directly evokes GABA release in olfactory bulb granule cells. *Journal of Neuroscience* **20**:5124–5134.

- [50] HALÁSZ, N., HÖKFELT, T., NORMAN, A. W. AND GOLDSTEIN, M. (1985). Tyrosine hydroxylase and 28k-vitamin D-dependent calcium binding protein are localized in different subpopulations of periglomerular cells of the rat olfactory bulb. *Neuroscience Letters* **61**:103–107.
- [51] HAMILTON, K. A. AND KAUER, J. S. (1988). Responses of mitral/tufted cells to orthodromic and antidromic electrical-stimulation in the olfactory bulb of the tiger salamander. *Journal of Neurophysiology* **59**:1736–1755.
- [52] HAMILTON, K. A. AND KAUER, J. S. (1989). Patterns of intracellular potentials in salamander mitral/tufted cells in response to odor stimulation. *Journal of Neurophysiology* **62**:609–625.
- [53] HARRISON, T. A. AND SCOTT, J. W. (1986). Olfactory bulb responses to odor stimulation: analysis of response pattern and intensity relationships. *Journal of Neurophysiology* **56**:1571–1589.
- [54] HENDIN, O., HORN, D. AND HOPFIELD, J. J. (1994). Decomposition of a mixture of signals in a model of the olfactory bulb. *Proceedings of the National Academy of Sciences of the USA* **91**:5942–5946.
- [55] HENDIN, O., HORN, D. AND TSODYKS, M. V. (1997). The role of inhibition in an associative memory model of the olfactory bulb. *Journal of Computational Neuroscience* **4**:173–182.
- [56] HENDIN, O., HORN, D. AND TSODYKS, M. V. (1998). Associative memory and segmentation in an oscillatory neural model of the olfactory bulb. *Journal of Computational Neuroscience* **5**:157–169.
- [57] HINDS, J. W. AND MCNELLY, N. A. (1977). Aging of the rat olfactory bulb: growth and atrophy of constituent layers and changes in size and number of mitral cells. *Journal of Comparative Neurology* **171**:345–368.
- [58] HOPFIELD, J. J. (1991). Olfactory computation and object perception. *Proceedings of the National Academy of Sciences of the USA* **88**:6462–6466.
- [59] HOPFIELD, J. J. (1995). Pattern recognition computation using action potential timing for stimulus representation. *Nature* **376**:33–36.
- [60] HOSHINO, O., KASHIMORI, Y. AND KAMBARA, T. (1998). An olfactory recognition model based on spatiotemporal encoding of odor quality in the olfactory bulb. *Biological Cybernetics* **79**:109–120.
- [61] IMAMURA, K., MATAGA, N. AND MORI, K. (1992). Coding of odor molecules by mitral/tufted cells in rabbit olfactory bulb. I. aliphatic compounds. *Journal of Neurophysiology* **68**:1986–2002.
- [62] ISAACSON, J. S. (1999). Glutamate spillover mediates excitatory transmission in the rat olfactory bulb. *Neuron* **23**:377–384.
- [63] ISAACSON, J. S. AND STROWBRIDGE, B. W. (1998). Olfactory reciprocal synapses: dendritic signalling in the CNS. *Neuron* **20**:749–761.
- [64] JAHR, C. E. AND STEVENS, C. F. (1990). Voltage dependence of NMDA-activated macroscopic conductances predicted by single-channel kinetics. *Journal of Neuroscience* **10**:3178–3182.
- [65] JOHNSON, B. A. AND LEON, M. (2000). Molecular representations of odorants in the glomerular layer of the rat olfactory bulb and the effects of stimulus concentration. *Journal of Comparative Neurology* **422**:496–509.
- [66] JOHNSON, B. A. AND LEON, M. (2000). Odorant molecular length: one aspect of the olfactory code. *Journal of Comparative Neurology* **426**:330–338.
- [67] KASHIWADANI, H., SASAKI, Y. F., UCHIDA, N. AND MORI, K. (1999). Synchronized oscillatory discharges of mitral/tufted cells with different molecular receptive ranges in the rabbit olfactory bulb. *Journal of Neurophysiology* **82**:1786–1792.

- [68] KENDRICK, K. M., DA COSTA, A. P. C., BROAD, K. D., OHKURA, S., GUEVARA, R., LÉVY, F. AND KEVERNE, E. B. (1997). Neural control of maternal behaviour and olfactory recognition of offspring. *Brain Research Bulletin* **44**:383–395.
- [69] KENDRICK, K. M., LÉVY, F. AND KEVERNE, E. B. (1992). Changes in the sensory processing of olfactory signals induced by birth in sheep. *Science* **256**:833–836.
- [70] KISHI, K., MORI, K. AND OJIMA, H. (1984). Distribution of local axon collaterals of mitral, displaced mitral, and tufted cells in the rabbit olfactory-bulb. *Journal of Comparative Neurology* **225**:511–526.
- [71] KLENOFF, J. R. AND GREER, C. A. (1998). Postnatal development of olfactory receptor cell axonal arbors. *Journal of Comparative Neurology* **390**:256–267.
- [72] KOSAKA, T., HATAGUCHI, Y., HAMA, K., NAGATSU, I. AND WU, J. Y. (1985). Coexistence of immunoreactivities for glutamate decarboxylase and tyrosine hydroxylase in some neurons in the periglomerular region of the rat main olfactory bulb: possible coexistence of gamma-aminobutyric acid (GABA) and dopamine. *Brain Research* **343**:166–171.
- [73] KURAHASHI, T., LOWE, G. AND GOLD, G. H. (1994). Suppression of odorant responses by odorants in olfactory receptor cells. *Science* **265**:118–120.
- [74] LAM, Y. W., COHEN, L. B., WACHOWIAK, M. AND ZOCHOWSKI, M. R. (2000). Odors elicit three different oscillations in the turtle olfactory bulb. *Journal of Neuroscience* **20**:749–762.
- [75] LAURENT, G. (1996). Dynamical representation of odors by oscillating and evolving neural assemblies. *Trends in Neuroscience* **19**:489–496.
- [76] LAURENT, G. (1999). A systems perspective on early olfactory coding. *Science* **286**:723–728.
- [77] LAURENT, G., WEHR, M. AND DAVIDOWITZ, H. (1996). Temporal representations of odors in an olfactory network. *Journal of Neuroscience* **16**:3837–3847.
- [78] LI, Z. (1990). A model of olfactory adaptation and sensitivity enhancement in the olfactory bulb. *Biological Cybernetics* **62**:349–361.
- [79] LI, Z. AND HERTZ, J. (2000). Odor recognition and segmentation by coupled olfactory bulb and cortical networks. *Network* **11**:83–102.
- [80] LI, Z. AND HOPFIELD, J. J. (1989). Modeling the olfactory bulb and its neural oscillatory processings. *Biological Cybernetics* **61**:379–392.
- [81] LINSTER, C. AND GERVAIS, R. (1996). Investigation of the role of interneurons and their modulation by centrifugal fibres in a neural model of the olfactory bulb. *Journal of Computational Neuroscience* **3**:225–246.
- [82] LINSTER, C. AND HASSELMO, M. (1997). Modulation of inhibition in a model of olfactory bulb reduces overlap in the neural representation of olfactory stimuli. *Behavioural Brain Research* **84**:117–127.
- [83] LINSTER, C. AND MASSON, C. (1996). A neural model of olfactory sensory memory in the honeybee's antennal lobe. *Neural Computation* **8**:94–114.
- [84] LINSTER, C., MASSON, C., KERSZBERG, M., PERSONNAZ, L. AND DREYFUS, G. (1993). Computational diversity in a formal model of the insect olfactory macrolomerulus. *Neural Computation* **5**:228–241.
- [85] MACLEOD, K., BÄCKER, A. AND LAURENT, G. (1998). Who reads temporal information contained across synchronized and oscillatory spike trains? *Nature* **395**:693–698.

- [86] MACRIDES, F. AND SCHNEIDER, S. P. (1982). Laminar organization of mitral and tufted cells in the main olfactory-bulb of the adult hamster. *Journal of Comparative Neurology* **208**:419–430.
- [87] MAEX, R. AND DE SCHUTTER, E. (1998). Synchronization of Golgi and granule cell firing in a detailed network model of the cerebellar granule cell layer. *Journal of Neurophysiology* **80**:2521–2537.
- [88] MALNIC, B., HIRONO, J., SATO, T. AND BUCK, L. B. (1999). Combinatorial receptor codes for odors. *Cell* **96**:713–723.
- [89] MARTINEZ, D. P. AND FREEMAN, W. J. (1984). Periglomerular cell action on mitral cells in olfactory bulb shown by current source density analysis. *Brain Research* **308**:223–233.
- [90] MASSON, C. AND LINSTER, C. (1996). Towards a cognitive understanding of odor discrimination: combining experimental and theoretical approaches. *Behavioural Processes* **35**:63–82.
- [91] MEISAMI, E. (1989). A proposed relationship between increases in the number of olfactory receptor neurons, convergence ratio and sensitivity in the developing rat. *Developmental Brain Research* **46**:9–19.
- [92] MEREDITH, M. (1992). Neural circuit computation: complex patterns in the olfactory bulb. *Brain Research Bulletin* **29**:111–117.
- [93] MOMBAERTS, P., WANG, F., DULAC, C., CHAO, S. K., NEMES, A., MENDELSOHN, M., EDMONDSON, J. AND AXEL, R. (1996). Visualizing an olfactory sensory map. *Cell* **87**:675–686.
- [94] MORI, K., KISHI, K. AND OJIMA, H. (1983). Distribution of dendrites of mitral, displaced mitral, tufted, and granule cells in the rabbit olfactory-bulb. *Journal of Comparative Neurology* **219**:339–355.
- [95] MORI, K., NAGAO, H. AND SASAKI, Y. F. (1998). Computation of molecular information in mammalian olfactory systems. *Network* **9**:R79–R102.
- [96] MORI, K., NAGAO, H. AND YOSHIHARA, Y. (1999). The olfactory bulb: coding and processing of odor molecule information. *Science* **286**:711–715.
- [97] MORI, K., NOWYCKY, M. C. AND SHEPHERD, G. M. (1981). Electro-physiological analysis of mitral cells in the isolated turtle olfactory-bulb. *Journal of Physiology (London)* **314**:281–294.
- [98] MORI, K. AND TAKAGI, S. F. (1978). An intracellular study of dendrodendritic inhibitory synapses on mitral cells in the rabbit olfactory bulb. *Journal of Physiology (London)* **279**:569–588.
- [99] MOTOKIZAWA, F. (1996). Odor representation and discrimination in mitral tufted cells of the rat olfactory-bulb. *Experimental Brain Research* **112**:24–34.
- [100] MOTOKIZAWA, F. AND OGAWA, Y. (1997). Discharge properties of mitral/tufted cells in the olfactory bulb of cats. *Brain Research* **763**:285–287.
- [101] NEMITZ, J. W. AND GOLDBERG, S. J. (1983). Neuronal responses of rat pyriform cortex to odor stimulation: an extracellular and intracellular study. *Journal of Neurophysiology* **49**:188–203.
- [102] NICKELL, W. T., BEHBEHANI, M. M. AND SHIPLEY, M. T. (1994). Evidence for GABA_B-mediated inhibition of transmission from the olfactory nerve to mitral cells in the rat olfactory-bulb. *Brain Research Bulletin* **35**:119–123.
- [103] NICKELL, W. T., SHIPLEY, M. T. AND BEHBEHANI, M. M. (1996). Orthodromic synaptic activation of rat olfactory-bulb mitral cells in isolated slices. *Brain Research Bulletin* **39**:57–62.

- [104] NOWYCKY, M. C., MORI, K. AND SHEPHERD, G. M. (1981). Blockade of synaptic inhibition reveals long-lasting synaptic excitation in isolated turtle olfactory bulb. *Journal of Neurophysiology* **46**:649–658.
- [105] OKUTANI, F., KABA, H., TAKAHASHI, S. AND SETO, K. (1998). The biphasic effects of locus coeruleus noradrenergic activation on dendrodendritic inhibition in the rat olfactory bulb. *Brain Research* **783**:272–279.
- [106] ORONA, E., RAINER, E. C. AND SCOTT, J. W. (1984). Dendritic and axonal organization of mitral and tufted cells in the rat olfactory-bulb. *Journal of Comparative Neurology* **226**:346–356.
- [107] PANHUBER, H., LAING, D. G., WILLCOX, M. E., EAGLESON, G. K. AND PITTMAN, E. A. (1985). The distribution of the size and number of mitral cells in the olfactory-bulb of the rat. *Journal of Anatomy* **140**:297–308.
- [108] PETRALIA, R. S. AND WENTHOLD, R. J. (1992). Light and electron immunocytochemical localization of AMPA selective glutamate receptors in the rat brain. *Journal of Comparative Neurology* **318**:329–354.
- [109] PETRALIA, R. S., YOKOTANI, N. AND WENTHOLD, R. J. (1994). Light and electron microscope distribution of the NMDA receptor subunit NMDAR1 in the rat nervous system using a selective anti-peptide antibody. *Journal of Neuroscience* **14**:667–696.
- [110] PINSKY, P. F. AND RINZEL, J. (1994). Intrinsic and network rhythmogenesis in a reduced Traub model for CA3 neurons. *Journal of Computational Neuroscience* **1**:39–60.
- [111] POMEROY, S. L., LAMANTIA, A. S. AND PURVES, D. (1990). Postnatal construction of neural circuitry in the mouse olfactory bulb. *Journal of Neuroscience* **10**:1952–1966.
- [112] PRESS, W. H., FLANNERY, B. P., TEUKOLSKY, S. A. AND VETTERLING, W. T. (1989). *Numerical Recipes: The Art of Scientific Computing*. Cambridge University Press, Cambridge.
- [113] PRICE, J. L. AND POWELL, T. P. S. (1970). The morphology of the granule cells of the olfactory bulb. *Journal of Cell Science* **7**:91–123.
- [114] PRICE, J. L. AND POWELL, T. P. S. (1970). The synaptology of the granule cells of the olfactory bulb. *Journal of Cell Science* **7**:125–155.
- [115] PROTOPAPAS, A. D., VANIER, M. AND BOWER, J. M. (1998). Simulating large networks of neurons. In: C. Koch and I. Segev (editors), *Methods in Neuronal Modeling: From Ions to Networks*, chapter 13, pp. 461–498. MIT Press, Cambridge, Massachusetts, 2nd edition.
- [116] PUOPOLI, M. AND BELLUZZI, O. (1996). Sodium current in periglomerular cells of rat olfactory bulb in vitro. *NeuroReport* **7**:1846–1850.
- [117] PUOPOLI, M. AND BELLUZZI, O. (1998). Functional heterogeneity of periglomerular cells in the rat olfactory bulb. *European Journal of Neuroscience* **10**:1073–1083.
- [118] RALL, W. AND AGMON-SNIR, H. (1998). Cable theory for dendritic neurons. In: C. Koch and I. Segev (editors), *Methods in Neuronal Modeling: From Ions to Networks*, pp. 27–92. MIT Press, Cambridge, Massachusetts, 2nd edition.
- [119] RALL, W. AND SHEPHERD, G. M. (1968). Theoretical reconstruction of field potentials and dendrodendritic synaptic interactions in olfactory bulb. *Journal of Neurophysiology* **31**:884–915.
- [120] REYHER, C. K. H., LÜBKE, J., LARSEN, W. J., HENDRIX, G. M., SHIPLEY, M. T. AND BAUMGARTEN, H. G. (1991). Olfactory bulb granule cell aggregates: morphological evidence for interperikaryal electrotonic coupling via gap junctions. *Journal of Neuroscience* **11**:1485–1495.

- [121] ROYET, J. P., DISTEL, H., HUDSON, R. AND GERVAIS, R. (1998). A re-estimation of the number of glomeruli and mitral cells in the olfactory bulb of rabbit. *Brain Research* **788**:35–42.
- [122] RUBIN, B. D. AND KATZ, L. C. (1999). Optical imaging of odorant representations in the mammalian olfactory bulb. *Neuron* **23**:499–511.
- [123] SCHILD, D., GEILING, H. AND BISCHOFBERGER, J. (1995). Imaging of L-type Ca^{2+} channels in olfactory bulb neurones using fluorescent dihydropyridine and a styryl dye. *Journal of Neuroscience Methods* **59**:183–190.
- [124] SCHNEIDER, S. P. AND SCOTT, J. W. (1983). Orthodromic response properties of rat olfactory bulb mitral and tufted cells correlate with their projection patterns. *Journal of Neurophysiology* **50**:358–378.
- [125] SCHOPPA, N. E., KINZIE, J. M., SAHARA, Y., SEGERSON, T. P. AND WESTBROOK, G. L. (1998). Dendrodendritic inhibition in the olfactory bulb is driven by NMDA receptors. *Journal of Neuroscience* **18**:6790–6802.
- [126] SCHOPPA, N. E. AND WESTBROOK, G. L. (1999). Regulation of synaptic timing in the olfactory bulb by an A-type potassium current. *Nature Neuroscience* **2**:1106–1113.
- [127] SCHUTTER, E. D. (1999). Using realistic models to study synaptic integration in cerebellar Purkinje cells. *Reviews in the Neurosciences* **10**:233–245.
- [128] SCHUTTER, E. D. AND BOWER, J. M. (1994). An active membrane model of the cerebellar Purkinje cell. I. Simulation of current clamps in slice. *Journal of Neurophysiology* **71**:375–400.
- [129] SCHUTTER, E. D. AND BOWER, J. M. (1994). An active membrane model of the cerebellar Purkinje cell. II. Simulation of synaptic responses. *Journal of Neurophysiology* **71**:401–419.
- [130] SEGEV, I. AND BURKE, R. E. (1998). Compartmental models of complex neurons. In: C. Koch and I. Segev (editors), *Methods in Neuronal Modeling: From Ions to Networks*, pp. 1–25. MIT Press, Cambridge, Massachusetts, 2nd edition.
- [131] SHADLEN, M. N. AND NEWSOME, W. T. (1994). Noise, neural codes and cortical organisation. *Current Opinion in Neurobiology* **4**:569–579.
- [132] SHEN, G. Y., CHEN, W. R., MIDTGAARD, J., SHEPHERD, G. M. AND HINES, M. L. (1999). Computational analysis of action potential initiation in mitral cell soma and dendrites based on dual patch recordings. *Journal of Neurophysiology* **82**:3006–3020.
- [133] SHEPHERD, G. M. (1972). Synaptic organisation of the mammalian olfactory bulb. *Physiological Reviews* **52**:864–917.
- [134] SHEPHERD, G. M. (1994). *Neurobiology*. Oxford University Press, Oxford, 3rd edition.
- [135] SHEPHERD, G. M. AND GREER, C. A. (1998). Olfactory bulb. In: G. M. Shepherd (editor), *The Synaptic Organization of the Brain*, chapter 5, pp. 159–203. Oxford University Press, Oxford, 4th edition.
- [136] SINGER, W. AND GRAY, C. M. (1995). Visual feature integration and the temporal correlation hypothesis. *Annual Review of Neuroscience* **18**:555–586.
- [137] SOFTKY, W. R. (1995). Simple codes versus efficient codes. *Current Opinion in Neurobiology* **5**:239–247.
- [138] STOPFER, M., BHAGAVAN, S., SMITH, B. H. AND LAURENT, G. (1997). Impaired odour discrimination on desynchronisation of odour-encoding neural assemblies. *Nature* **390**:70–74.

- [139] STRATFORD, K., MASON, A., LARKMAN, A., MAJOR, G. AND JACK, J. (1989). The modelling of pyramidal neurones in the visual cortex. In: R. Durbin, C. Miall and G. Mitchison (editors), *The Computing Neuron*, chapter 16, pp. 296–321. Addison-Wesley, Wokingham.
- [140] STRAUSFELD, N. J. AND HILDEBRAND, J. G. (1999). Olfactory systems: common design, uncommon origins? *Current Opinion in Neurobiology* **9**:634–639.
- [141] TRAUB, R. D., BIBBIG, A., FISAHN, A., LEBEAU, F. E. N., WHITTINGTON, M. A. AND BUHL, E. H. (2000). A model of gamma-frequency network oscillations induced in the rat CA3 region by carbachol in vitro. *European Journal of Neuroscience* **12**:4093–4106.
- [142] TRAUB, R. D., JEFFERYS, J. G. R., MILES, R., WHITTINGTON, M. A. AND TÓTH, K. (1994). A branching dendritic model of a rodent CA3 pyramidal neurone. *Journal of Physiology (London)* **481**:79–95.
- [143] TRAUB, R. D., WONG, R. K. S., MILES, R. AND MICHELSON, H. (1991). A model of a CA3 hippocampal pyramidal neuron incorporating voltage-clamp data on intrinsic conductances. *Journal of Neurophysiology* **66**:635–650.
- [144] TRELOAR, H., WALTERS, E., MARGOLIS, F. AND KEY, B. (1996). Olfactory glomeruli are innervated by more than one distinct subset of primary sensory olfactory neurons in mice. *Journal of Comparative Neurology* **367**:550–562.
- [145] VAN DEN POL, A. N. (1995). Presynaptic metabotropic glutamate receptors in adult and developing neurons: autoexcitation in the olfactory bulb. *Journal of Comparative Neurology* **359**:253–271.
- [146] VAN VREESWIJK, C., ABBOTT, L. F. AND ERMENTROUT, G. B. (1994). When inhibition not excitation synchronizes neural firing. *Journal of Computational Neuroscience* **1**:313–321.
- [147] VANIER, M. C. AND BOWER, J. M. (1999). A comparative survey of automated parameter-searching methods for compartmental neural models. *Journal of Computational Neuroscience* **7**:149–171.
- [148] VOSSHALL, L. B., AMREIN, H., MOROZOV, P. S., RZHETSKY, A. AND AXEL, R. (1999). A spatial map of olfactory receptor expression in the *Drosophila* antenna. *Cell* **96**:725–736.
- [149] WANG, F., NEMES, A., MENDELSON, M. AND AXEL, R. (1998). Odorant receptors govern the formation of a precise topographic map. *Cell* **93**:47–60.
- [150] WANG, X. Y., MCKENZIE, J. S. AND KEMM, R. E. (1996). Whole-cell K⁺ currents in identified olfactory bulb output neurones of rats. *Journal of Physiology (London)* **490**:63–77.
- [151] WEHR, M. AND LAURENT, G. (1996). Odour encoding by temporal sequences of firing in oscillating neural assemblies. *Nature* **384**:162–166.
- [152] WELLIS, D. P. AND KAUER, J. S. (1994). GABAergic and glutamatergic synaptic input to identified granule cells in salamander olfactory bulb. *Journal of Physiology (London)* **475**:419–430.
- [153] WHITE, J., HAMILTON, K. A., NEFF, S. R. AND KAUER, J. S. (1992). Emergent properties of odor information coding in a representational model of the salamander olfactory bulb. *Journal of Neuroscience* **12**:1772–1780.
- [154] WILSON, M. AND BOWER, J. M. (1992). Cortical oscillations and temporal interactions in a computer simulation of piriform cortex. *Journal of Neurophysiology* **67**:981–995.
- [155] WILSON, M. AND SHEPHERD, G. M. (1995). Olfactory cortex. In: M. A. Arbib (editor), *The Handbook of Brain Theory and Neural Networks*, pp. 669–673. MIT Press, Cambridge, Massachusetts.

- [156] WOOLF, T. B., SHEPHERD, G. M. AND GREER, C. A. (1991). Local information processing in dendritic trees: subsets of spines in granule cells of the mammalian olfactory bulb. *Journal of Neuroscience* **11**:1837–1854.
- [157] YANG, X., RENKEN, R., HYDER, F., SIDDEEK, M., GREER, C. A., SHEPHERD, G. M. AND SCHULMAN, R. G. (1998). Dynamic mapping at the laminar level of odor-elicited responses in rat olfactory bulb by functional MRI. *Proceedings of the National Academy of Sciences of the USA* **95**:7715–7720.
- [158] YOKOI, M., MORI, K. AND NAKANISHI, S. (1995). Refinement of odor molecule tuning by dendrodendritic synaptic inhibition in the olfactory bulb. *Proceedings of the National Academy of Sciences of the USA* **92**:3371–3375.